



Volume 1, January 2016

ISSN: 2455-2259

JOURNAL OF ENERGY AND ENVIRONMENTAL SUSTAINABILITY

- Biofuels ■ Energy Storage System ■ Fuels Cells
- Solar Energy ■ Thermo-chemical Conversion of Biomass
- Transportation ■ Energy Sustainability ■ Environmental Sustainability
- Fossil and Non-fossil Sources of Energy
- New and Renewable Sources and Processes of Energy
 - Solid Waste Management
- Thermal Energy Devices ■ Waste Treatment

Available online at www.jees.in

Journal of Energy and Environmental Sustainability is an official publication of the International Society for Energy, Environment and Sustainability (www.iitk.ac.in/isees/index.htm) dedicated to the areas of conventional and renewable energy that are relevant for environmental sustainability. The journal publishes two issues in a year and offers a platform for high-quality research in the interdisciplinary areas of energy and environmental science and engineering.

About the journal

The journal publishes original articles and reviews on the topics relevant to its scope. The aim of the journal is to advance and disseminate knowledge in the relevant areas of energy and environmental sustainability. The topics covered by the journal include biofuels, energy storage system, fuels cells, solar energy, thermo-chemical conversion of biomass and transportation, etc. For detailed subject classification/topics to know the scope, please refer guide for authors and subject classification.

Editorial board

Editor-in-Chief

Prof Avinash Kumar Agarwal, Indian Institute of Technology, Kanpur, India

Honorary Executive Adviser

Prof Ashok Pandey, CSIR-National Institute for Interdisciplinary Science and Technology, Trivandrum, India

Editors

Prof Suresh Kumar Aggarwal, University of Illinois at Chicago, USA

Prof. Kuni Kitagawa, Nagoya University, Japan

Prof RP Sharma, Indian Institute of Technology, Chennai, India

Prof. Franz Winter, Technical University, Vienna, Austria

Associate Editor

Prof Bhola R Gurjar, Indian Institute of technology, Roorkee, India

Prof. Abhijit Kushari, Indian Institute of Technology, Kanpur, India

Prof. Achintya Mukhopadhyay, Jadavpur University, Kolkata, India

Members

Dr Thallada Bhaskar, CSIR-Indian Institute of Petroleum, Dehradun, India

Prof Edgard Gnansounou, EPFL, Switzerland

Prof Gustaaf Jacobs, San Diego State University, USA

Dr Samir Khanal, University of Hawaii, USA

Prof Duu Jong Lee, National Taiwan University, Tai Pei, Taiwan

Prof Keat-Teong Lee, University Sains Malaya, Kula Lumpur, Malaysia

Dr S Venkata Mohan, CSIR-Indian Institute of Chemical Technology, Hyderabad, India

Prof Hao Huu Ngo, University of Technology, Sydney, Australia

Dr Deepak Pant, Flemish Institute for Technological Research VITO, Belgium

Prof Albert Ratner, University of Iowa, USA

Prof RV Ravikrishna, Indian Institute of Science, Bangalore, India

Dr Sibendu Som, Argonne National Lab, USA

Printed at

Mark Offset Press, Trivandrum

Phone : 0471-2400832

E-mail : marktvm@hotmail.com

JOURNAL OF ENERGY AND ENVIRONMENTAL SUSTAINABILITY

Volume I 2016

EDITOR-IN-CHIEF

PROF. AVINASH KUMAR AGARWAL

HONORARY EXECUTIVE ADVISER

PROF. ASHOK PANDEY

EDITORS

PROF. SURESH KUMAR AGGARWAL

PROF. KUNI KITAGAWA

PROF. R.P SHARMA

PROF. FRANZ WINTER



Journal of Energy and Environmental Sustainability, 1 (2016)

[An official publication of the International Society for Energy, Environment and Sustainability]

CONTENTS

ENERGY SUSTAINABILITY

- CFD Simulations of Complete Circulating Dual Fluidized Bed Systems for Chemical Looping Combustion
Subhodeep Banerjee, Xiao Zhang, Ramesh K. Agarwal 1-9

ENVIRONMENTAL SUSTAINABILITY

- Organic Species Emitted as a Part of Combustion Residue: Fate and Transformation in the Ambient Air
Tarun Gupta, Dharmendra Kumar Singh 10-18
- Numerical Investigation of Swirling Hydrogen Flames: Effect of Swirl and Fuel Jet in Coherent Structures
V Suresh Balaji, Ashoke De, Santanu De 19-33

NEW AND RENEWABLE SOURCES AND PROCESSES OF ENERGY

- Slow Pyrolysis of Jatropha Seed De-oiled Cake and Estimation of Kinetic Parameters
Bhavya B Krishna, Bijoy Biswas, Jitendra Kumar, Rawel Singh, Thallada Bhaskar 34-39
- Startup of Microbial Fuel Cells with Pure Ferric Iron-reducing Bacteria Isolates
Lihong Liu, Duu-Jong Lee, Aijie Wang, Nanqi Ren, Lei Zhang, Jia-Nian Shen 40-46
- Qualitative *in vitro* Evaluation of Plant Growth Promoting Activity of Electrogenic Bacteria From Biohydrogen Producing Microbial Electrolysis Cell Towards Biofertilizer Application
C.Nagendranatha Reddy, K.Arunasri, Dileep Kumar Yeruva, K.Vamshi Krishna, S.Venkata Mohan 47-51
- Catalytic Hydrolysis of Cotton Stalk Biomass Using a Reusable Solid Carbon Acid Catalyst
Mandavi Goswami, S. Meena, S. Navatha, R.B.N. Prasad, B.L.A. Prabhavathi Devi, Rajeev Kumar Sukumaran, Ashok Pandey 52-55

THERMAL ENERGY DEVICES

- Evolution, Trends and Applications of Endoscopy in Internal Combustion Engines
Avinash Kumar Agarwal, Akhilendra Pratap Singh, Anuj Agarwal 56-66
- A Review on the Effects of Biodiesel Blends on Compression Ignition Engine NO_x Emissions
Arun Balakrishnan, Ramkumar N. Parthasarathy, Subramanyam R. Gollahalli 67-76

WASTE TREATMENT

- Advances in Granular Growth Anaerobic Membrane Bioreactor (G-AnMBR) for Low Strength Wastewater Treatment
Cheng Chen, Wenshan Guo, Huu Hao Ngo 77-83



CFD Simulations of Complete Circulating Dual Fluidized Bed Systems for Chemical Looping Combustion

Subhodeep Banerjee, Xiao Zhang, Ramesh K. Agarwal*

Washington University in St. Louis, 1 Brookings Dr., St. Louis, MO 63130, USA

ARTICLE INFO

Received : 12 September 2015
Revised : 28 November 2015
Accepted : 29 November 2015

Keywords:

Chemical Looping, Dual Fluidized Bed Reactors, Multi-phase Flow, Granular Flow Eulerian Simulation, Discrete Element Method

ABSTRACT

Chemical-looping combustion (CLC) is a next generation combustion technology that shows great promise in addressing the need for high-efficiency low-cost carbon capture from fossil fueled power plants. Although there have been a multitude of experimental studies on CLC in recent years, the number of CFD simulations in the literature has been more limited. In this paper, simulation of a CLC reactor is developed using the Eulerian approach in the commercial CFD solver ANSYS Fluent based on a laboratory-scale experiment with a dual fluidized bed CLC reactor to model the chemical reactions in the system. The solid phase consists of a Fe-based oxygen carrier while the gaseous fuel used is syngas. Later, the detailed hydrodynamics in a CLC system designed for solid coal fuel are studied based on a cold flow experimental setup at National Energy Technology Laboratory using the Lagrangian particle-tracking approach. To the authors' knowledge, this work is among the very few CFD simulations of a complete circulating dual fluidized bed system for CLC in three-dimension. It highlights the importance of 3-D simulation of CLC systems and the need for more accurate empirical reaction rate data for future CLC simulations.

© 2016 ISEES, All rights reserved

1. Introduction

The relationship between the global surface temperature of the Earth and the concentration of CO₂ was discovered by Arrhenius (1896). The concentration of CO₂ in the atmosphere has risen from a value of 280 ppm in pre-industrial times to around 370 ppm today. This increase is due to the carbon emissions from fossil fueled power plants and other anthropogenic sources. Since fossil fuels remain the world's main energy source, there is an imminent need for high-efficiency carbon capture technologies to avoid the unequivocal warming of the global climate system (IPCC, 2007). One technology that has shown great promise in recent years for high-efficiency low-cost carbon capture is chemical-looping combustion (CLC).

The CLC process typically utilizes dual fluidized bed reactors—an air reactor and a fuel reactor—and a metal oxide oxygen carrier that circulates between the two reactors, as illustrated in Figure 1(a). Another setup for CLC that has been documented in the literature employs a single vessel with a packed bed of oxygen carrier that is alternately used as an air and fuel reactor via a high temperature gas switching system, shown in Figure 1(b). The main advantage of CLC is that the combustion of fuel in the fuel reactor takes place in the absence of air using oxygen provided by the oxygen carrier. Thus, the flue stream from the fuel reactor is not contaminated or diluted by gases such as nitrogen. This provides a high-purity CO₂ stream available for capture at the fuel reactor outlet without the need for an expensive gas separation process. The reduced oxygen carrier from the fuel reactor is pneumatically transported to the air reactor

where it is re-oxidized by oxygen from air and circulated back to the fuel reactor to complete the loop.

The only energy cost of separation associated with CLC is the cost of solid recirculation; research has shown that this is only about 0.3% of the total energy released by the CLC process (Lyngfelt et al., 2001). This is considerably lower than the benchmark for pre-combustion technologies for carbon capture such as oxy-fuel combustion where the oxygen separation process can consume about 15% of the total energy. Therefore, CLC holds promise as the next-generation combustion technology due to its potential to allow CO₂ capture with little effect on the efficiency of the power plant. Several studies on the energy and exergy of CLC systems in the literature suggest that power efficiencies greater than 50% can be achieved along with nearly complete CO₂ capture (Ishida et al., 1987, 1996; Wolf et al., 2001; Marion, 2006; Andrus et al., 2008).

The oxygen carrier used in CLC directly affects the performance of the CLC system. Since iron is among the cheapest and most abundant metals available on Earth, Fe-based metal oxides such as hematite (Fe₂O₃) are commonly used as the oxygen carrier for CLC. However, past experience with CFD simulations employing the discrete element method has shown that the mass of a fluidized bed of pure Fe₂O₃ particles, given its density of 5,240 kg/m³, is too large and impedes successful fluidization (Banerjee and Agarwal, 2015a). There are also issues with particle agglomeration at high temperatures. The use of an oxygen carrier based on Fe combined with an inert support material has been proposed to circumvent the drawbacks of the pure Fe₂O₃ oxygen carrier (Hossain and de Lasa, 2008). The analysis of several iron oxide particles has

* Corresponding Author: Email: rka@wustl.edu; Phone: +1-314-935-6091

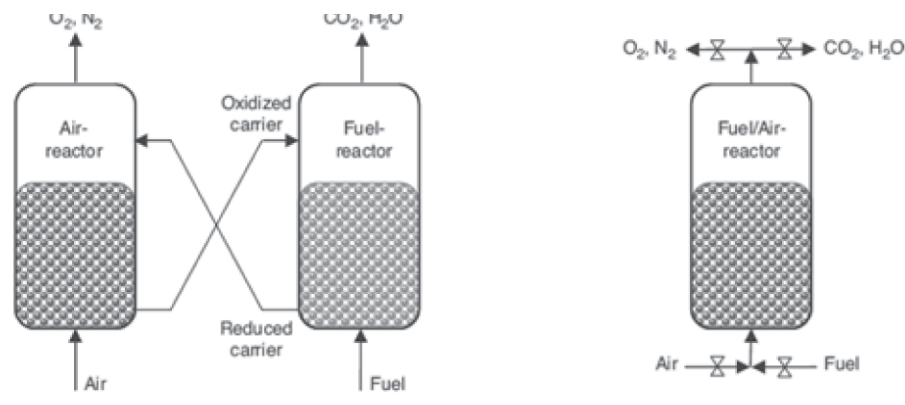


Figure 1: Schematic representation of a chemical-looping combustion system with (a) interconnected fluidized beds, and (b) packed bed with alternating flow (Kruggel-Emden et al., 2011)

shown that an oxygen carrier consisting of 60% Fe₂O₃ by mass and 40% Al₂O₃ provides excellent reactivity for use in CLC and its hardness and resistance to agglomeration is ideal for fluidized bed operation (Johansson, 2007). The Al₂O₃ is inert and acts as a porous support providing a higher surface area for reaction.

Setting up and executing a laboratory experiment can be an expensive and laborious process. On the other hand, CFD provides an efficient means to analyze the performance of a CLC system and characterize the fluid mechanics and chemical kinetics in the system. Initial CFD studies in the field demonstrated the capability of computational methods to model a CLC system and were not based on any particular experiment (Jung and Gamwo, 2008; Deng et al., 2008). Later, the work of Mahalatkar et al. (2011a, 2011b) based on a single reactor setup similar to Figure 1(b) showed that CFD simulation is able to match the reaction mechanics inside a CLC fuel reactor with reasonable accuracy. However, the single reactor setup "cannot be operated with solid fuels and the design and operation of the hot gas switching system is problematic" (Kruggel-Emden et al., 2011). It is desirable to use solid coal for CLC operation due to its likelihood to remain the dominant fossil fuel in the near future, necessitating the use of the dual fluidized bed setup shown in Figure 1(a). The single reactor simulations do not provide any information about the circulation of oxygen carrier inside a dual fluidized bed setup. Therefore, it is important to establish a credible CFD simulation based on a dual fluidized bed setup for CLC.

In the present study, the laboratory experiment of Abad et al. (2007) is used as a basis to perform a detailed CFD simulation of a CLC system. The Eulerian or continuum approach is used for modeling the solid phase. The fluidization behavior in both air and fuel reactor beds and the circulation of the oxygen carrier between the beds is investigated and compared with the experiment. Chemical reactions in the fuel reactor are also considered and the CFD data is validated against the outlet concentrations of various flue gases. Later, the cold flow behavior of the full CLC system at National Energy Technology Laboratory (NETL) is modeled in three dimensions employing the Lagrangian discrete element method (DEM) to follow up on the CFD simulation conducted for this case previously by Parker (2012). The tracking of individual solid particles in time and their interactions with each other as well as with the ambient fluid provide an accurate and realistic representation of the multiphase flow field. These simulations in this work are among the very few present in the current literature of a complete circulating dual fluidized bed setup.

2. Eulerian Simulation of the Experimental CLC Reactor of Abad et al (2007)

In this section, the laboratory scale experiment of Abad et al. (2007) is used as a basis to perform a detailed CFD simulation of a CLC system using the Eulerian multi-fluid approach. It is one of the first CFD models of a complete circulating dual fluidized bed setup. The fluidization behavior in both air and fuel reactor beds and the circulation of the oxygen carrier between the beds is investigated and compared with the experiment. Chemical reactions in the fuel reactor are also considered and the CFD data is validated against the outlet concentrations of various flue gases.

2.1 Description of Experimental Setup

The experiment uses the two-compartment fluidized bed design proposed by Chong et al. (1986) and further investigated by Yang et al. (2003). The experimental reactor setup is illustrated in Figure 2 (a). Dimensions and additional details can be found in the work of Abad et al. (2007). The experiment used a Fe-based oxygen carrier consisting of 60% Fe₂O₃ by mass and 40% Al₂O₃. The particular batch of oxygen carrier used by Abad et al. (2007) was sintered at 1100°C and is designated as F6A1100. The gaseous fuels used in the experiment are natural gas, consisting of primarily CH₄ and syngas consisting of a mixture of 50% CO and 50% H₂. The oxygen carrier particles in the air reactor are oxidized in the presence of air; the fluidizing velocity is greater than the terminal velocity of the particles and carries the particles upwards. The flow then undergoes a sudden expansion in the particle separator at the top of the reactor, which causes the particles to fall back down into the down-comer and enter the fuel reactor.

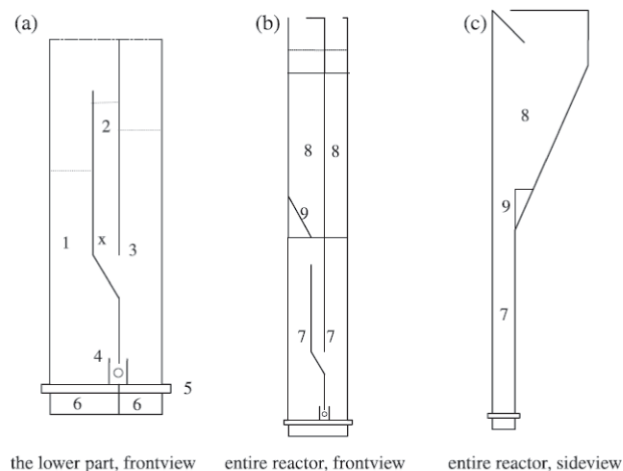


Figure 2 (a): Sketch of experimental reactor: (1) air reactor, (2) down-comer, (3) fuel reactor, (4) slot, (5) gas distributor plate, (6) wind box, (7) reactor part, (8) particle separator, (9) leaning wall. The symbols (x) and (o) indicate fluidization in the down-comer and slot.

The fluidizing velocity in the fuel reactor is below the terminal velocity of the particles, therefore a bubbling bed behavior is exhibited. Therefore, the particles do not reach the particle separator in the fuel reactor. The pressure in the fuel reactor is controlled via a water trap connected to the flue stream of the reactor to ensure minimal gas leakage between the fuel reactor and the air reactor through the down-comer and slot. The flue streams from both reactors are led to a gas analyzer (Rosemount, model NGA-2000) where the concentrations of various gases are measured.

2.2 Numerical Solution Procedure

The modeling work in this paper is performed using the commercial CFD simulation package ANSYS Fluent, release version 14.5 (ANSYS, 2012a, 2012b). Since the flow inside the CD-CLC fuel reactor is chemically active with heat transfer, all the equations of fluid dynamics - the continuity equation, the Navier-Stokes momentum equations, and the energy equation - are considered to compute the flow field. The solid phase is approximated as an Eulerian fluid phase whereby particle variables such as mass, velocity, temperature, etc. are averaged over a region that is large compared to the particle size. Thus, the Eulerian approach only accounts for the bulk behavior of the solids. Constitutive equations for the solid phase pressure and viscosity are required to model the interactions between the solid and gas phases. These are provided by the kinetic theory of granular flow, which is an extension of the classical kinetic gas theory that includes inelastic inter-particle interactions (Patil et al., 2004a, 2004b). The Eulerian framework for modeling a multiphase flow involving a granular solid and a gas has been in use for a few decades and has proven reliable in capturing the experimental behavior.

2.1.1. Eulerian Two-Fluid Model Equations

The standard set of fluid dynamics equations that are used in the commercial CFD software ANSYS Fluent are well-documented in the literature. For multiphase simulations using the Eulerian approach, the standard equations of fluid motion are slightly modified to account for the presence of additional phases by including the porosity α defined as the volume fraction of the respective phase in the computational cell where the equations are applied (ANSYS, 2012b). The continuity equation for phase q is given as

$$\frac{\partial}{\partial t}(\alpha_q \rho_q) + \nabla \cdot (\alpha_q \rho_q \mathbf{u}_q) = \sum (\dot{m}_{pq} - \dot{m}_{qp}) \quad (1)$$

where \dot{m}_{pq} is the mass transfer rate from the p th phase to the q th phase. Each phase (gas or solid) consists of a number of species. A transport equation is solved for each species,

$$\frac{\partial}{\partial t}(\alpha_q \rho_q Y_{iq}) + \nabla \cdot (\alpha_q \rho_q \mathbf{u}_q Y_{iq}) = \sum (\dot{m}_{ij}^{qp} - \dot{m}_{ji}^{pq}) \quad (2)$$

where Y_{iq} is the mass fraction of the species i in the q th phase and \dot{m}_{ij}^{qp} is the mass transfer rate from the j th species of the p th phase to the i th species in the q th phase. In the present study, one gas phase and one solid phase is considered, corresponding to the fuel-gas mixture and the oxygen carrier respectively.

The momentum equation for the gas phase is given as

$$\frac{\partial}{\partial t}(\alpha_g \rho_g \mathbf{u}_g) + \nabla \cdot (\alpha_g \rho_g \mathbf{u}_g \mathbf{u}_g) = -\alpha_g \nabla p + \nabla \cdot \bar{\tau}_g + \alpha_g \rho_g \mathbf{g} + \sum (\mathbf{R}_{sg} + \dot{m}_{sg} \mathbf{u}_{sg} - \dot{m}_{gs} \mathbf{u}_{gs}) \quad (3)$$

where the terms in the summation are source terms added to the standard form of the Navier-Stokes momentum equations to account for the momentum transfer between the solid phase and the gas phase. Specifically, $\mathbf{R}_{sg} = b_{sg} (\mathbf{u}_s - \mathbf{u}_g)$ is the momentum transfer due to interphase drag and the other terms are due to the transfer of mass. The momentum equation for the solid phase follows from the momentum equation for the gas phase with the source term for interphase drag being equal but opposite.

$$\frac{\partial}{\partial t}(\alpha_s \rho_s \mathbf{u}_s) + \nabla \cdot (\alpha_s \rho_s \mathbf{u}_s \mathbf{u}_s) = -\alpha_s \nabla p + \nabla \cdot \bar{\tau}_s + \alpha_s \rho_s \mathbf{g} + \sum (\mathbf{R}_{rs} + \dot{m}_{rs} \mathbf{u}_{rs} - \dot{m}_{sr} \mathbf{u}_{sr}) \quad (4)$$

For the flow conditions in a fuel reactor, the gas can be considered as an incompressible fluid. The fluid stress tensor is simply the Cauchy stress tensor with zero bulk viscosity,

$$\bar{\tau}_g = \alpha_g \mu_g (\nabla \mathbf{u}_g + \nabla \mathbf{u}_g^T) \quad (5)$$

On the other hand, the granular solid stress tensor considers all terms in the Cauchy stress tensor,

$$\bar{\tau}_s = -p_s \bar{\mathbf{I}} + \alpha_s \mu_s (\nabla \mathbf{u}_s + \nabla \mathbf{u}_s^T) + \alpha_s \lambda_s (\nabla \cdot \mathbf{u}_s) \bar{\mathbf{I}} \quad (6)$$

where p_s is the solids pressure, μ_s is the granular viscosity, and λ_s is the

granular bulk viscosity. The definition of these terms and the interphase exchange coefficient β_{sg} provide the basis for the Eulerian approach for multiphase flow simulation. The solids pressure and granular bulk viscosity used in the present work are according to Lun et al. (1984); the granular viscosity is according to Gidaspow (1992).

The experiment of Abad et al. (2007) utilizes a riser and a bubbling bed for the air reactor and the fuel reactor respectively whereas the down-comer resembles a packed bed. Therefore, the simulation is expected to include a range of solid loadings from dilute to densely packed. The Gidaspow model is well-suited for this work because it accounts for the differences in the solid-gas interaction behavior in dilute and dense regions by switching between the drag prediction of the Ergun equation (Ergun, 1952) and the drag model of Wen and Yu (1966) based on the solids fraction α_s . For $\alpha_s > 0.8$, the Gidaspow model for the exchange coefficient β_{sg} gives

$$\beta_{sg} = \frac{3}{4} C_D \frac{\alpha_s \alpha_g \rho_g |\mathbf{u}_s - \mathbf{u}_g|}{d_s} \alpha_g^{-2.65}; C_D = \frac{24}{\alpha_g \text{Re}_s} \left[1 + 0.15 (\alpha_g \text{Re}_s)^{0.687} \right] \quad (7)$$

Conversely, for $\alpha_s \leq 0.8$,

$$\beta_{sg} = 150 \frac{\alpha_s (1 - \alpha_g) \mu_g}{\alpha_g d_s^2} + 1.75 \frac{\rho_g \alpha_s |\mathbf{u}_s - \mathbf{u}_g|}{d_s} \quad (8)$$

where d_s is the particle diameter and Re_s is the Reynolds number based on d_s .

Finally, the energy equation for phase q is expressed in terms of the enthalpy as

$$\frac{\partial}{\partial t}(\alpha_q \rho_q h_q) + \nabla \cdot (\alpha_q \rho_q \mathbf{u}_q h_q) = \alpha_q \frac{\partial p}{\partial t} + \nabla \cdot (\bar{\tau}_q \cdot \mathbf{u}_q) - \nabla \cdot \mathbf{q}_q + S_q + \sum \mathbf{Q}_{pq} \quad (9)$$

where h_q and \mathbf{q}_q are the specific enthalpy and heat flux of phase q respectively. As with the continuity and momentum equations, source terms are implemented to account for the transfer of enthalpy between phases. In particular, S_q is the enthalpy source due to chemical reaction and \mathbf{Q}_{pq} is the heat transfer from the p th phase to the q th phase. The interphase heat transfer in the current simulation is modeled based on Gunn (1978).

2.2.2 Chemical Reaction Scheme and Rates

The oxygen carrier used in the numerical simulation is F6A1100, consisting of 60% Fe_2O_3 and 40% inert Al_2O_3 by mass, following the experiment of Abad et al. (2007). Of the two gaseous fuels used in the experiment, only syngas has been considered in the current work because the chemical kinetics for the reaction of Fe_2O_3 with the non-methane components of natural gas is not available. The metal oxide reduction reactions that are used in the simulation are



Exact reaction rates for the reduction of F6A1100 with CO and H_2 are not available in the literature; the reaction rates are assumed to be the same as the reduction rates for hematite (pure Fe_2O_3) with CO and H_2 obtained from the experiment of Mattisson et al. (2005) and further developed by Mahalatkar et al. (2011b) for the simulation of chemical reactions in a single fuel reactor with solid fuel. Based on these papers, the reaction rates \dot{m} (in kg/s per cell volume or $\text{kg}/(\text{m}^3\text{-s})$) of the fuel gases with Fe_2O_3 are given by

$$\dot{m}_{\text{H}_2} = \frac{k_{\text{H}_2} R_o}{2 MW_{\text{O}_2}} \rho_{\text{avg}} \alpha_s \left(Y_{\text{Fe}_2\text{O}_3} + Y_{\text{Fe}_3\text{O}_4} \frac{v_{\text{Fe}_2\text{O}_3} MW_{\text{Fe}_2\text{O}_3}}{v_{\text{Fe}_3\text{O}_4} MW_{\text{Fe}_3\text{O}_4}} \right) (1 - X)^{2/3} MW_{\text{H}_2} \quad (12)$$

and

$$\dot{m}_{\text{CO}} = \frac{k_{\text{CO}} R_o}{2 MW_{\text{O}_2}} \rho_{\text{avg}} \alpha_s \left(Y_{\text{Fe}_2\text{O}_3} + Y_{\text{Fe}_3\text{O}_4} \frac{v_{\text{Fe}_2\text{O}_3} MW_{\text{Fe}_2\text{O}_3}}{v_{\text{Fe}_3\text{O}_4} MW_{\text{Fe}_3\text{O}_4}} \right) (1 - X)^{2/3} MW_{\text{CO}} \quad (13)$$

where k is the nominal reaction rate based on the Arrhenius rate, R_o is the oxygen carrying capacity, MW is the molecular weight (in kg/kmol),

Y is the mass fraction, ν is the stoichiometric coefficient, and X is the conversion fraction based on the fully reduced state; in each case, the subscript identifies the species under consideration. More details of the reaction rate derivation can be found in the work of Mahalatkar et al. (2011b). The reaction rates identified in Eq. (12) and Eq. (13) are implemented into the numerical simulation through separate user-defined functions.

2.3. Three-dimensional Simulation of Abad et al. Experiment

The results of the 2-D simulation of the experiment of Abad et al. (2007) were discussed in previous work (Banerjee and Agarwal, 2015b). Although the 2-D model successfully captured the salient features of the fluidization behavior in the dual fluidized bed system, it was unable to produce the expected concentrations of CO_2 and H_2O in the fuel reactor because of the inadequacy of the 2-D simulation in modeling the gaseous diffusion, which is an inherently 3-D process. Therefore, a 3-D simulation of Abad et al.'s experiment is considered in this work to obtain a closer fit for the chemical reactions between the simulation and experiment. The 3-D computational domain is an exact representation of the geometry of Abad et al. (2007) shown in Figure 2 (a). A structured mesh is used with a relatively fine grid in the lower part of the reactor and a coarser grid in the upper regions. The mesh used for the 3-D simulations is shown in Figure 2(b).

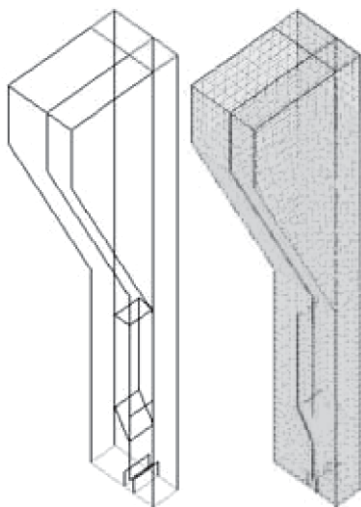


Figure 2(b): Computational domain (L) and grid (R) for 3-D CFD simulation

The oxygen carrier used in the experiment has an apparent density of $2,150 \text{ kg/m}^3$ and porosity of 0.56 with a diameter of $90\text{-}212 \text{ }\mu\text{m}$; the average value of $150 \text{ }\mu\text{m}$ is used in the simulation. The initial solids loading in the bed is about 300 g, of which 110 g is in the fuel reactor, in line with the experiment. The reactors are set to atmospheric pressure and the gage pressures at the outlets are set at zero. The pressure differential between the reactors, controlled by a water trap in the experiment to minimize leakage, was not implemented in the simulation because the data was not available. It is expected that the pressure differential is a secondary mechanism and the dense solid packing in the down-comer and slot will be sufficient to keep the leakage to a minimal. Lastly, the temperature for the simulation was set at 1123 K, in line with the reference condition specified from the experiment. The numerical parameters used in the CFD simulation are summarized in Table 1. It should be noted that the secondary phase mass fraction has been set to zero at both fuel and air reactor inlets, i.e., no new oxygen carrier is added.

The experiment of Abad et al. (2007) was operated for 60 hours without replacing the oxygen carrier or adding new material. However, the complete reactor simulation of 60 hours is beyond the scope of CFD at this time. Instead, the initial batch processing results of Abad et al. (2007) are used to validate the CFD simulation in the present work. For these batch operations, the initial oxygen carrier mass in the fuel reactor is sufficient for reacting with all the incoming fuel, so the fuel conversion is not affected by the re-oxidation in the air reactor. The CFD simulation is thus considerably simplified by setting the fluidization gas in the air reactor to an inert gas (in this case, nitrogen).

Table 1: Modeling parameters for 3-D CFD simulation of the Abad et al. experiment

Primary phase	Fuel-gas mixture
Secondary phase	Oxygen carrier (F6AL1100)
Average particle diameter	150 μm
Average particle density	2150 kg/m^3
Initial bed mass	$\sim 180 \text{ g}$
Fluidizing gas composition in fuel reactor	50% CO , 50% H_2
Fluidizing gas composition in air reactor	100% N_2
Inlet boundary condition in fuel reactor	Velocity inlet with velocity 0.1 m/s
Inlet boundary condition in air reactor	Velocity inlet with velocity 0.5 m/s
Outlet boundary condition in fuel reactor	Pressure outlet at atmospheric pressure
Outlet boundary condition in air reactor	Pressure outlet at atmospheric pressure
Operating temperature	1123 K
Solids pressure	Lun et al. (1984)
Granular bulk viscosity	Lun et al. (1984)
Granular viscosity	Gidaspow (1992)
Drag law	Gidaspow (1992)
Heat transfer coefficient	Gunn (1978)
Numerical scheme	Phase-coupled SIMPLE
Time step size	0.0005 s
Iterations per time step	20

The 3-D simulation was run on a Dell workstation with a quad-core Intel Xeon CPU. 30 seconds of simulation completed in approximately 96 hours. The contours of the mass fraction of CO_2 for the 3-D simulation are shown in Figure 2(c). In comparison to the 2-D simulation results (Banerjee and Agarwal, 2015b), there is greater diffusion in the 3-D case as expected. The local mass fraction of CO_2 at the base of the bed, where the injected CO first comes into contact with the Fe_2O_3 and begins to react is around 15%. Owing to the increased diffusion in 3-D, the CO_2 spreads through the fuel reactor more homogeneously as it travels towards the fuel reactor outlet; the vortex patterns seen in the 2-D case are absent. The contours of the mass fraction of H_2O display the same characteristics. The quantitative effects of this can be observed from the plot of the mass fractions of CO_2 and H_2O at the fuel reactor outlet given in Figure 3. The mass fractions of both CO_2 and H_2O are initially lower than in the 2-D case. This is because these gases now have to diffuse through the nitrogen present in the fuel reactor instead of displacing it and thus reach the outlet more slowly. The large fluctuations in the outlet mass fraction caused by pockets of reversed flow in the 2-D case are eliminated. Since reversed flow does not develop in the current simulation, the mass fractions keep increasing as the simulation progresses and more and more CO_2 and H_2O

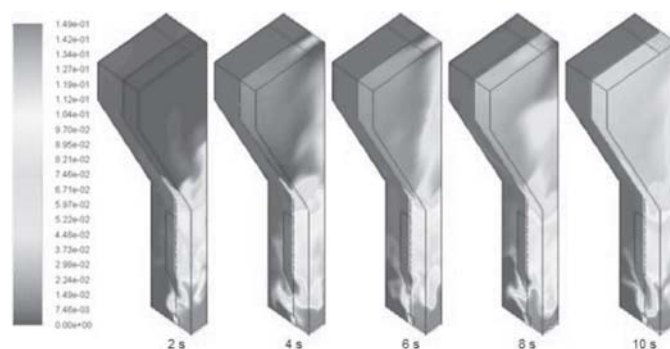


Figure 2(c): Contours of CO_2 mass fraction for the first ten seconds of 3-D simulation showing the increased diffusion and absence of the vortex pattern compared to the 2-D case

are produced. By 20 seconds, the mass fractions of both CO_2 and H_2O have exceeded their stagnation values from the 2-D simulation (shown by dotted lines in Figure 3). By 30 seconds, the mass fraction of H_2O reaches the expected value from the batch experiments of Abad et al.

(2007). However, it is noted that although the final outlet mass fraction of CO_2 after 30 seconds is higher than the 2-D case, it does not reach the experimental value.

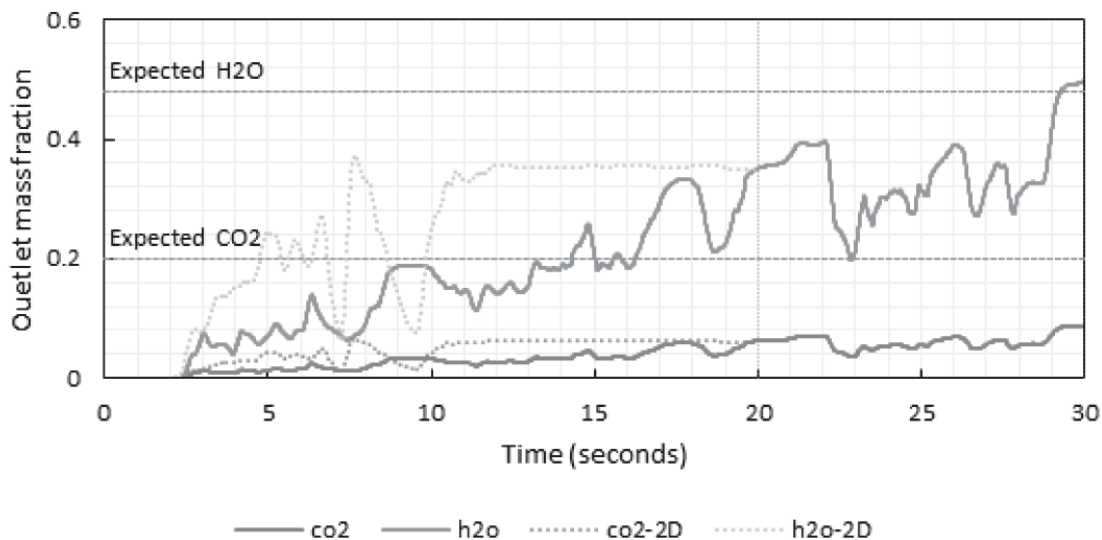


Figure 3: Mass fractions of CO_2 and H_2O at the fuel reactor outlet for the 3-D simulation

The 3-D simulation shows a significant improvement in the mass fraction measurements of the flue gases at the fuel reactor outlet. However, there is still some discrepancy in the mass fraction of CO_2 , which may be due to various external factors. In Abad et al.'s experiment (2007), the gas streams from the reactors were pipelined to an electric cooler and then to the gas analyzer. The experiments of Taylor (1954) showed that significant apparent diffusion can occur in gases when they travel through pipes. Thus, it is reasonable to expect that the concentrations measured by Abad et al. (2007) in the gas analyzer may be different from the concentrations present right at the fuel reactor outlet. It should also be noted that the reaction rate kinetics used in the simulation were based on the experimental study of Mattisson et al. (2005) using hematite, whereas the oxygen carrier used in the experiment of Abad et al. (2007) was F6A1100. One of the reasons F6A1100 is preferred over Fe_2O_3 as the oxygen carrier for CLC operation is its improved reactivity, caused by an increase in apparent surface area due to the presence of the porous Al_2O_3 (Johansson, 2007). As such, it stands to reason that the experiment shows a higher concentration of the reaction products compared to the current simulation. Further research is required to determine more accurate empirical formulas for the reduction of F6A1100 specifically to improve the accuracy of the results of the CFD simulation.

3. Lagrangian Simulation of Complete CLC Reactor at NETL

The Eulerian two-fluid model can accurately capture the bulk behavior of the solid phase in the dual fluidized bed reactor for CLC using gaseous fuels. However, since coal is projected to remain one of the dominant fossil fuels in the near future, the concept of coal-direct chemical-looping combustion (CD-CLC) with in situ gasification has garnered significant interest in recent years. In a CD-CLC system, the oxygen carrier needs to be formed into particles with a relatively larger diameter compared to the pulverized coal for easier separation. The work of Gryczka et al. (2009) with the larger particles has suggested that accurate numerical representation of particle dynamics is not likely to be achieved using the multiphase granular solid phase approximation due to "the inadequacies of the continuum model." The inaccuracy arises from the non-physical closure terms used in the Eulerian model such as the frictional solids viscosity or the solids pressure based on the kinetic theory of granular flow. Thus, for a more detailed understanding of the hydrodynamics in a multiphase system inside a CLC reactor, the Lagrangian particle-based approach is employed to study the CD-CLC reactor system at National Energy Technology Laboratory, previously investigated by Parker (2012).

3.1. Description of Experimental Setup

The geometry of the CD-CLC system used at NETL comprises an air reactor, cyclone, loop-seal, and fuel reactor, as shown later in Figure 5(a).

The entire geometry is approximately 12 ft. high. In the cold flow experiment, the oxygen carrier particles start from the bottom of the air reactor and move up along the riser and into the cyclone. In the cyclone, the particles are separated from the air stream and drop into the loop-seal due to the gravity. After passing through the slightly fluidized loop-seal, the particles move into the fuel reactor. The oxygen carrier particles leave the fuel reactor, pass through an L-valve and then return to the air reactor. Dimensions and additional descriptions of the various components of

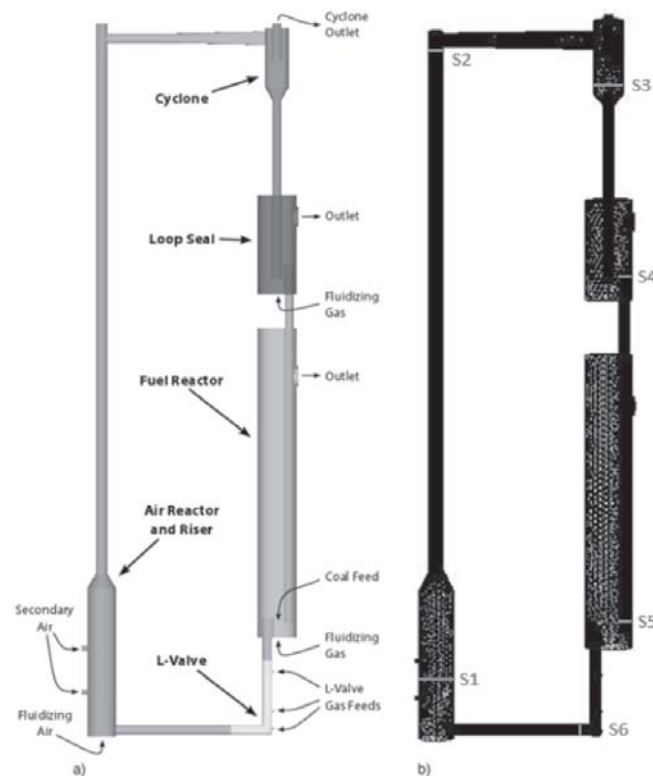


Figure 5(a): (a) Geometry of the coal-direct chemical-looping combustion system at NETL (Parker, 2012), and (b) computational mesh with static pressure measurement locations marked as "S"

the CD-CLC geometry of NETL can be found in the work of Parker (2012). The computational grid, also shown in Figure 6, is an exact representation of the geometry. The oxygen carrier particles in the cold flow experiment are primarily ilmenite (FeTiO_3) with some uncombined TiO_2 and Fe_2O_3 as well. The ilmenite particles had a size distribution of $13 \mu\text{m}$ to $320 \mu\text{m}$. The particle size used in the numerical simulation corresponds to the median particle size of $150 \mu\text{m}$ with the average density of ilmenite of $4,450 \text{ kg/m}^3$.

3.2 Numerical Solution Procedure

The equations for mass and momentum conservation for the fluid phase are identical to those used in the Eulerian model given in Eqs. (1) and (3) with the exception that the source term in Eq. (3) for the solid-gas momentum exchange term, R_{sg} , is obtained from the average of the drag forces acting on all the discrete particles in a given computational cell. The shear stress term in the momentum equation is given in Eq. (5). Since the current simulation considers a cold flow with no species transport, the energy and species conservation equations are not applicable in this case.

3.2.1 Particle Equations

In the Lagrangian approach, each solid particle is tracked individually. The motion of each solid particle is obtained by summing the forces acting on the particle and applying Newton's second law of motion. The resulting force balance equation, which is integrated to obtain the motion of the solid particle, is given by

$$m_s \frac{\partial \mathbf{u}_s}{\partial t} = \sum \mathbf{F}_i = \mathbf{F}_{gra} + \mathbf{F}_{buo} + \mathbf{F}_{drag} + \mathbf{F}_{pre} + \mathbf{F}_{saf} + \mathbf{F}_{Mag} + \mathbf{F}_{con} \quad (14)$$

In Equation (14), \mathbf{F}_{gra} and \mathbf{F}_{buo} are bulk forces due to gravity and buoyancy respectively. \mathbf{F}_{drag} , \mathbf{F}_{pre} , \mathbf{F}_{saf} and \mathbf{F}_{Mag} are hydrodynamic forces due to momentum transfer between the solid particles and the surrounding fluid, namely the drag force due to fluid viscosity, the pressure force due to pressure gradient, Saffman lift force due to inter-particle friction, and the Magnus force due to particle spin respectively. Owing to the large difference between the solid particle density and the fluid density, the pressure force can be dropped from Eq. (14) without loss of accuracy; the Magnus force can also be dropped because of negligible particle rotation.

\mathbf{F}_{con} is the contact force on the particles due to collision with other particles or walls. In this paper, this contact force is computed using the soft-sphere model, which decouples its normal and tangential components (ANSYS, 2012b). The normal force on any particle involved in a collision is given by

$$\mathbf{F}_{con}^n = (k\delta + \gamma(\mathbf{u}_{12} \cdot \mathbf{e}))\mathbf{e} \quad (15)$$

where k is the spring constant of the particle, δ is the overlap between the particle pair involved in the collision as illustrated in Figure 4, γ is the damping coefficient, \mathbf{u}_{12} is the relative velocity vector of the colliding pair, and \mathbf{e} is the unit vector. For large values of k , the results of the soft-sphere model are interchangeable with those obtained using a hard-sphere model (Link, 1975). The tangential contact force is calculated based on the normal force as $\mathbf{F}_{con}^t = \mu \mathbf{F}_{con}^n$ where the coefficient of friction μ is given as a function of the relative tangential velocity v_r by

$$\mu(v_r) = \begin{cases} \mu_{stick} + (\mu_{stick} - \mu_{glide})(v_r/v_{glide} - 2)(v_r/v_{glide}) & \text{if } v_r < v_{glide} \\ \mu_{glide} & \text{if } v_r \geq v_{glide} \end{cases} \quad (16)$$

3.2.2. Solid-Gas Momentum Exchange

It is essential to evaluate the momentum exchange between the solid and fluid phase for multiphase flow modeling using the coupled CFD/DEM solver; this is done by considering the drag force. The transfer of momentum from the fluid to a solid particle as it moves through each cell in the computational domain is attributed to the drag force exerted on the particle by the fluid, and is modeled as

$$\mathbf{F}_{drag} = F_D(\mathbf{u}_f - \mathbf{u}_p) \quad (17)$$

where \mathbf{u}_f is the fluid velocity, \mathbf{u}_p is the particle velocity, and F_D is the net drag coefficient,

$$F_D = \frac{18\mu C_D Re_p}{\rho_p d_p^2 24} \quad (18)$$

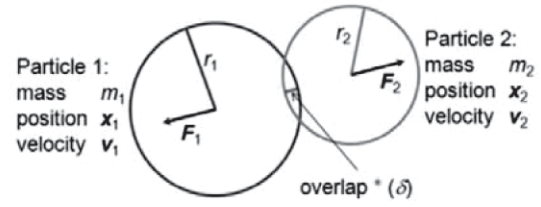


Figure 4: Schematic of particle collision model for DEM

where μ , ρ_p , and d_p are the viscosity of the gas and the density and diameter of the solid particle respectively. C_D and Re_p are the particle drag coefficient for a sphere and the relative Reynolds number based on the particle diameter respectively. Re_p is defined as

$$Re_p = \frac{\rho_f d_p |\mathbf{u}_f - \mathbf{u}_p|}{\mu} \quad (19)$$

The drag coefficient can be modeled using various empirical relations. The spherical or Stokes drag law is chosen in this work for its simplicity.

3.2.3. Parcel Concept

The computational cost of the DEM approach is driven by the number of collisions between particles; to track each individual particle in a CLC system using the DEM approach is extremely computationally demanding since the total number of particles increases drastically as the particle size becomes smaller. Therefore, the parcel methodology first proposed by Patankar and Joseph (2001) is employed in this work to overcome the high computational cost.

According to Patankar and Joseph (2001), one parcel can represent a group of particles with the same properties such as density and size. The mass used in collisions is that of the whole parcel rather than a single particle. By summing the mass and volume of each individual particle in the parcel, the total mass m_p and volume V_p of the parcel can be obtained. The radius of the parcel is then determined by the mass of the entire parcel and the particle density. For a given point in the fluid flow, the driving force of a parcel due to fluid forces is assumed to be the same as the sum of the fluid force acting on the group of particles it represents.

$$\mathbf{F}_{f,p} = \sum_{i=1}^{N_p} \mathbf{F}_{f,i} \quad (20)$$

where N_p is the number of particles in the parcel, and \mathbf{F}_i is the net fluid force acting on a parcel p or particle i depending on the subscript. The acceleration due to inter-particle collision forces and particle-wall collisions forces are computed based on the mass properties of the parcel.

3.3. Cold Flow Simulation of NETL CD-CLC Reactor System

The boundary conditions for the cold flow simulation are obtained from Parker (2012) and are summarized in Table 2. Particles are injected into the air reactor, loop-seal, and air reactor and allowed to settle prior to the start of the simulation. A total of 717,879 particles in total are injected into the system-73,360 particles in the air reactor, 365,057 in the fuel reactor, and 279,462 in the loop-seal. After the particles are settled in each bed, the CFD/DEM model is run to simulate 360 ms of cold flow operation. The development of particle movement is shown in the Figure 5(b) at 10 ms intervals with the particles colored by velocity magnitude.

Table 2: Boundary conditions for cold flow simulation

Unit	Flow Boundaries		Flow rate (m/s)
	Boundary	Gas	
Air reactor	Fluidizing air	Air	20
Fuel reactor	Fluidizing gas	N_2	4
Loop-seal	Fluidizing gas	N_2	2
L-valve	Stripper (upper)	N_2	0.5
	Aeration (middle)	N_2	1
	Eductor (lower)	N_2	1
Unit	Pressure Boundaries		Pressure (kPa)
	Boundary	Gas	
Fuel reactor	Outlet	N_2	101.325
Loop-seal	Outlet	N_2	101.325
Cyclone	Outlet	Air	101.325

According to Figure 5(b), the particles in the air reactor reach the top of the riser at around 190 ms, and then move horizontally along the pipe towards the cyclone. The horizontal movement is driven by two secondary gas injections on the side of the air reactor. After another 40 ms, the particles enter the cyclone and start to drop down to the loop-seal. Due to an erroneously high gas velocity in the loop-seal and fuel reactor during the initial startup, the particles in these chambers are also shot up to the top. Once the gas injections are reduced to their correct values of 2 m/s

and 4 m/s respectively at 210 ms, the particles settle down again. From this point on, it is expected that the particles in the loop-seal will drop into the fuel reactor and the L-valve, and finally be pushed back into the air reactor by the gas injection in the L-valve. 360 ms is not sufficient time to see the complete particle recirculation; however, the pressure contours in Figure 5(c) show the development of favorable pressure gradients for particle recirculation as simulation time increases.

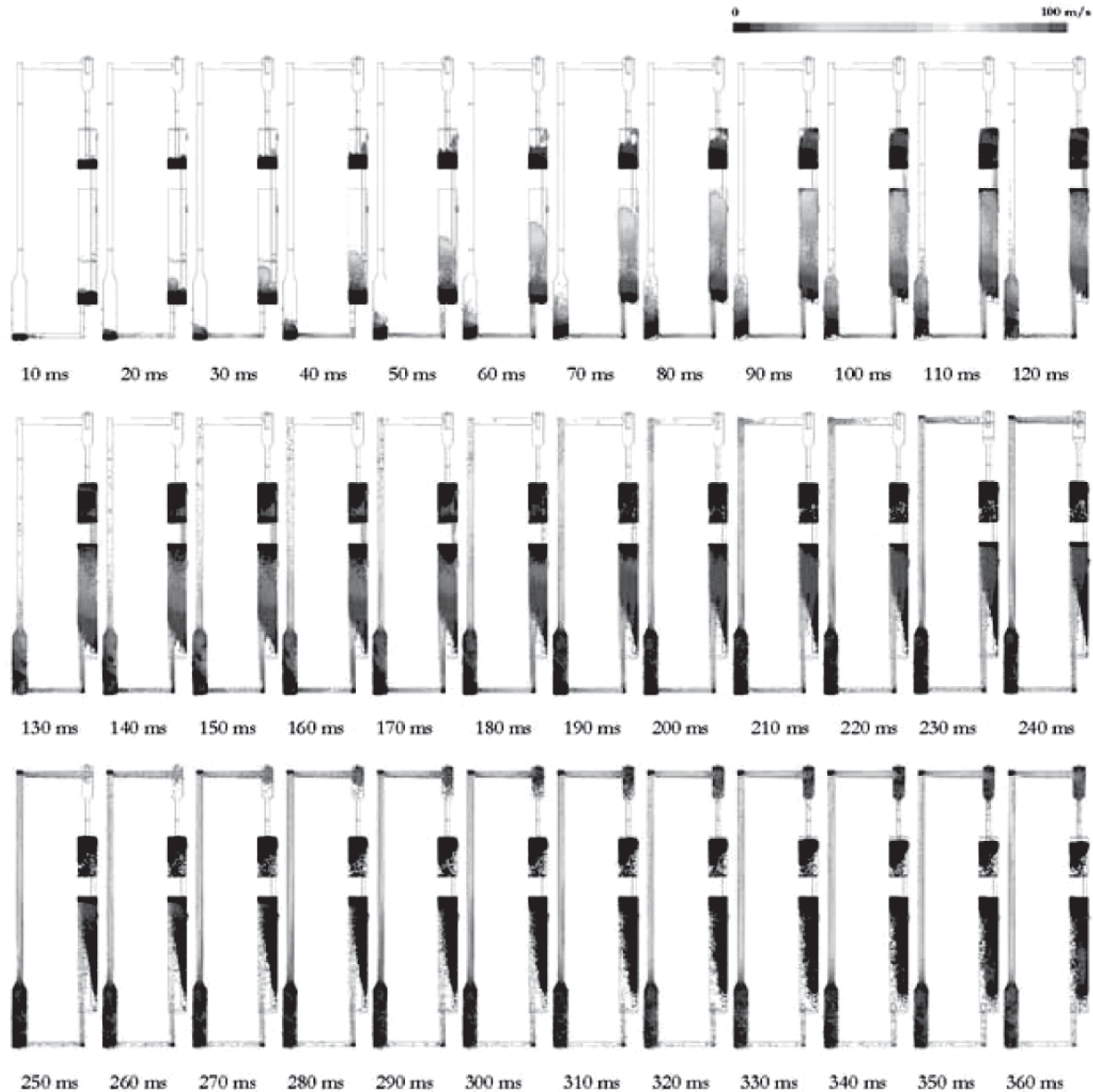


Figure 5(b): Particle tracks colored by velocity magnitude for the first 360 ms of cold flow simulation

The static pressure in the system is evaluated at the surfaces S1-S6 shown in Figure 5(a) to quantify the pressure gradients observed in Figure 5(c); the static pressures variation at 360 ms is presented in Figure 6. The arrows indicate the particle movement direction. It can be observed from Figure 6 that there is a consistent positive pressure differential between surface S1 (air reactor bed) through to S5 (fuel reactor bed), which confirms that particle continuous recirculation can occur between these surfaces. The pressure gradient between S5 and S1 via S6 (L-valve) is an adverse gradient. However, since the particle movement through the L-valve is driven by the gas injection into the L-valve, the adverse gradient does not affect the overall particle recirculation.

Conclusion

In this work, a 3-D CFD simulation for a complete circulating dual fluidized bed system was developed for chemical-looping combustion based on the 300 W laboratory-scale reported data. The oxygen carrier is modeled as an Eulerian fluid phase. The results of this study highlight the importance of capturing the 3D diffusion of gases in the reactor to ensure that accurate results are obtained for the chemical reactions. The 3-D model produced significantly improved results for the outlet concentrations of gases from the fuel reactor when compared to the experiment. The detailed particle hydrodynamics in a complete circulating CLC system for solid fuels was also investigated using the Lagrangian particle-tracking

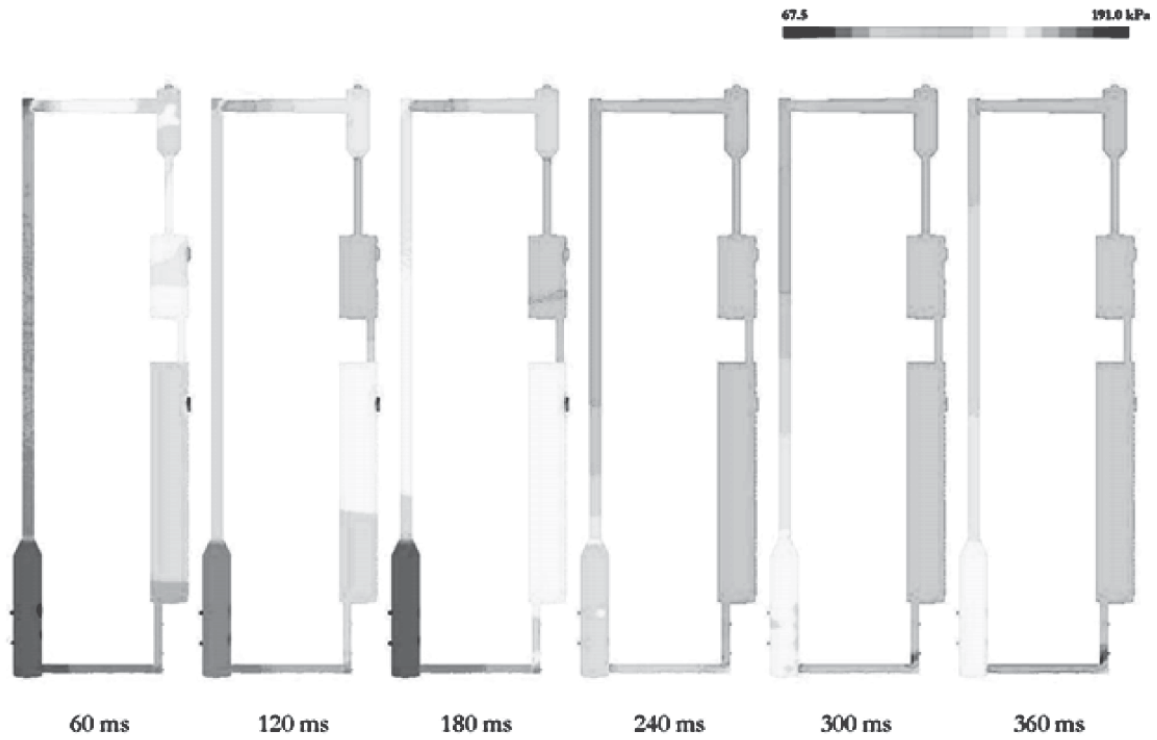


Figure 5(c): Pressure contours for cold flow inside the CLC apparatus

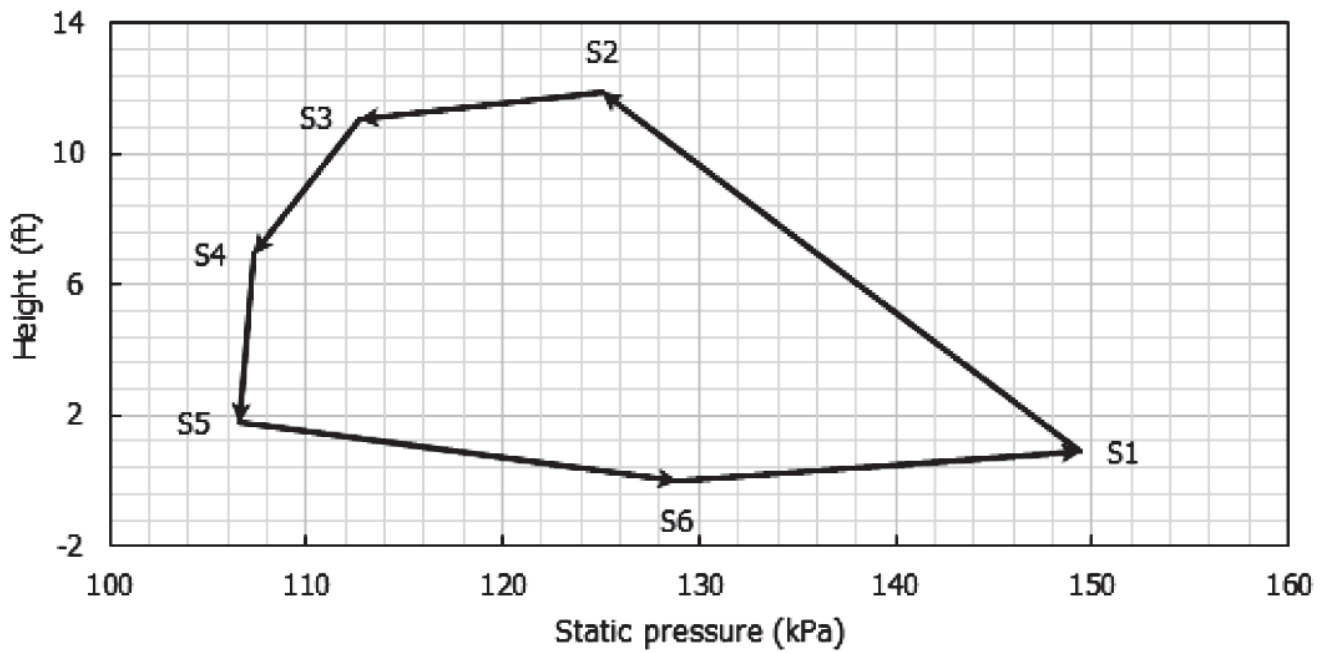


Figure 6: Static pressure at surfaces S1-S6 in the CD-CLC system shown in Figure 6 at t=360 ms

DEM approach employing the CLC reactor at NETL. The development of particle flow was investigated as well as the pressure contours. The static pressure contours and gradients showed evidence of favorable conditions for particle recirculation.

References

- Abad, A., Mattisson, T., Lyngfelt, A., and Johansson, M., 2007, "The use of iron oxide as oxygen carrier in a chemical-looping reactor," *Fuel*, 86, pp. 1021-1035.
- Andrus, H.E. et al. 2008, "Hybrid combustion-gasification chemical looping coal power technology development phase III-final report," National Energy Technology Laboratory, Albany, OR.
- ANSYS, 2012a, "ANSYS FLUENT User's Guide," ANSYS, Inc., Canonsburg, PA.
- ANSYS, 2012b, "ANSYS FLUENT Theory Guide," ANSYS, Inc., Canonsburg, PA.
- Arrhenius, S., 1896, "On the influence of carbonic acid in the air upon the temperature of the ground," *Philos. Mag.*, 41, pp. 237-277.
- Banerjee, S. and Agarwal, R.K., 2015a, "Transient reacting flow simulation of spouted fluidized bed for coal-direct chemical looping combustion," *J. Thermal Sci. Eng. Appl.*, 7(2). DOI: 10.1115/1.4029951.
- Banerjee, S. and Agarwal, R.K., 2015b, "An Eulerian approach to CFD simulation of a chemical-looping combustion reactor with chemical reactions," Proc. 40th Int. Technical Conference on Clean Coal & Fuel Systems, Clearwater, FL.
- Chong, Y.O., Nicklin, D.J., and Tait, P.J., 1986, "Solid exchange between adjacent fluid beds without gas mixing," *Powder Technol.* 47, pp. 151-156.
- Deng, Z. et al., 2008, "Multiphase CFD modeling for a chemical looping combustion process (fuel reactor)," *Chem. Eng. Tech.*, 31(12), pp. 1754-1766.
- Ergun, S., 1952, "Fluid flow through packed columns," *Chem. Eng. Prog.*, 48, pp. 89-94.
- Fang, M. et al., 2003, "Experimental research on solid circulation in a twin fluidized bed system," *Chem. Eng. J.*, 94, pp. 171-178.
- Gidaspow, D., 1992, "Multiphase Flow and Fluidization," Academic Press, San Diego, CA.
- Gryczka, O. et al., 2009, "Characterization and CFD modeling of the hydrodynamics of a prismatic spouted bed apparatus," *Chem. Eng. Sci.*, 64, pp. 3352-3375.
- Gunn, D.J., 1978, "Transfer of heat or mass to particles in fixed and fluidized beds," *Int. J. Heat Mass Transfer*, 21, pp. 467-476.
- Hossain, M.M. and de Lasa, H.I., 2008, "Chemical-looping combustion (CLC) for inherent CO₂ separations-a review," *Chemical Engineering Science*, 63, pp. 4433-4451.
- IPCC, 2007, "Climate Change 2007: Synthesis Report. Contribution of Working Groups I, II and III to the Fourth Assessment Report of the Intergovernmental Panel on Climate Change [Core Writing Team, Pachauri, R.K., and Reisinger, A. (eds.)]" IPCC, Geneva, Switzerland.
- Ishida, M., Jin, H., and Okamoto, T., 1996, "A fundamental study of a new kind of medium material for chemical-looping combustion," *Energy & Fuels*, 10(4), pp. 958-963.
- Ishida, M., Zheng, D., and Akehata, T., 1987, "Evaluation of a chemical-looping-combustion power-generation system by graphic exergy analysis," *Energy*, 12(2), pp. 147-154.
- Johansson, M., 2007, "Screening of oxygen-carrier particles based on iron-, manganese-, copper- and nickel oxides for use in chemical-looping technologies," Ph.D. dissertation, Chalmers University of Technology, Göteborg, Sweden.
- Jung, J. and Gamwo, I., 2008, "Multiphase CFD-based models for chemical looping combustion process: fuel reactor modeling," *Powder Technol.*, 183, pp. 401-409.
- Kruggel-Emden, H., Stepanek, F., and Munjiza, A., 2011, "A study on the role of reaction modeling in multi-phase CFD-based simulations of chemical looping combustion," *Oil & Gas Sci. Tech.*, 66(2) pp. 313-331.
- Link, J.M., 1975, "Development and validation of a discrete particle model of a spout-fluid bed granulator," Ph.D. dissertation, University of Twente, Enschede, The Netherlands.
- Lun, C.K.K., Savage, S.B., Jeffrey, D.J., and Chepurmy, N., 1984, "Kinetic theories for granular flow: inelastic particles in Couette flow and slightly inelastic particles in general flow field." *J. Fluid Mech.*, 140, pp. 223-256.
- Lyngfelt, A., Leckner, B., and Mattisson, T., 2001, "A fluidized-bed combustion process with inherent CO₂ separation; application of chemical-looping combustion," *Chem. Eng. Sci.*, 56(10), pp. 3101-3113.
- Mahalatkar, K., Kuhlman, J., Huckaby, E.D., and O'Brien, T., 2011a, "Computational fluid dynamic simulations of chemical looping fuel reactors utilizing gaseous fuels," *Chem. Eng. Sci.*, 66(3), pp. 469-479.
- Mahalatkar, K., Kuhlman, J., Huckaby, E.D., and O'Brien, T., 2011b, "CFD simulation of a chemical-looping fuel reactor utilizing solid fuel," *Chem. Eng. Sci.*, 66(16), pp. 3617-3627.
- Marion, J.L., 2006, "Technology options for controlling CO₂ emissions from fossil fueled power plants," Proc. 5th Annual Conference on Carbon Capture and Sequestration, Alexandria, VA.
- Mattisson, T. et al., 2005, "Capture of CO₂ in Coal Combustion. ECSC Coal RTD Prog-ramme Final Report," ECSC-7220-PR125.
- Parker, J., 2012, "Simulation of coal particles in a full chemical looping combustion system," CPFD Software, LLC, Albuquerque, NM.
- Patankar, N.A. and Joseph, D.D., 2001, "Modeling and numerical simulation of particulate flows by the Eulerian-Lagrangian approach," *Int. J. Multiphase Flow*, 27, pp. 1659-1684.
- Patil, D.J., Annaland, M.V., and Kuipers, J.A.M., 2004a, Critical comparison of hydro-dynamic models for gas-solid fluidized beds-Part I: Bubbling gas-solid fluidized beds operated with a jet, *Chem. Eng. Sci.*, 60(1), pp. 57-72.
- Patil, D.J., Annaland, M.V., and Kuipers, J.A.M., 2004b, Critical comparison of hydro-dynamic models for gas-solid fluidized beds-Part II: Freely bubbling gas-solid fluidized beds, *Chem. Eng. Sci.*, 60(1), pp. 73-84.
- Taylor, G.I., 1954, "The dispersion of matter in turbulent flow through pipes," *Proc. R. Soc. London. Ser. A, Math. Phys. Sci.*, 223, pp. 446-448.
- Wen, C.Y. and Yu, H.Y., 1966, "Mechanics of fluidization," *Chem. Eng. Prog. Symp. Ser.*, 62, pp. 100-111.
- Wolf, J., Anheden, M., and Yan, J., 2001, "Performance analysis of combined cycles with chemical looping combustion for CO₂ capture," Proc. 18th International Pittsburgh Coal Conference, Pittsburgh, PA.



Organic Species Emitted as a Part of Combustion Residue: Fate and Transformation in the Ambient Air

Tarun Gupta*, Dharmendra Kumar Singh

Department of Civil Engineering and Center for Environmental Science and Engineering, Indian Institute of Technology Kanpur, Kanpur 208016–India

ARTICLE INFO

Received : 30 August 2015
Revised : 27 September 2015
Accepted : 28 September 2015

Keywords:

PAHs; SOA; Reactive organic gases (ROGs),
Volatile organic compounds (VOCs),
Engine emission.

ABSTRACT

Organic species emitted as a part of combustion residue are one of the major components of both gaseous and particulate emission. These species gets diluted and transformed when they come in contact with the atmospheric gases. The gas to particulate conversion of SVOC (semi volatile organic compound) leads to the formation of SOA (secondary organic aerosol). Gas to particle conversion is very sensitive to the level of dilution. Combustion generated particulates are formed as a result of a complex process. The precise mechanism of SOA formation is still not completely understood but it is largely attributed to oxidation of reactive organic gases (ROGs) and gas to particle phase conversion. Polycyclic aromatic hydrocarbons (PAHs) present in the combustion products may also get transformed upon dilution and oxidation when emitted in the ambient atmosphere. PAHs and their derivatives are formed by the incomplete combustion of organic materials arising from combustion and due to anthropogenic emissions. The PAH concentration varies significantly in various rural and urban environments and their concentration are mainly influenced by the level of vehicular and domestic emissions. Diagnostic ratio (DR) approaches allow either individual PAHs or their combination to be used for identifying their origin sources. This paper discusses the fate and transformation of SOA and Polycyclic aromatic hydrocarbons (PAHs) largely emitted from combustion sources. The effect of temperature and relative humidity on the formation of SOA and a brief discussion on its measurement and analysis has also been described in this study. Finally, a brief discussion on various health effects attributed to combustion generated species has been provided.

© 2016 ISEES, All rights reserved

1. Introduction

Poor air quality attracts a high level of interest among the scientific community and engages public in various forums due to the known relationship between exposure to many air pollutants and increased adverse health effects on the human health (Yang and Omaye, 2009; Ruckerl et al., 2011). In addition, air pollution can seriously deteriorate visibility (Hyslop, 2009) may damage buildings materials and cultural heritage (Watt et al., 2009) and has direct and indirect effects upon climate (Ramanathan and Feng, 2009; Jaidevi et al., 2011). While air pollution remains a major problem for developing countries (Fenger, 2009; Liaquat et al., 2009) because of the rapid growth of population, energy demand and economic growth, developed countries have largely experienced significant decline in the concentrations of many air pollutants over the past decade (Fenger, 2009; Liaquat et al., 2009). In early nineteenth century, fossil fuels have dominated transportation sector since the invention of internal combustion (IC) engines. In order to effectively control environmental pollution and alleviate its harmful effects, exhaust characterization at the engine outlet is essential (Eastwood, 2008).

Exposure to particulates emitted from vehicular tail pipes lead to adverse health effects on our health which largely depends upon the physico chemical composition of these particles. PM properties determine their true residence time and availability as sorption sites and their deposition inside the human respiratory system (Schroedar et al., 1999; Krahl et al., 2008, 2003; Agarwal et al., 2013, 2011). Complex processes

in the combustion chamber such as air–fuel mixing, combustion chamber geometry, fuel droplet spray, and temperature and pressure conditions of the cylinder charge during combustion dictate the type and amount of PM formation that is emitted in the tail pipe (Flynn et al., 1999; Dhar and Agarwal, 2013). Formation of particulates in a diesel engine is very sensitive to actual air–fuel ratio present in the premixed reaction zones of the combustion chamber where soot precursors are initially generated (Flynn et al., 1999).

Diesel engines are among the most efficient power sources, which emit comparatively lower amounts of CO and HC emissions as compared to the gasoline engines but higher amounts of oxides of nitrogen (NO_x) and particulate matter (Agarwal et al., 2015). NO_x and PM are both related with deleterious effects on the human health.

2. Chemical characterization of particulate matter

2.1. Chemical composition of particulate matter

Heterogeneous combustion takes place inside the diesel engine. Fuel is injected into the combustion chamber towards the end of the compression stroke in a conventional CI engines. Modern diesel engines are equipped with common rail direct injection (CRDI) system, and split injection capabilities, i.e. fuel can be injected in pilot injection, main injection and post injection in the same engine cycle. When fuel is injected into the combustion chamber at a very high injection pressure, it breaks

* Corresponding Author: E-mail: tarun@iitk.ac.in

into large number of small droplets under the influence of high combustion chamber pressure, prevailing at the end of compression stroke. Resistance to high pressure fuel droplets are generated by compressed air in the combustion chamber, which produce further fragmentation of small droplets into finer droplets and results in a better combustion scenario.

The diesel particulate matter (DPM) is comprised of elemental carbon, organic carbon, nitrates, sulfates and metals (in trace quantity) (Fig. 1). DPM can act as an excellent carrier for adsorbed organic and inorganic compounds due to its large surface area. Mass of emitted particles per mile from diesel engines are nearly 10 times higher than that of a conventional gasoline engines, and 30–70 times more than the engines equipped with catalytic converters (Godlee, 1993).

A major portion of DPM has a size smaller than 1 μm . The residence time of its constituents in the atmosphere may change from a few hours to several days. These particles can travel long distances and, are also capable of penetrating to our deeper parts of our lungs and in turn can cause adverse health effects as ultrafine particles can also enter in the blood stream and get translocated to different vital organs (Agarwal et al., 2015; Gupta et al., 2010).

2.2. Occurrence of Elemental and organic carbon (EC/OC)

Elemental carbon and organic carbon are the two main constituents of the combustion exhaust particulates. A large number of studies have explored the EC and OC content of diesel particulates. As a consequence of heterogeneous combustion with the CI engines, unburned and partially burnt hydrocarbons are emitted. Under high temperatures and pressures present inside the combustion chamber, a fraction of hydrocarbons, which are present in a locally fuel rich, undergoes pyrolysis and lead to the formation of nuclei mode particles (Fig. 2). Most of the hydrogen atoms get stripped off the hydrocarbon chains and only carbon atoms remain. As a result of this, carbon core formation takes place, which is also called as 'soot'. Carbon undergoes cyclization, and sheet like structure formation and eventually nano-tube like structures called spherules are formed (Abbass et al., 1991).

Volatile organic materials usually condense over the solid and dry soot and these particles further grow. This condensed organic material also known as the soluble organic fraction is extremely harmful for humans. This condensed organic matter contains hundreds of organic compounds formed as a result of complex organic species formation pathways during fuel pyrolysis inside combustion chamber. Some of the organic compounds are known carcinogens such as polyaromatic hydrocarbons (PAHs), Benzene-Toluene-Ethyl-benzene-Xylene (BTEX).

2.3. Unregulated emissions

Regulated gases (CO, THC and NO_x) and particulate matter (PM) are currently covered by legislations for their control. Vehicles/ engines also emit large number of other emissions, most of which are in very small quantities except CO₂ and moisture, which are classified as unregulated emissions. In some emission legislations, CO₂ is now included as regulated species. Unregulated emissions are important from health point of view. Ravindra et al. (2008) signaled in their research that there should be emission regulations for carcinogenic compounds like PAHs, carbonyl compounds and BTEX as these are toxic species emitted by diesel engines.

2.3.1. Carbonyl compounds

A large number of different harmful compounds are emitted by diesel engines and many compounds are still unknown. The term carbonyl signifies to the carbonyl functional group, which is a divalent group comprising of a carbon atom double-bonded to oxygen. Carbonyls have significant occurrence in the engine exhaust. Various studies have assessed carbonyl emissions by using its derivatives with 2, 4-di-nitro-phenyl-hydrazine (DNPH) (McDonald et al., 2004; Schauer et al., 1999; Schauer et al., 2002; Grosjean et al., 2001; Kristensson et al., 2004).

Carbonyl emissions result in the formation of secondary organic aerosols (SOA) by forming oligomers (Loeffler et al., 2006). Contribution of carbonyls in diesel particles also augments their physiological response (Madden et al., 2003). Pang et al. (2006) examined the characteristics of carbonyl emissions from a diesel engine fuelled with biodiesel-ethanol-diesel blend. They found that acetaldehyde was the carbonyl compound emitted in the highest concentration, followed by formaldehyde, acetone, propionaldehyde and benzaldehyde, respectively. They reported 1–12% higher total carbonyl emissions with biodiesel-ethanol-diesel blend depending upon the engine operating condition. They also reported that carbonyl emissions increased with increasing engine speed while minimum carbonyl emissions were found at 50% engine load, when the engine was operated at a constant speed (Ho et al., 2012).

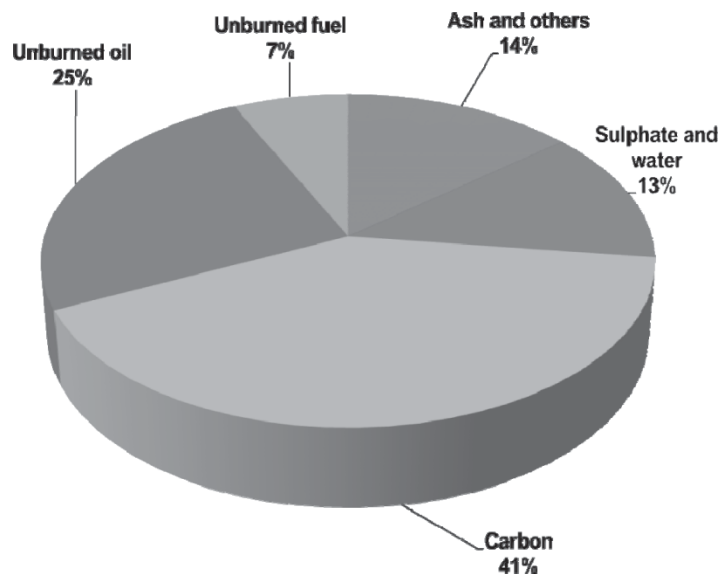


Figure 1: Composition of typical diesel particulate (Adapted from Kittelson, 1998)

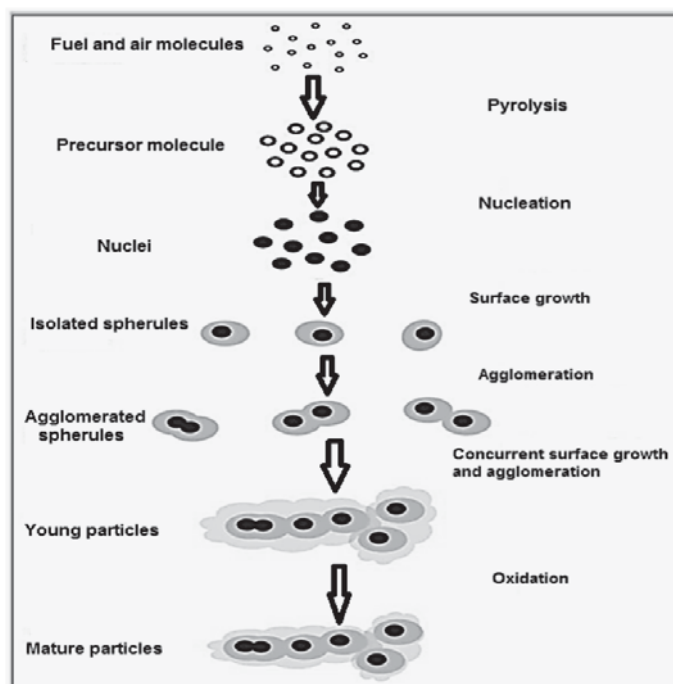


Figure 2: Schematic view of soot formation adopted from particulate emissions from vehicles by (Adapted from Eastwood, 2008)

Ho et al. (2012) measured and quantified 15 different carbonyl species and formaldehyde was the most dominant compound, followed by acetaldehyde and acetone. They observed that formaldehyde was 54.8–60.8% of the total carbonyl compounds present in the exhaust. They took samples at various locations in the city of Hong Kong and found that the formaldehyde concentration was quite high as compared with the theoretical value predicted in summer, which suggests significant effect of photochemical reactions in formaldehyde production in the ambient atmosphere.

2.3.2. Benzene, toluene, ethyl-benzene and xylene (BTEX)

Petroleum products such as gasoline include these compounds (BTEX), which have harmful effects on humans. Cheung et al. (2009) reported levels of BTEX emissions from a diesel engine fuelled with mineral diesel, biodiesel and biodiesel blends with methanol (5%, 10%, and 15%) at a constant engine speed of 1800 rpm and compared for five

different loads. Higher oxygen content in the biodiesel fuel leads to oxidation of BTEX. They reported that higher engine load resulted in lower BTEX emission in the engine exhaust.

Di et al. (2009) and Takada et al. (2003) also observed lower BTEX emissions at higher engine loads. Ballesteros et al. (2008) used biodiesel and reported relatively lower aromatic emissions. Machado and Arbillá (2008) obtained a strong correlation between carbonyl emissions and biodiesel content ($R^2 > 0.96$). They reported that esters in biodiesel may be a main source of these carbonyl emissions. Liu et al. (2009) and Cheung et al. (2009) signified that carbonyl emissions increase with increasing biodiesel content at lower engine load however; they get reduced at higher engine loads. Xue et al. (2011) concluded that biodiesel reduces the emission of aromatic and poly-aromatic compounds. They also recommended that carbonyl emissions increase in general with biodiesel content because biodiesel provides extra inherent oxygen present within the fuel molecules.

2.3.3. Polycyclic aromatic hydrocarbons (PAHs)

PAHs are well known carcinogens and are produced due to both incomplete combustion of fuel. Ravindra et al. (2008) organized a database to recognize and characterize the PAH emissions in their study. They also reported the factors affecting PAH emissions. Most of the possible human carcinogenic PAHs were found adsorbed on to the PM surface. There are no rigorous regulations for PAH emissions but these pollutants should get high priority due to their adverse impact on the human health. Fig. 3 shows the USEPA priority listed PAHs. Some of compounds shown in Fig. 3 are conceived as 'probable human carcinogen' (B2), while some are not listed as 'human carcinogens' (D) (Ravindra et al., 2008). Singh et al. (2015) measured the total average mass concentration of 16 major PAHs in a study carried out in Kanpur during fog time collected PM₁ and it was found to be 616.31 ± 30.31 ng/m³. Similarly, other studies carried out in the ambient air of different places around the world for different particle size are shown in Table 1.

Table 1. A summary of total PAHs concentration (ng/m³) in various cities of the world (Adapted from Singh et al., 2015)

Study area	Particle size	No. of PAHs	"PAH (ng/m ³)"
Chennai, India	PM _{2.5}	11	517.1
Coimbatore, India	PM ₁₀	13	90.4
Agra, India	PM ₁₀	18	97.9
Delhi, India	TSP	12	669.9
Kanpur, India	PM ₁	16	616.31
Seoul, South Korea	TSP	15	89.3
Tehran, Iran	PM ₁₀	16	44.2
Mexico City, Mexico	PM _{2.5}	11	310
Shenzhen, South China	TSP	16	128
Taiyuan, China	TSP	8	1,504.7

The toxicity of these PAH compounds are highly dependent on their molecular structure. Two isomers of PAHs with different structures show different toxicity. Therefore, EPA has classified these PAH compounds into different categories. Lea-Langton et al. (2008) collected particulate samples for diesel, biodiesel and cooking oil for comparison and analysis of particulate bound PAH emissions from a heavy duty DI diesel engine. Most of the particulate bound PAHs were lower in both the biofuels compared to mineral diesel, especially at low load conditions and most of the larger PAHs such as benzo(a)anthracene, chrysene, benzo(b)fluoranthene and benzo(k)fluoranthene were oxidized by diesel oxidation catalyst

(DOC). They also conveyed that fluoranthene was absent in mineral diesel but was present in particulates, which was an indication of pyrolytic formation of fluoranthene in engine combustion chamber.

Zielinska (2005) assessed physical and chemical transformations of primary diesel emissions. They found that transformation of primary diesel emissions in the atmosphere is very crucial from the human health perspective. Primary diesel exhaust reacts primarily with OH radicals, ozone, NO_x radicals and sunlight present in the ambient air. Monocyclic aromatics of primary diesel exhaust reacts with OH radicals and produce various aromatic compounds such as phenols, glyoxal, quinones, nitro-PAHs, and aromatic aldehydes.

Recently, it is reported that PAHs presents in the diesel particulates are one of the key factor, which adversely affect human health. PAHs include various PAHs, which reveal different toxic properties. EPA has listed 16 PAHs as carcinogenic, probable carcinogenic and possible carcinogenic and the molecular structure of these are shown in Fig. 3.

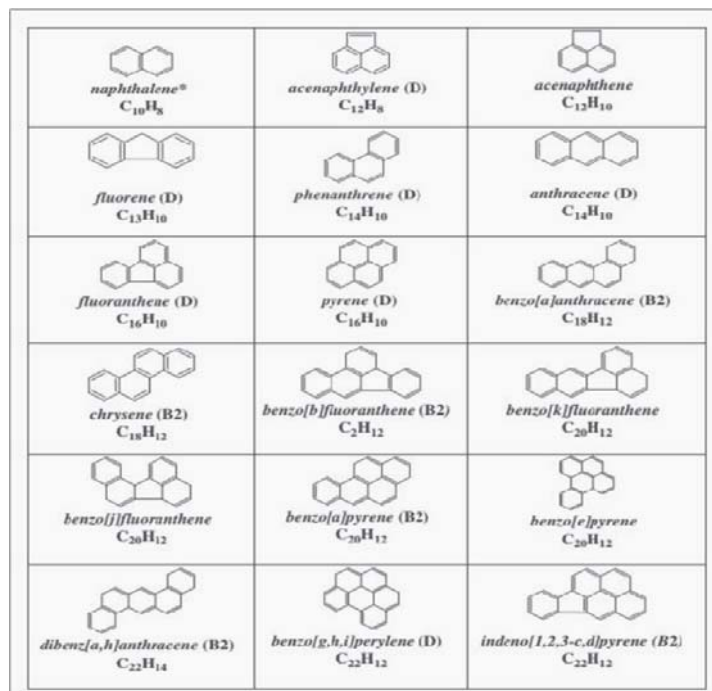


Figure 3. Priority listed PAHs.*Not included in priority list; D (not listed as to human carcinogenicity); B2 (probable human carcinogen) (Adapted from Ravindra et al., 2008)

Researchers (Karavalakis et al., 2009; Pan et al., 2000) have presented detail speciation of PAHs adsorbed on the diesel particulates. Each PAH has a different toxic potential for carcinogenic effects hence speciation of PAHs is a very important (Nisbet and LaGoy, 1992). There are some studies, which inform about the toxic potentials of individual PAH species. A summary of total PAHs concentration (ng/m³) in ambient air of various cities in the world is shown in Table 1.

Singh et al. (2015) reported that, diesel engine is the main source of PAHs by analyzing the fog time collected PM₁ by diagnostic ratios, shown in Table 2. Figure 4 shows the speciation of major PAHs concentration

Table 2. Diagnostic ratios (DR) of PAHs used as source indicator and comparison of diagnostic ratios of fog time collected submicron particles in Kanpur (Adopted from Singh et al., 2015)

Diagnostic ratio (DR)	Value	DR (sources)
Indeno[1,2,3cd]pyrene/(Indeno[1,2,3-cd]pyrene +benzo[ghi]perylene)	0.58	0.56 (coal) and 0.35–0.70 (diesel)
Indeno[1,2,3 cd]pyrene/benzo[ghi]perylene	1.37	<"1 (diesel)
Fluoranthene/(fluoranthene+pyrene)	0.73	>0.5 (diesel)
Benzo[b]fluoranthene/benzo[k]fluoranthene	0.62	>0.5 (diesel)
B[a]P/Benzo[ghi]perylene	1.17	0.5–0.6 (traffic emission)>1.25 (brown coal) ^a
B[a]P/(B[a]P+chrysene)	0.39	<"0.5 (diesel)
Pyrene/B[a]P	2.22	<"1 (petrol engine)<"10 (diesel engine)
Fluorene/(fluorene+pyrene)	0.55	>0.5 (diesel)

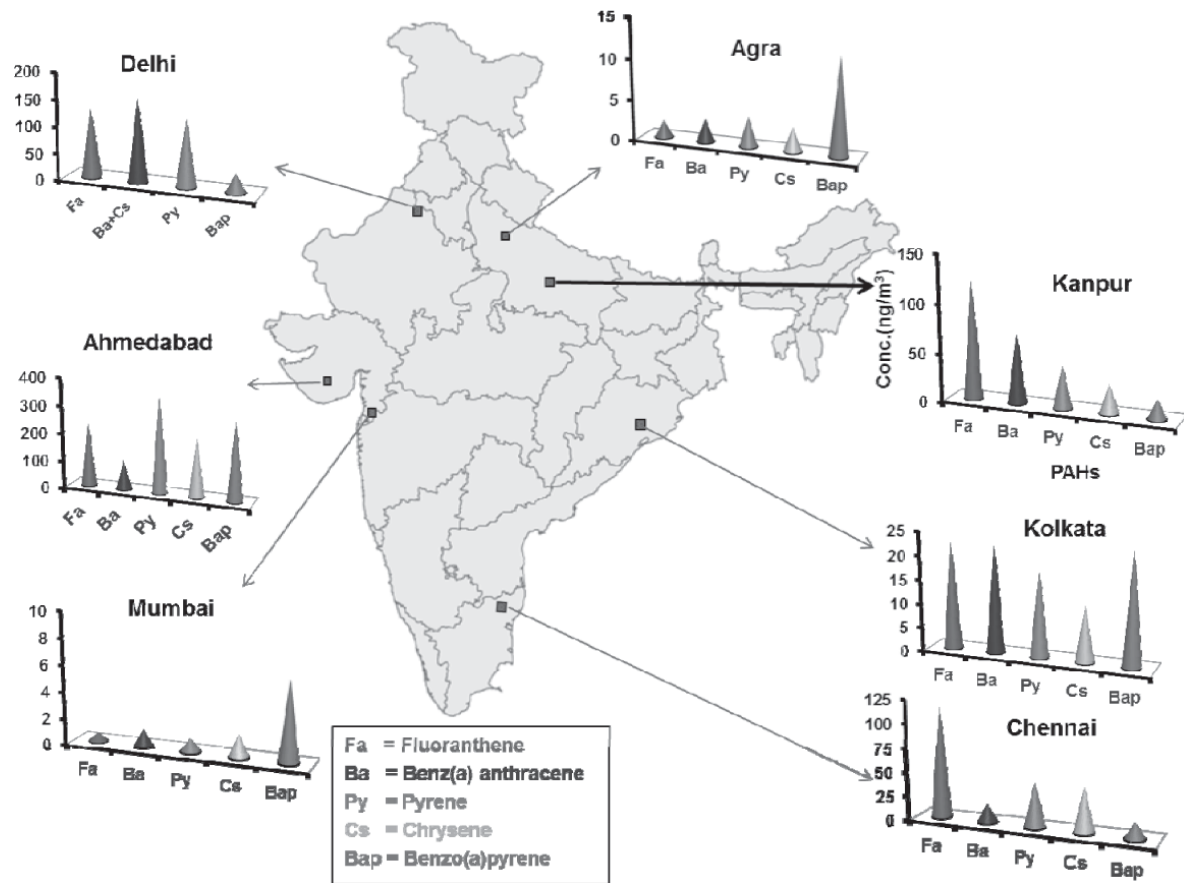


Figure 4: Speciation of major PAHs concentration (ng/m^3) of high molecular weight PAHs and Benzo[a]pyrene in some major cities of India (Adapted from Singh et al., 2015)

(ng/m^3) of high molecular weight PAHs and benzo[a]pyrene in some major cities of India (Singh et al., 2015). Polycyclic aromatic hydrocarbons (PAHs) are one of the most toxic and harmful class of chemical species present in the engine exhausts (Gupta et al., 2010).

Diesel emission is comprised of a complex mixture of various organic compounds (OC) or soluble organic fraction (SOF), nitrates, sulfate, metals, and irritants (such as acrolein, ammonia, PAHs) which are usually adsorbed over elemental carbon (EC) core. Excessive operation of diesel engines given their fuel economy, durability and power advantage has given rise to exponentially higher levels of diesel exhaust emissions. Diesel emissions are mainly categorized as regulated emissions (nitrogen oxides, unburnt hydrocarbons, carbon monoxide and particulates) and unregulated emissions (aldehydes, benzene, toluene, xylene (BTX), polycyclic aromatic hydrocarbons (PAHs), etc.) (Dusek and Amann, 2000).

Current emission standards look merely at the mass concentration of tail pipe exhaust. However, recent studies have associated the deleterious human health effects to the overwhelmingly large number of tiny diesel exhaust particles (Diaz et al., 2012). Recent efforts of reducing emissions have focused on advancements in combustion, engine technology, high pressure fuel injection jets, and use of enhanced after-treatment and PM control technologies (Khair and Majewski, 2006). Even though mass emissions have lowered significantly from the modern diesel engines, particle number emissions still continue to rise up (Gupta and Agarwal, 2010).

Bergmann et al. (2009) showed that diesel particulate filters (DPF) significantly lower the PM mass emitted from the diesel engine. However, more number of nuclei mode particles are emitted downstream of DPF and it also lead to more number of particles formed due to gas to particle emission with abundance of sulphate particles (Bergmann et al., 2009).

Particles formation in the exhaust tail pipe is a fairly complicated process. VOC get condensed over nuclei seed particles, get diluted and

undergo oxidation upon being emitted into the atmosphere. Gas to particle conversion process is aided by the various oxidizing agents present in the ambient air (Kaul et al., 2011). Upon exiting the tail-pipe, emissions undergo cooling and oxidation and the secondary emissions like secondary organic aerosol (SOA) are formed. The ambient temperature, the amount and time of dilution dictates the resultant aerosol properties (Robinson et al., 2007).

About 90% of the PM mass for the diesel exhaust is present as two submicron modes: a nuclei-mode (7.5–56 nm); and accumulation mode (56–1000 nm) (Johnson et al., 1992). Primary carbon spheres with adsorbed organics along with sulphate form accumulation mode (Baumgard and Johnson, 1992). The nuclei mode on the other hand is dominated by the elemental carbon (EC). Several studies have shown that higher amounts of fuel sulfur results in higher number of nuclei-mode particles (Baumgard and Johnson, 1992; Opris et al., 1993). In order to examine the contribution of lubricating oil and diesel to resulting PM emission, researchers have conducted various parametric investigations (Abbass et al., 1991). About one-fourth of the unburnt diesel and three-fourths of the lubricating has been shown to contribute towards the soluble organic fraction (Kittelson, 1998). A very tiny portion of SOF mass also results from pyrolysis and incomplete combustion of diesel (Figure 5).

Ultrafine particulates emitted from a diesel engine have a very high number concentration, a tiny mass concentration, and a large surface area. Due to this large surface area, they provide sorption sites for other contaminants (Cass et al., 2000). By use of mass spectrometry one recent study showed strong evidence that unburnt lubricating oil was the main source for the organic components of nanoparticles (Tobias et al., 2001). Another study showed that about 1% of the SOF was monocarboxylic acids, and about 90% of them were either unbranched, or cyclic alkanes (Rogge et al., 1993). The rest of the particles were refractory materials like oxides of the metals.

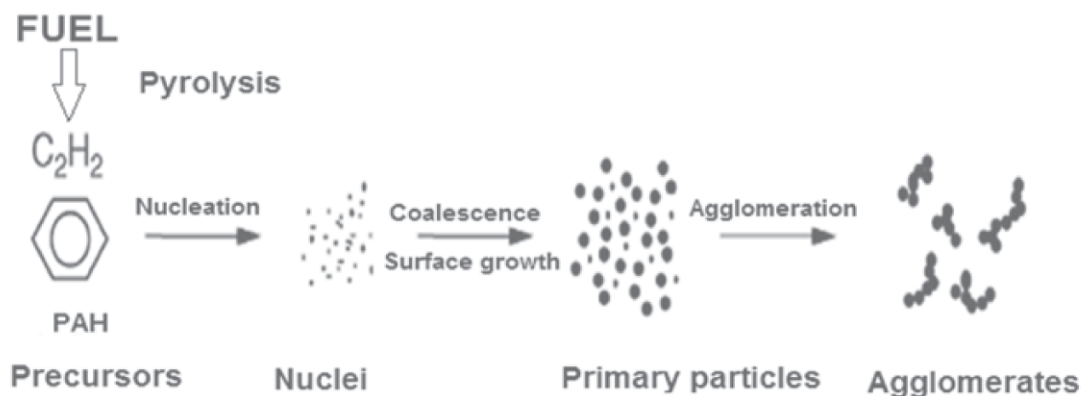


Figure 5: Schematic diagram of particulate formation during a typical combustion process (Adapted from Eastwood, 2008)

Diesel engine emissions also consists of PAHs and PAH-derivatives and they are distributed both in the gas and particle phase as they are formed at high temperature (Bildeman, 1988; Kittelson, 1985). They can get transformed to nitro-PAHs upon reaction of parent hydrocarbons with ambient NO_x. Unburned PAHs present in the fuel, the electrophilic nitration of PAHs in the engine, crankcase oils, are the major source of emitted PAHs. A wide variety of both gas- and particle- phase PAHs are present in the diesel exhaust (National Research Council, 1999; Jensen and Hites, 1983; Barbella, 1988).

One study reported presence of over 100 oxy-PAH polar fractions of a diesel PM extract (Schuetzle and Frazier, 1986), and it contained species like hydroxyl, ketone, acid anhydride, and nitro -PAH derivatives. It has been reported that majority of the nitro-PAH are formed during the expansion/exhaust stroke. PAH emissions levels from heavy-duty diesel engine vehicles are reported to be much higher as compared to those emanating from light-duty gasoline cars (Honda, 1984). The diesel fuel structures and the operational engine parameters largely affect both the chemical composition as well as the toxicity of the diesel emissions (Westerholm and Li, 1994). Hence, by reducing the fuel PAH contents we can significantly lower the toxicity of the engine exhaust.

3. Secondary organic aerosol

Organic compounds contribute as a dominant portion of the ambient

aerosols (Seinfeld and Pandis, 2012). Present analytical methods have facilitated us to quantitatively evaluate these organic fractions. The oxidation of Volatile Organic Carbon (VOC) results in the formation of Secondary Organic Aerosol (SOA). The composition and formation mechanism for SOA needs to be carefully studied to effectively control it.

3.1. SOA formation

Oxidation of the reactive organic gases (ROG) results in the formation of SOA. Natural as well as anthropogenic sources such as solvents, vegetation and ocean emissions, combustion of wood, biomass, and fossil fuels etc. are accountable for ROG formation (Seinfeld and Pandis, 2012; Jacobson et al., 2000). The most common ROG found in the atmosphere are alkanes, alkenes, aromatics and phenols. Semi-volatile organic carbon (SVOC) is formed via oxidation of the precursor ROGs.

The species having their saturation vapor pressure below a certain pressure are known as semi-volatile (Turpin et al., 2000). The rate of oxidation of precursor ROGs should be high in order for SOA formation to take place. Next comes partitioning of the SVOCs into the aerosol phase. There should be sufficient amount of SVOC having low saturation vapor pressure. Thus, SOA formation intrinsically depends upon reactivity or volatility (Grosjean and Seinfeld, 1989). Figure 6 shows a schematic view of SOA formation in the atmosphere.

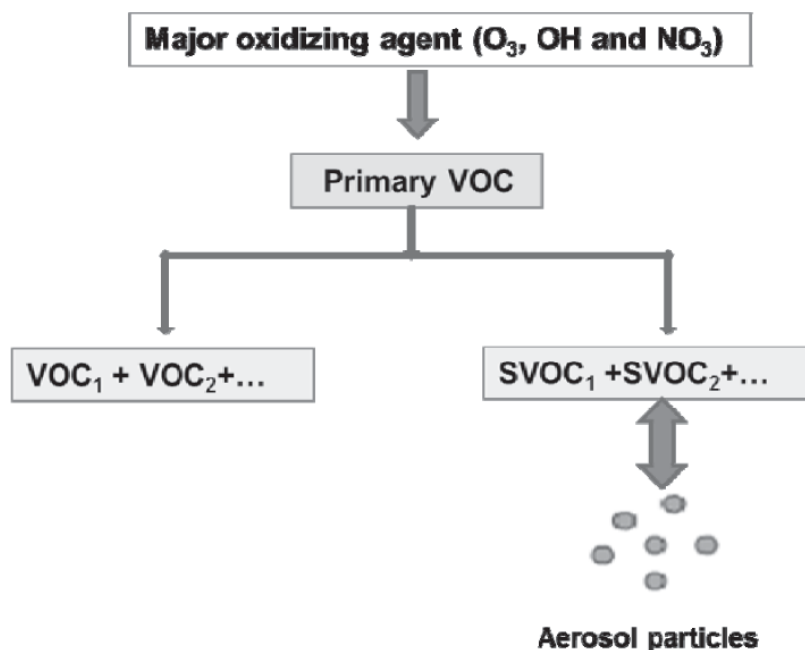
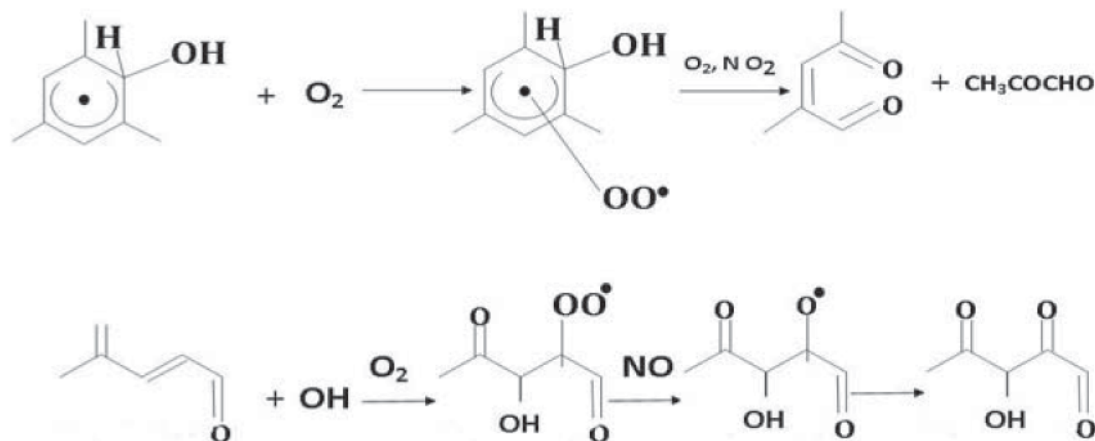


Figure 6: Schematic overview of SOA formation (Adapted from Dusek and Amann, 2000)

Present analytical methods can recognize only a few of the reaction products obtained from the oxidation of the precursor ROGs. This is the major reason identified for the lack of complete understanding of SOA. GC/MS methods can only identify a few of the organic compounds in the aerosol; hence the pathways predicted from this method do not give the total mass of the SOA formed. FTIR microscopy also does not give the information on individual species (Holes et al., 1997; Blando et al., 1998).

Therefore, the information of the various pathways of oxidation of the precursor VOCs and properties of the aerosol formed leftover is still incomplete. The oxidation of trimethylbenzene can give an indication of some of the difficulties in identifying the oxidation pathways. The oxidation of trimethylbenzene by OH radical can occur either by the addition of OH radical to the ring or by the abstraction of a hydrogen atom (Seinfeld and Pandis, 1998).

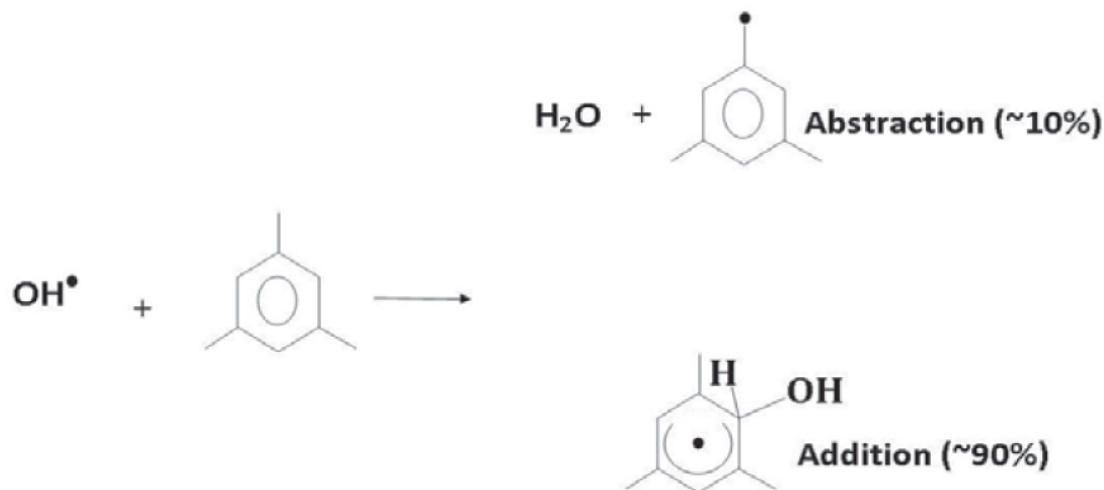


Schematic view of abstraction and addition pathways, adopted from Holes et al. (1997).

Compounds like aromatic aldehydes and aromatic nitrates are the end products of the hydrogen abstraction pathway. There is another pathway that can lead to the formation of multifunctional aromatics with nitrate and hydroxyl groups, or unsaturated dicarbonyls formed by splitting of the ring. These dicarbonyls can further get oxidized to polycarbonyls

with or without the hydroxyl groups. FTIR analysis of the oxidation products of 1, 3, 5 Trimethylbenzene shows that the aerosol is formed mostly by ring opening reactions, since the fraction of aromatic species in the particles is only 5–10% (Blando et al., 1998). Organic species in the aerosol phase are highly oxidized and comprised of about three carbonyl groups and one hydroxyl group per average molecule.

The principal reaction pathway giving this 'average molecule' is shown as follows:



Schematic view of pathway leading to the 'average molecule' in the aerosol phase after oxidation of 1, 3,5-Trimethyl Benzene, (adapted from Blando et al., 1998)

Gas chromatography analysis of the oxidation products of 1, 2, 4 trimethylbenzene produces an equal fraction of ring fragmentation and ring retaining products (Forstner et al., 1997a). Consequently, this analyzable fraction cannot act as a representative of the total organic aerosol produced by the oxidation of trimethylbenzene. Furthermore, a major portion of the known fraction is composed of furandiones that cannot be identified using FTIR spectroscopy. Therefore, it is not obligatory that the pathways prominent for the average molecule are same as that of the real atmospheric oxidation. The difference in the chemistry of 1, 3, 5 and 1, 2, 4 trimethylbenzene can affect the production of SOA composition.

Various studies have proposed that the contribution of absorption in gas to particle conversion in the atmosphere is more than that from

condensation. Smog chamber experiments showed that the aerosol yield depends upon the mass of the organic aerosol produced (Odum et al., 1997, 1996), which could not be possible if condensation had been the dominant gas to particle conversion mechanism. It is very challenging to identify whether adsorption or absorption is the dominant gas to particle conversion mechanism in the atmosphere. Some experimental results have revealed that in urban aerosol absorption is the dominant mechanism.

3.2. Effects of temperature and relative humidity on SOA formation

3.2.1. Temperature

An increase in temperature raises the efficiency for ROGs but at the same time it decreases the partitioning coefficient (Leach et al., 1999). This occurs since all the gas to particle conversion mechanisms follow an inverse relationship with saturation vapor pressure p_0 of the corresponding

SVOC, and p_0 increases exponentially with temperature. As a result SOA formation prefers an optimum temperature at which both effective oxidation and condensation occurs. It has been proposed that this temperature falls in the range of 15°C–20°C (Strader et al., 1999).

According to Strader et al. (1999) the SOA concentration curve attains maxima at 17°C. With increasing engine load, engine exhaust temperature increases consequently the temperature of the diluted exhaust in the photochemical chamber rises with increase in the engine load. Higher chamber temperature aids in oxidation of VOCs into SOC to a certain degree but also results in lower gas to particle conversions if the temperatures are too high. Hence, the oxidation of the VOCs becomes more efficient with increasing engine load (Gupta et al., 2010)

3.2.2. Relative Humidity

Relative humidity affects all the three gas to particle conversion mechanisms. It has been found that in inorganic compounds, water soluble SVOCs can easily nucleate with water vapor nevertheless not much is identified in the case of organic SVOCs (Seinfeld and Pandis, 1998). Rise in relative humidity results in the decrease in the adsorption of SVOCs to particle surfaces, as now they have to compete with a relatively larger number of water molecules for the same number of sorption sites (Story et al., 1995). However, when the particle surface is completely covered with a layer of water then the adsorption of SVOC starts rising again. Differences in humidity can increase or decrease the absorption of SVOCs over the ambient aerosol. There can be variations in the values of activity coefficient for dissolution of SVOCs in dry and wet organic aerosols (Goss and Schwarzenbach, 1998).

The droplet formation potential of a particle also depends on its hygroscopic properties and physical state (solid, liquid, heterogeneous) in addition to the availability of water vapor and temperature of the ambient air. If the absorbing aerosol is liquid then at elevated relative humidity the polar and acidic species will dissolve more easily, than that of non-polar and insoluble compounds and would grow at a faster rate. Typically, smog chamber experiments are carried out at low relative humidity; hence this effect has not been looked in detail in the previous studies. Furthermore, a recent study shows that contribution of diesel vehicles to SOA formation is more prominent in summer, whereas it is dominated by gasoline engines in the winter (Saxena and Hildemann, 1996).

3.3. Oxidation of Reactive Organic Gases (ROGs)

(a) **Gas Phase Oxidation:** O_3 , OH radical and NO_3 radical are the 3 major ambient oxidizing agents. Hydroxyl radical (OH) formed by photolysis of ozone in the presence of moisture. There are compounds (oxygenated aliphatic, saturated aliphatic, aromatics) which are not as reactive and indicate limited activity in presence of OH radicals. O_3 and NO_3 can oxidize double bond containing ROGs. A few of these oxidation products are observed in the particle phase because of their lower vapor pressure such as polyols, dicarboxylic acids, amino acids and other such multifunctional compounds (Rogge et al., 1993; Forstner, 1997a, 1997b; Blando et al., 1998; Limbeck and Puxbaum, 1999; Blando and Turpin, 2000; Ghio et al., 2000).

(b) **Liquid Phase Oxidation:** Most of the precursor gases emitted by anthropogenic sources are water insoluble nevertheless their hygroscopicity rises with aging. Fogs and clouds being rich in oxidizing agents result in the adsorption of hygroscopic VOCs. Carboxylic acids, glyoxal, esters, and organo sulfur compounds are the common products of fog and cloud processing (Samet et al., 2009). Studies have shown presence of several mono and di-carboxylic acids in the sampled rain water and fog (Abbass et al., 1991; Samet et al., 2009). Formaldehyde can also get collected in the fog droplets (Facchini et al., 1992). A recent study (Aumont et al., 2000) proposed that carboxylic acid formation is mostly dominated by VOC oxidation in the aqueous phase.

4. Health Effects of Diesel particulates and associated with other combustion sources

Numerous acute and chronic studies have critically examined diesel engine exhaust toxicity. Laboratory animals have served as good models and their results have been extrapolated for humans when looking at responses to diesel particulate matter (DPM) (International Life Sciences Institute, 2000; US EPA, 2002). Many studies reported that exposure to diesel exhaust results in acute eye and bronchial irritation, nausea, lightheadedness, phlegm and cough.

In addition, a number of chronic studies involving laboratory rats, mice, and monkeys, have been conducted recently to monitor the respiratory as well as systemic effects when exposed to DPM (Diaz-

Sanchez et al., 1996). Acute exposures to very high concentrations of raw diesel exhaust cause respiratory inflammation. Also, the nasal deposition of extremely high doses of diesel exhaust PM enhances the immunological responses to various ambient antigens. Lifetime exposures of lab animals to elevated concentrations of DPM have shown to cause chronic inflammation and fibrosis. The semi-volatile and soot borne organic material has been clinically shown to be mutagenic both to animal skin and respiratory tract. In one of the studies, the nasal instillation of a diesel exhaust aerosol in a group of human subjects lead to increase of local immunoglobulin E (IgE) and cytokine responses to antigen (Diaz-Sanchez et al., 1997; Diaz-Sanchez et al., 1999; Ghio et al., 2000). Organic fraction of diesel exhaust has been associated chiefly for their observed health response in the test population (Ghio and Huang, 2004).

In addition to diesel exhaust, various other sources of ultrafine particles include tobacco smoke; welding fumes, smoke from cooking stoves running on biomass or kerosene, and thermal power plants. Insoluble nanoparticles, their large surface area provides ample scope for catalytic reactions that results in the formation of (ROS) free radicals that are responsible for oxidative stress, inflammation and apoptosis. Huge surface areas of the nanoparticles which provide enormous adsorption sites for toxic species like PAHs to attach are correlated very well with their toxic effects.

Healthy human volunteers exposed for a short period to concentrated ambient particles (Blando et al., 1998), showed varied health effects. Simultaneous chemical speciation followed by PCA leads to interesting conclusions. A few studies have also supported acute effect of the short-term exposure to high level of PM and ozone on our systemic circulation system. Adverse health effects have been identified even for healthy individuals who are exposed to enormously large number of ultrafine particles under controlled exposure (Gupta et al., 2004). Daily individuals get exposed to combustion generated products either indoors (home, occupational settings) or outdoors (traffic, field work). However, few of them only respond to their high levels of air pollutants. This anomaly may be explained by the differences inherently present between individuals due to their health conditions, age and genetic variation.

5. Conclusions

The main goal of this review was to provide an overview on the current state of knowledge combustion generated organics and to summarize the key characteristics of these organic species as well as their impacts on the human health. Organic compounds form a major fraction of airborne particles and hence it is significant to measure and identify the organic contaminants and especially the PAHs and SOA proportion emitted primarily from the different combustion sources. The control and abatement of these organic residues requires the knowledge of the nature, source, and extent of pollution and hence existing literature has been reviewed to synthesize the available information on the formation, sources of these organic compounds. This review provides researchers with a holistic picture of this grave issue and provides ample proof for implementation of policy related initiatives and interventions.

References

- Abbass, M.K., Andrews, G.E., Williams, P.T., and Bartle, K.D., 1991. The influence of diesel fuel composition on particulate PAH emissions. SAE Paper No. 892079.
- Agarwal, A.K., Gupta, T., Kothari, A., 2011. Particulate emissions from biodiesel vs diesel fuelled compression ignition engine. *Renew. Sustain. Energ. Rev.* 15, 3278–3300.
- Agarwal, A.K., Gupta, T., Dixit, N., Shukla, P.C., 2013. Assessment of toxic potential of primary and secondary particulates/aerosols from biodiesel vis-a-vis mineral diesel fuelled engine. *Inhal. Toxicol.* 25, 325–332.
- Agarwal, A.K., Gupta, T., Shukla, P.C., Dhar, A., 2015. Particulate emissions from biodiesel fuelled CI engines. *Energ. Convers. Manage.* 94, 311–330.
- Aumont, B., Madronich, S., Bey, I., Tyndall, G.S., 2000. Contribution of secondary VOC to the composition of aqueous atmospheric particles: A modeling approach. *J. Atmos. Chem.* 35, 59–75.
- Ballesteros, R., Hernandez, J., Lyons, L., Cabanas, B., Tapia, A., 2008. Speciation of the semivolatiles hydrocarbon engine emissions from sunflower biodiesel. *Fuel* 87, 1835–1843.
- Barbella, G.T., 1988. Soot and unburnt liquid hydrocarbon emissions from diesel engines. *Combust. Sci. Technol.* 59, 183–198.
- Baumgard, K.J., Johnson, J.H., 1992. The effect of low sulfur fuel and a ceramic particle filter on diesel exhaust particle size distributions. *SAE Transactions* 101, 691–699.
- Bergmann, M., Kirchner, U., Vogt, R., Benter, T., 2009. On-road and laboratory investigation of low-level PM emissions of a modern diesel particulate filter equipped diesel passenger car. *Atmos. Environ.* 43, 1908–1916.
- Bildeman, T.F., 1988. Atmospheric Process. *Environ. Sci. Technol.* 22, 361–367.
- Blando, J.D., Porcja, R.J., Li, T.H., Bowman, D., Lioy, P.J., Turpin, B.J., 1998.

- Secondary formation and the Smoky Mountain organic aerosol: An examination of aerosol polarity and functional group composition during SEAVS. *Environ. Sci. Technol.* 32, 604–613.
12. Blando, J.D., Turpin, B.J., 2000. Secondary organic aerosol formation in cloud and fog droplets: a literature evaluation of plausibility. *Atmos. Environ.* 34, 1623–1632.
 13. Cass, G.R., Hughes, L.A., Bhawe, P., Kleeman, M.J., Allen, J.O., Salmon, L.G., 2000. The chemical composition of atmospheric ultrafine particles. *Philos. Trans. R. Soc. Lond. A Math. Phys. Sci.* 358, 2581–2592.
 14. Cheung, C., Zhu, L., Huang, Z., 2009. Regulated and unregulated emissions from a diesel engine fueled with biodiesel and biodiesel blended with methanol. *Atmos. Environ.* 43, 4865–4872.
 15. Dhar, A., Agarwal, A.K., 2013. Effect of multiple injections on particulate size-number distributions in a common rail direct injection engine fueled with karanja biodiesel blends. *SAE Technical Paper* 2013–01–1554.
 16. Di, Y., Cheung C, Huang Z., 2009. Experimental investigation on regulated and unregulated emissions of a diesel engine fueled with ultra-low sulfur diesel fuel blended with biodiesel from waste cooking oil. *Sci. Total Environ.* 407, 835–846.
 17. Diaz, E.A., Chung, Y., Papapostolou, V., J. Lawrence, M.S. Long, V., Hatakeyama, B., Gomes, Y., Calil, Sato, R., Koutrakis, P., 2012. Effects of fresh and aged vehicular exhaust emissions on breathing pattern and cellular responses—pilot single vehicle study. *Inhal. Toxicol.* 24, 288–295.
 18. Diaz-Sanchez, D., Tsien, A., Casillas, A., Dotson, A.R., and Saxon, A., 1996. Enhanced nasal cytokine production in human beings after in vivo challenge with diesel exhaust particles. *J. Allergy Clin. Immunol.* 98, 114–123.
 19. Diaz-Sanchez, D., 1997. The role of diesel exhaust particles and their associated polyaromatic hydrocarbons in the induction of allergic airway disease. *Allergy*, 52 (38 suppl.), 52–56.
 20. Diaz-Sanchez, D., Garcia, M.P., Wang, M., Jyrala, M., and Saxon, A., 1999. Nasal challenge with diesel exhaust particles can induce sensitization to a neoallergen in the human mucosa. *J. Allergy Clin. Immunol.* 104, 1183–1188.
 21. Dusek, U., Amann, M., 2000. Secondary Organic Aerosol—Formation Mechanisms and Source Contributions in Europe. IIASA Interim report IR–00–066.
 22. Eastwood, P., 2008. Particulate emissions from vehicles, John Wiley & Sons.
 23. Facchini, M. S., Fuzzi, J. Lind, H.F.O., Kalina, M. H., Puxbaum, W. Winiwarter, B., Arends, W., Wobrock, W., Jaeschke., 1992. Phase partitioning and chemical reactions of low molecular weight organic compounds in fog. *Tellus B*, 44, 533–544.
 24. Fenger, J., 2009. Air pollution in the last 50 years from local to global. *Atmos. Environ.* 43, 13–22.
 25. Flynn, P.F., Durrett, R.P., Hunter, G.L., zur Loye, A.O., Akinyemi, O. Dec, J.E, et al., 1999. Diesel combustion: an integrated view combining laser diagnostics, chemical kinetics, and empirical validation. *SAE Technical Paper* 1999–01–0509.
 26. Forstner, H.J., Flagan, R.C., Seinfeld, J.H., 1997a. Secondary organic aerosol from the photooxidation of aromatic hydrocarbons: Molecular composition. *Environ. Sci. Technol.* 31, 1345–1358.
 27. Forstner, H.J., Flagan, R.C., Seinfeld J.H., 1997b. Molecular speciation of secondary organic aerosol from photooxidation of the higher alkenes: 1-octene and 1-decene, *Atmos. Environ.*, 31, 1953–1964.
 28. Ghio, A.J., Kim, C., Devline, R.B., 2000. Concentrated ambient particles induce mild pulmonary inflammation in healthy human volunteers. *Am. J. Respir. Crit. Care Med.* 162, 981–988.
 29. Ghio, A.J., Huang, Y.C.T., 2004. Exposure to concentrated ambient particles (CAPs): a review. *Inhal. Toxicol.* 16, 53–59.
 30. Godlee, F. 1993. Air pollution II: road traffic and modern industry. *Br. Med. J.* 303, 1539–1543.
 31. Goss, K.-U., Schwarzenbach, R. P., 1998. Gas/Solid and Gas/Liquid partitioning of organic compounds: Critical evaluation of equilibrium constants. *Environ. Sci. Technol.* 32, 2025–2032.
 32. Grosjean, D., Seinfeld, J.H., 1989. Parameterization of the formation potential of secondary organic aerosols. *Atmos. Environ.* 23, 1733–1747.
 33. Grosjean, D., Grosjean, E., Gertler, A.W., 2001. On-road emissions of carbonyls from light-duty and heavy-duty vehicles. *Environ. Sci. Technol.* 35, 45–53.
 34. Gupta, T., Demokritou, P., Koutrakis, P., 2004. Development and evaluation of an ultrafine particle concentrator for inhalation toxicological studies. *Inhal. Toxicol.* 16, 851–862.
 35. Gupta, T., Kothari, A., Srivastava, D.K., Agarwal, A.K., 2010. Measurement of number and size distribution of particles emitted from a mid-sized transportation multipoint port fuel injection gasoline engine. *Fuel*, 89, 2230–2233.
 36. Gupta, T., Agarwal, A.K., 2010. Toxicology of Combustion Products Handbook of Combustion Vol. 1: Fundamentals and Safety. Edited by Maximilian Lackner, Franz Winter, and Avinash . Agarwal Copyright WILEY-VCH Verlag GmbH & Co. KGaA, Weinheim ISBN: 978-3-527-32449-1357-377.
 37. Ho, S.S.H., Ho, K.F., Lee, S.C., Cheng, Y., Yu, J.Z, Lam, K.M, et al. 2012. Carbonyl emissions from vehicular exhausts sources in Hong Kong. *J. Air Waste Manag. Assoc.* 62, 221–34.
 38. Holes, A., Eusebi, A., Grosjean, D., Allen, D.T., 1997. FTIR analysis of aerosol formed in the photooxidation of 1, 3, 5-trimethylbenzene. *Aerosol Sci. Technol.* 26, 516–526.
 39. Honda, T., 1984. In-situ emission levels of carcinogenic and mutagenic compounds from diesel and gasoline engine vehicles on an express way. *Environ. Sci. Technol.* 18, 895–902.
 40. Hyslop, N.P., 2009. Impaired visibility: the air pollution people see. *Atmos. Environ.* 43, 182–195.
 41. International Life Sciences Institute (ILSI), 2000. The relevance of the rat lung response to particle overload for human risk assessment, in ILSI Risk Science Institute Workshop, vol. 12 (1–2) (ed. D.E. Gardner), Inhalation Toxicology, pp. 1–148.
 42. Jacobson, M., Hansson, H.C., Noone, K., Charlson, R., 2000. Organic atmospheric aerosols: Review and state of the science. *Rev. Geophys.* 38, 267–294.
 43. Jaidevi, J., Tripathi, S.N., Gupta, T.B., Singh, N., Gopalakrishnan, V., Dey, S., 2011. Observation-based 3-D view of aerosol radiative properties over Indian Continental Tropical Convergence Zone: Implications to regional climate, *Tellus*, 63B, 971–989.
 44. Jensen, T.E., Hites, R.A., 1983. Aromatic diesel emissions as a function of engine condition. *Anal. Chem.*, 55, 594–599.
 45. Johnson, J.H., Bagley, S.T., Gratz, L.D., Leddy, D.G., 1992. A review of diesel particulate control technology and emissions effects. *SAE Paper No.* 940233.
 46. Karavalakis, G., Stournas, S., Bakeas, E., 2009. Effects of diesel/biodiesel blends on regulated and unregulated pollutants from a passenger vehicle operated over the European and the Athens driving cycles. *Atmos. Environ.* 43, 1745–1752.
 47. Kaul, D., Gupta, T., Tripathi, S.N., Tare, V., Collett, Jr J., 2011. Secondary organic aerosol: a comparison between foggy and nonfoggy days, *Environ. Sci. Technol.* 45, 7307–7313.
 48. Khair, M.K., Majewski, W.A., 2006. Diesel emissions and their control, in, *SAE Technical Paper*.
 49. Kittelson, D.B., 1985. Measurements of PAH in the cylinders of an operating diesel engine. *EPA Report No.* 600/D-85/ 012.
 50. Kittelson, D.B., 1998. Engine and nanoparticles: a review. *J. Aerosol Sci.* 29, 575–588.
 51. Krahl, J., Munack, A., Ruschel, Y., Schröder, O., Bünger J., 2008. Exhaust gas emissions and mutagenic effects of diesel fuel, biodiesel and biodiesel blends. *SAE Technical Paper* 2008–01–2508.
 52. Krahl, J., Munack, A., Schröder, O., Stein, H., Bünger, J., 2003. Influence of biodiesel and different designed diesel fuels on the exhaust gas emissions and health effects. *SAE Technical Paper*, 2003–01–3199.
 53. Kristensson, A., Johansson, C., Westerholm, R., Swietlicki, E., Gidhagen, L., Wideqvist, U., et al. 2004. Real-world traffic emission factors of gases and particles measured in a road tunnel in Stockholm, Sweden. *Atmos. Environ.* 38, 657–673.
 54. Leach, K. B., Kamens, R. M., Strommen, M. R., Jang, M., 1999. Partitioning of semivolatile organic compounds in the presence of a secondary organic aerosol in a controlled atmosphere. *J. Atmos. Chem.* 33, 241–264.
 55. Lea-Langton, A., Li, H., Andrews, G.E., 2008. Comparison of particulate PAH emissions for diesel, biodiesel and cooking oil using a heavy duty DI diesel engine. *SAE Technical Paper* 2008–01–1811.
 56. Liaquat, A.M., Kalam, M.A., Masjuki, H.H., Jayed, M.H., 2010. Potential emissions reduction in road transport sector using biofuel in developing countries. *Atmos. Environ.* 44, 3869–3877.
 57. Limbeck, A., Puxbaum, H., 1999. Organic acids in continental background aerosols. *Atmos. Environ.* 33, 1847–1852.
 58. Liu, Y.Y., Lin, T.C., Wang, Y.J., Ho, W.L., 2009. Carbonyl compounds and toxicity assessments of emissions from a diesel engine running on biodiesels. *J. Air Waste Manage. Assoc.* 59, 163–171.
 59. Loeffler, K.W., Koehler, C.A., Paul, N.M., De, Haan, D.O., 2006. Oligomer formation in evaporating aqueous glyoxal and methyl glyoxal solutions. *Environ. Sci. Technol.* 40, 6318–6323.
 60. Machado, C. S., Arbilla, G., 2008. Carbonyl emissions in diesel and biodiesel exhaust. *Atmos. Environ.* 42, 769–775.
 61. Madden, M.C., Dailey, L.A., Stonehuerner, J.G, Harris, D.B., 2003. Responses of cultured human airways epithelial cells treated with diesel exhaust extracts will vary with the engine load. *J. Toxicol. Environ. Health A* 66, 2281–2297.
 62. McDonald, J.D., Barr, E.B., White, R.K., Chow, J.C., Schauer, J.J., Zielinska, B., et al. 2004. Generation and characterization of four dilutions of diesel engine exhaust for a subchronic inhalation study. *Environ. Sci. Technol.* 38, 2513–2522.
 63. National Research Council., 1999. Automotive fuel economy, National Research Council Committee on Fuel Economy of Automobiles and Light Trucks, Energy Engineering Board, National Academy Press, Washington, DC.
 64. Nisbet, I.C., LaGoy, P.K., 1992. Toxic equivalency factors (TEFs) for polycyclic aromatic hydrocarbons (PAHs). *Regul. Toxicol. Pharmacol.* 16, 290–300.
 65. Odum, J. R., Hoffmann, T., Bowman, F., Collins D., Flagan, R. C., Seinfeld J. H., 1996. Gas/Particle partitioning and secondary organic aerosol yields. *Environ. Sci. Technol.* 30, 2580–2585.
 66. Odum, J. R., Jungkamp, T. W. P., Griffin, R. J., Flagan, R. C., Seinfeld J. H., 1997. The atmospheric aerosol formation potential of whole gasoline vapor. *Science* 274, 96–99.
 67. Opris, C.N., Gratz, L.D., Bagley, S.T., Baumgard, K.J., Leddy, D.G., and Johnson, J.H., 1993. The effects of fuel sulfur concentration on regulated and unregulated heavy-duty diesel emissions. *SAE Paper No.* 930733.
 68. Pan, J., Quarderer, S., Smeal, T., Sharp, C., 2000. Comparison of PAH and nitro-PAH emissions among standard diesel fuel, biodiesel fuel, and their blend on diesel engines. In: Proceedings of the 48th ASMS conference on mass spectrometry and allied topics, Long Beach, CA.
 69. Pang X, Shi X, Mu Y, He H, Shuai S, Chen H, et al. 2006. Characteristics of carbonyl compounds emission from a diesel-engine using biodiesel-ethanol-diesel as fuel. *Atmos. Environ.* 40, 7057–65.

70. Ramanathan, V., Feng, Y., 2009. Air pollution, greenhouse gases and climate change: global and regional perspectives. *Atmos. Environ.* 43, 37–50.
71. Ravindra, K., Sokhi, R., Van Grieken, R., 2008. Atmospheric polycyclic aromatic hydrocarbons: source attribution, emission factors and regulation. *Atmos. Environ.* 42, 2895–2921.
72. Robinson, A.L., Donahue, N.M., Shrivastava, M.K., Weitkamp, E.A., Sage, A.M., Grieshop, A.P., Lane, T.E., Pierce, J.R., Pandis, S.N., 2007. Rethinking organic aerosols: Semivolatile emissions and photochemical aging. *Science*, 315, 1259–1262.
73. Rogge, W.F., Hildemann, L.M., Mazurek, M.A., and Cass, G.R., 1993a. Sources of fine organic aerosol II: Noncatalyst and catalyst-equipped automobiles and heavy-duty diesel trucks. *Environ. Sci. Technol.*, 27, 636–651.
74. Rogge, W.F., Mazurek, M.A., Hildemann, L.M., Cass, G.R., Simoneit, B.R., 1993b. Quantification of urban organic aerosols at a molecular level: identification, abundance and seasonal variation. *Atmospheric Environment. Part A. General Topics*, 27, 1309–1330.
75. Ruckerl, R., Schneider, A., Breitner, S., Cyrus, J., Peters, A., 2011. Health effects of Particulate air pollution a review of epidemiological evidence. *Inhal. Toxicol.* 23, 555–592.
76. Samet, J.M., Rappold, A., Gaff, D., Cascio, W.E., Berntsen, J.H., Huang, Y.C.T., Herbst, M., Bassett, M., Montilla, T., Hazucha, M.J., Bromberg, P.A., Devlin, R.B., 2009. Concentrated ambient ultrafine particle exposure induces cardiac changes in young healthy volunteers. *Am. J. Respir. Crit. Care Med.*, 179, 1034–1042.
77. Saxena, P., Hildemann, L.M., 1996. Water-soluble organics in atmospheric particles: A critical review of the literature and application of thermodynamics to identify candidate compounds. *J. Atmos. Chem.* 24, 57–109.
78. Schauer, J.J., Kleeman, M.J., Cass, G.R., Simoneit, B.R., 1999. Measurement of emissions from air pollution sources. 2. C1 through C30 organic compounds from medium duty diesel trucks. *Environ. Sci. Technol.* 33, 1578–1587.
79. Schauer, J.J., Kleeman, M.J., Cass, G.R., Simoneit, B.R., 2002. Measurement of emissions from air pollution sources. 5. C1–C32 organic compounds from gasoline powered motor vehicles. *Environ. Sci. Technol.* 36, 1169–1180.
80. Schroeder, O., Krahl, J., Bünger, J., 1999. Environmental and health effects caused by the use of biodiesel. SAE Technical Paper 1999-01-3561.
81. Schuetzle, D. and Frazier, J.A., 1986. Factors influencing the emission of vapor and particulate phase components from diesel engines, in *Carcinogenic and Mutagenic Effects of Diesel Engine Exhaust* (eds N. Ishinishi, A. Koizumi, R.O. McClellan, and W. Stöber), Elsevier Science Publishers, pp. 41–63.
82. Seinfeld, J. H. and Pandis, S. N., 1998. *Atmospheric Chemistry and Physics: From Air Pollution to Climate Change*, John Wiley & Sons, New York.
83. Seinfeld, J.H., and Pandis, S.N. 2012. *Atmospheric chemistry and physics: from air pollution to climate change*, John Wiley & Sons,
84. Singh, D.K., Sharma, S., Habib, G., Gupta, T., 2015. Speciation of atmospheric polycyclic aromatic hydrocarbons (PAHs) present during fog time collected submicron particles. *Environ. Sci. Pollut. Res.* 22, 12458–12468.
85. Story, J.M., Luo, W., Isabelle, L. M., Pankow, J.F., 1995. Gas/solid partitioning of semi-volatile organic compounds to model atmospheric solid surfaces as a function of relative humidity. *Environ. Sci. Technol.* 29, pp. 2420–2428.
86. Strader, R., Lurmann, F., Pandis, S. N., 1999. Evaluation of secondary organic aerosol formation in winter. *Atmos. Environ.* 33, 4849–4863.
87. Takada, K., Yoshimura, F., Ohga, Y., Kusaka, J., Daisho, Y., 2003. Experimental study on unregulated emission characteristics of turbocharged DI diesel engine with common rail fuel injection system. SAE Technical Paper 2003-01-3158.
88. Tobias, H.J., Beving, D.E., Ziemann, P.J., Sakurai, H., Zuk, M., Mc Murry, P.H., Zarling, D., Waytulonis, R., and Kittelson, D.B., 2001. Chemical analysis of diesel engine nanoparticles using a nano-DMA/thermal desorption particle beam mass spectrometer. *Environ. Sci. Technol.* 35, 2233–2243.
89. Turpin, B.J., Saxena, P., Andrews, E., 2000. Measuring and simulating particulate organics in the atmosphere: problems and prospects. *Atmos. Environ.* 34, 2983–3013.
90. U.S. Environmental Protection Agency, 2002. Health assessment document for diesel engine exhaust. EPA Report No. 600/8-90-057F.
91. Watt, J., Tidblad, J., Kucera, V., Hamilton, R. (Eds.), 2009. *The Effects of Air Pollution on Cultural Heritage*. Springer, New York, p. 306.
92. Westerholm, R., Li, H., 1994. A multivariate statistical analysis of fuel related polycyclic aromatic hydrocarbon emissions from heavy-duty diesel vehicles. *Environ. Sci. Technol.* 28, 965.
93. Xue, J., Grift, T.E., Hansen, A.C., 2011. Effect of biodiesel on engine performances and emissions. *Renew. Sustain. Energ. Rev.* 15, 1098–10116.
94. Yang, W., Omaye, S.T., 2009. Air pollutants, oxidative stress and human health. *Mutat. Res.* 674, 45–54.
95. Zielinska, B., 2005. Atmospheric transformation of diesel emissions. *Exp. Toxicol. Pathol.* 57, 31–42.



Numerical Investigation of Swirling Hydrogen Flames: Effect of Swirl and Fuel Jet in Coherent Structures

V. Suresh Balaji¹, Ashoke De^{*1}, Santanu De²

¹Department of Aerospace Engineering, ²Department of Mechanical Engineering Indian Institute of Technology, Kanpur-208 016, India

ARTICLE INFO

Received : 03 September 2015
 Revised : 09 October 2015
 Accepted : 10 October 2015

Keywords:

Swirling hydrogen flames,
 Large Eddy Simulation,
 Precessing Vortex Core

ABSTRACT

The present work reports on the numerical investigation of turbulent swirling flames using Large Eddy Simulation (LES) methodology in conjunction with presumed shape PDF (Probability Density Function) based combustion models. The LES with dynamic-smagorinsky eddy viscosity model is used to study the different complex unsteady structures involved in the flow field. Sydney swirl burner, which is considered as a reliable benchmark for numerical studies in swirling flames, is chosen as a test case. Two isothermal and three reacting test cases are considered for the present study. In the isothermal calculations, a precession vortex core is accurately captured. The precession vortex core structures, responsible for the instability in hydrogen-methane reacting cases, are analyzed using different visualization techniques. Phase averaging technique is also used to analyze the different repeated coherent structures responsible for the instability in the flow field.

© 2016 ISEES, All rights reserved

1. Introduction

Efficient use of energy and reduction of emissions are the most essential design parameters for any engineering appliances, especially in propulsive devices. This gives rise to the need for constant progress in the research areas of combustion to meet the stringent emission regulations and environment requirements. From the past, fossil fuel has been the attracting fuel for combustion devices. However, the emissions of unburned hydrocarbons, nitrogen oxides, carbon monoxide and other pollutants create the need for an alternate for fossil fuel application. Use of hydrogen fuel instead of fossil fuels is one of the efficient ways of handling the present day crises in the energy and to reduce the impact of emissions on environment. However, the use of pure hydrogen as a fuel for combustion systems is highly inclined towards safety issues owing to highly inflammable nature of hydrogen, particularly during transportation processes. So, by blending hydrogen with other fossil fuels, this inflammable risk factor can be reduced. Besides, combustion in swirling flows is one of the most widely used techniques as it shows a significant enhancement in stability of the flame with the help of recirculation zones. Besides enhancing the stability, better mixing is achieved which gives rise to the increase in combustion efficiency thereby reducing the pollutant emissions. In addition to that, the flame length is reduced by enhancing mixing, which results in reduction in combustion chamber length. However, swirling flow coherent structures such as Precessing vortex core (PVC). Even though it helps in large scale turbulent mixing, PVC also produces undesirable noises and instability of the flame. So, it is very much essential

to have deeper insight to the analysis of the swirling flows in order to have an optimized design and improved combustion efficiency. So, to have a sustainable combustion technology, combustion of hydrogen blended fuels in swirling flows is one of the attractive methods in the research areas of hydrogen energy.

Several studies are reported in the literature on non premixed combustion of hydrogen blended fuels. Dinesh et al. (2012) studied the combustion of syngas with different proportions of hydrogen blended with NO and CO. And it was reported that there was a significant change in unsteady and steady flame temperature with the different proportion of hydrogen in the fuel. In the contest of swirling flames with hydrogen, LES in combination with presumed shape PDF approach was applied to Hydrogen-methane swirling flame by Malasekara et al. (2010). It was concluded in that work that LES could be a very useful tool in accurate modeling of combustion characteristics and its capability was expected to grow in future. In another study, Dinesh et al. (2006) has studied a single hydrogen-methane flame from Sydney swirl burner using LES technique and observed some discrepancy in the mixture fraction predictions. In a follow up work, Dinesh et al. (2009) studied the instability mechanism associated with three methane-hydrogen flames of Sydney swirl burner. Kempf et al. (2008) studied one pure methane case and two methane-hydrogen case from Sydney swirl burner with two different LES programs with different SGS models and numerical techniques to have a code-independent analysis of these flames. Stein and Kempf (2007) studied one pure methane case and one methane-hydrogen case, and revealed some challenging features and difficulties of LES in predicting the complex flow structures.

* Corresponding Author: E-mail address: ashoke@iitk.ac.in, Tel.: +91-512-2597863

Besides, some non-hydrogen reacting cases are studied using LES and reported in the literature. El-Asrag and Menon (2005) reported a study on reactive swirling flame database of Sydney Swirl burner using LES with sub grid mixing and combustion model based on the Linear Eddy Mixing approach. The recirculation zone size, flame structure and its length were studied. Dinesh et al. (2005) studied two swirling flames and the different dynamics involved in the flow are explored. Hu et al. (2008) studied swirling non premixed flame using LES technique for validation of different sub-grid scale models. LES technique in combination with PDF based approach is applied by James et al. (2007) to have comparative study on the pure methane and methane-air flames. The model predicted the flow physics well and the different coherent structures were captured. Overall, it was concluded that LES is a very useful tool in accurate modeling of non premixed flames and expected to grow in future as it could produce an accurate amount of flow characteristics.

In addition, several studies are reported in literature on the swirling reacting and non-reacting flows. Syred and Beer (1974) presented a detailed review on combustion in swirling flows. Lilly (1977) reported a review on swirl flows in combustion and summarized the advancements in experimental techniques and numerical predictions in dealing with swirling flows. Candel et al. (2014) presented a complete review on the dynamics of the swirling flow and the different issues to be studied further. Malasekara et al. (2008) reported a study on swirling non premixed isothermal jets using LES. Experimentally observed vortex break down and different structures were successfully reproduced in the LES simulations and the potential for LES in industrial applications was emphasized. Dinesh et al. (2009) studied an isothermal flame from Sydney swirl burner database and proved that LES is adequately accurate and computationally efficient than Direct Numerical Simulation. Another study is reported in isothermal jet of Sydney swirl burner by Yang et al. (2010). Proper Orthogonal decomposition is applied to study the different coherent structures involved in the flow. Another work by Ranga Dinesh et al. (2005) reports for the need of further improvement in the LES technique to capture the different dynamics of the flow. The recirculation zone, vortex break down and precessing vortex core are studied by Yang and Soren (2012). Comparative study between Reynolds Average Navier Stokes formulation and LES technique is reported for one isothermal flow by Yang and Soren (2012). In this study, it was observed that the vorticity fields captured were different for LES and RANS technique with LES captured the most realistic predictions. More recently, De and Acharya (2012) investigated both non-reacting and reacting methane-hydrogen premixed flames using LES, which also exhibit the capability of LES technique in predicting such flows. Moreover, several experimental studies are reported in the literature in the context of swirling flames (Al-abdeli and Masri, 2003, 2004; Masri et al., 2004; Al-abdeli et al., 2006).

From the above review, it can be concluded that LES has been proved to be a powerful technique in dealing with turbulent swirling flames. Also, from the literature, it is seen that the database of Sydney swirl burner offers challenging flames with various complexity and interesting flow behaviors. Most of the studies in the context of swirling flows are inclined towards non reacting flows and reacting flows of non-hydrogen flames. Very few studies are reported in the context of swirling hydrogen blended flames, while only few studies reported on the instability analysis of these flames. However, none of the studies is reported on the effects of interaction of swirl and the fuel jet velocity in the instability of hydrogen blended swirling flames. In this study, the effect of swirl number and the fuel jet velocity in the instability of hydrogen based swirling flames is analyzed using LES technique with presumed shape PDF approach. To do so, two non-reacting cases and three hydrogen cases from Sydney swirl database are simulated and analyzed. Firstly, the simulation of non-reacting cases provides the basic idea on the hydrodynamic behavior of the flow field followed by the simulations of methane-hydrogen case which presents the vital information on the effect of hydrogen addition. Finally, the simulation of three hydrogen cases, in which the first two cases contains same fuel jet velocity with different swirl number and the last two cases contains same swirl number with different fuel jet velocities, are carried out. This study provides the effect of swirl number and the fuel jet velocity in the turbulent structures of hydrogen based swirling flames. Phase averaging technique is used to visualize the repeated structures, in order to explore the interactions between fuel and swirling jet.

2. Numerical Details

2.1. Flow modeling using LES

In order to model the turbulence, LES is used where the large scale structures are resolved and the small scale structures are modeled. Hence,

the filtered governing equations for the conservation of mass, momentum, energy and species transport are solved in the present work (Bhaya et al., 2014). Dynamic Smagorinsky model is used for sub-grid stress modeling (Smagorinsky, 1963; Germano et al., 1991), where the gradient approximation is invoked to relate the unresolved stresses to resolved velocity field and given as:

$$\tilde{u}_i u_j - \tilde{u}_i \tilde{u}_j = -2\nu_t \bar{S}_{ij} \quad (1)$$

$$\text{Where } \nu_t = C_s^2 (\Delta)^2 |\bar{S}| \quad (2)$$

$$\bar{S}_{ij} = \left(\frac{\partial \bar{u}_i}{\partial x_j} + \frac{\partial \bar{u}_j}{\partial x_i} \right) \quad (3)$$

$$|\bar{S}| = \sqrt{2\bar{S}_{ij}\bar{S}_{ij}} \quad (4)$$

and S is the mean rate of strain. The coefficient C_s is evaluated dynamically (Smagorinsky, 1963; Germano et al., 1991).

2.2 Combustion modelling: Steady Flamelet (SF) Model

In this CFD solution, the chemistry is completely described by the two quantities (i.e.) the mixture fraction f and the scalar dissipation rate χ . The scalar dissipation term is an equivalent term for strain rate and represents the departure from equilibrium. This reduction of two variables enables flamelet calculations to be pre-calculated and stored in table which reduces the computational cost. Hence, by transferring the equation from physical space to mixture fraction space, a simplified set of equations in mixture fraction space are solved. Therefore, N equations are solved for species mass fraction along with one equation for temperature as given below:

$$\frac{1}{2} \rho \chi \frac{\partial^2 Y_i}{\partial f^2} + S_i = 0 \quad (5)$$

$$\frac{1}{2} \rho \chi \frac{\partial^2 T}{\partial f^2} - \frac{1}{C_p} \sum_i H_i S_i + \frac{1}{2C_p} \rho \chi \left[\frac{\partial C_p}{\partial f} + \sum_i C_{p,i} \frac{\partial Y_i}{\partial f} \right] \frac{\partial T}{\partial f} = 0 \quad (6)$$

where Y_i , T , ρ , S , are the species mass fraction, temperature, density and chemical production rate of species respectively. Also, C_p and $C_{p,i}$ are the mixture-averaged specific heat and species specific heat respectively.

The scalar dissipation rate is defined as, $\chi = 2D|\nabla f|^2$ (7) where D is the diffusion coefficient. The scalar dissipation rate at the flame surface χ_{st} is closed by

$$\chi_{st} = \frac{a_s \exp\left(-2\left[\text{erfc}^{-1}(2f_{st})\right]^2\right)}{\pi}$$

where χ_{st} is the scalar dissipation rate at $f = f_{st}$

a_s is the characteristic strain rate

f_{st} is the stoichiometric mixture fraction

erfc^{-1} is the inverse complementary error function.

3. Test Case

The schematic view of the Sydney swirl burner is shown in Fig. 1(a). The central fuel jet has a diameter of 3.6 mm. The central jet is surrounded with a ceramic bluff-body of 50 mm in diameter. The swirling air flow is made to come out through the annulus of diameter 5 mm. The swirling flow consists of two components: the annular axial velocity U_s and the annular swirling velocity W_s . The whole setup is placed into a wind

tunnel with 130 X 130 mm square cross section sides which delivers an external co flow ambient velocity U_e , which is kept constant (Masri et al., 2004). Three tangential acclivitous ports with a diameter 7 mm each are used to create the swirl component. The swirl strength is quantified by the geometrical swirl number S_g ($S_g = W_s/U_s$). The characteristics of the swirling flow are altered by changing these three bulk velocities and also the geometrical swirl number. The test case and the corresponding boundary conditions used are tabulated in the Table 1.

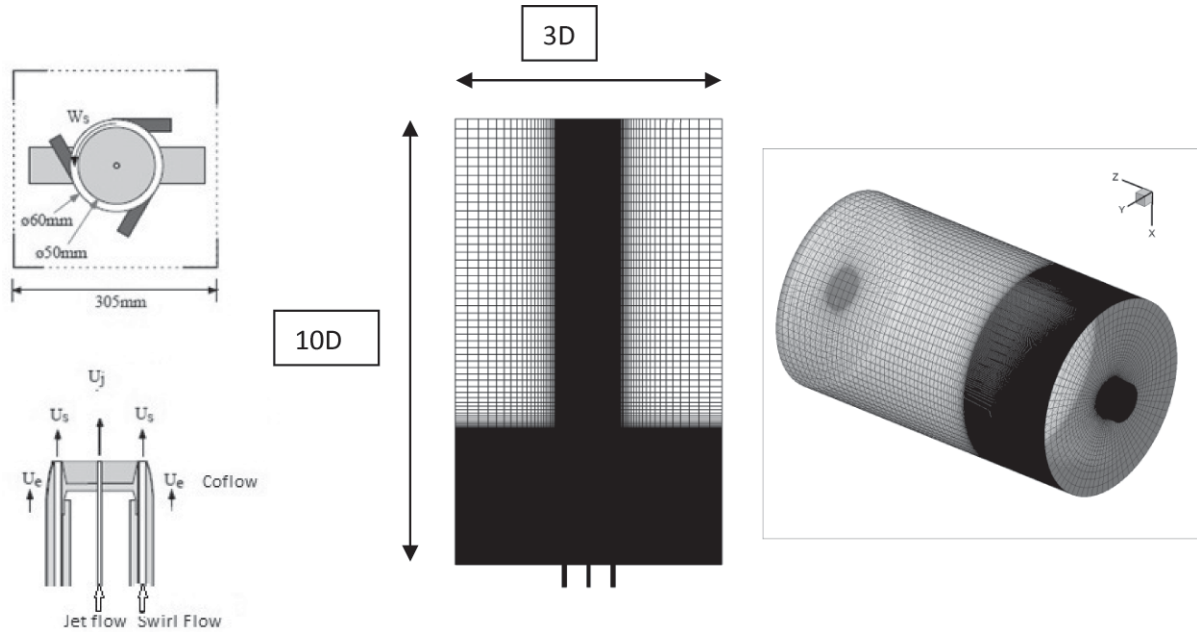


Figure 1(a): Schematic of Sydney swirl burner and LES grid

Table 1: Boundary Conditions for the simulated cases

	CASE	FUEL	U_j	U_s	W_s	U_e	S_g
Isothermal case	N29S054	-	66	29.7	16	20	0.54
	N16S159	-	66	16.26	25.85	20	1.59
Methane-Hydrogen case	SMH1	CH ₄ - H ₂ (1:1)	140.8	42.8	13.8	20	0.3
	SMH2		140.8	29.7	16	20	0.5
	SMH3		226	29.7	16	20	0.5

4 Computational Domain

Sydney swirl burner is used as a test case for studying the combustion in swirling flows. The three dimensional grid comprises of 2.8M cells and is extended upto 500 mm in the downstream direction, 150 mm in radial direction and 25 mm in the upstream direction. A non uniform node distribution is used with 335 nodes in the axial direction, 114 nodes in the radial direction and 80 nodes in the azimuthal direction. The 'O' grid is used near the central jet to have a uniform distribution of grid in the azimuthal direction as depicted in Fig. 1(a). This grid is used for the simulation of cold flow and pure methane case. For the hydrogen-methane case, the grid comprises of 5.9M cells with 682 nodes in the axial direction, 114 nodes in the radial direction and 80 nodes in the azimuthal direction.

The simulations are carried out using the commercial software package ANSYS FLUENT-15.0 (Ansys, 2010). The convective term in the momentum equation is discretized using second order bounded central differencing scheme while the second order discretization is consistently used for all the terms and a pressure based segmented algorithm is used for solving all the equations. The turbulence chemistry interaction is modeled using steady Flamelet model and GRI3.0 mechanism (Smith et al., 1999), with 53 species and 325 reactions, is used to represent the chemistry. The PISO algorithm is used in pressure velocity coupling. The boundary condition at the outlet is set to pressure outlet while the symmetry boundary condition is used at the radial boundary. The boundary condition at the fuel inlet and swirl inlet is generated using 1/7- power law profile.

5 Results & Discussion

5.1 Grid Resolution

The resolution of grid plays a predominant role in LES calculations in capturing the different flow structures involved in the flow. A lot of indicators are reported in the literature for determining LES grid resolution. In this study, two methods proposed by Pope (2000) and Celik et al. (2005) are used to find the quality of grid. In the first method as proposed by Pope (2000), to have good LES predictions, at-least 80% of the kinetic energy should be resolved. This is done by finding the ratio of turbulent kinetic energy, k_{tur} , and the total turbulent kinetic energy, $k_{tot} = k_{tur} + k_{sgs}$, and the value is checked for the resolution of the grid. The k_{tur} is calculated from the predicted rms velocities and the k_{sgs} is calculated separately using a UDF during the iteration process (Bhaya et al., 2014). In addition to a LES test filter, the UDF uses the grid filter size and the test filter kinetic energy from the solver to calculate k_{sgs} using the formula (Bhaya et al., 2014)

$$k_{sgs} = \frac{\Delta_{sgs}}{\Delta_{test}} k_{test} \quad (9)$$

Figure 1(b) shows the grid resolution using this technique and it is confirmed that more than 85% of the turbulent kinetic energy is resolved throughout the domain especially in the shear layer region. Another method as proposed by Celik et al. (2005) uses eddy viscosity ratio as an

indicator for examining the grid resolution. The formulation of this method is given by

$$LES_IQ = \frac{1}{1 + 0.05 \left(\frac{\nu_{t,eff}}{\nu} \right)^{0.53}} \quad (10)$$

In this formulation $\nu_{t,eff}$ denotes the effective viscosity, which is the sum of laminar and turbulent viscosity, and ν denotes the laminar viscosity. The LES quality index should be greater than 0.8 for good LES predictions [33]. Fig. 1(b) shows the LES quality index distribution throughout the domain and it confirms the quality of the present grid.

5.2 Non-Reacting flow results

This section presents the computed results of two non reacting cases. Before presenting the analysis of hydrodynamic behavior of the flame, the present LES calculation is validated with the experimental measurements. Fig. 2(a) depicts the comparison of LES predictions with the experimental measurements of low swirl and high swirl cases at different axial locations. The predictions show overall good agreement with the experimental measurements both in upstream and downstream regions. The center line axial velocity near the burner is well capture in both low swirl and high swirl cases. At $Z/D = 1.4$, the central line negative velocity is captured well, which indicates that the recirculation zone is captured accurately. While looking at a single three dimensional stream trace from the fuel jet for these cases, it is observed that two distinct recirculation regions: one near the bluff body region and another

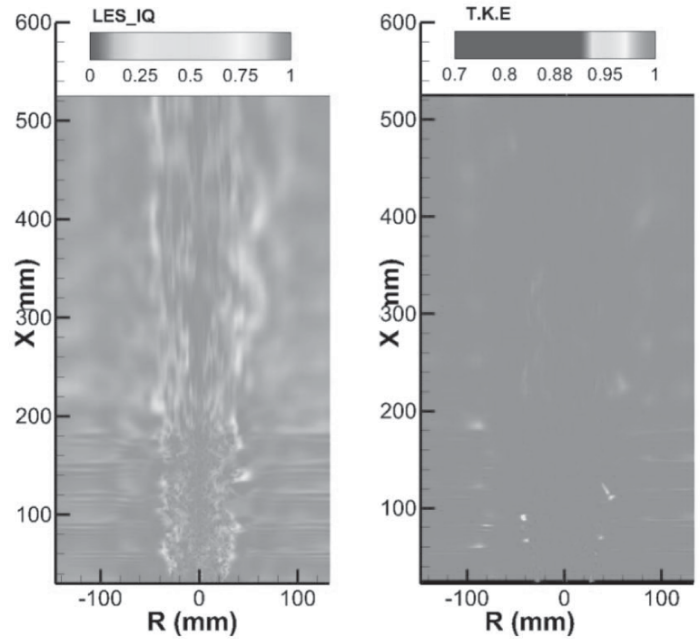


Figure 1(b): Resolution of Grid using LES quality criteria (Celik et al., 2005) (Left) and Resolution of the turbulent kinetic energy (Right) in the domain

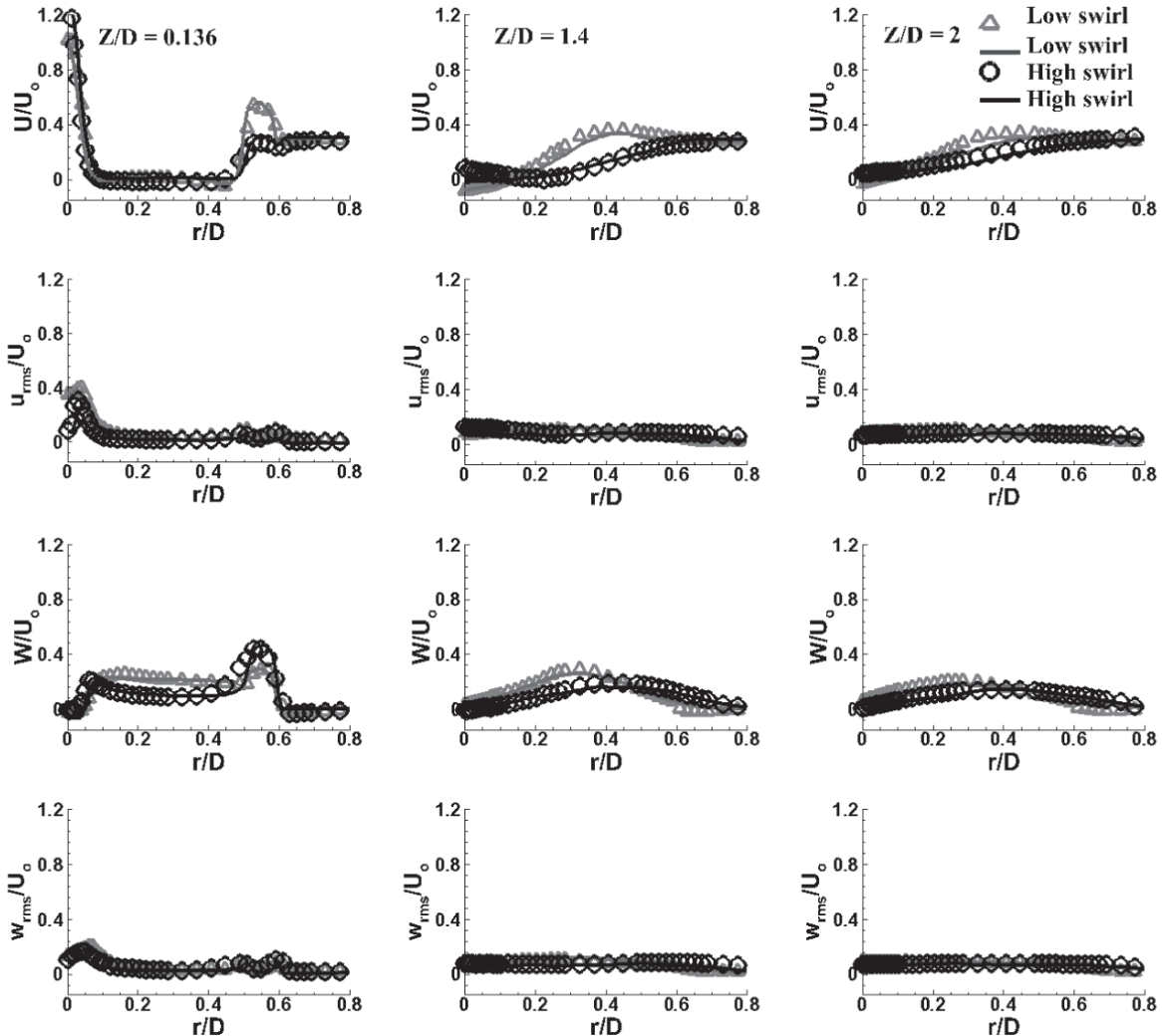


Figure 2(a): Radial plot of mean and rms velocity of non reacting case: Symbols are measurements and lines are predictions

one in the downstream position; whereas in the high swirl case, a single long recirculation region is captured. In the high swirl case, the axial momentum flux is lesser compared to the low swirl case. In addition, the tangential momentum flux is predominant in the high swirl case. This predominant tangential momentum and the adverse pressure gradient causes high swirl case with a single recirculation region.

Further, the detailed precessing vortex core (PVC) structure is visualized using the second eigen value method. Fig. 2(b) shows the comparison of PVC structures of both high and low swirl cases. The

PVC structure is clearly visible in low swirl case whereas it diffuses much quickly in high swirl case. Further, Fast Fourier Transform (FFT) technique is used to analyze the frequency corresponding to the oscillation of this PVC structure. A clear peak of frequency at around 488Hz for high swirl case and two different peaks for low swirl case; one near bluff body region at around 162 Hz and another peak at around 325 Hz in the downstream position (Figs. 3(a-c)) are observed. This agrees with the two distinct structures in the low swirl case and a single long recirculation region of high swirl case.

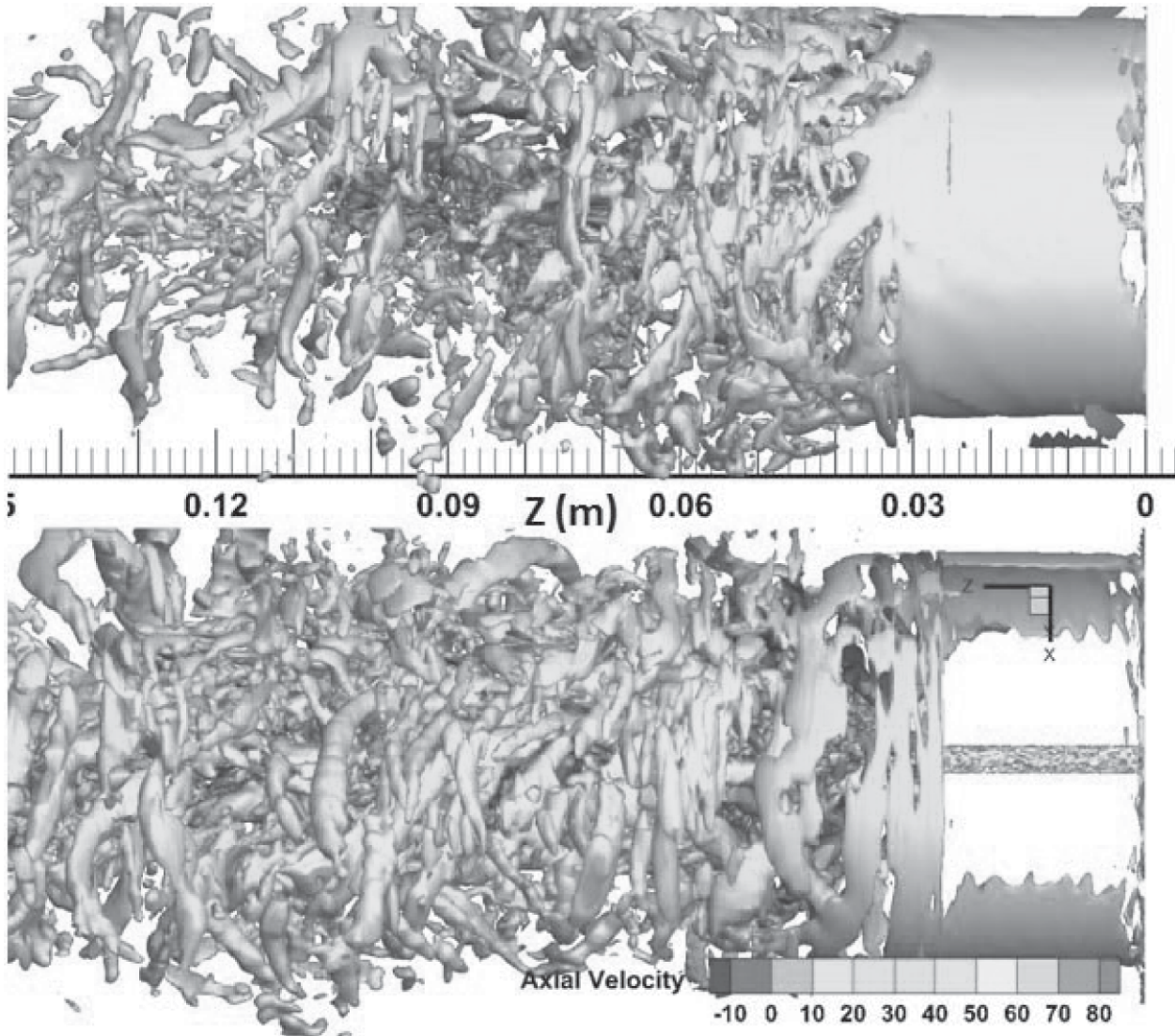


Figure 2(b): PVC structure visualization of non reacting case: Low swirl case (top), high swirl case (bottom)

Further, the inner structures responsible for this observed frequency are explored using phase averaging technique. Figs. 3(a-c) show the five phases of a complete cycle corresponding to two peaks of low swirl case and one peak of high swirl case respectively. And the each phase is averaged over four complete cycles to eliminate the high frequency oscillations. In Fig. 3(a) at phase 1, it clearly shows a formation of a vortex due to swirling air, induced behind the bluff body in both the sides of fuel jet. This shedding vortex, which grows in size by interacting with the smaller vortex formed, changes its shape in phase 2 due to the change in pressure fluctuations shown in Fig. 3(a). Fig. 3(b) shows the phase averaging data for second peak of low swirl case. The data presented here at each phase is averaged over five complete cycles to remove the high frequency oscillations. At phase 1, it clearly shows a formation of a vortex due to swirling air, induced behind the bluff body in both the sides in upstream position. This shedding vortex changes its shape in phase 2 due to the change in pressure fluctuations shown in Fig. 3(b). Then in phase 3, the same vortex grows in size and regains its shape in phases 4 and 5. The same characteristics are shown in both the sides. In addition to

that, along the center line at a axial location of around $Z/D = 1.5$ from the exit plane, where the vortex breakdown phenomenon is observed, a clear change in the shape of recirculation bubble through different phases is observed. From the phase analysis, three distinct regions of repeating dominant structures is observed; the upstream position near the bluff body, downstream position along the center line and the neck region. The same pattern of interaction in the phase averaged data is observed for the second peak of low swirl. However, the interaction is more concentrated in the downstream position, where the distinct peak frequency is observed.

Fig. 3(c) shows the phase averaged instantaneous velocity vector of high swirl case representing the five phases of frequency. The dominant frequency is found at 488 Hz. Based on this frequency, each phase is averaged over five complete cycles and the result is presented here. In the figure, an already formed recirculation zone near the fuel jet along the axial line changes its shape through the different phases and regain its structure in the fifth phase. Similarly, a shedding vortex near the bluff body is getting elongated through third phase and regains its shape in the fifth phase. The PVC structure shown in Fig. 2(b) is compared with the

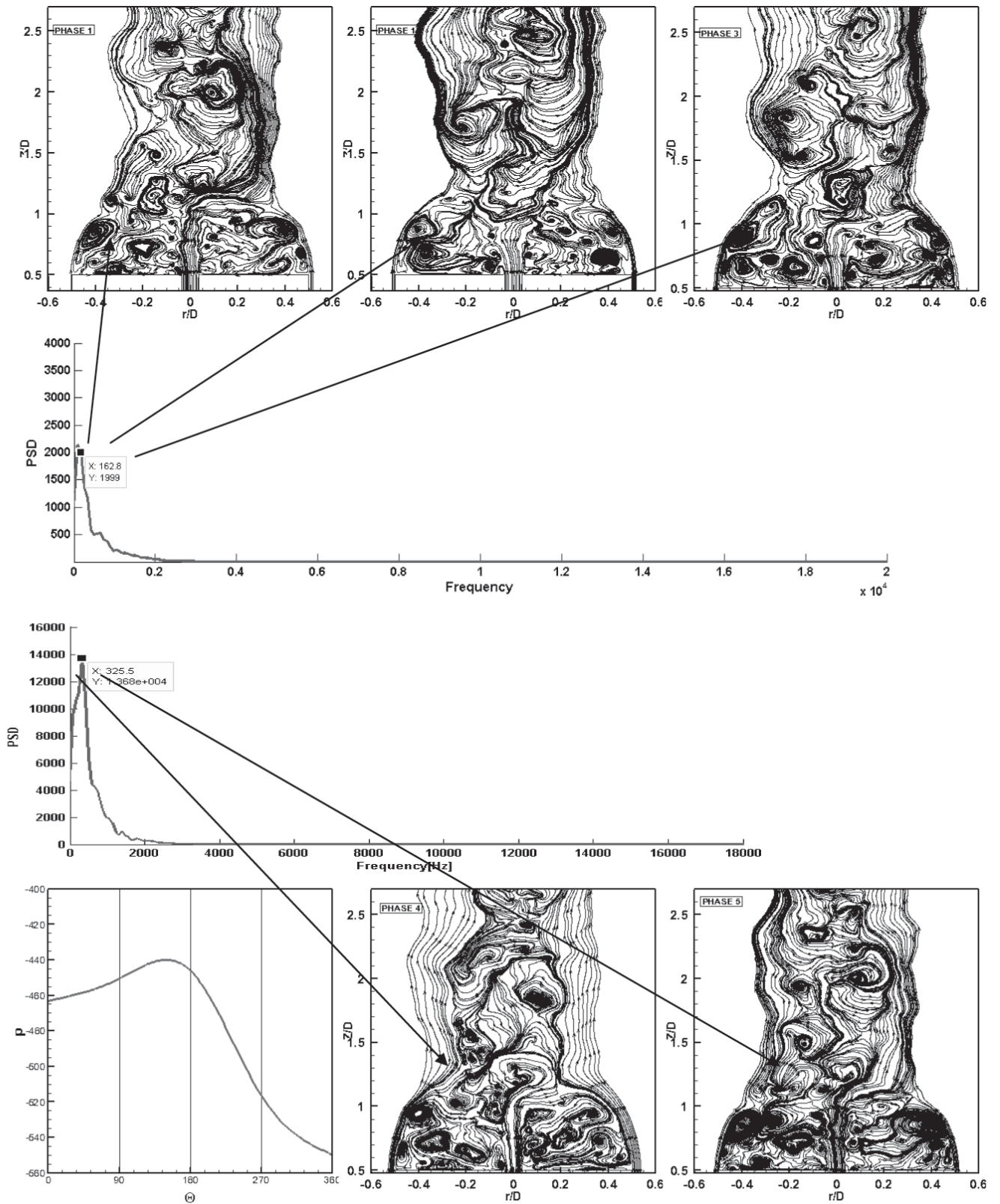


Figure 3(a): Phase averaged data for instantaneous flow from Phase 1-5 at an oscillation of 162Hz for Low swirl case

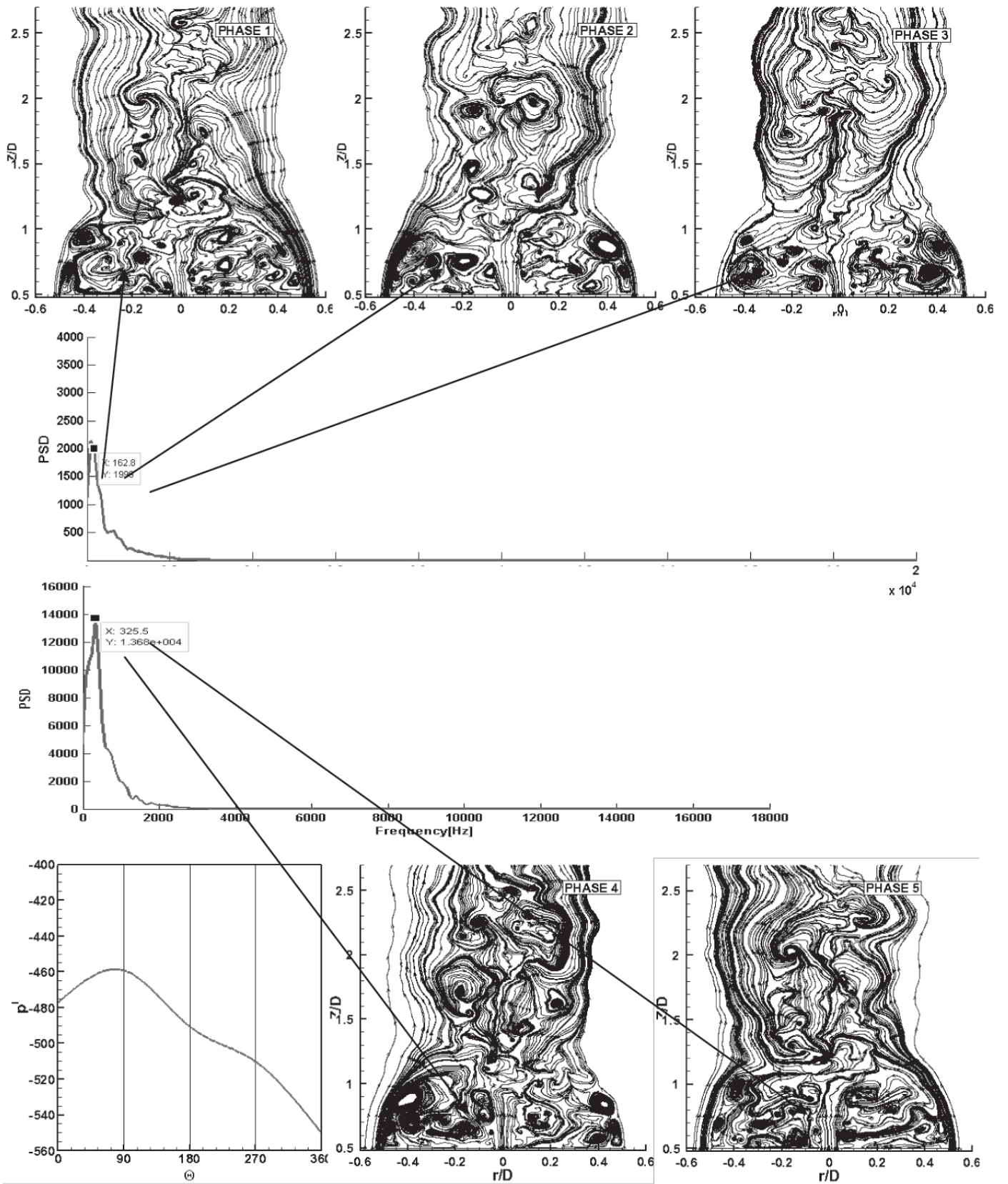


Figure 3(b): Phase averaged data for instantaneous flow from Phase 1-5 at an oscillation of 325Hz for Low swirl case

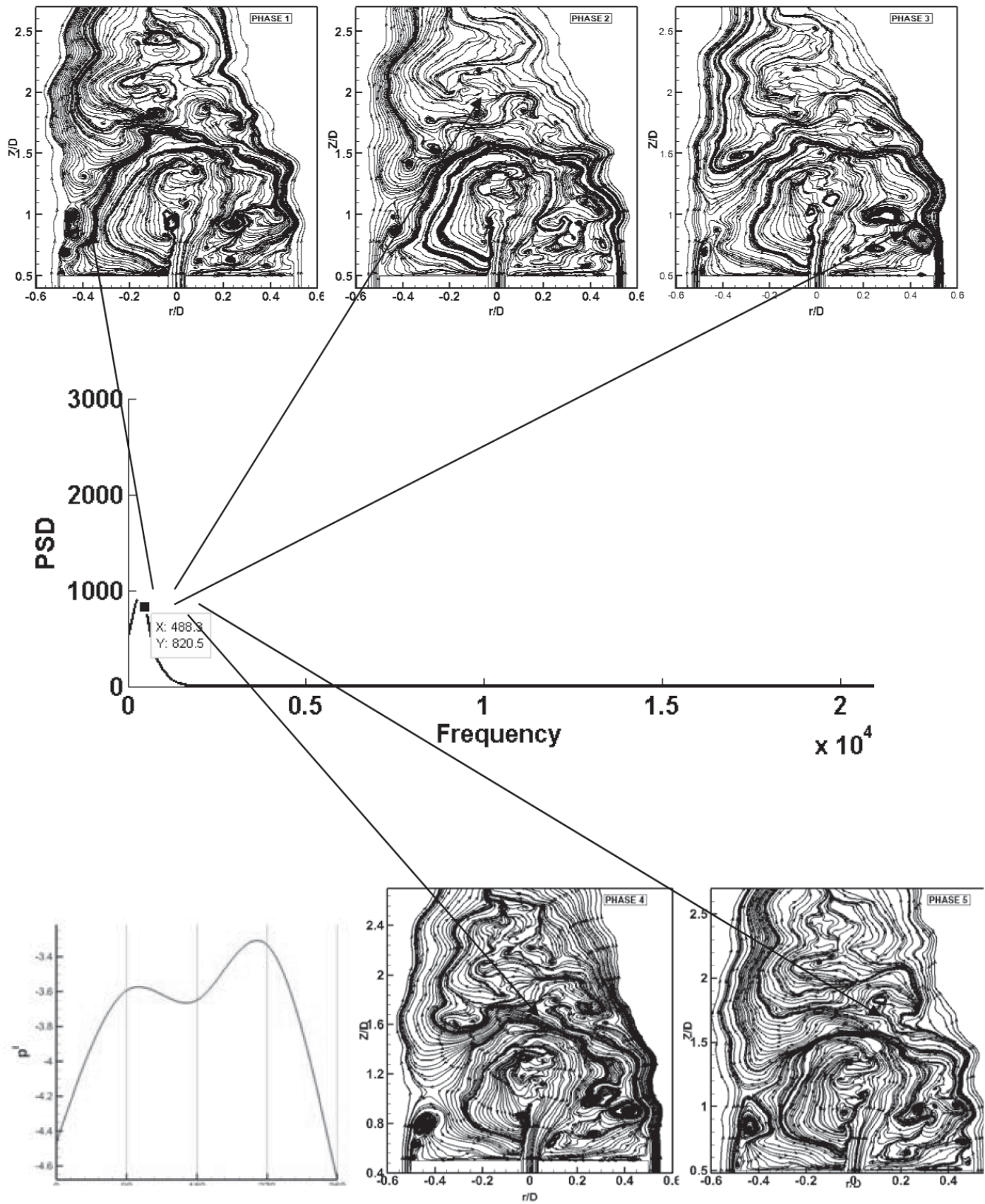


Figure 3(c): Phase averaged data for instantaneous flow from Phase 1-5 at an oscillation of 488Hz for High swirl case

phase averaged data. In low swirl case, due to the presence of secondary vortex breakdown bubble, the PVC structure is prolonged whereas in high swirl case the PVC structure diffuses quickly due to the absence of secondary recirculation region.

5.3 Reacting flow results

This section presents the flow characteristics of hydrogen blended flames.

5.3.1 Validation with Experimental Measurements

Initially, the pure methane flame is simulated followed by the hydrogen blended flames. Fig. 4(a) exhibits the mean and rms velocity predictions

of the SMH1 case and SMH2 case respectively. The central line axial velocity at the burner exit is well predicted. At around $Z/D = 0.4$, the negative velocity is also predicted well. However, the recirculation bubble is extended upto $Z/D = 0.8$ and the negative velocity at this position is not captured. In the downstream position, the centre line velocity is over predicted and the prediction shows improvement in the radial positions. The predictions shows overall good agreement with the experimental measurements. The mean tangential velocity predictions shows overall good agreement with slight over prediction in the radial direction at about $r/D = 0.2$. The rms tangential velocity predictions also show good agreement with the experimental measurements. Some discrepancies are observed near the bluff body induced recirculation zone. But overall the predictions show good agreement with the experimental measurements.

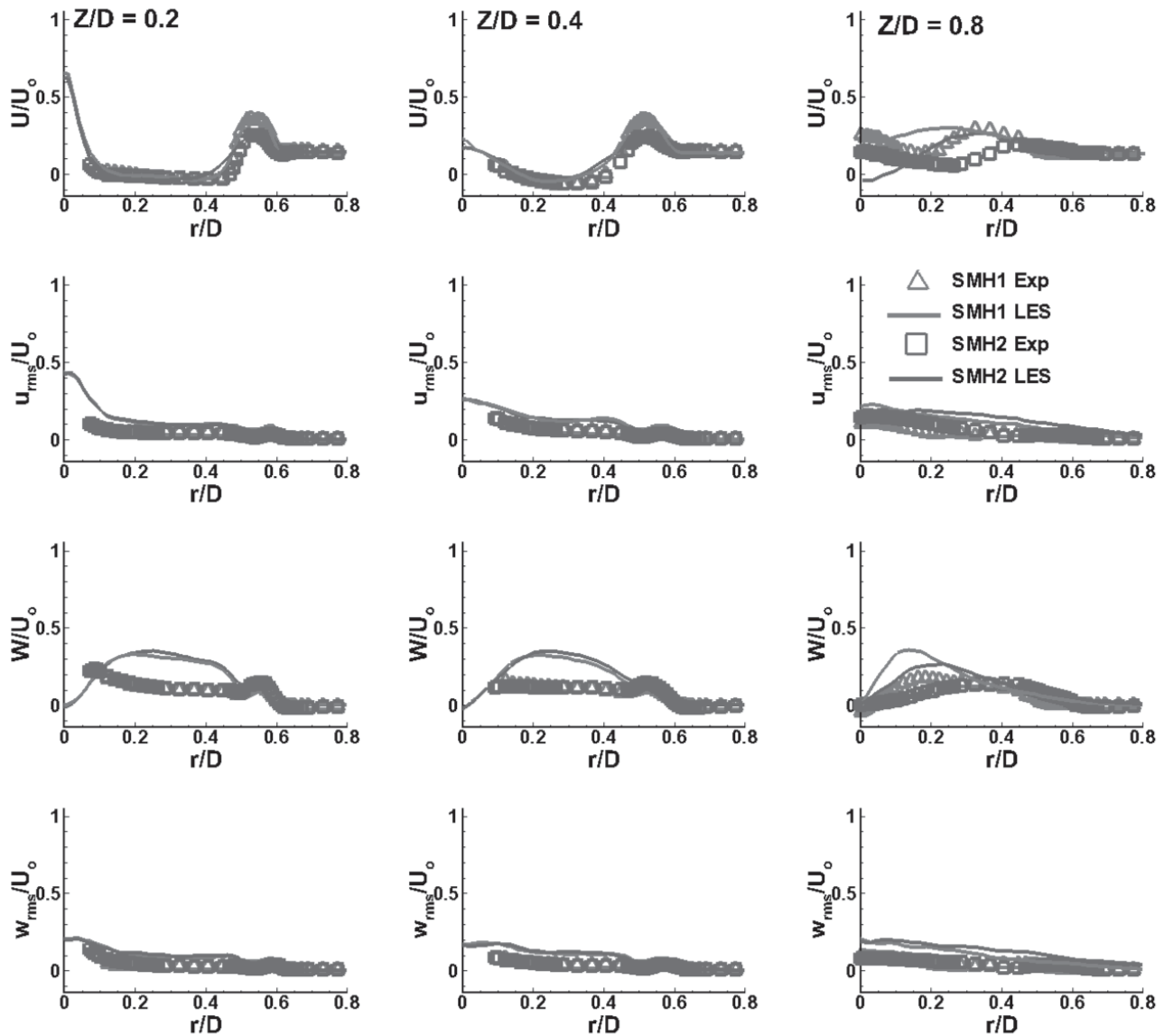


Figure 4(a): Radial Plot of Mean and rms velocity predictions for Hydrogen flames

Fig. 4(b) shows the temperature predictions in different downstream locations. In the upstream position, the temperature is over predicted till $r/D=0.4$. Then in the further radial positions, the predictions shows good match with the experimental measurements. The predictions improved along the downstream positions. There is an under prediction of mean mixture fraction in the central line. This creates the discrepancies in the temperature predictions. There are some discrepancies in the temperature and mean mixture fraction predictions but overall the predictions shows good agreement with the experimental measurements.

6.3.2 Analysis of Precessing Vortex core

Fig. 5 shows the PVC structure visualization of hydrogen flames. From the visualization of PVC structure, it is clear that even though the hydrogen flame is relatively longer than methane flame, qualitatively the vortex breakdown is much rapid in hydrogen flames. This can be attributed to high diffusivity of hydrogen fuel. In addition to that, the frequency of the oscillation is identified using FFT analysis. Interestingly, in spite of different boundary conditions, a peak frequency of around 48 Hz is

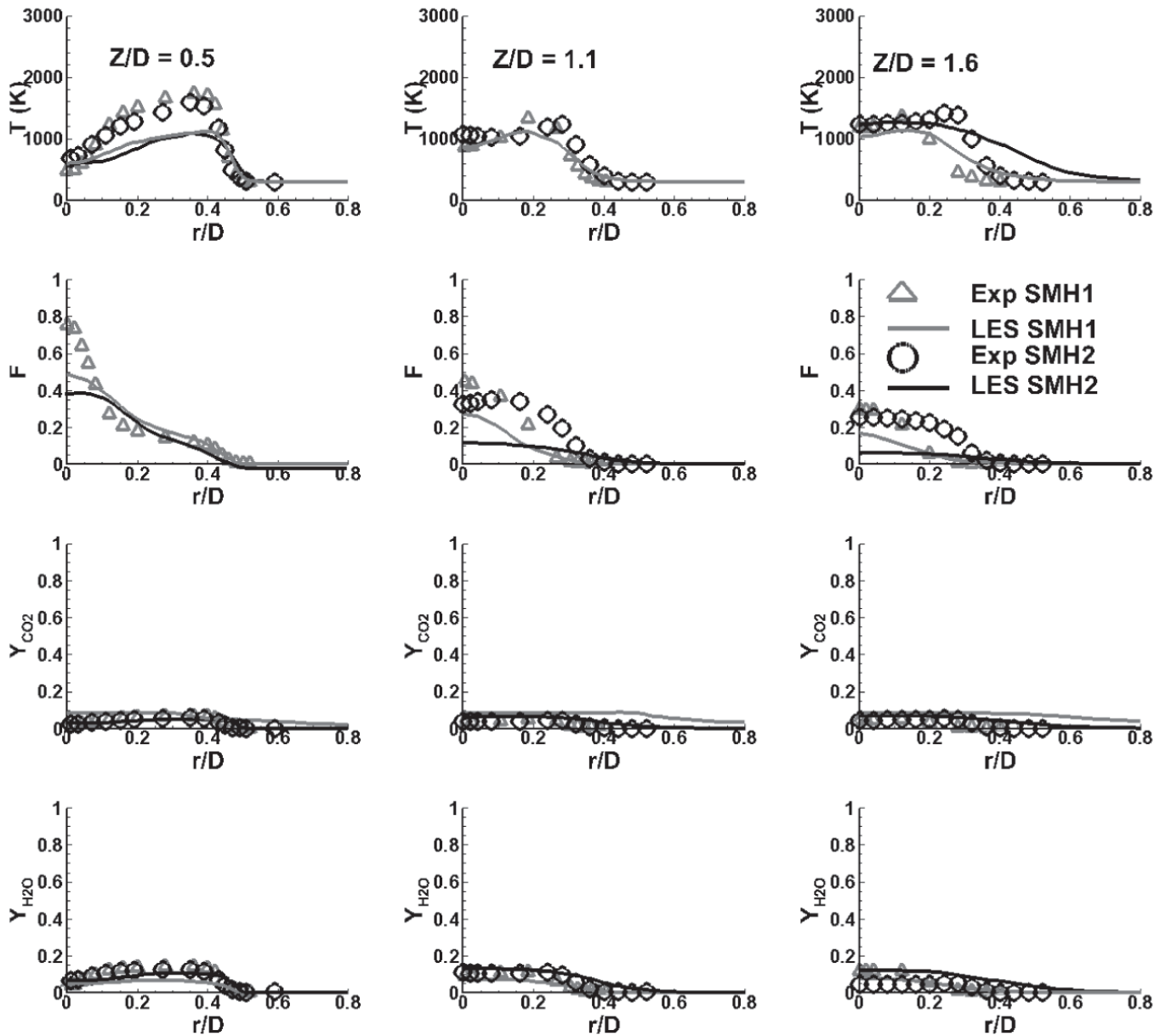


Figure 4(b): Radial Plot of Temperature (T), Mixture Fraction (F) and Mass Fraction predictions for Hydrogen flames

identified in all the three cases. However, there is a clear difference in the PVC structures of these three flames. Hence the phase averaged data is utilized to explore the PVC structures in details.

To reveal the inner structure of the PVC, five phases representing a complete cycle of the oscillating frequency is presented (Figs. 6(a-c)), and each phase is averaged over 4 complete cycles to remove high frequency oscillations. In SMH1 case, the vortices trailing from the swirling flow interacts with the bluff body induced vortices and then change its shape in phase 2. The interaction pattern is observed in the same manner for SMH2 case. Whereas in the SMH2 case, the vortices from the fuel jet is also interacts with swirling flow induced vortices. These vortices clearly change its shape through phase 3 and phase 4. Further, they regain their original shape as in phase 1, which finishes one complete cycle.

The SMH1 and SMH2 have same fuel jet velocity but different swirl velocity, whereas the SMH2 and SMH3 have same swirl velocity but different fuel jet velocity. The vortex breakdown is comparatively very high in SMH3 case. This shows the importance of fuel jet velocity in the characteristics of the flame. This can be seen in phase averaged data as

well. In SMH3 case, where the fuel velocity is very high, through all the phases, the interaction between the vortices is concentrated only in the shear layer. Also, in both SMH1 and SMH3 case, the axial momentum flux is relatively higher compared with SMH2 case. So, as a consequence, in SMH2 case, the vortex trailing from the swirling jet, interacts with the vortex from fuel jet and grows in the size. This is reflected in the PVC structure visualization, where the vortex break down process is delayed in SMH2 case but it is very quick in both SMH1 and SMH3.

While comparing all three hydrogen cases, the repeating structures are mainly concentrated towards the outer shear layer, and the formation of PVC structure depends on the interaction of these structures with the incoming fuel jet. Though the shape and size of the inner vortical structures are different for three hydrogen flames, the interaction is mainly concentrated in the outer shear layer. The difference in the inner structures is responsible for the variation in PVC structures. However, as the mode of interaction is not similar in all the three flames, the oscillating frequency is same.

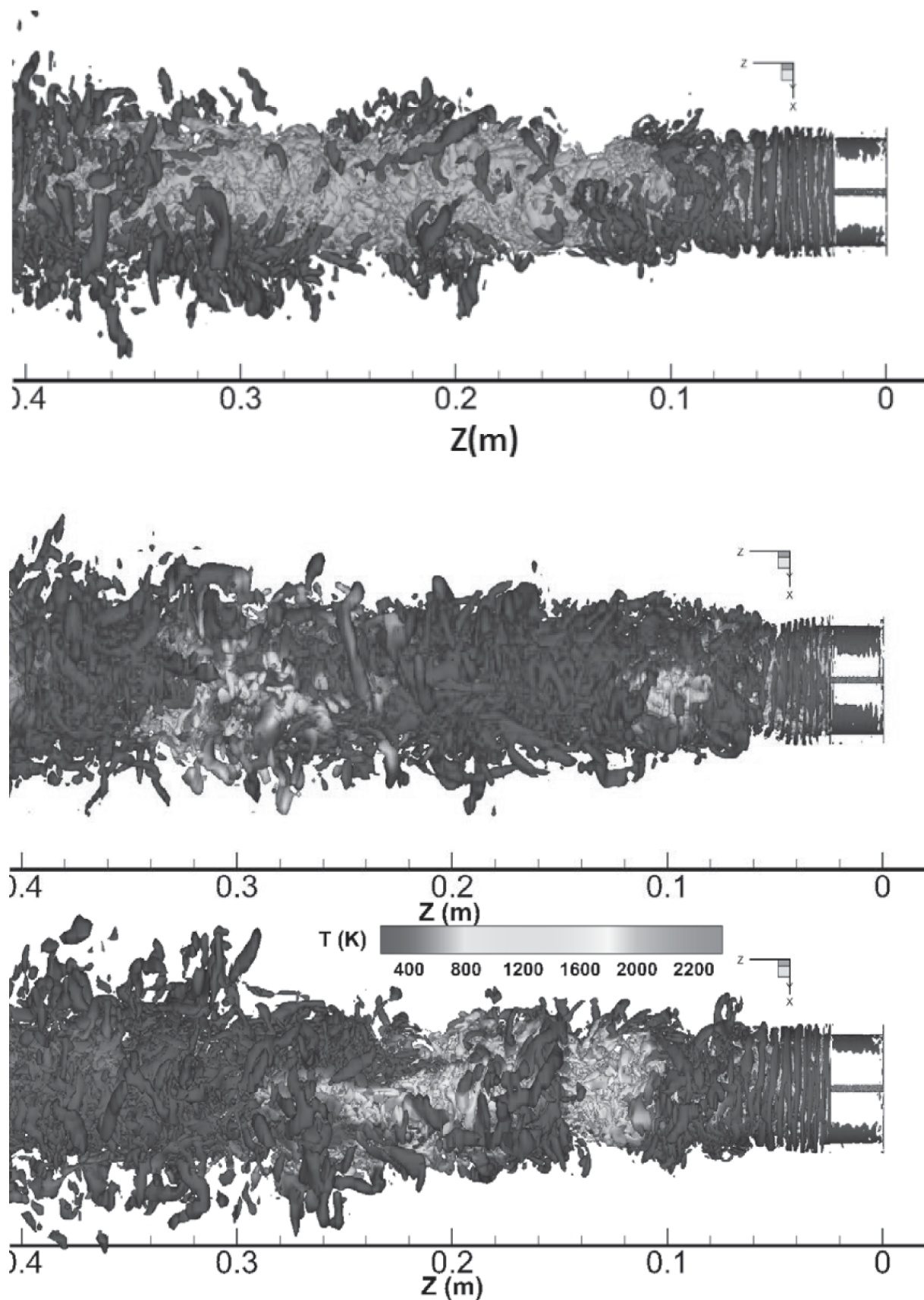


Figure 5: PVC visualization of SMH1, SMH2, SMH3 flames using Second Eigen Value method

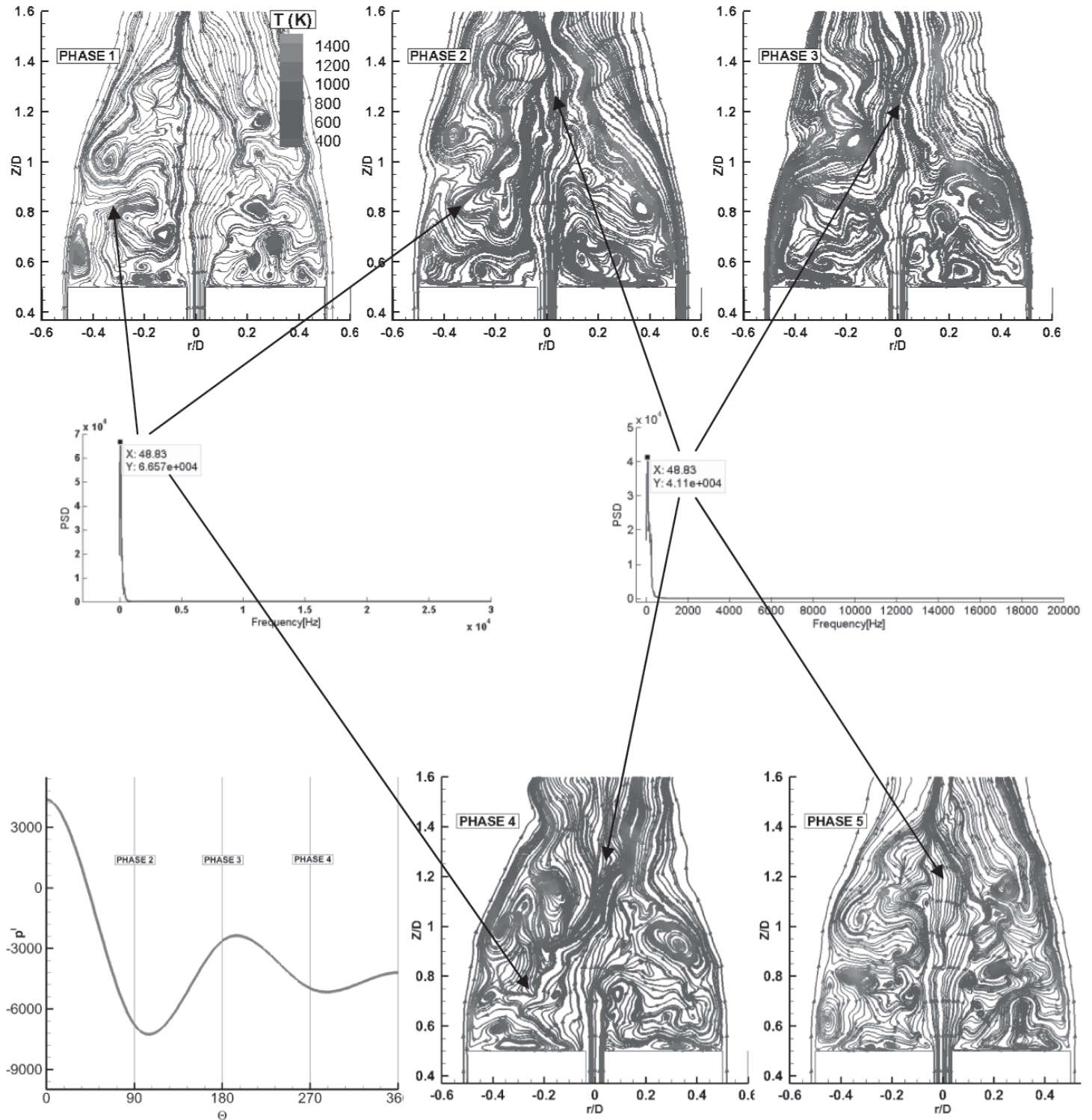


Figure 6(a): Phase averaged data for instantaneous flame from Phase 1-5 at an oscillation of 48 Hz for SMH1 flame

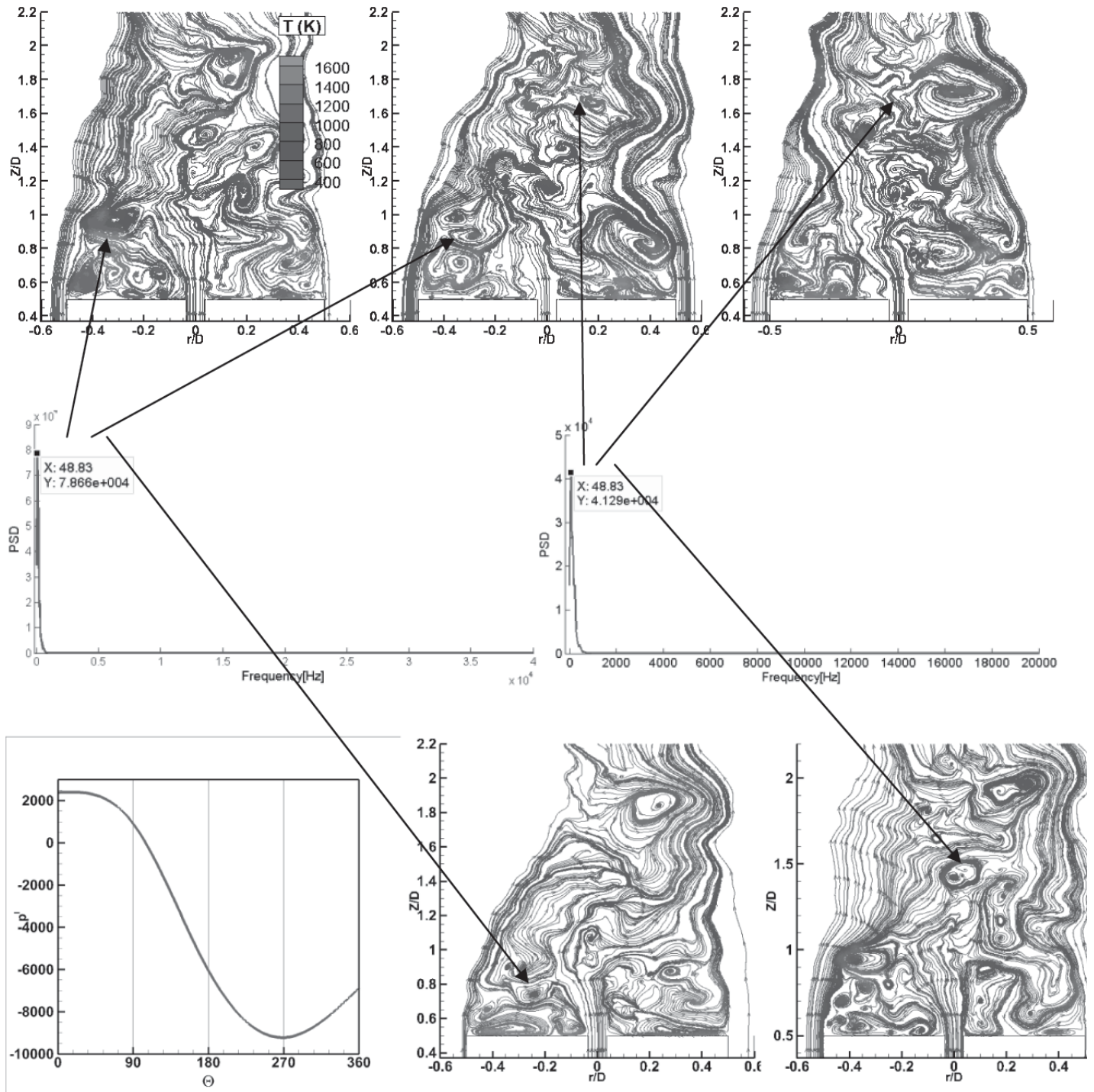


Figure 6(b): Phase averaged data for instantaneous flame from Phase 1-5 at an oscillation of 48 Hz for SMH2 flame

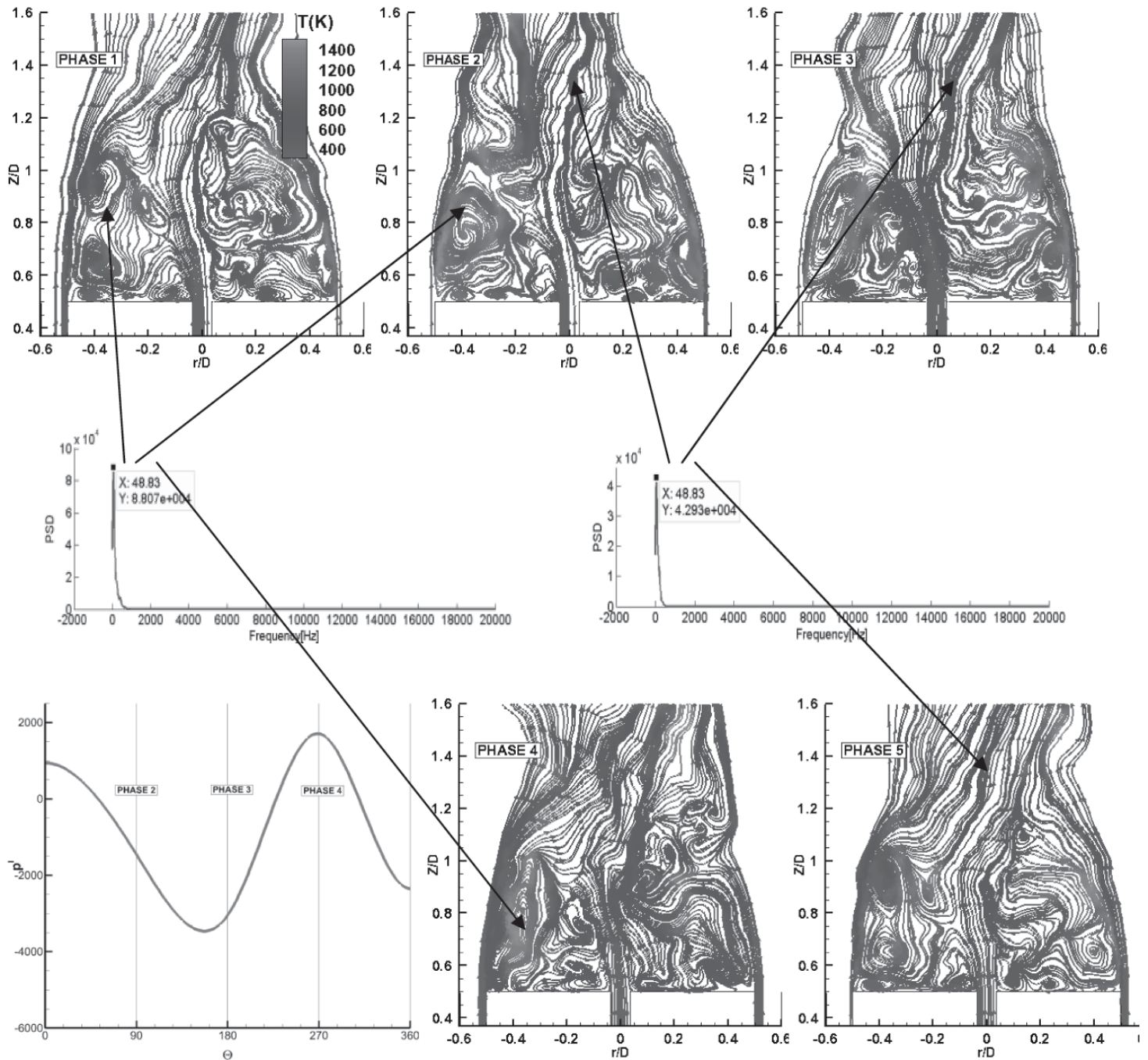


Figure 6(c): Phase averaged data for instantaneous flame from Phase 1-5 at an oscillation of 48 Hz for SMH3 flame

6 Conclusions

Large Eddy Simulation technique is successfully applied in studying the effect of swirl and fuel jet velocity in the instability characteristics of the hydrogen blended flames. The Precessing Vortex structure is explored using the second eigen value method. In the non reacting case, the vortex break down is very quick in the high swirl case, while the phase averaging technique explains the repeating structure responsible for the oscillation of PVC structure. In case of hydrogen flames, SMH1 and SMH3 cases shows quicker vortex breakdown process compared to SMH3 case. And the phase averaging technique reveals that the interaction between vortices is concentrated only in the shear layer in SMH1 and SMH3 case, where

the axial momentum is high. And in SMH3 case, the shedding vortex from the swirl jet interacts with the vortex from the fuel jet and grows in size further and in turns causes the delay in vortex breakdown found in PVC structure. However, phase averaging technique further reveals that the mode of interaction between the coherent structures is identical for all the three hydrogen flames which causes the oscillating frequency to be same for all the three hydrogen flames.

Acknowledgment

The authors would like to acknowledge the IITK computer center (www.iitk.ac.in/cc) for providing the resources to perform the computation work, data analysis and article preparation.

References

- 1) Al-Abdeli, Y.M., Masri, A.R., 2003. Recirculation and Flow Field Regimes of Unconfined Non-Reacting Swirling Flows. *Exp. Therm. Fluid Sci.*, 27(5), 655-665.
- 2) Al-Abdeli, Y.M., Masri, A.R., 2004. Precession and Recirculation in Turbulent Swirling Isothermal Jets'. *Combust. Sci. Technol.*, 176(5-6), 645-665.
- 3) Al-Abdeli, Y.M., Masri, A.R., Marquez, G.R., Staner, S., 2006. Time-varying behaviour of turbulent swirling nonpremixed flames. *Combust. Flame*, 146(1), 200-214.
- 4) Ansys Fluent 15.0 User's Guide, 2010. Ansys Inc., Csnosburg, PA, USA.
- 5) Bhaya, R., De, A., Yadav, R., 2014. Large Eddy Simulation of Mild Combustion Using PDF-Based Turbulence-Chemistry Interaction Models. *Combust. Sci. Technol.*, 186(9), 1138-1165.
- 6) Candel, S., Durox, D., Schuller, T., Bourgoquin, J.F., Moeck, J.P., 2014. Dynamics of swirling flames. *Annu. Rev. Fluid Mech.*, 46, 147-173.
- 7) Celik, I., Cehreli, Z., Yavuz, I., 2005. Index of resolution quality for large eddy simulation. *J. Fluid Eng.*, 127, 949-58.
- 8) De, A., Acharya, S., 2012. Dynamics of upstream flame propagation in a hydrogen-enriched premixed flame. *Int. J. Hydrog. Energ.*, 37(22), 17294-17309.
- 9)
- 10) De, A., Acharya, S., 2012. Parametric study of upstream flame propagation in hydrogen-enriched premixed combustion: Effects of swirl, geometry and premixedness. *Int. J. Hydrog. Energ.*, 37(19), 14649-14668.
- 11) El-Asrag, H., Menon, S., 2005. Large Eddy Simulation of a Swirling Non-Premixed Flame. 41st AIAA/ASME/SAE/ASEE Jt. Propuls. Conf., Ariz., USA.
- 12) Germano, M., Piomelli, U., Moin, P., Cabot, W.H., 1991. A dynamic subgrid-scale eddy viscosity model. *Phys. Fluids*, A 3, 1760-1765.
- 13) Smith, G.P., Golden, D.M., Frenklach, M., Moriarty, N.W., Eiteneer, B., Goldenberg, M., Bowman, C.T., Hanson, R.K., Song, S., Gardiner Jr, W.C., Lissianski, V.V, Qin, Z., 1999. http://www.me.berkeley.edu/gri_mech/
- 14) Hu, L.Y., Zhou, L.X., Luo, Y.H., 2008. Large-eddy simulation of the Sydney swirling nonpremixed flame and validation of several subgrid-scale models. *Numer. Heat Transf., Part B: Fundam.*, 53(1), 39-58.
- 15) James, S., Zhu, J., Anand, M.S., 2007. Large eddy simulations of turbulent flames using the filtered density function model. *Proc. Combust. Inst.*, 31(2), 1737-1745.
- 16) Kempf, A., Malalasekera, W., Ranga Dinesh, K.K.J., Stein, O., 2008. Large eddy simulations of swirling non-premixed flames with flamelet models: a comparison of numerical methods. *Flow Turbul. Combust.*, 81(4), 523-561.
- 17) Lilley, D.G., 1977. Swirl flows in combustion: A rev.. *AIAA J*, 15(8), 1063-78.
- 18) Malalasekera, W., Ranga Dinesh, K.K.J., Ibrahim, S.S., Masri, A.R., 2008. LES of Recirculation and Vortex Breakdown. *Combust. Sci. Technol.*, 180(5), 809-32.
- 19) Malalasekera, W., Ibrahim, S.S., Masri, A.R., Sadasivuni, S.K., Gubba, S.R., 2010. Large eddy simulation of premixed and non-premixed combustion. *Proc. of the 37th Natl. & 4th Int. Conf. on Fluid Mechanics and Fluid Power*, Chennai, India.
- 20) Masri, A.R., Kalt, P.A.M., Barlow, R.S., 2004. The Compositional Structure of Swirl-Stabilised Turbulent Non-premixed Flames. *Combust. Flame*, 137(1), 1-37.
- 21) Pope, S.B., 2000. *Turbulent Flows*. Camb. Univ. Press, Camb., U. K.
- 22) Ranga Dinesh, K.K.J., Jiang, X., Kirkpatrick, M.P., Malalasekera, W., 2012. Combust. charact. of H₂/N₂ and H₂/CO syngas nonpremixed flames. *Int. J. Hydrog. Energ.*, 37(21), 16186-16200.
- 23) RangaDinesh, K.K.J., Malalasekera, W., Ibrahim, S.S., Kirkpatrick, M.P., 2006. Large eddy simulations of turbulent non-premixed swirling flames. *Turbul., Heat and Mass Transf. (THMT05)*, Dubrovnik, HR.
- 24) RangaDinesh, K.K.J., Jenkins, K.W, Kirkpatrick, M.P., Malalasekera, W., 2009. Identification and analysis of instability in non-premixed swirling flames using LES. *Combust. Theory Model*, 13(6), 947-971.
- 25) RangaDinesh, K.K.J., Kirkpatrick, M.P., 2009. Study of jet precession, recirculation and vortex breakdown in turbulent swirling jets using LES. *Comput. Fluids*, 38(6), 1232-1242.
- 26) RangaDinesh, K.K.J., Malalasekera, W., Ibrahim, S.S., Kirkpatrick, M.P., 2005. Large Eddy Simulation of isothermal flows. 5th Asia-Pac. conf. on combust., Univ. of Adel., Adel., Aust..
- 27) Stien, O., Kempf, A., 2007. LES of the Sydney swirl flame series: A study of vortex breakdown in isothermal and reacting flows. *Proc. Combust. Inst.*, 31, 1755-1763.
- 28) Smagorinsky, J., 1963. General circulation experiments with the primitive equations. I. The basic experiment. *Mon. Weather Rev.*, 91(3), 99-164.
- 29) Syred, N., Beer, J.M., 1974. Combustion in swirling flows: a review. *Combust. and Flame*, 23(2), 143-201.
- 30) Yang, Y., Søren, K.K., 2012. Comparison of Reynolds Averaged Navier-Stokes Based Simulation and Large-eddy Simulation for One Isothermal Swirling Flow. *J. Therm. Sci.*, 21(2), 154-61.
- 31) Yang, Y., Søren, K.K., 2012. Large-eddy simulations of the non-reactive flow in the Sydney Swirl burner. *Int. J. Heat Fluid Flow*, 36, 47-57.



Slow Pyrolysis of Jatropha Seed De-oiled Cake and Estimation of Kinetic Parameters

Bhavya B Krishna^{a,b}, Bijoy Biswas^a, Jitendra Kumar^a, Rawel Singh^{a,b}, Thallada Bhaskar^{a,b,*}

^aThermo-catalytic Processes Area, Bio-Fuels Division (BFD), CSIR-Indian Institute of Petroleum, Dehradun 248005, India

^bAcademy of Scientific and Innovative Research (AcSIR), New Delhi, India

ARTICLE INFO

Received : 24 July 2015
Revised : 14 August 2015
Accepted : 20 August 2015

Keywords:

Jatropha;
de-oiled cake;
slow pyrolysis;
bio-oil;
bio-char;
kinetic parameter estimation

ABSTRACT

Jatropha seed de-oiled cake is a potential source for the production of valuable hydrocarbons. The pyrolysis of the de-oiled cake yields bio-oils that could have several potential applications for use as fuel/chemicals. In this study the pyrolysis of jatropha seed de-oiled cake was carried out at different temperatures ranging from 300 to 500 °C. The maximum yield of bio-oil at 38.4 wt.% with a conversion of 63 % was obtained at 450 °C. After pyrolysis, these products were characterised using several physico-chemical characterisation techniques such as FT-IR, ¹H NMR, GC-MS, XRD and SEM. From these it was observed that the bio-oil obtained was primarily composed of phenolic compounds and the nature of bio-char indicated the conversion of the components of lignocellulosic biomass. The frequency factor and the activation energy calculated using the first order rate equation was 2.38 s⁻¹ and 5.31 kJ mol⁻¹ respectively. These values are much lower compared to those obtained from thermo-gravimetric analysis measurements indicating good heat and mass transfer in the experimental set up.

© 2016 ISEES, All rights reserved

1. Introduction

Researchers all over the world continue to search for sustainable energy sources which have become more critical owing to the geo-political and environmental problems associated with fossil fuels. Renewable energy is now receiving greater thrust for the production of energy due to the depletion of available fossil fuel resources. Recently, heat and electricity are being produced from renewable sources like the sun, wind, geothermal, ocean tidal energy etc. The electricity generated from these sources is used on a small scale possibly to power electric cars, however heavy duty vehicles and the aviation industry are still dependent on liquid fuels. Apart from transportation sector, the chemical and petrochemical industries are still solely dependent on biomass for renewable and sustainable sources of carbon (Meuwese et al., 2013). This gap in the energy demand and supply provides an opportunity for the use of another unconventional and clean energy source from biomass, which are now at the forefront in research for the production of alternative liquid fuels.

Biomass is defined as any organic matter that is derived by the process of photosynthesis. The second-generation of bio-fuels are obtained from feedstocks that are non-edible in nature, mainly from agriculture and forest residues in addition to energy crops specifically grown for bio-fuel manufacture.

Pyrolysis forms the basis of thermo-chemical conversion in most cases and is defined as the chemical changes occurring when heat is applied to any organic material in the absence of oxygen. Slow pyrolysis is characterised by slow heating rates ranging from 5 to 40 °C min⁻¹ with

residence time of 30-60 minutes under inert sweeping gas flow.

De-oiled cakes are secondary products that are obtained after the production of bio-diesel or jet fuel from non-edible oils. They are generally thrown away or burnt. Further as they do not compete for fodder this secondary processing of oil cakes provide a significant added advantage.

Several potential sources of de-oiled cake for use as feedstock have been studied previously and some of them are listed here. Chutia et al., have shown that *Mesua ferrea* L. de-oiled cake (Chutia et al., 2013) and *Pongamia glabra* de-oiled cake are potential feedstocks for thermo-chemical conversion to produce useful hydrocarbons. In the case of the *Pongamia glabra* de-oiled cake pyrolysis, maximum oil yield of 30.60 wt.% was obtained at 500 °C with a heating rate of 40 °C min⁻¹ (Chutia et al., 2014). Ground nut de-oiled cake has also been subjected to pyrolysis and 50 wt.% of bio-oil has been obtained (Agrawalla et al., 2011). Smets et al., have carried out the slow pyrolysis of rapeseed cake in the presence of catalysts such as Na₂CO₃, HZSM-5 and α-Al₂O₃. In the absence of catalysts at 550 °C, bio-oil yield of 47.1 wt.% and conversion of 72.1% were observed (Smets et al., 2013). For the raspberry seed cake, they observed that at 450 °C bio-oil yield of 44.4 wt.% was obtained by slow pyrolysis (Smets et al., 2014). De-oiled canola meal required an optimum temperature of 500 °C to get a maximum bio-oil yield of 10-24 wt.% (Azargohar et al., 2013). Soyabean oil cake is seen to require the lowest temperature so far reported at 400 °C to give bio-oil yield of 25.8 wt.% with a heating rate of 50 °C min⁻¹ (Sensoz & Kaynar, 2006).

* Corresponding Author: E-mail: tbhaskar@iip.res.in; thalladab@yahoo.com

We have already reported the hydrolysis of jatropha seed de-oiled cake (Balagurumurthy et al., 2013b) along with its kinetic parameters (Balagurumurthy et al., 2013a). In this manuscript we report for the first time the results of the slow pyrolysis of jatropha seed de-oiled cake along with the kinetic parameters assuming a first order reaction.

2. Materials and methods

2.1. Materials

The feedstock jatropha seed de-oiled cake (JSDC) was obtained from a local bio-diesel production unit. The gross calorific value was found using the Parr 6300 Bomb Calorimeter. The trace metal analysis was carried out using the DRE, PS-3000 UV, Leeman Labs Inc., Inductively Coupled Plasma-Atomic Emission Spectroscopy instrument. The moisture content was obtained from the HR- 83 Mettler Toledo Halogen Moisture Analyzer.

The elemental analysis was carried out in an Elementar Micro Vario Cube unit. The ^1H NMR spectra was recorded in the Bruker Ultrashield 500 Plus instrument using CDCl_3 as a solvent.

Powder X-ray diffraction patterns were collected on Bruker D8 advance X-ray diffractometer fitted with a Lynx eye high-speed strip detector and a $\text{Cu K}\alpha$ radiation source. Diffraction patterns in the 2° - 80° region were

recorded with a 0.04 step size (step time= 4s).

The FT-IR spectra were recorded on a Nicolet 8700 FT-IR spectrometer with the sample powder diluted in KBr. SEM images were collected on the FEI Quanta 200 F, using a tungsten filament doped with lanthanum hexaboride (LaB_6) as an X-ray source, fitted with an ETD (Everhart Thornley Detector), which preferentially work as a secondary electron detector. The sample for the SEM was subjected to dispersal on a carbon paper coated adhesive followed by a gold coating step.

2.2. Experimental procedure

Thermal pyrolysis of jatropha seed de-oiled cake was carried out at various temperatures of 300, 350, 400, 450 and 500 $^\circ\text{C}$ under atmospheric pressure of nitrogen. The batch fixed bed reactor is made up of glass (length: 280 mm; i.d. 34 mm) and K-type thermocouples have been used as shown in figure 1. The feed samples used in this study were milled in a laboratory ultra-centrifugal mill and the sample then obtained was sieved in standard mesh to obtain particle size of 0.5-2 mm. At first, 10g of the feed was loaded into the reactor and the reactor was purged with nitrogen to remove the inside air. The nitrogen flow rate during pyrolysis was 50 ml min^{-1} . The starting temperature was the ambient room temperature at 25 $^\circ\text{C}$ and the heating rate to reach the pyrolysis temperature was set around 25 $^\circ\text{C min}^{-1}$. Once final pyrolysis temperature was attained, the

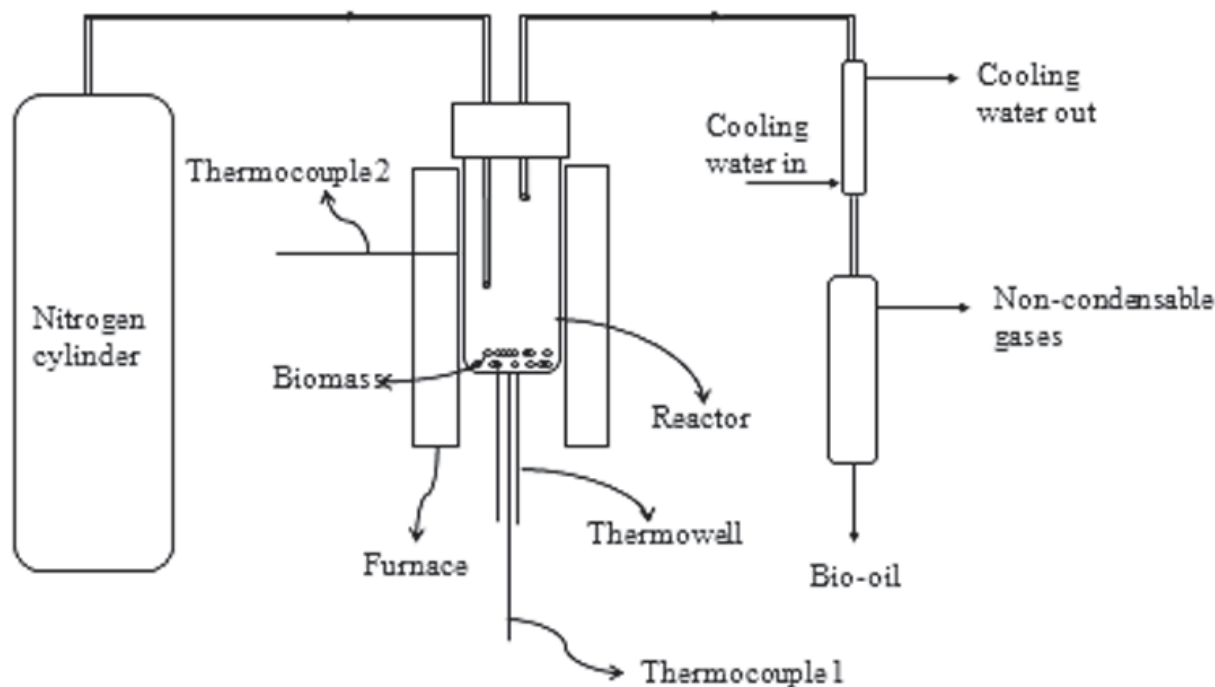


Fig. 1 Line diagram of experimental unit

reactor was maintained at the required temperature for a period of 1 h to ensure that all condensable vapours were collected. Biomass bed temperature has been taken as the pyrolysis temperature and another thermocouple indicated the skin temperature of the reactor. The vapours formed after the reaction was condensed using cooling water maintained at 2 $^\circ\text{C}$. Water in bio-oil was removed by the addition of anhydrous sodium sulphate and acetone was used to recover the organic fraction. Conversion as defined in this process is the amount of solid that has been converted into liquid or gaseous products. The remaining solid after the reaction left in the reactor is termed as bio-char. The experiments have been carried out in duplicates and the average values have been reported which are within a standard deviation of ± 1.0 wt%.

Bio-char yield, wt.% = $\frac{[(\text{Weight of reactor after reaction}) - (\text{Weight of empty reactor})]}{(\text{Weight of feed taken})} \times 100$

Gas yield, wt.% = $100 - (\text{Bio-oil yield, wt.\%} + \text{Bio-char yield, wt.\%})$

Conversion, % = $100 - (\text{Bio-char yield, wt.\%})$

3. Results and discussions

The organic fraction of the bio-oil was characterised using FT-IR, ^1H NMR and GC-MS. The solid bio-char has been characterised using FT-IR, XRD and SEM. The elemental analysis of JSDC was found to contain: carbon (43.63 wt.%), hydrogen (5.35 wt.%), nitrogen (3.91 wt.%) and sulphur (0.43 wt.%). The gross calorific value of the feedstock was found to be 20.05 MJ/kg and moisture content was 7.2 wt.%. Na, Mg, P and Ca are the major trace metals present in the feedstock and these are known to naturally occur in their structure. The compositional analysis of jatropha curcas seed de-oiled cake are as follows: 10.3 wt.% ash, 43.5 wt.% holocellulose, 13.9 wt.% lignin and 5.5 wt.% pentosan content.

The yields of bio-oil, gas and bio-char from slow pyrolysis of jatropha seed de-oiled cake at various pyrolysis temperatures of 300, 350, 400, 450 and 500 $^\circ\text{C}$ have been shown in table 1. With increase in temperature from 300 to 450 $^\circ\text{C}$, the yield of bio-oil is seen to increase. At 300 $^\circ\text{C}$, the bio-oil yield was 34.5 wt.% and increased slightly to 34.7 wt.% at 350 $^\circ\text{C}$. Further as the temperature was increased to 400 $^\circ\text{C}$, the yield of bio-oil

Table 1: Product yields by slow pyrolysis of jatropha seed de-oiled cake at different temperatures

Temperature, °C	Bio-oil, wt. %	Gas, wt. %	Bio-char, wt. %	Conversion, %
300	34.5	19.5	46	54
350	34.7	22.3	43	57
400	36.5	24.5	39	61
450	38.4	24.6	37	63
500	37.8	26.2	36	64

increased to 36.5 wt.% and reached a maximum of 38.4 wt.% at 450 °C. The yield of bio-oil reduced to 37.8 wt.% at 500 °C. The conversion followed a similar increasing trend from 54 to 63 % as the temperature was raised from 300 to 450 °C. At 500 °C, there was a slight increase in the conversion to 64 % but as mentioned before the bio-oil yield was reduced.

The gas yield increased steadily from 300 to 400 °C. Initially the yield was 19.5 wt.% at 300 °C and increased to 22.3 wt.% at 350 °C and then was observed to be 24.5 wt.% at 400 °C. There was not much difference in the gas yield at 400 and 450 °C but at 500 °C, the gas yield increased to 26.2 wt.%. This increase in non-condensable gases yield at higher temperatures of 500 °C might be due to the increased primary cracking of the biomass. It might also be due to the secondary cracking of the bio-char formed which could also be the reason for reduced bio-char formation or in turn increased conversion. Thus, the optimum pyrolysis temperature for jatropha seed de-oiled cake is concluded to be 450 °C at the given experimental conditions.

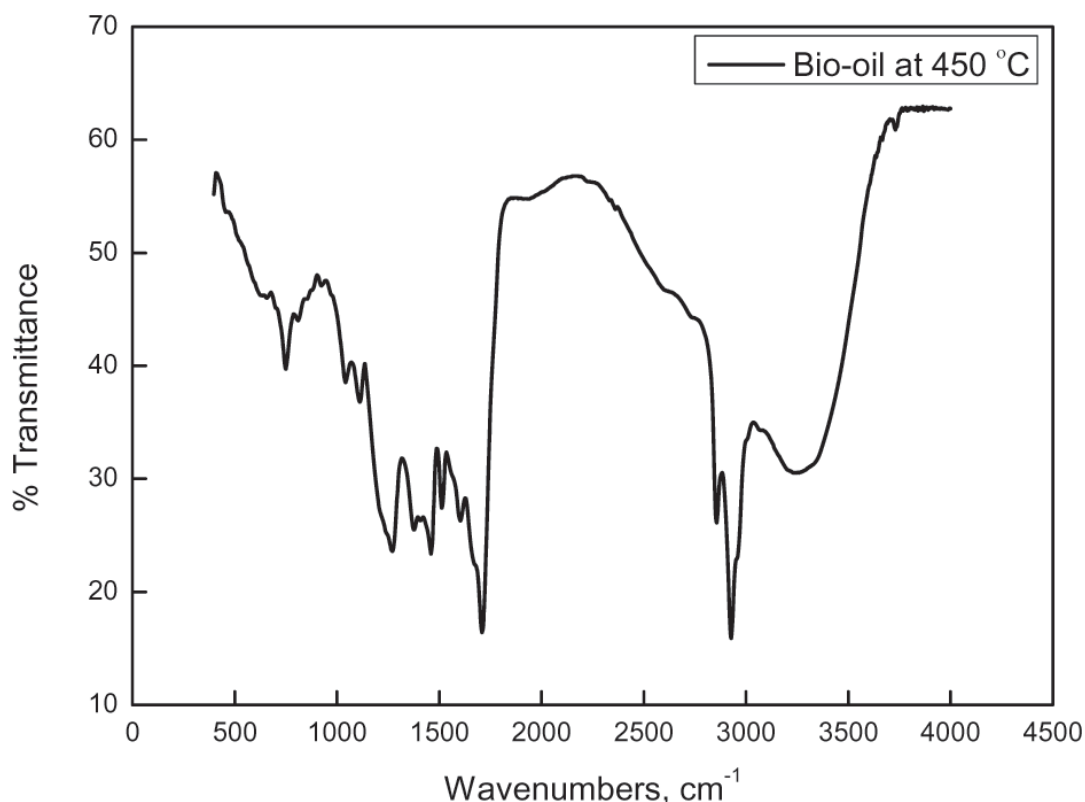
The optimum conditions observed in this study are in line with those observed for raspberry seed cake (Smets et al., 2014) and ground nut de-oiled cake (Agrawalla et al., 2011) at 450 °C though the bio-yields observed in both the cases was around 50 wt.%. De-oiled canola meal required optimum temperature of 500 °C to produce liquid bio-oil yield of 10-24 wt.% which was less than jatropha seed de-oiled cake (Azargohar et al., 2013). In case of rapeseed cake with lower holocellulose and lignin content than the feed used in this study, higher optimum temperatures of 550 °C were observed but the yield of bio-oil (47 wt.%) was higher than

de-oiled canola meal and jatropha seed de-oiled cake as in this study (Smets et al., 2013).

3.1. Bio-oil characterisation

The organic fraction of the bio-oil was characterized using FT-IR, ¹H NMR and GC-MS. The bio-oil obtained at 450 °C was seen to be rich in functionalities due the presence of several peaks in the FT-IR spectra (figure 2). The broad peaks at 3253 cm⁻¹ indicates the presence of the stretching O-H band due to the presence of phenols or alcohols. The presence of alkanes can be identified by the peaks at 2925 and 2856 cm⁻¹ attributed to the C-H stretching. The C=O stretching vibrations at around 1710 cm⁻¹ might be due to the presence of carbonyl compounds such as aldehydes, ketones, carboxylic acids or esters. The presence of nitrogenous compounds or aromatic rings leads to some of the peaks in the range of 1500-1610 cm⁻¹ (Agrawalla et al., 2011). The other peaks in the spectra are attributed to the out of plane bending vibrations of the C-H groups, and the stretching of the C-O-C bonds in polar aromatic compounds etc (Putun et al., 2007).

The ¹H NMR technique illustrated that the downfield region from 0.5-1.5 ppm corresponds to the protons present in the short chain aliphatics attached to carbon atoms which are atleast 2 bonds away from C=C or heteroatom. The next region from 1.5 to 3.0 ppm corresponds to protons on the aliphatic carbon atoms which are bonded to C=C either on the aromatic or olefinic or are two bonds away from a heteroatom. The organic fraction of the bio-oil obtained is seen to be rich in aliphatic protons (77%) as observed in other de-oiled cake pyrolysis liquids as

**Fig. 2** FT-IR of bio-oil obtained at 450 °C

well (Azargohar et al., 2013). The next region 3.0-4.4 ppm corresponds to protons that are attached to the carbon atoms next to an aliphatic alcohol or ether or a methylene group which bonds two aromatic rings. The amount of protons resonating in this region is 6%. The region from 4.4-6.0 ppm represents hydrogen atoms of carbohydrate-like molecules. The amount of protons in this region is negligible which clearly indicates the conversion. The range 6.0-8.5 ppm represents the aromatic region of the spectrum. It encompasses the protons in benzenoid molecules and heteroaromatics which amounts to 16% (Mullen et al., 2009).

The compounds identified by GC-MS are grouped into phenolic compounds and aromatic ethers, acids/ esters, hydrocarbons, carbonyl compounds, nitrogen compounds and non-classified compounds and their area percentage are shown in table 2.

The organic fraction of the bio-oil is rich in phenolic compounds and aromatic ethers which are mainly derived from the lignin fraction of the biomass. As it is a de-oiled cake, some long chain acids and esters have also been identified. Nitrogen containing compounds have also been identified which corroborates the findings through FT-IR. Hydrocarbons and carbonyl compounds are also found in small quantities in the bio-oil. Similar compounds have been identified in case of de-oiled groundnut cake (Agrawalla et al., 2011).

Table 2: Compounds identified by GC-MS

Compound	Area %
Phenolic compounds and aromatic ethers	
Phenol	2.67
Phenol, 2-methyl-	4.95
Phenol, 2-methoxy-	18.00
Phenol, 2,4-dimethyl-	2.36
Phenol, 3-ethyl-	3.08
Creosol	5.33
Catechol	4.07
1,2-Benzenediol, 3-methoxy-	1.97
Phenol, 4-ethyl-2-methoxy-	7.98
2-Methoxy-4-vinylphenol	3.25
Phenol, 2-methoxy-3-(2-propenyl)-	1.21
Phenol, 2-methoxy-4-propyl-	1.88
trans-Isoeugenol	5.06
Homovanillic acid	6.28
4-Methyl-2,5-dimethoxybenzaldehyde	1.37
Phenol, 2,6-dimethoxy-4-(2-propenyl)-	2.89
Acids/ esters	
Propanoic acid	1.29
9-Octadecenoic acid, methyl ester, (E)-	2.73
Methyl stearate	0.63
Pentadecanoic acid, 14-methyl-, methyl ester	1.25
Methyl 10-trans,12-cis-octadecadienoate	0.93
Hydrocarbons	
2-Pentene, 3,4-dimethyl-, (E)-	3.10
4-Propyl-1,1'-diphenyl	1.63
Carbonyl compounds	
2-Cyclopenten-1-one, 2-hydroxy-3-methyl-	0.81
2-Acetylcyclopentanone	1.24
2-Cyclopenten-1-one, 3-methyl-	1.36
Nitrogen compounds	
5-Hepten-2-amine, N,6-dimethyl-	2.32
2-Propanone, (1-methylethylidene)hydrazone	0.84
Cyclopentanemethanol, 1-amino-	1.91
4-Piperidinone, 2,2,6,6-tetramethyl-	2.44
9-Octadecenamide, (Z)-	0.63
Non-classified compounds	
2H-Pyran-2-one, 4-hydroxy-3,6-dimethyl-	0.66
2H-Pyran-2-one, 3-acetyl-4-hydroxy-6-methyl-	2.18

3.2. Bio-char characterization

The bio-char obtained at temperatures from 300 to 500 °C was also characterized using FT-IR. Characterization of bio-char obtained at 450 °C and feed JSDC have been carried out using XRD and SEM.

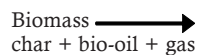
The bio-chars are seen to have a reduced functionality since they are converted into bio-oil or non-condensable gases (figure 3). The intensity of the O-H stretching vibrations at around 3400 cm⁻¹ is seen to reduce with increase in the pyrolytic temperature due to the decomposition reactions leading to the formation of phenolic compounds as observed in the bio-oil. The intensity of the symmetric and asymmetric C-H group peaks also reduce with the increase in temperature as the bio-char becomes more aromatic in nature. This is corroborated by the presence of peaks due to the C=C vibrations of aromatics at around 1600 cm⁻¹. The peak due to the -CH₂- scissoring of alkanes at around 1400 cm⁻¹ is also seen to reduce with increase in temperature. The peak due to O-H deformation is also observed in the bio-char spectra. Bio-char was of similar nature in case of de-oiled canola cake as well (Azargohar et al., 2013).

The XRD patterns of the feed along with bio-char obtained at 450°C is shown in figure 4. The peak at 2θ approximately around 15 ° and 21 ° in the feed corresponds to several crystallographic planes of cellulose. These peaks are not observed in the bio-char indicating the conversion of cellulose in the feed. The bio-char is amorphous in nature and also seems to be rich in carbon content further corroborating the conversion (Wu et al., 2012).

The SEM images of jatropha seed de-oiled cake feed and bio-char at optimum conditions (450 °C) are shown in figure 5. All the images are provided at the same resolution and the scale is 10µm. The feed has a non-porous and rough surface but the bio-char has tiny eruptions on its surface. This might be due to the loss of moieties from the macromolecular backbone of the biomass.

3.3. Kinetic parameter estimation

In this study, we have assumed a Global model where the lignocellulosic biomass is taken as such and is not divided into its individual components. The reaction is assumed to be a first order reaction and it is also assumed that the feedstock is decomposed in a single step directly to liquid bio-oil, gas and bio-char.



$$-\ln(1-X) = Kt$$

Where X= conversion (100-char %)

t= 1 hour (residence time in the reactor once the pyrolysis temperature is reached)

The model can be expressed with Eq. (1) below, where n is the reaction order and k (T) is the reaction rate constant defined by the Arrhenius equation Eq. (2).

The Arrhenius rate equation was employed to calculate the frequency factor, A and activation energy, E.

$$dX/dT = k(T) * (1-X)^n \dots\dots\dots (1)$$

$$K = Ae^{-E/RT}$$

$$\ln K = \ln A - E/RT \dots\dots\dots (2)$$

The slope of graph of ln K vs. (1/T) (table 3 and figure 6) gives the value of E and the intercept gives the value of A. The value of A and E are found to be 2.38 s⁻¹ and 5.31 kJ/mol respectively which are less than those observed by TGA (Chutia et al., 2013). The low value of activation energy and frequency factor indicates that there is good mass and heat transfer in the reactor used here.

4. Conclusions

Slow pyrolysis of jatropha seed de-oiled cake was carried out and the optimum temperature was found to be 450 °C for maximum bio-oil yield. Phenolic compounds and aromatic ethers were the major fraction of compounds that were present in the organic fraction of the bio-oil. The physico-chemical characterization of bio-char indicated the opening of the macromolecular structure of biomass and led to the conversion of the feedstock into bio-oil or non-condensable gases. The first order rate equation was used to calculate the frequency factor and activation energy of the process. They were found to be 2.38 s⁻¹ and 5.31 kJ mol⁻¹ respectively. It was noted that these are lower compared to those obtained from the thermo-gravimetric analysis indicating efficient heat and mass transfer in the reactor system.

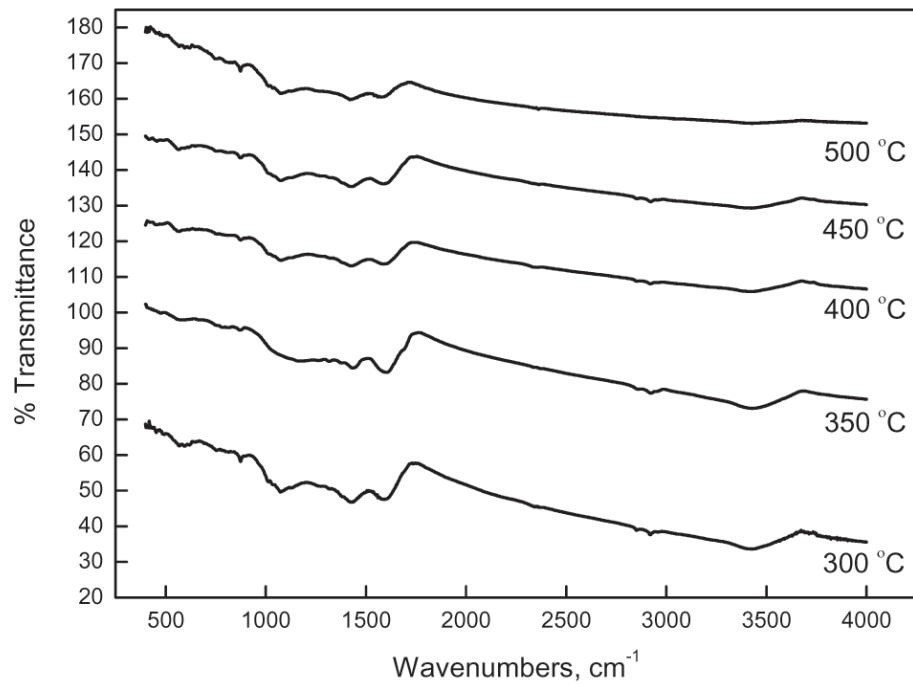


Fig. 3 FT-IR of bio-char obtained at 300, 350, 400, 450 and 500 °C

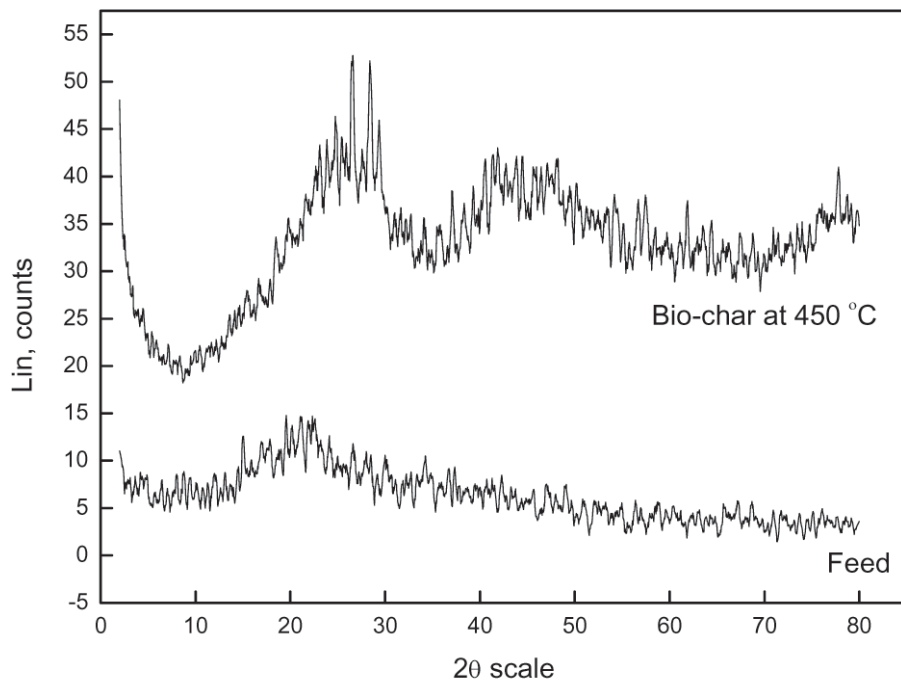


Fig. 4 XRD patterns of feed and bio-char obtained at 450 °C

Table 3: Kinetic parameter estimation

T (°C)	T (K)	Conversion	K	ln K	1/T, (K ⁻¹)
300	573	0.54	0.776529	-0.25292	0.001745
350	623	0.57	0.84397	-0.16964	0.001605
400	673	0.61	0.941609	-0.06017	0.001486
450	723	0.63	0.994252	-0.00576	0.001383
500	773	0.64	1.021651	0.02142	0.001294

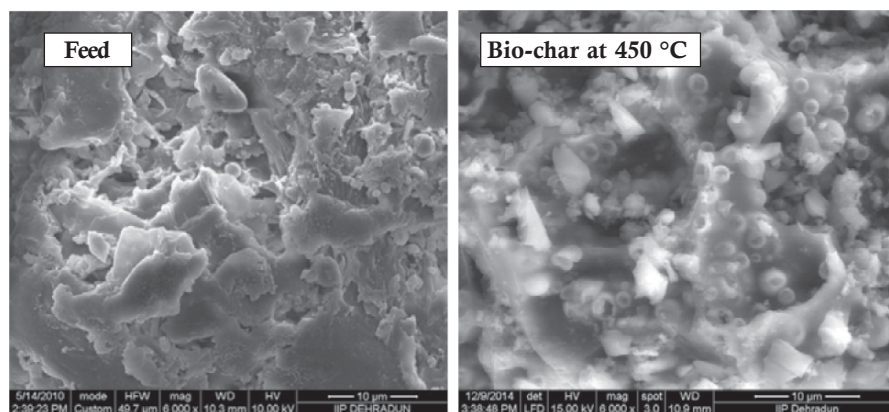


Figure 5: SEM of feed and bio-char obtained at 450 °C

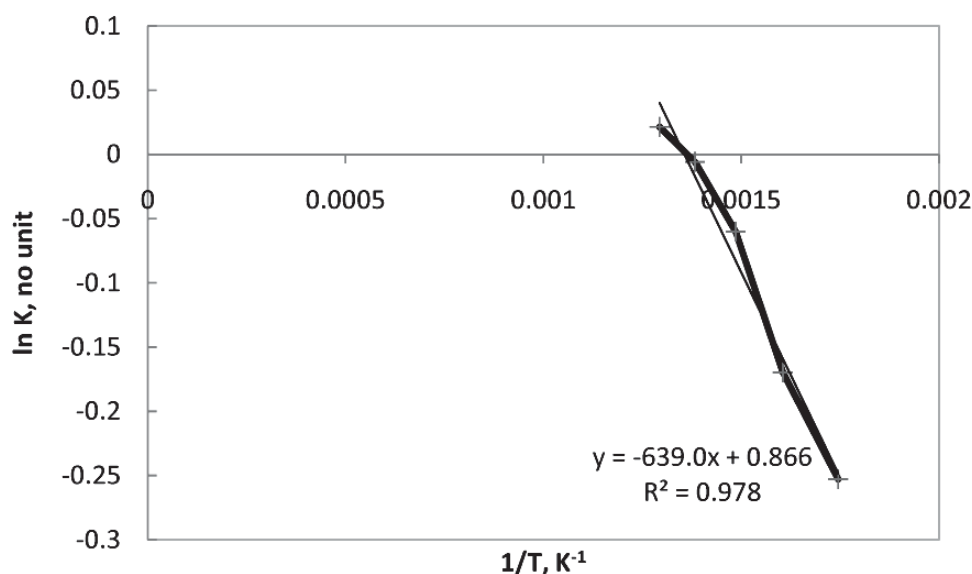


Figure 6: ln K vs. 1/T graph for kinetic parameter estimation

Acknowledgements

The authors thank The Director, CSIR-Indian Institute of Petroleum, Dehradun, for his constant encouragement and support. RS thanks Council of Scientific and Industrial Research (CSIR), New Delhi, India, for providing Senior Research Fellowship (SRF). The authors thank CSIR in the form of XII Five Year Plan project (CSC0116/BioEn) and Ministry of New and Renewable Energy for providing financial support.

References

- Agrawalla A, Kumar S, Singh RK, 2011, Pyrolysis of groundnut de-oiled cake and characterization of the liquid product, *Bioresource Technology*, 102(22), 10711-10716
- Azargohar R, Nanda S, Rao BVSK, Dalai AK, 2013, Slow Pyrolysis of Deoiled Canola Meal: Product Yields and Characterization, *Energy & Fuels*, 27(9), 5268-5279
- Balagurumurthy B, Bhaskar T, Goyal HB, Adhikari DK, 2013a, Hydrolysis of Jatropha Seed de-Oiled Cake: Estimation of Kinetic Parameters, *Waste Biomass Valorization*, 4(3), 503-507
- Balagurumurthy B, Bhaskar T, Kumar KLNS, Goyal HB, Adhikari DK, 2013b, Effect of pressure on the hydrolysis of Jatropha seed deoiled cake, *Journal of Material Cycles and Waste Management*, 15(3), 328-334
- Chutia RS, Katak R, Bhaskar T, 2014, Characterization of liquid and solid product from pyrolysis of Pongamia glabra deoiled cake, *Bioresource Technology*, 165, 336-342
- Chutia RS, Katak R, Bhaskar T, 2013, Thermogravimetric and decomposition kinetic studies of Mesua ferrea L. deoiled cake, *Bioresource Technology*, 139, 66-72
- Meuwese AM, Schenk NJ, Moll HC, Uiterkamp AJMS, 2013, Biobased Chemicals in a Carbon-Restricted World, *Environmental Science & Technology*, 47(22), 12623-12624
- Mullen CA, Strahan GD, Boateng AA, 2009, Characterization of Various Fast-Pyrolysis Bio-Oils by NMR Spectroscopy, *Energy & Fuels*, 23, 2707-2718
- Putun AE, Ozbay N, Varol EA, Uzun BB, Ates F, 2007, Rapid and slow pyrolysis of pistachio shell: Effect of pyrolysis conditions on the product yields and characterization of the liquid product, *International Journal of Energy Research*, 31(5), 506-514
- Senzos S, Kaynar I, 2006, Bio-oil production from soybean (*Glycine max L.*); fuel properties of Bio-oil, *Industrial Crops and Products*, 23(1), 99-105
- Smets K, Roukaerts A, Czech J, Reggers G, Schreurs S, Carleer R, Yperman J, 2013, Slow catalytic pyrolysis of rapeseed cake: Product yield and characterization of the pyrolysis liquid, *Biomass and Bioenergy*, 57, 180-190
- Smets K, Schreurs S, Carleer R, Yperman J, 2014, Valorization of raspberry seed cake by flash and slow pyrolysis: Product yield and characterization of the liquid and solid fraction, *Journal of Analytical and Applied Pyrolysis*, 107, 289-297
- Wu W, Yang M, Feng Q, McGrouther K, Wang H, Lu H, Chen Y, 2012, Chemical characterization of rice straw-derived biochar for soil amendment, *Biomass and Bioenergy*, 47(0), 268-276



Startup of Microbial Fuel Cells with Pure Ferric Iron-reducing Bacteria Isolates

Lihong Liu^{1,2}, Duu-Jong Lee^{3,4,*}, Aijie Wang², Nanqi Ren², Lei Zhang¹, Jia-Nian Shen¹

¹School of Earth Sciences, Northeast Petroleum University, Daqing 163318, China

²State Key Laboratory of Urban Water Resource and Environment, Harbin Institute of Technology, Harbin 150090, China

³Department of Chemical Engineering, National Taiwan University of Science and Technology, Taipei 106, Taiwan

⁴Department of Chemical Engineering, National Taiwan University, Taipei 106, Taiwan

ARTICLE INFO

Received : 30 July 2015
Revised : 13 September 2015
Accepted : 23 September 2015

Keywords:

Microbial fuel cell
Iron-reducing bacteria
Gram-positive
Gram-negative

ABSTRACT

Ferric iron-reducing bacteria (FRB) can transfer intercellular electrons to a surrounding solid, a function also exhibited by the anode-respiring bacteria for microbial fuel cells (MFC). This study isolated from river sediment two FRB, a Gram-negative strain (*Geobacter* sp. LAR-2, GenBank No. KC211015) and a Gram-positive strain (*Clostridium* sp. LAR-3, GenBank No. KC211016), and individually started up MFC using these two isolates as inocula at anodic compartment. The LAR-2-MFC had an open-circuit voltage (OCV) of 610 mV and maximum power density (P_{max}) of 860 mW m⁻². The corresponding OCV and P_{max} of LAR-3-MFC were 630 mV and 310 mW m⁻², respectively. The resistances of electron transfer across anodic biofilms, electrolytes and cathodes were characterized. The tests with these two FRB support the hypothesis with FRB being effectively functioned as anode-respiring bacteria for MFC. Keywords: Microbial fuel cell; Iron-reducing bacteria; Gram-positive; Gram-negative

© 2016 ISEES All rights reserved

1. Introduction

The microbial fuel cells (MFCs) can oxidize electron donors on anode and transfer the excess electrons through external loading to cathodes to be received by electron acceptors [Inoue et al., 2013; Chou et al., 2014; Yoshizawa et al., 2014; Zhang et al., 2015; Koroglu et al., 2014]. For instance, when sulfide and oxygen are used respectively as the electron donor and acceptor, a sulfide-MFC can be established [Lee et al., 2012].

The bioactivity of anode-respiring bacteria (ARB) in anodic biofilm often determines the performance of an MFC [Mohan et al., 2014]. The ARB can conduct extracellular electron transfer via direct electron transfer (DET) and/or mediated electron transfer (MET) [Kim et al. 1999], which is also held by iron-reducing bacteria (FRB), such as *Shewanella* and *Geobacter* sp., that can grow upon reduction of Fe(III) [Kostka et al. 2002]. Most ARB strains were identified from anodic biofilm of an operating MFC (recent review is available in [Huang et al., 2015]). Conversely, the studies on the use of pure cultures FRB isolated from non-MFC samples as inoculum for startup of an MFC are rare [Liu et al., 2014].

The confirmation of the capability of an FRB to function as an ARB has practical significance for rapid screening effective exoelectrogenic bacteria for MFC handling very different substrates. However, it is unclear whether both Gram-positive and Gram-negative FRB isolated from the same environmental site can be effective to startup an MFC. Mixed culture tests encounter difficulty for detailed interpretation of experimental

data. This study isolated two strains from environmental samples with high iron-reducing capability. These two strains, one is a Gram-positive bacterium and the other is a Gram-negative bacterium, were individually used as inoculum for anodic compartment of MFCs.

2. Material and Methods

2.1 Strain screening, isolation and identification

Sludge samples were collected from sediment at intersection of A-Shi River and Songhua River, Heilongjiang, China. The samples were cultivated in tubes with iron-reducing medium (per liter): (NaHCO₃, 2.5 g; KH₂PO₄, 0.6 g; NH₄Cl, 1.5 g; yeast extract 0.5 g; sodium acetate, 1.36 g; Ferric citrate, 50 mM; Wolfe's vitamin solution, 5 ml; Wolfe's trace metal solution, 10 ml; pH 6.9) at 30°C. The medium was shaken at 130 rpm. Those with white, black or gray precipitates were collected for identification. The sediment was then seeded to fresh iron-reducing medium for another run of cultivation. This procedure was repeated for over ten times to enrich the consortium.

The so-obtained consortium was then diluted and spread onto the solidified agar tubes containing iron-reducing medium. The colonies formed on the agar were pickup and diluted and spread on new agar. This process was repeated for more than ten times. The cell morphology of the so-obtained isolates was observed by a phase-contrast microscope. The biochemical characteristics of the isolates were highlighted using API 20A, API-20NE and API-ZYM. The fatty acids were extracted, saponified

* Corresponding Author: E-mail: djlee@ntu.edu.tw

and methylated according to the protocol of the Sherlock Microbial Identification System (MIDI). The genomic DNA of collected cells was extracted using the PowerSoil DNA Isolation Kit (MoBio, Carlsbad, CA, USA) following the manufacturer's instructions. The procedures of 16S rRNA gene identification by polymerase chain reaction (PCR) and denaturing gradient gel electrophoresis (DGGE) tests were available in [Zhang et al., 2015]. Purified PCR products were ligated to vector pMD19 and cloned into *Escherichia coli* DH5 α competent cells. The randomly selected 50 clones were sequenced using the ABI Prism model 3730XL (Applied Biosystems, CA, USA). The 16S rRNA gene sequences were analyzed using BLASTN and EzTaxon.

2.2 MFC and tests

Two double-chambered MFCs of size 7 \times 7 cm² and length 10.5 cm were started up with the isolates obtained in Sec. 2.1. A Ultrex CMI-7000 membrane (Ultrax Membrane International Inc., Glen Rock, NJ, USA) was the cation exchange membrane (CEM). Both anodes and cathodes were made of carbon cloth of area 14.0 cm² (WOS1002, CeTech. Co., Taichung, Taiwan). The cathode contained 0.5 mg/cm² Pt catalyst. Other reactor details are available in [Liu et al., 2011].

Before MFC tests, the anode compartment was degassed. Both electrodes were hung from titanium wires and were connected through an external 1000 Ω resistor. Reference Ag/AgCl electrode (type 217, XianRen Industries Co., Shanghai, China) was installed into the anodic chamber for conducting electrochemical measurements.

The enriched Fe(III)-reducing consortium was fed into the anode chamber of the MFC for cultivation in medium (per liter): Na₂HPO₄ 4.57 g, NaH₂PO₄ 2.45 g, NH₄Cl 0.31 g, Wolfe's vitamin solution 5 ml, and Wolfe's mineral solution 12.5 ml, pH 6.9. NaAc (20 mM) was used as carbon source for all MFC tests. The cathodic medium was a mixture of 50 mM potassium ferricyanide and 100 mM PBS.

The voltage drop over an external load 1000 Ω of individual MFC was recorded at 180 s intervals. Linear sweep voltammetry (LSV) of tested MFC were conducted at 1 mV/s [Nien et al., 2011; Watson et al. 2011] using an electrochemical workstation (model CHI611, CH Instruments, Inc. Austin, TX, USA). The CV tests were conducted on anode from -0.6 to +1.0 V. The electrochemical impedance spectroscopy (EIS) experiments were performed by Zahner™ IM6ex potentiostat-AC frequency analyzer equipment with frequency of the AC signal was varied from 100 kHz to 10 mHz with an amplitude of 5 mV. Impedance experiments were performed under galvanostatic closed circuit conditions at 400 mA for the tested biofilms. The initial electrical potentials for anode tests and for cathode tests were at -0.5 V and +0.25 V, respectively.

2.3 Other measurements

The XRD spectra of dried samples were obtained with a Bruker D8 Advance X-ray Diffractometer (Bruker AXS, Congleton, UK) with a Cu anode (40 kV and 30 mA) and scanning from 5 $^{\circ}$ to 90 $^{\circ}$. Cell lipids were extracted with the modified as described by [Santala et al., 2011] and were characterized by direct trans-esterification-gas chromatography method with methyl pentadecanoate as an internal standard.

3. Results and Discussion

3.1 Strain isolation and identification

Two isolates, LAR-2 and LAR-3, obtained from the screening and cultivation process showed efficient Fe(III)-reducing capability (suspension colors in cultivation tubes as indicators). The XRD patterns (not shown) for the freeze-dry precipitates from these suspension showed characteristic peaks for FeCO₃. Hence, the isolates have convert Fe(III) into Fe(II) during Fe(III)-reducing tests.

Atomic force microscope observation (not shown) reveals that the strain LAR-2 is short rod-shaped, no capsule-forming, with flagellum, 0.5–0.7 μ m wide and 0.8–1 μ m long microorganism. Also, the strain LAR-3 is short rod-shaped, no capsule, with flagellum, 0.3–0.5 μ m wide and 0.8–1 μ m long microorganism.

The physiological analysis (Tables 1 and 2) shows that both LAR-2 and LAR-3 can utilize urea, glucose, mannitol, lactose, sucrose, maltose, salicin, xylose, cattle gelatin, esculin, citrate, glycerol, mannose, melezitose, raffinose, sorbitol and trehalose, but cannot utilize cellobiose or rhamnose. The differences are the former cannot use tryptophan and arabinose while the latter can. Both strains contain alkaline phosphatase, esterase (C4), esterase (C8), leucine arylamidase, cystine arylamidase, trypsin, chymotrypsin, acid phosphatase, naphtha-AS-BI-phosphohydrolase, a-galactosidase, \hat{a} -galactosidase, a-glucosidase, \hat{a} -glucosidase, but do not have esterase (C14), leucine aromatic aminotransferase, \hat{a} -glucuronidase, a-nannosidase, \hat{a} -fucosidase. LAR-2 has N-acetyl-glucosaminidase but has

no leucine aromatic aminotransferase; LAR-3 has valine arylamidase.

The FAME chromatograms (Tables 3 and 4) revealed the major peaks with predominant fatty acids. Comparison with database reveal no fitting based on FAME spectra for either LAS-2 or LAR-3.

The 16S rRNA sequence analysis revealed that strain LAR-2 belongs to delta subclass of the Proteobacteria and most closely related to *Geobacter sulfurreducens* PCA^(T) (98.41%), *Geobacter hydrogenophilus* H2^(T) (95.11%) (Table 5). The phylogenetic analyses based on 16S rRNA gene sequences indicated that the strain LAR-2 formed a lineage in the Deltaproteobacteria (Fig. 1a). Meanwhile, the 16S rRNA sequence analysis revealed that strain the LAR-3 belongs to Clostridia and most closely related

Table 1. Physiological and biochemical tests for isolates*

API-A			API-20NE		
Carbon source	LAR-2	LAR-3	Substrate	LAR-2	LAR-3
IND	-	+	NO3	+	+
URE	+	+	TRP	+	+
GLU	+	+	GLU	+	+
MAN	+	+	ADH	+	-
LAC	+	+	URE	+	+
SAC	+	+	ESC	+	+
MAL	+	+	GEL	+	+
SAL	+	+	PNPG	+	+
XYL	+	+	GLU	+	+
ARA	-	+	ARA	+	+
GEL	+	+	MNE	+	+
ESC	+	+	MAN	+	+
GLY	+	+	NAG	+	+
CEL	+	+	MAL	+	+
MNE	+	+	GNT	+	+
MLZ	+	+	CAP	-	-
RAF	+	+	ADI	-	-
SOR	+	+	MLT	+	+
RHA	-	+	CIT	+	+
TRE	+	+	PAC	+	+
SPOR	-	+			
GRAM	pink	purple			
COCC	rod	rod			

*Includes urea, glucose, mannitol, lactose, sucrose, maltose, salicin, xylose, cattle gelatin, esculin, ferric citrate, glycerol, mannose, melezitose, raffinose, sorbitol, trehalose, tryptophan, arabinose, cellobiose and rhamnose.

Table 2. Physiological API-ZYM identification for isolates.

Enzyme	LAR-2	LAR-3
control	-	-
alkaline phosphatase	+	+
esterase (C4)	+	+
esterase lipase (C8)	+	+
esterase (C14)	-	-
leucine arylamidase	+	+
valine arylamidase	+	+
cysteineacrylamidase	+	+
trypsin	+	+
chymotrypsin	+	+
acid phosphatase	+	+
naphtha-AS-BI-phosphohydrolase	+	+
a-galactosidase	+	+
\hat{a} -galactosidase	+	+
\hat{a} -glucuronidase	-	-
a-glucosidase	+	+
\hat{a} -gucoisidase	+	+
N-acetylglucosaminidase	+	-
a-nannosidase	-	-
\hat{a} -fucosidase	-	-

Table 3. Identification of fatty acids of LAR-2.

No.	RT	Response	Peak Name	Percent	Comment1
1	3.162	857	10:00	0.34	
2	4.779	655	12:00	0.25	
3	6.932	419	14:0 anteiso	0.15	
4	10.215	20408	Sum In Feature 3	7.19	16:1 w7c/16:1 w6c
5	10.519	119599	16:00	42.03	
6	12.261	527	17:00	0.18	
7	13.522	1811	Sum In Feature 5	0.62	18:2 w6,9c/18:0 ante
8	13.619	54712	18:1 w9c	18.79	
9	13.713	37567	Sum In Feature 8	12.89	18:1 w7c
10	14.021	5384	18:00	1.84	
11	15.11	8543	19:0 iso	2.91	
12	15.608	37656	19:0 cyclo w8c	12.79	0

Table 4. Identification of fatty acids of LAR-3.

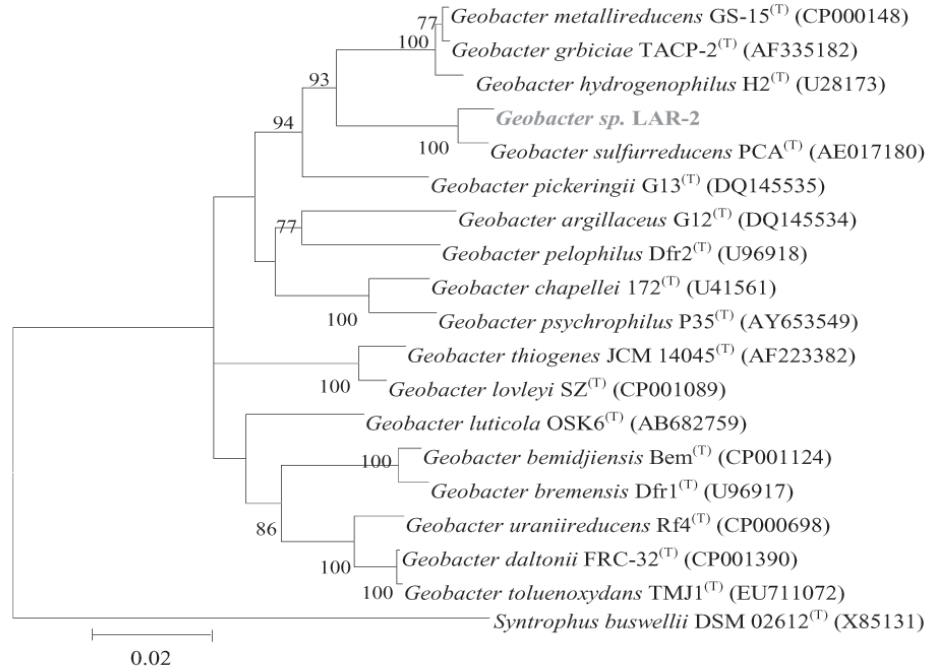
No.	RT	Response	Peak Name	Percent	Comment
1	3.145	599	10:00	0.21	
2	4.761	642	12:00	0.21	
3	7.287	26210	14:00	8.21	
4	10.196	26508	Sum In Feature 3	8.02	16:1 w7c/16:1 w6c
5	10.501	136208	16:00	41.07	
6	12.042	2556	17:0 cyclo	0.76	
7	12.235	381	17:00	0.11	
8	13.501	1355	Sum In Feature 5	0.4	18:2 w6,9c/18:0 ante
9	13.593	28705	18:1 w9c	8.43	
10	13.689	18064	Sum In Feature 8	5.3	18:1 w7c
11	14	4238	18:00	1.24	
12	14.133	877	18:1 w7c 11-methyl	0.26	
13	14.839	1372	19:1 iso I	0.4	
14	15.089	7018	19:0 iso	2.04	
15	15.526	21043	Sum In Feature 7	6.11	19:0 cyclo w10c/19w6
16	15.586	58579	19:0 cyclo w8c	17	
17	17.037	771	20:2 w6,9c	0.22	

Table 5. Blast results of strain LAR-2 based on the 16S rRNA genes.

Name	Accession No	Similarity(%)	Diff/Total nt
<i>Geobacter sulfurreducens</i> PCA ^(T)	AE017180	98.41	24/1514
<i>Geobacter hydrogenophilus</i> H2 ^(T)	U28173	95.11	68/1391
<i>Geobacter metallireducens</i> GS-15 ^(T)	CP000148	94.78	79/1514
<i>Geobacter grbciae</i> TACP-2 ^(T)	AF335182	94.66	80/1499
<i>Geobacter pickeringii</i> G13 ^(T)	DQ145535	94.41	84/1504
<i>Geobacter argillaceus</i> G12 ^(T)	DQ145534	93.5	95/1461
<i>Geobacter pelophilus</i> Dfr2 ^(T)	U96918	92.87	105/1473
<i>Geobacter thiogenes</i> JCM 14045 ^(T)	AF223382	92.8	109/1513
<i>Geobacter lovleyi</i> SZ ^(T)	CP001089	92.6	112/1513
<i>Geobacter luticola</i> OSK6 ^(T)	AB682759	92.55	110/1476
<i>Geobacter bemidjensis</i> Bem ^(T)	CP001124	92.46	114/1511
<i>Geobacter chappellei</i> 172 ^(T)	U41561	92.41	111/1463
<i>Geobacter daltonii</i> FRC-32 ^(T)	CP001390	92.33	116/1512
<i>Geobacter uraniiireducens</i> Rf4 ^(T)	CP000698	92.26	117/1512
<i>Geobacter psychrophilus</i> P35 ^(T)	AY653549	92.18	116/1484
<i>Geobacter bremensis</i> Dfr1 ^(T)	U96917	92.12	116/1472
<i>Geobacter toluenoxydans</i> TMJ1 ^(T)	EU711072	92	115/1438
<i>Syntrophus buswellii</i> DSM 02612 ^(T)	X85131	85.92	213/1513
<i>Geobacter sulfurreducens</i> PCA ^(T)	AE017180	98.41	24/1514
<i>Geobacter hydrogenophilus</i> H2 ^(T)	U28173	95.11	68/1391
<i>Geobacter metallireducens</i> GS-15 ^(T)	CP000148	94.78	79/1514
<i>Geobacter grbciae</i> TACP-2 ^(T)	AF335182	94.66	80/1499
<i>Geobacter pickeringii</i> G13 ^(T)	DQ145535	94.41	84/1504
<i>Geobacter argillaceus</i> G12 ^(T)	DQ145534	93.5	95/1461
<i>Geobacter pelophilus</i> Dfr2 ^(T)	U96918	92.87	105/1473
<i>Geobacter thiogenes</i> JCM 14045 ^(T)	AF223382	92.8	109/1513
<i>Geobacter lovleyi</i> SZ ^(T)	CP001089	92.6	112/1513
<i>Geobacter luticola</i> OSK6 ^(T)	AB682759	92.55	110/1476
<i>Geobacter bemidjensis</i> Bem ^(T)	CP001124	92.46	114/1511
<i>Geobacter chappellei</i> 172 ^(T)	U41561	92.41	111/1463
<i>Geobacter daltonii</i> FRC-32 ^(T)	CP001390	92.33	116/1512
<i>Geobacter uraniiireducens</i> Rf4 ^(T)	CP000698	92.26	117/1512
<i>Geobacter psychrophilus</i> P35 ^(T)	AY653549	92.18	116/1484

to *Clostridium celerecrescens* DSM 5628^(T)(99.45%), *Clostridium sphenoides* DSM 632^(T)(98.83%), *Clostridium indolis* DSM 755^(T)(98.28%), *Clostridium methoxybenzovorans* SR3^(T)(98.23%), *Clostridium saccharolyticum* WM1^(T)(98.02%) (Table 6). The phylogenetic analyses based on 16S rRNA gene sequences indicated that the strain LAR-3 formed a lineage in the Clostridiales (Fig. 1b).

On the basis of the above characterization, the strain LAR-2 is a Gram-negative, no spore-forming, and anaerobic bacterium, confirmed to be closely affiliated to *Geobacter* sp.. The gene sequence was deposited in GenBank under accession no. KC211015. The strain LAR-3 is a Gram-positive, spore-forming and anaerobic bacterium, confirmed to be closely affiliated to *Clostridium* sp. with gene sequence accession number at GenBank No. KC211016.



(a)

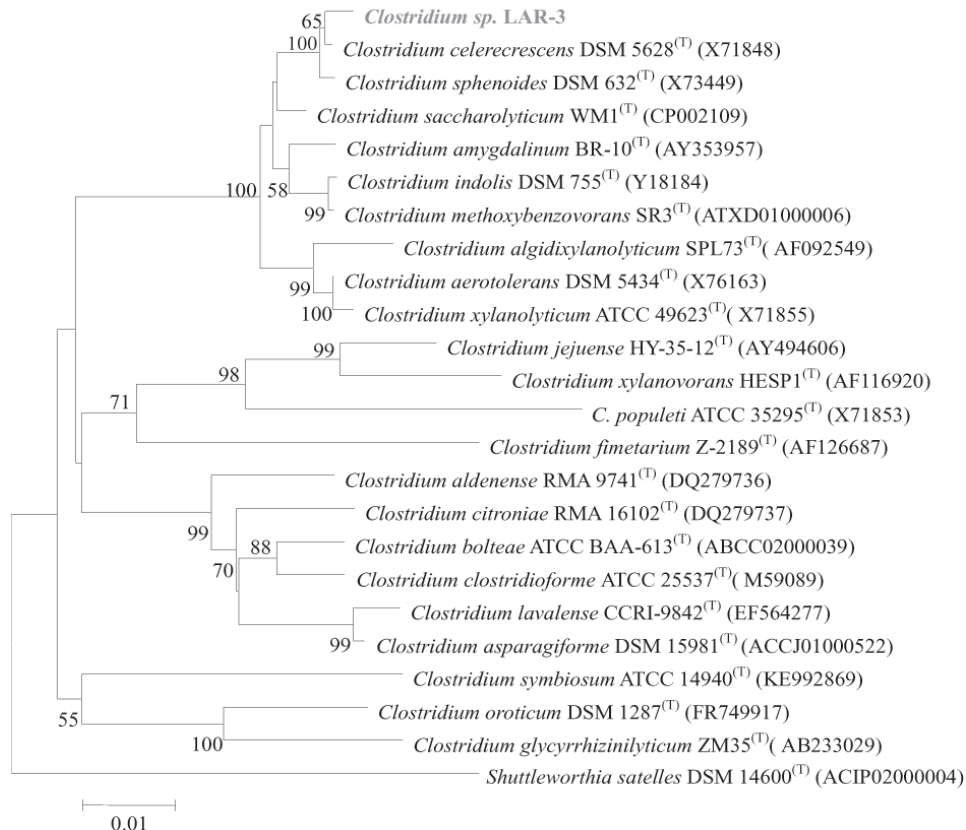


Fig. 1. Neighbor-joining showing phylogenetic positions of isolated strains LAR-2(a) /LAR-3 (b) and related species based on 16S rRNA gene sequence comparisons. Bootstrap values are indicated at nodes. Only bootstrap values >50% are shown. Scale bar, 1% sequence dissimilarity (one substitution per 100 nt). Representative sequences in the dendrogram were obtained from EzTaxon (accession number in parentheses).

Table 6. Blast results of strain LAR-3 based on the 16S rRNA genes.

Name	Accession	Pairwise Similarity(%)	Diff/Total nt
<i>Clostridium celerecrescens</i> DSM 5628 ^(T)	X71848	99.45	8/1462
<i>Clostridium sphenoides</i> DSM 632 ^(T)	X73449	98.83	17/1457
<i>Clostridium indolis</i> DSM 755 ^(T)	Y18184	98.28	25/1457
<i>Clostridium methoxybenzovorans</i> SR3 ^(T)	ATXD01000006	98.23	26/1467
<i>Clostridium saccharolyticum</i> WM1 ^(T)	CP002109	98.02	29/1466
<i>Clostridium amygdalinum</i> BR-10 ^(T)	AY353957	97.59	35/1451
<i>Clostridium aerotolerans</i> DSM 5434 ^(T)	X76163	97.55	35/1426
<i>Clostridium xylanolyticum</i> ATCC 49623 ^(T)	X71855	97.12	42/1456
<i>Clostridium algidixylanolyticum</i> SPL73 ^(T)	AF092549	96.93	45/1466
<i>Clostridium boltea</i> ATCC BAA-613 ^(T)	ABCC02000039	93.86	90/1465
<i>Clostridium aldenense</i> RMA 9741 ^(T)	DQ279736	93.68	87/1376
<i>Clostridium clostridioforme</i> ATCC 25537 ^(T)	M59089	93.08	101/1459
<i>Clostridium lavalense</i> CCRI-9842 ^(T)	EF564277	93.04	100/1436
<i>Clostridium symbiosum</i> ATCC 14940 ^(T)	KE992869	92.97	103/1466
<i>Clostridium asparagiforme</i> DSM 15981 ^(T)	ACCJ01000522	92.97	103/1465
<i>Clostridium citroniae</i> RMA 16102 ^(T)	DQ279737	92.82	102/1420
<i>Clostridium oroticum</i> DSM 1287 ^(T)	FR749917	92.62	108/1463
<i>Clostridium glycyrrhizinilyticum</i> ZM35 ^(T)	AB233029	92.01	117/1465
<i>Clostridium jejuense</i> HY-35-12 ^(T)	AY494606	91.89	117/1443
<i>Clostridium fimetarium</i> Z-2189 ^(T)	AF126687	91.61	123/1466
<i>Clostridium xylanovorans</i> HESP1 ^(T)	AF116920	91.01	131/1457
<i>Clostridium populeti</i> ATCC 35295 ^(T)	X71853	90.56	137/1451
<i>Shuttleworthiasatelles</i> DSM 14600 ^(T)	ACIP02000004	89.21	158/1464

3.2 MFC tests

3.2.1 LAR-2

Figure 2a shows the $V-t$ curves for LAR-2-MFC. After a lag phase of 25 d, the cell voltage was increased to about 310 mV, then fluctuated in the next 10 d. The peak voltage gradually increased to over 600 mV since 2nd cycle, indicating formation of mature anodic biofilm in MFC. The LAR-2-MFC was successfully started up.

The LAR-2-MFC had an OCV of 610 mV (Fig. 2b). Reducing external load yielded an increase in electrical current and reduction in cell voltage. The mild initial drop in voltage indicates the presence of activation losses of 5 mV. When reaching $V=470$ mV, the power density peaked at 860 mW m⁻². The short circuit current density (I_{sc}) was 1.67 A m⁻². The cell power shoot proposed by [Nien et al., 2011] was noted for the present MFC.

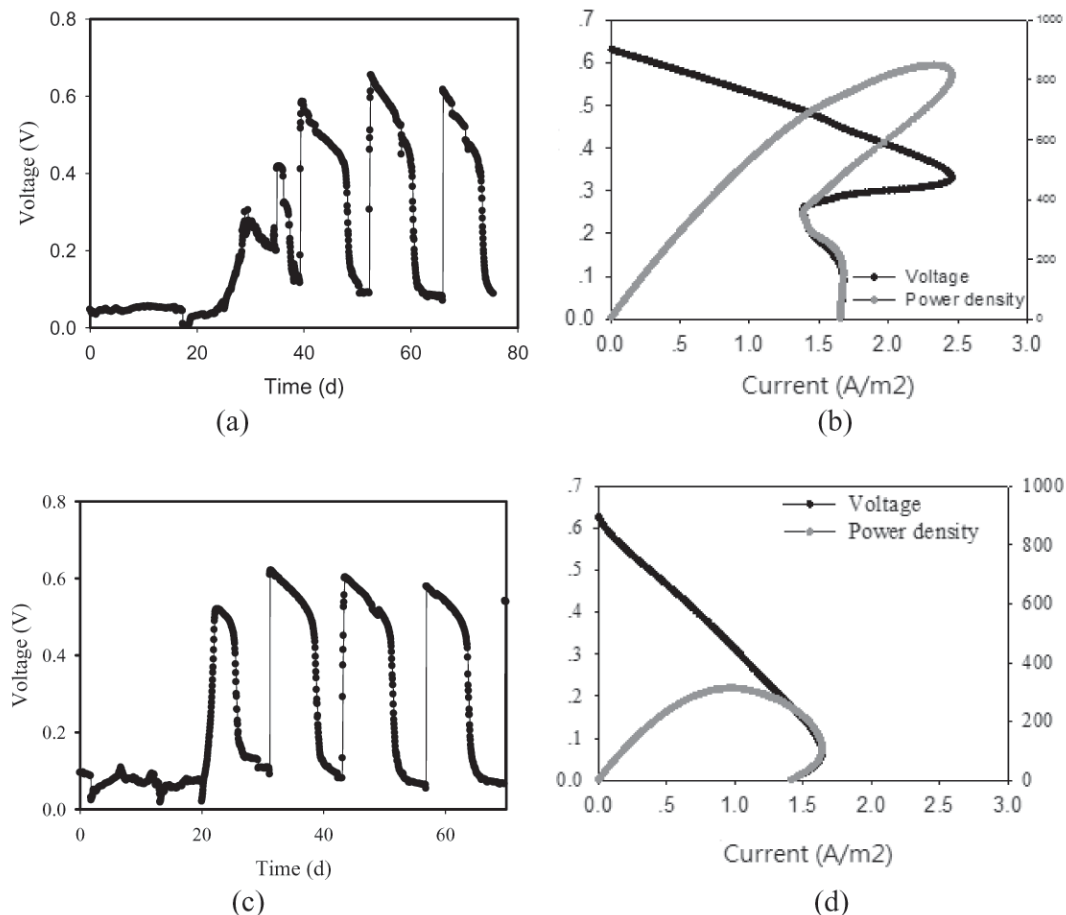


Fig. 2. MFC performance after startup. (a) $V-t$ curve. LAR-2, voltage in mV. (b) Polarization curve and power density curve for LAR-2. Power density in mW/m². (c) $V-t$ curve. LAR-3, voltage in mV. (d) Polarization curve and power density curve for LAR-3. Power density in mW/m².

Nyquist plots (Fig. 3a) for the LAR-2-MFC revealed a typical MFC performance curve. The electrolyte resistances were low ($<10\Omega$). The polarization resistances for anode and cathode were estimated by the diameters for the first semi-circles as 65Ω and 70Ω , respectively. The biofilm-anode polarization resistance was estimated based on the diameter for the second semi-circle as 740Ω for anode. The anodic biofilm of LAR-2-MFC had high activity but contributed principally the cell resistance in the test.

3.2.2 LAR-3

Figure 2c shows the $V-t$ curves for LAR-3-MFC. After a lag phase of 20 d, the cell voltage was increased to about 520 mV, then gradually dropped to <100 mV in next 5–8 d. The peak voltage gradually increased from 520 mV to over 600 mV since 2nd cycle, indicating successful startup of the MFC.

The LAR-3-MFC had an OCV of 630 mV (Fig. 2d) and $P_{max}=323$ mW m^{-2} at $V=415$ mV. The short circuit current density (I_{sc}) was 1.41 A m^{-2} . The cell power shoot was also observed for this MFC. Nyquist plots (Fig. 3b) estimated the polarization resistances for anode and cathode to be 610Ω and 190Ω , respectively.

3.3 FRB for MFC startup

This study confirmed that the two isolated FRB can be independently used as the inoculum for developing anodic biofilms of MFC. The so-started up MFC has high OCV, suggesting high bioelectrochemical activity of the cultivated LAR-2 and LAR-3 biofilms.

The extracellular electron transfer can be achieved by *c*-type cytochrome proteins in the outer membrane of FRB with heme being the active center or by yielding electron shuttlers. The electrolyte resistances for anode, cathode and whole cells ranged 10–20 Ω , suggesting low electrolyte resistance in the tested MFC cell. The *Geobacter sp.* is a Gram-negative strain that has thin cell walls. Conversely, The *Clostridium sp.* is a Gram-positive strain that has thick cell wall. The nature of cell walls may affect the observed biofilm polarization resistance for anode, 65Ω for LAR-2 and 610Ω for LAR-3. Reguera et al. [2005] proposed that their *Geobacter* strain utilized conductive pili for transferring electron to the surface of iron oxides. Park et al. [2001] proposed that their *Clostridium* strain may utilize direct electron transfer (DET) pathway in MFC operation. The more efficient electron pathway by *Geobacter sp.* may also correspond to the higher P_{max} (860 mW m^{-2}) than for the *Clostridium sp.* (313 mW m^{-2}).

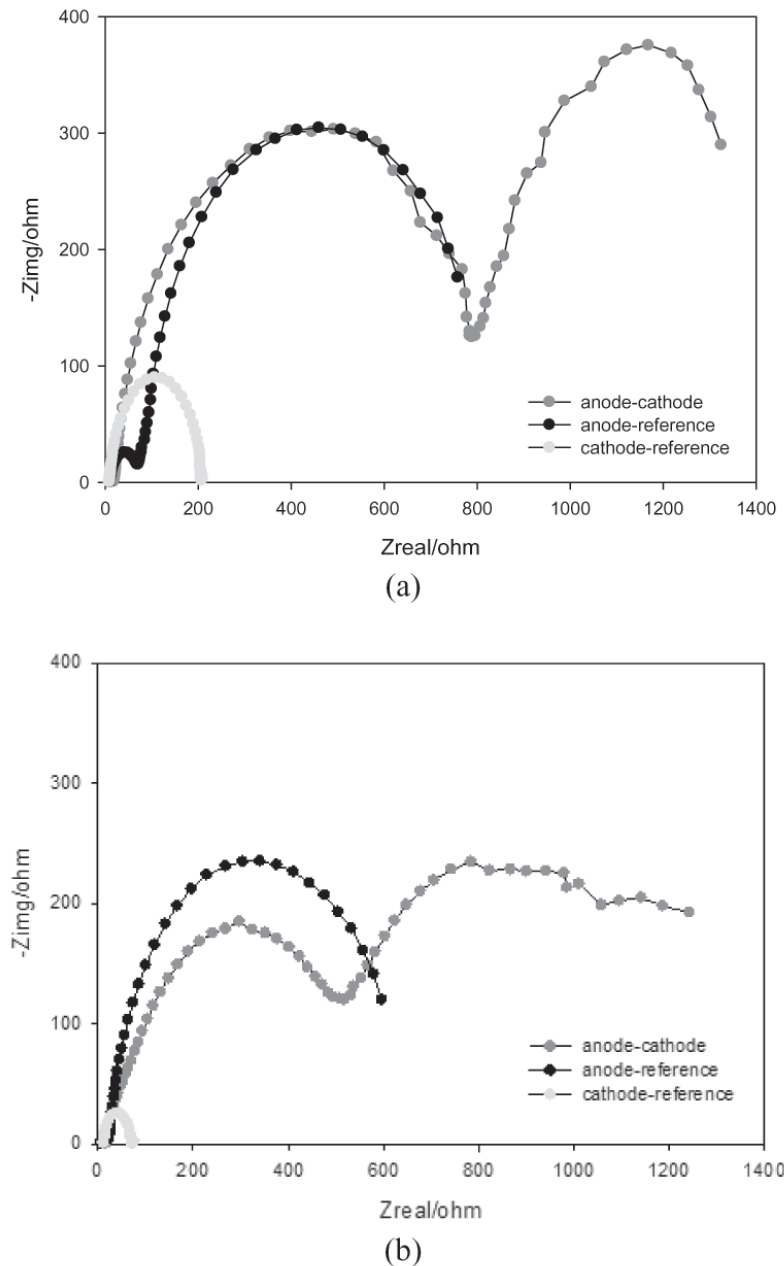


Fig. 3. Nyquist plot for anode, cathode and whole cell. (a) LAR-2-MFC, (b) LAR-3-MFC.

Power overshoot occurred in both LAR-2 and LAR-3 tests. Restated, as external loads were decreased, the cell resistance suddenly increased leading to decreases in both cell voltage and electrical current under high electrical current regimes. Power overshoot is commonly noted for MFC with mixed culture [Liu et al., 2011; Nien et al., 2011; Ieropoulos et al., 2010]. The present observations confirmed that the MFCs with single cultures can also have power overshoot. The sudden increase in resistance for extracellular electron transfer on anode surface is proposed to induce the occurrence of power overshoot [Nien et al., 2011]. The present study revealed that both Gram-positive and Gram-negative strains can have power overshoot, hence the electron saturation at cell membrane for all bacterial strains can occur at high current conditions. This is not welcome since the occurrence of power overshoot limits the cell output. Mature biofilm with excess exoelectrogens may lead to high MFC current, but the increment will not be unlimited owing to the biological nature of FRB in the biofilm

4. Conclusions

The *Geobacter* sp. LAR-2 (Gram-negative) and the *Clostridium* sp. LAR-3 (Gram-positive) were isolated and identified using biochemical tests and PCR-DGGE tests. These two strains were confirmed to be FRB via XRD tests on the precipitate yielded. The LAR-2-MFC was successfully started up with OCV of 610 mV, P_{max} = 860 mW m⁻² and polarization resistance for anode of 65Ω. The LAR-3-MFC was also started up with OCV = 630 mV, P_{max} = 323 mW m⁻², and polarization resistances for anode of 610Ω. These two FRBs were confirmed to be functioning well as ARB for MFC, with the former being a preferred FRB for MFC operation than the latter. The MFCs with single cultures can also have power overshoot

5. Acknowledgements

This work is supported by NSFC project No. 51278128.

6. References

- Inoue K, Ito T, Kawano Y, Iguchi A, Miyashara M, Suzuki Y, Watabane K., 2013. Electricity generation from cattle manure slurry by cassette-electrode microbial fuel cells, *Journal of Bioscience and Bioengineering* 116, 610–615.
- Chou TY, Whiteley CG, Lee DJ, 2014. Anodic potential on dual-chambered microbial fuel cell with sulphate reducing bacteria biofilm. *International Journal of Hydrogen Energy* 39, 19225–19231.
- Yoshizawa T, Miyahara M, Kouzuma A, Watanabe K, 2014. Conversion of activated-sludge reactors to microbial fuel cells for wastewater treatment coupled to electricity generation. *Journal of Bioscience Bioengineering* 118, 533–539 (2014).
- Zhang GD, Zhao QL, Jiao Y, Lee DJ, 2015. Long-term operation of manure-microbial fuel cell. *Bioresource Technology* 180, 365–369.
- Koroglu EO, Ozkaya B, Denktas C, Cakmakci M, 2014. Electricity generating capacity and performance deterioration of a microbial fuel cell fed with beer brewery wastewater. *Journal of Bioscience and Bioengineering* 118, 672–678.
- Lee CY, Ho KL, Lee DJ, Su A, Chang JS, 2012. Electricity harvest from nitrate/sulfide-containing wastewaters using microbial fuel cell with autotrophic denitrifier, *Pseudomonas* sp. C27. *International Journal of Hydrogen Energy* 37, 15827–15832.
- Mohan SV, Velvizhi G, Modestra JA, Srikanth S, 2014. Microbial fuel cell: Critical factors regulating bio-catalyzed electrochemical process and recent advancements. *Renewable and Sustainable Energy Reviews* 40, 779–797.
- Kim BH, Kim HJ, Hyun MS, Park DH, 1999. Direct electrode reaction of Fe(III)-reducing bacterium, *Shewanella putrefaciens*. *Journal of Microbiology and Biotechnology* 9, 127–131.
- Kostka JE, Dalton DD, Skelton H, Dollhopf S, Stucki JW, 2002. Growth of iron(III)-reducing bacteria on clay minerals as the sole electron acceptor and comparison of growth yields on a variety of oxidized iron forms. *Applied and Environmental Microbiology* 68, 6256–6262.
- Huang JJ, Zhu NW, Cao YL, Peng Y, Wu PX, Dong WH, 2015. Exoelectrogenic bacterium phylogenetically related to *Citrobacter freundii*, isolated from anodic biofilm of a microbial fuel cell. *Applied Biochemistry and Biotechnology* 175, 1879–1891.
- Liu TX, Li XM, Zhang W, Hu M, Li FB, 2014. Fe(III) oxides accelerates microbial nitrate reduction and electricity generation by *Klebsiella pneumoniae* L17. *Journal of Colloid and Interface Science* 423, 25–32.
- Liu LH, Lee CY, Ho KC, Nien PC, Su A, Wang AJ, Ren NQ, Lee DJ 2011. Occurrence of power overshoot for two chambered MFC at nearly steady-state operation. *Int. J. Hydrogen Energy* 36, 13896 - 13899.
- Santala S, Efimova E, Kivinen V, Larjo A, Aho T, Karp M, Santala V, 2011. Improved triacylglycerol production in *Acinetobacter baylyi* ADP1 by metabolic engineering, *Microbiol Cell Factories* 10, 36.
- Nien PC, Lee CY, Ho KC, Adav SS, Liu LH, Wang AJ, Ren NQ, Lee DJ, 2011. Power overshoot in two-chambered microbial fuel cell (MFC). *Bioresource Technology* 102, 4742–4746.
- Watson VJ, Logan BE, 2011. Analysis of polarization methods for elimination of power overshoot in microbial fuel cell. *Electrochemistry Communications* 13, 54–56.
- Reguera G, McCarthy KD, Mehta T, Nicol JS, Tuominen MT, Lovley DR, 2005. Extracellular electron transfer via microbial nanowires. *Nature* 435, 1098–1101.
- Park HS, Kim BH, Kim HS, Kim HJ, Kim GT, Kim M, Chang IS, Park YK, Chang HI, 2001. A novel electrochemically active and Fe(III)-reducing bacterium phylogenetically related to *Citrobacter butyricum* isolated from a microbial fuel cell. *Anaerobe* 7, 297–306.
- Ieropoulos I, Winfield J, Greenman J, 2010. Effects of flow-rate inoculum and time on the internal resistance of microbial fuel cells. *Bioresource Technology* 101, 3520–3525.



Qualitative *in vitro* Evaluation of Plant Growth Promoting Activity of Electrogenic Bacteria from Biohydrogen Producing Microbial Electrolysis Cell towards Biofertilizer Application

C.Nagendranatha Reddy, K.Arunasri, Dileep Kumar Yeruva, K.Vamshi Krishna, S.Venkata Mohan*

Bioengineering and Environmental Sciences (BEES), CSIR-Indian Institute of Chemical Technology (CSIR-IICT), Hyderabad-500 007, India

ARTICLE INFO

Received : 31 August 2015
Revised : 07 November 2015
Accepted : 10 November 2015

Keywords:

Biofertilizer; Bacterial Isolates;
Siderophores; Indole Acetic Acid;
Antifungal Activity

ABSTRACT

DBio-fertilizers confer a sustainable alternate to chemical fertilizers through their plant growth promoting activities and contribute significantly to enhance soil fertility and crop yields. The present study identifies five bacterial strains (K7, K8, K9, K11 and K18) isolated from a different microbiome (Microbial Electrolysis Cell; MEC) to have nitrogen fixing capability. Consequently, the isolates were identified by 16S ribosomal RNA gene sequencing analysis as *Bacillus safensis* strain K7, *B. nealsonii* strain K8, *B. nealsonii* strain K9, *Leifsonia shinshuensis* strain K11 and *Streptomyces griseoviridis* strain K18. Since the isolates exhibited nitrogen fixation property which is one of the important characteristics of plant growth promoting activity, these strains were further evaluated for other biofertilizer properties viz. phosphate solubilization, indole acetic acid (IAA) production, siderophores activity and anti-fungal activity. The results showed that siderophore activity was observed in both K7 and K18 strains while IAA production and antifungal activity was observed in K7 and K18 strains respectively. Phosphate solubilization was observed only in K9. The results illustrate that *Streptomyces griseoviridis* strain K18, *Bacillus safensis* strain K7 and *B. nealsonii* strain K9 hold promise to be used as a biofertilizer with potential plant growth promoting activity.

© 2016 ISEES, All rights reserved

1. Introduction

Chemical based fertilizers in agriculture have imposed a negative impact on the overall environment and soils. Thus, bio-fertilizer, which is ecofriendly and have no adverse effects on environment and living beings as well are in great demand (Khan et al., 2009). Biofertilizers accelerate certain microbial processes in the soil by increasing the extent of availability of nutrients in a form easily assimilated by plants and are extremely advantageous in enriching soil fertility and fulfilling plant nutrient requirements by supplying the organic nutrients through microorganism and their by-products (Rajasulochana and Krishnamoorthy., 2014). They add nutrients to the soil through natural processes of atmospheric nitrogen fixation, phosphate solubilization and mobilization, translocate minor elements like zinc, and copper, secreting plant growth promoting substances like Indole acetic acid (IAA), siderophores, vitamins and amino acids etc., and also shun plant pathogenic fungi, thereby improving the soil health and crop production. Symbiotic integration of plant and microorganisms is synergistic in nature as plants supply root borne carbon compounds, that can be metabolized for bacterial growth and bacteria provide soluble nutrients in return (Perez et al., 2007). Use of biofertilizers is one of the important components of integrated nutrient management, as they provide eco-friendly organic agro-input and restore the soil's natural nutrient cycle and build soil organic matter for sustainable agriculture (Mohammadi and Sohrabi, 2012). Knowledge of using organic biofertilizers dates back to history with production and usage of compost. Bio-fertilizers do not contain any synthetic chemicals which are detrimental

to the living soil and does not add any pollution to nature like chemical fertilizers. Efficient strains of nitrogen fixing, phosphate solubilizing, siderophores activity, IAA productivity and antifungal activity in combination will provide good scope for production of biofertilizers having plant growth promoting properties (Shahab et al., 2009).

In the present study, an attempt was made to evaluate the biofertilization abilities of the isolates from Microbial Electrolysis Cell (MEC). Previous reports on microbial diversity in MEC have shown that the microbial populations are rich in electrogenic bacteria having biohydrogen production capacity (Venkata Mohan and Lenin Babu., 2011; Venkata Mohan et al., 2007; Kannaiah Goud et al., 2012). The microbial diversity studies have also demonstrated that the enriched electrogenic bacteria are mostly anaerobic or microaerophilic having the ability to form biofilm or colonize on biotic (plant roots) or abiotic (electrode) surfaces (Puente et al., 2004). These electrogenic bacteria has exhibited the ability to colonize plant roots and utilize root exudates formed by plant rhizosphere as substrate for their metabolic activities and simultaneously release electrons, protons and microbial metabolites to the external environment enumerating the positive function of rhizosphere (Chiranjeevi et al., 2012). So, it was assumed that the isolated strains might also exhibit plant growth promoting activity. However, so far no reports are available on using electrogenic bacteria for evaluating plant growth promoting and biofertilizer activity. Thus in the present study, the bacterial isolates from MEC were initially screened for diazotrophy and later on for other biofertilizer capabilities.

* Corresponding Author: E-mail: vmohan_s@yahoo.com; Tel/Fax: +91-40-27191765

2. Experimental Methodology

2.1 Bioreactor

A single chambered MEC is used to produce Bio-H₂ by electro fermenting the volatile fatty acid (VFA) effluents (4000 mg/l and 8000 mg/l) generated from acidogenic fermentation with simultaneous waste treatment is used for isolation of potent organisms which can withstand the potential of 0.6 V. Maximum cumulative H₂ production (CHP) and hydrogen production rate (HPR) of 39.35 ml and 0.057 mmol/h was observed at 0.6 V respectively and maximum amount of VFA utilization as substrate is observed to be 68% at 0.6 V (Annie Modestra et al., 2015).

2.2 Bacterial strains Cultivation

Five bacterial strains viz., K7, K8, K9, K11 and K18 screened from MEC system were used in the study to evaluate the biofertilizer activity. Cultures were grown on nutrient agar plates by streak plate method for 48 hours at 37°C and the representative colonies, according to their morphologies and nitrogen fixing ability, were selected for further characterization. Colonies were re-streaked on nutrient agar plates until a pure culture was obtained. A single colony was picked from these plates and transferred to 50 ml of nutrient broth and incubated for growth at 37°C (150 rpm). Overnight grown cultures were used for various biofertilization assay procedures unless until mentioned.

2.3 Characterization and Identification of isolates

Following the selection of pure isolates, 5 isolates were identified based on grams staining and microscopy. Colony morphology of all the isolates grown on nutrient agar plates was also studied. Sequencing of 16S rRNA gene was done to identify the bacteria. Colony PCR was used to amplify the 16S rRNA gene using universal primers 27F (5'-AGAGTTTGATCMTGGCTCAG-3') and 1525R (5'-AAGGAGGTGTCCARCC-3'). Small amount of pure isolated colony obtained after streaking was picked and subjected to lysis by heating at 95°C for 10 min. The cell lysate obtained cells was used as DNA template for amplification of 16S rRNA gene. Polymerase chain reaction was performed in a 50 µl reaction volume using the primers described above. PCR was performed using the thermal cycler (Eppendorf, Germany) and according to the protocol described previously (Kannaiah Goud and Venkata Mohan., 2013). PCR product was separated by electrophoresis on 1% agarose gel stained with ethidium bromide and photographed under UV illumination using Gel Doc (Molecular Imager G: BOX EF System; Syngene). The 1 kb ladder was used to check the amplification of the product obtained. PCR product was cleaned using QIAquick PCR purification kit (Qiagen) according to the manufacturer's instructions and purified PCR product was used for sequencing. 16S rRNA gene sequencing was done as described previously (Lane, 1991) using above described primers. For the resultant sequences obtained by sequencing, a BLAST algorithm search was performed to identify the nearest taxa. The 16S rRNA sequences of the related members were downloaded from the database (<http://www.ncbi.nlm.nih.gov>) and aligned using MEGA 6 (Tamura et al., 2007). Phylogenetic trees were constructed based on neighbour joining method using MEGA 6.

2.4 Screening for Nitrogen Fixation Activity

Nitrogen free media (1000 ml; Sucrose- 20 g, Dipotassium phosphate- 1 g, Magnesium sulphate- 0.5 g, Sodium chloride- 0.5 g, Ferrous sulphate- 0.1 g, Sodium molybdate- 0.005 g, Calcium carbonate- 2 g, Agar- 15 g) was dissolved in distilled water and transferred to test tubes for autoclaving (Jensen., 1942). After autoclaving, the cooled media was inoculated with the specific strains, incubated for 2 days and checked for growth by measuring the optical density (OD) at 600nm using UV-Visible Spectrophotometer

2.5 Screening for IAA production

Bacterial isolates were screened for their ability to produce IAA in tryptophan media (5 g of casein peptone, 0.5 g of D-tryptophan, 2.5 g of sodium chloride dissolved in 500 ml of distilled water and adjusted to pH 7.5). The media was transferred into test tubes and autoclaved for 15 min at 121°C. The autoclaved media was inoculated with specific strains in duplicate with standard inoculum 350 x10⁵ CFU/ml and incubated for 48 h (37°C). 1 ml of chloroform was added to the test tube followed by 2.1 ml of Kovac's reagent (25 ml of Conc. HCl mixed with 75 ml of amyl alcohol and 5 g of para dimethyl amino benzaldehyde; stored in closed vials at 4°C). The appearance of pink color in the test tube indicates the capability of that particular strain for producing IAA (Mohite., 2013).

2.6 Phosphate solubilization

The phosphate solubilisation activity of the isolated strains was evaluated using PVK medium (1000 ml; Glucose-10 g, tri-calcium phosphate-5 g, ammonium sulphate-0.5 g, sodium chloride-0.2 g, magnesium sulphate-0.1 g, potassium chloride-0.2 g, yeast extract-0.5 g, manganese sulphate-0.002 g, ferrous sulphate-0.002 g and agar powder-15 g) (Pikovskaya., 1948). The dissolved media was subjected to autoclaving for 15 min prior to preparation of petri plates. The petriplates filled with PVK medium was spread with serially diluted samples and incubated for 48-72 h. The halo and colony diameters were measured after 5 days of the incubation where halo size was calculated by deducting colony diameter from total halozone diameter (Nguyen et al., 1992).

2.7 Screening of bacterial isolates for Siderophore Activity

Simple succinate media (SSM; 1000 ml, ammonium sulphate- 1 g, dipotassium phosphate-6 g, magnesium sulphate-0.2 g, potassium dihydrogen phosphate-3 g, succinic acid- 4 g; pH 7) was used to detect siderophore activity colorimetrically. Autoclaved media after inoculation with test strains were subjected to incubation at room temperature for 48 h. Fully grown culture was centrifuged (9000 rpm; 12 min) and absorbance was recorded at wavelengths between 350 and 450 nm. The presence of peaks at these particular wavelengths signifies the presence of siderophores (Ines et al., 2012).

2.8 Antifungal Activity

The antifungal activity of the strains was assessed by performing germination test (Hernández-Albíter et al., 2007). Fine ground nut (*Arachis hypogaea*) seeds were used to determine the effectiveness of the isolated strains. Plastic trays were spread with wet sterilized cotton to provide moisture content for the seeds to germinate and the whole setup was autoclaved prior to experiment. In control, the seeds were treated with sodium hypochlorite (5% NaOCl) for 5 min to disinfect them from fungi present on the seed coat and then washed with distilled water to remove traces of sodium hypochlorite. Two day old culture is centrifuged (8000 rpm, 10 min) and the pellet obtained was washed twice in saline and coated on the seeds. The trays were incubated for 4 days and checked for seeds sprouting activity

3. Results and Discussion

3.1 Bacterial strains isolation and characteristics

In the present study, isolates from MEC reactor were used for screening the nitrogen fixing capabilities. Out of eleven, five bacterial isolates viz., K7, K8, K9, K11 and K18 were selected for further characterization according to their morphologies and nitrogen fixation ability (Table 1). Selected strains showed various colony morphologies when grown on nutrient agar plates aerobically at 37°C and were also observed to be positive for gram staining. They also showed rod shape morphology and were motile in nature. The gene sequences obtained were used as BLAST queries against the NCBI database with the results indicating that the bacteria isolates were *Bacillus safensis* NBRC 100820 (NR_113945), *Bacillus nealsonii* DSM 15077 (NR_044546), *Bacillus nealsonii* DSM 15077 (NR_044546), *Leifsonia shinsuensis* DB 102 (NR_043663) and *Streptomyces griseoviridis* NBRC 12874 (NR_112313). All the sequences showed 99% similarity in 16S rRNA coding gene sequence with their nearest neighbours (Fig. 1). However, the phylogenetic analysis revealed that the sequences were distantly clustered with their nearest neighbouring species. Further, it was observed that the strains K7, K8 and K9 belonged to phylum *Firmicutes* and strains K11 and K18 belonged to phylum *Actinobacteria*. Apart from this, pair wise comparison of 16S rRNA gene sequences of *Bacillus nealsonii* strains K8 and K9 was done to identify the similarity between them and results showed that only 96% similarity between each other. Difference in 16S rRNA gene sequence is also evidenced in their phenotypic characteristics such as colony morphology and in phosphate solubilization properties. The strains characterized from MEC may be regarded as a safe industrial microorganism as there was no study till date reporting their specific pathogenicity (Lateef et al., 2015; Chauhan et al., 2014; Monteiro-Vitorello et al., 2004; Sharma., 2014)

3.2 Nitrogen Fixation Activity

Nitrogen fixation is the second most important process after photosynthesis which has significant function in crop production. Nitrogen is an essential component of soil and plays an important role in plant growth by forming ammonia or nitrates from atmospheric nitrogen fixation (Kanimozhi and Panneerselvam., 2010). The strains isolated were checked for nitrogen fixing activity, as elemental nitrogen is one of the key element

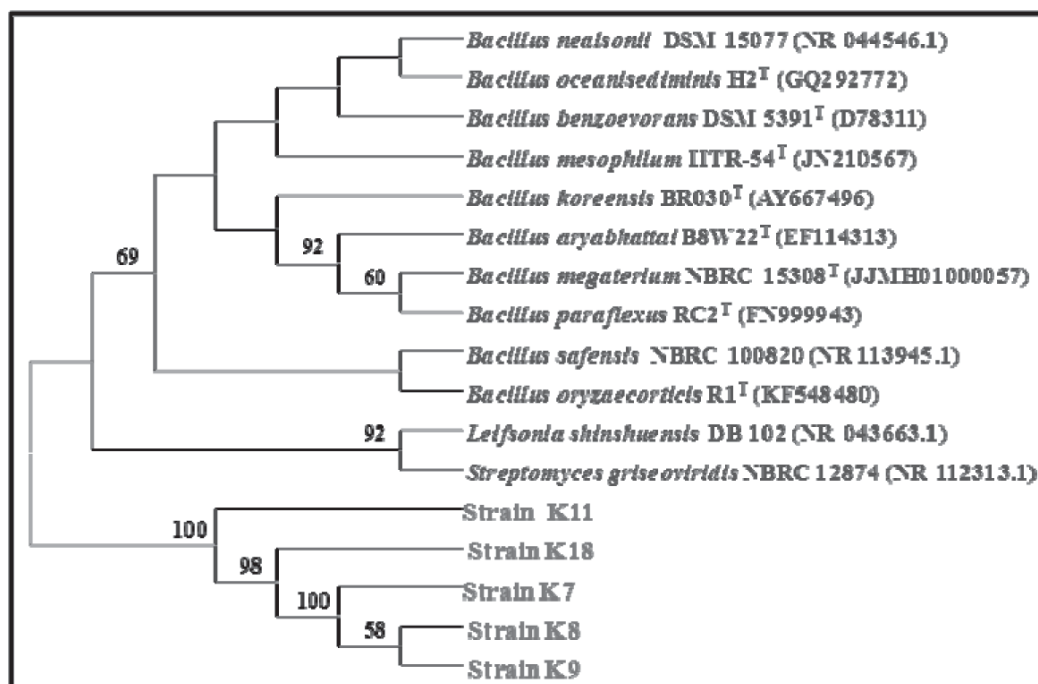


Figure 1: Dendrogram of isolates depicting nearest neighbouring species. strains K7, K8 and K9 belonged to phylum *Firmicutes* and strains K11 and K18 belonged to phylum *Actinobacteria*.

Table 1: Characteristics of the strains isolated from MEC

Isolate	Colony morphology	Gram's stain and Motility	16S rRNA sequence similarity (%)	Nearest neighbour	Taxonomy
K7	Flat irregular margin, opaque beige colored colony	+	99	<i>Bacillus safensis</i> NBRC 100820 (NR_113945)	<i>Firmicutes; Bacilli; Bacillales; Bacillaceae; Bacillus</i>
K8	Big shiny, yellow colored slimy colony	+	99	<i>Bacillus nealsonii</i> strain DSM 15077(NR_044546)	<i>Firmicutes; Bacilli; Bacillales; Bacillaceae; Bacillus</i>
K9	Small pale orange slimy circular colony	+	99	<i>Bacillus nealsonii</i> strain DSM 15077 (NR_044546)	<i>Firmicutes; Bacilli; Bacillales; Bacillaceae; Bacillus</i>
K11	Small slimy, transparent, white colored colony	+	99	<i>Leifsonia shinshuensis</i> DB 102(NR_043663)	<i>Actinobacteria; Actinobacteridae; Actinomycetales; Micrococcineae; Microbacteriaceae; Leifsonia.</i>
K18	Small circular, slimy, orange colored colonies	+	97	<i>Streptomyces griseoviridis</i> NBRC 12874(NR_112313)	<i>Actinobacteria; Actinobacteridae; Actinomycetales; Streptomycineae; Streptomycetaceae; Streptomyces.</i>

of proteins, nucleic acids and other cellular constituents and is the important parameters for the isolate to act as biofertilizer. Despite its abundance in atmosphere, it cannot be directly used by plants because of the high bond energy of nitrogen molecule. In order for nitrogen to be used as nitrogen source, it must be fixed (combined) in the form of ammonium (NH_4) or nitrate (NO_3) ions. Many bacteria and fungi can degrade organic matter or symbiotically fix nitrogen releasing useable nitrogen for reuse by other organisms (Gopalakrishnan et al., 2012; Nagendranatha Reddy et al., 2014).

Defined medium lacking nitrogen source is inoculated with respective cultures and incubated for 48 hrs. Any growth observed is because of the utilization of atmospheric nitrogen as sole nitrogen source. Out of eleven isolates screened for diazotrophy only five isolates depicted growth in the presence of atmospheric nitrogen and showed turbidity in the test tubes which is comparable to the growth in control having NH_4Cl as nitrogen source. Activity and growth of isolates varied with time to other isolates depicting the capabilities of individual strain towards nitrogen fixation. The isolates K7, K18, K8, K11 and K9 followed the order of highest absorbance recorded and all the strains showed gradual increment in the absorbance measure till 48 h depicting the growth of microorganisms by utilizing N_2 from atmosphere. K8, K9 and K11 isolates showed nominal

variation in the absorbance recorded. K18 showed little increment in the OD from the start of operation but K7 showed highest by 48h. Till 24 h, the K18 isolate depicted maximum growth. Ding et al., (2005) stated that almost all the *Bacillus* spp. are able to fix nitrogen from atmosphere.

3.3 IAA Production

IAA, produced by plant for its internal regulation of growth, is one of the most important physiologically active and abundant auxins in plant (Davies, 1995; Shahab et al., 2009). Specific microbes have the capability of producing IAA as secondary metabolite due to rich supply of substrates and it is the common product of L-tryptophan metabolism followed by several microorganisms. All the electrogenic bacterial isolates were screened for their ability to produce plant growth regulator, IAA. Out of the five bacterial strains assayed for IAA production *B. safensis* strain K7 showed red color reaction with Kovac's reagent indicating their ability to produce IAA. It is also demonstrated previously that *B. safensis* has the inherent character of producing IAA which is the indication of beneficial effect by the bacterial isolate on the plant growth stimulation (Kothari et al., 2013) and therefore, termed as plant growth promoting bacteria. About 80% of the soil isolates possess the activity of IAA and vary greatly in their inherent ability to produce IAA. Initially, the tryptophan

is first converted to indole 3-acetamide (IAM) by the enzyme tryptophan-2-monooxygenase followed by conversion of IAM to IAA by an IAM hydrolase. The genes that encode the pathway are *iaaM* and *iaaH* genes respectively. Interactions between IAA-producing bacteria and plants lead to diverse outcomes on the plant side, varying from phytostimulation to productivity (Spaepen et al., 2007).

3.4 Phosphate Solubilisation Activity

One of the essential mineral macronutrients, which are required for maximum yield of agriculturally important crops, is phosphorus. Due to its non-availability in useable form, phosphorus deficiency is a major constraint to crop production. The Phosphate solubilizing bacteria (PSB) have the ability to convert insoluble phosphates into available forms for plant via the process of acidification, chelation, exchange reactions, and production of gluconic acid. PSBs render more phosphates into the soluble form than required for their growth and metabolism by secreting organic acids and/or enzymes, the surplus get the plants (Vessey, 2003). It is possible that bacteria capable of phosphate solubilization may improve plant productivity both by hormonal stimulation and by supplying phosphate.

Qualitative estimation of phosphate solubilization was carried out using different bacterial isolates grown on PVK agar media for determining phosphate solubilizers. All the 5 isolates found to grow on PVK media but could not form halo zone around them except in K9 isolate. The criterion for phosphate solubilizers isolation is based on the formation of a visible halo zone on agar plates. According to deFreitas et al. (1997), good phosphate-solubilizers have the capability of forming halo zones with diameters higher than 15 mm. *B. nealsonii* strain K9 exhibited a halo zone of 6 mm around the colony depicting the frail phosphate solubilisation property. Reports also state that the strain *B. nealsonii* has the capability to solubilize insoluble phosphate in the liquid inoculants (Velineni and Brahmaprakash., 2011).

3.5 Siderophores Activity

Apart from phosphate in available form, iron is also essential for plant growth and for almost all life processes such as respiration and DNA synthesis. Despite being one of the most abundant elements in the Earth's crust, the bioavailability of iron in many environments such as the soil or sea is limited by the very low solubility of the Fe^{3+} ion (Kraemer., 2005). The predominant state of iron in aqueous, non-acidic, oxygenated environments cannot be readily utilized by organisms. Microorganisms utilize various iron uptake systems to secure sufficient supplies from their surroundings. One such kind is siderophores, strongest soluble Fe^{3+} binding agents, which are small and high-affinity iron chelating compounds secreted by microorganisms. Microbes release siderophores to scavenge iron from these mineral phases by formation of soluble Fe^{3+} complexes that can be taken up by transport mechanisms. Production of IAA, siderophores, etc., by microbial isolates varies greatly among different species and strains and depends on the availability of substrate.

Spectrophotometric analysis of the five isolates of the present study showed an absorption area between 350 and 450 nm with a sharp peak at about 400 nm, indicating the production of PVD type siderophores (Fig. 2). The maximum absorbance obtained for the isolate K18 was at 413 nm. The other strain, K7, showed the maximum absorbance between

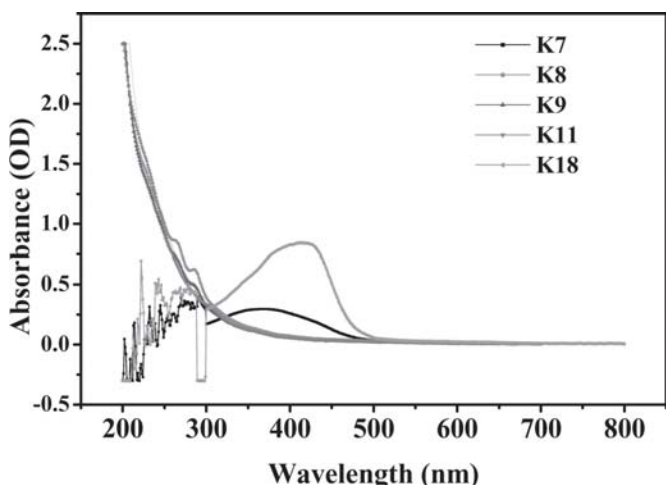


Figure 2: Siderophore activity depicted by K18 and K7 strains with the peaks observed at absorbance 350-450 nm

350 and 450 nm. Early reports supports the siderophore activity of *B. safensis* (Lateef et al., 2015; Kothari et al., 2013) and *S. griseoviridis* (Alam et al., 2012). Under iron deficiency, bacteria synthesize siderophore, which when excreted into extracellular environment, solubilizes and sequester the iron by binding and transport the iron in to the cell via., cell specific receptors recognition present on the outer membrane of the cell (Kraemer., 2005).

3.6 Antifungal Activity

Plants, apart from internal regulation of plant growth promoting substances, also face infections from Fungi thus reducing the yield of the plant and have adverse effects on the plant health. Evidence exist supporting the role of antibiotic activity of many bacterial strains prompting to screen these bacteria for antifungal property. To reduce the fungal infection to seed or to plant, strains that have inherent anti fungal activity have to be screened and applied as spray or as biofertilizer (Kaewchai et al., 2009). It has been reported that enhancement of plant growth characters, resistance to fungal diseases and yield components may be due to ability of soil microorganisms to provide plant by nutritional requirements, plant growth regulates.

Antifungal activity of bacterial isolates involves the usage of their genes, and/or products, such as metabolites, that reduce the negative effects of plant pathogens and promote positive responses by the plant (Couillerot et al., 2013). It has been evaluated by Germination test performed on ground nut seeds. The activity of all the bacterial isolates was evaluated in comparison to control (NaOCl treated). Fine groundnut seeds were soaked and coated with individual bacterial culture pellets and incubated (aseptic conditions) for 4 days. After 2 days of incubation, all the seeds except control were observed to have fungal contamination. But the seeds treated with K18 isolate showed comparatively lower (only one seed) fungal contamination as the strain inherently have antifungal properties. K18 isolate obtained from MEC bioreactor showed antifungal property whereas other bacterial isolates could not show any antifungal property. *Streptomyces griseoviridis* strain K18 exhibited broad-spectrum antifungal activity in vitro. *Streptomyces griseoviridis* is a naturally occurring soil bacteria which secretes various enzymes and metabolites that inhibit pathogen growth. It has been shown to promote the growth and yield of plants even in healthy crops. It is used for the control of damping off, root and stem rot, and wilt caused by *Fusarium* in greenhouse ornamentals and vegetables such as cucumbers, tomatoes and peppers (Jog et al., 2014). Seeds were also evaluated to check the impact of these bacterial isolates on the sprouting activity of seeds. Seeds coated with K18 strain sprouted immediately after 1 day whereas other strains depicted late sprouting activity. The seeds treated with K7, K8, K9 and K11 showed sprouting after 2 days. The antifungal activity of K18 strain inducing the sprouting activity indicates that it might be an ideal plant growth promoting as well as biocontrol agent, for its integrated use in disease and nutrient management strategies.

Overall *in vitro* plant growth promoting activities of all the electrogenically active bacterial isolates from MEC is depicted in Table 2. The data shows that isolates K18 (*S. griseoviridis*), K7 (*B. safensis*) and K9 (*B. nealsonii*) have multifaceted beneficial characteristics. K7 isolate isolated from MEC bioreactor has all the properties that biofertilizer has except the antifungal and phosphate solubilization activity. But, whereas K18 and K9 strains have antifungal and phosphate solubilization activity respectively. With the result obtained, three isolates namely K7, K9 and K18 isolates can be combined and evaluated for better and efficient biofertilizer activity. This gives the scope of developing biofertilizers with mixture of efficient bacteria for all the plant growth promoting towards production of biofertilizer. Due to its ability to protect plants, these isolates should be widely studied and commercially marketed as biopesticides, biofertilizers and soil amendments.

4. Conclusion

Biofertilizer production and application is a sustainable technology which helps to maintain natural soil resources, reduce negative impact on the environment and enhances crop productivity. Present study demonstrates the bio-prospecting of electrogenic bacteria for their ability to be used as biofertilizer and improve soil productivity. Besides nitrogen fixation, isolates exhibited different abilities of plant growth promotion. Hence, based on the demand for required biofertilizer activity, an integrated approach of co-culturing 3 different strains of the present study viz., *B. safensis* strain K7, *B. nealsonii* strain K9 and *S. griseoviridis* strain K18 may be employed to enhance crop yield to significant levels. This concept of co-culturing helps in providing the plant with all the essential growth promoting factors which are difficult to find in a single organism.

Table 2: Overall plant growth promoting activity of Bacterial isolates

Isolate	Phosphate Solubilization	IAA Production	Siderophores	Nitrogen Fixation	Antifungal
K7	-	+	+	+	-
K8	-	-	-	+	-
K9	+	-	-	+	-
K11	-	-	-	+	-
K18	-	-	+	+	+

From the result, it can be also be suggested that different microbiomes can also serve as a potential source for isolating bacteria with plant growth promoting activity apart from soil borne bacteria. This approach of biofertilizer development may reduce the dependence on chemical fertilizers and provides a step forward towards sustainable agriculture.

Acknowledgments

The authors wish to thank The Director, CSIR-IICT for support and encouragement in carrying out this work. The authors greatly acknowledge financial support by CSIR in the form of XII five year network project (SETCA, CSC-0113). CNR and KVK duly acknowledges CSIR, New Delhi for providing research fellowship. KA duly acknowledges DBT for providing research grant (No. BT/Bio-CARE/06/463/2011-12).

References

- Alam, M., Dharni, S., Khaliq, A., Srivatsava, S.K., Samad, A., Gupta, M.K., 2012. A promising strain of *Streptomyces* spp. With agricultural traits for growth promotion and disease management. Indian journal of Experimental biology. 50, 559-568
- Annie modestra, J., Lenin Babu, M., Venkata Mohan, S., 2015. Electro-fermentation of real-field acidogenic spent wash effluents for additional biohydrogen production with simultaneous treatment in a microbial electrolysis cell. Bioresour Technol. 150,308-315
- Chauhan, S., Sharma, P., Puri, N., Gupta, N., 2014. Purification and characterization of an alkali thermostable α mannanase from *Bacillus nealsonii* PN 11 and its application in mannoooligosaccharides preparation having prebiotic potential. Eur Food Res Technol. 238, 927-936
- Chiranjeevi, P., Mohanakrishna, G., Venkata Mohan., 2012. Rhizosphere mediated electrogenesis with the function of anode placement for harnessing bioenergy through CO₂ sequestration. Bioresour Technol. 124, 364-370
- Couillierot, O., Vatsa, p., Loqman, S., Ouhdouch, Y., Jane, H., Renault, J.H., Clement, C., Barka, E.A., 2013. Biocontrol and biofertilizer activities of the *Streptomyces anulatus* S37: an endophytic actinomycete with biocontrol and plant-growth promoting activities. Biological Control of Fungal and Bacterial Plant Pathogens. 86, 271-276
- Davies, P.J., 1995. Plant hormones: physiology, biochemistry, and molecular biology. Kluwer Academic Publishers, London, 6-7
- deFreitas, J.R., Banerjee, M.R., Germida, J.J., 1997. Phosphate solubilizing rhizobacteria enhance the growth and yield but not phosphorus uptake of canola (*Brassica napus* L). Biology Fertility Sols. 24, 358-364
- Ding, Y., Wang, J., Liu, Y., Chen, S., 2005. Isolation and identification of nitrogen-fixing *bacilli* from plant rhizospheres in Beijing region. Journal of Applied Microbiology. 99, 1271-1281
- Fuentes-Ramirez, L.E., Caballero-Mellado, J., 2005. Bacterial biofertilizers. In: Siddiqui ZA, editor. PGPR: biocontrol and biofertilization. The Netherlands: Springer; 143-172.
- Gopalakrishnan, S., Upadhyaya, H.D., Vadlamudi, S., Humayun, P., Sree Vidya, M., Alekha G., Singh, A., Vijayabharathi, R., Bhimineni, R., Seema, M., Rathore, A., Rupela, O., 2012. Plant growth-promoting traits of biocontrol potential bacteria isolated from rice rhizosphere. SpringerPlus 1:71, 1-7
- Hernández-Albiter, R.C., Barrera-Necha, L.L., BautistaBaños, S., Bravo-Luna, L., 2007. Antifungal Potential of Crude Plant Extracts on Conidial Germination of Two Isolates of *Colletotrichum gloeosporioides* (Penz.) Penz. and Sacc. Revista Mexicana de Fitopatología. 25,180-185
- Ines, M., Amel, K., Yousra, T., Neila, S., Imen, D., Marie, M.J., Abdennasseur, H., 2012. Effect of Dose-Response of Zinc and Manganese on Siderophores Production. American Journal of Environmental Sciences. 8, 143-151
- Jensen. H. L., 1942. Pro Line Soc. N.S.W., 57,205-212.
- Jog, R., Pandya, M., Naresh Kumar, G, Raj Kumar, S., 2014. Mechanism of phosphate solubilization and antifungal activity of *Streptomyces* spp. isolated from wheat roots and rhizosphere and their application in improving plant growth. Microbiology.160, 778-788
- Kaewchai, S., Soyong, K., Hyde, K.D., 2009. Mycofungicides and fungal biofertilizers. Fungal Diversity. 38, 25- 50
- Kanimozhi, K., and Pannerseelvam, A., 2010. Studies on isolation and nitrogen fixation ability of *Azospirillum* spp. isolated from Thanjavur district. Pelagia Research Library Der Chemica Sinica, 1, 138-145
- Kannaiah Goud, R., Veer Raghavulu, S., Mohana Krishna, G., Naresh, K., Venkata Mohan, S., 2012. Predominance of *bacilli* and *clostridia* in microbial community of biohydrogen producing biofilm sustained under diverse acidogenic conditions. International journal of Hydrogen Energy. 37, 4068-4076
- Kannaiah goud, R., Venkata Mohan, S., 2013. Prolonged applied potential to anode facilitate selective enrichment of bio-electrochemically active *Proteobacteria* for mediating electron transfer: Microbial dynamics and bio-catalytic analysis Bioresour Technol. 137, 160-170
- Khan, M.S., Zaidi, A., Musarrat, J., 2009. Microbes in Sustainable Agriculture, Nova Science Publishers, New York, USA
- Kothari, V.V., Kothari, R.K., Kothari, C.R., Bhatt, V.D., Nathani, N.M., Koringa, P.G., Joshi, C.G., Vyas, B.R.M., 2013. Genome sequence of salt-tolerant *Bacillus safensis* strain VK, isolated from saline desert area of Gujarat, India. Genome Announc. 1(5):e00671-13. doi:10.1128/genomeA.00671-13
- Kraemer, S.M., 2005. Iron oxide dissolution and solubility in the presence of siderophores. Aquatic Science. 66, 3-18
- Lane, D.J., 1991. 16S/23S rRNA 276 sequencing. In Nucleic Acid Techniques in Bacterial Systematics. pp 115-175. Edited by E. Stackebrandt & M. Good Fellow. Chichester: Wiley.
- Lateef, A., Adelere, I.A., Kana, E.B.G., 2015. The biology and potential biotechnological applications of *Bacillus safensis*. Biologia. 70, 411-419
- Mohammadi, K., Sohrabi, Y., 2012. Bacterial biofertilizers for sustainable crop production: A review. ARPN Journal of Agricultural and Biological Science. 7,307-316
- Mohite, B., 2013. Isolation and characterization of indole acetic acid (IAA) producing bacteria from rhizospheric soil and its effect on plant growth. J. Soil Sci. Plant Nutr. 13, 638-649
- Monteiro-Vitorello, C.B, Camargo, L.E., Van Sluys, M.A., Kitajima, J.P., Truffi, D., do Amaral, A.M., Harakava, R., de Oliveira, J.C., Wood, D., de Oliveira, M.C., Miyaki, C., Takita, M.A., da Silva, A.C., Furlan, L.R., Carraro, D.M., Camarotte, G., Almeida, N.F.Jr., Carrer, H., Coutinho, L.L., El-Dorry, H.A., Ferro, M.I., Gagliardi, P.R., Giglioti, E., Goldman, M.H., Goldman, G.H., Kimura, E.T., Ferro, E.S., Kuramae, E.E., Lemos, E.G., Lemos, M.V., Mauro, S.M., Machado, M.A., Marino, C.L., Menck, C.F., Nunes, L.R., Oliveira, R.C., Pereira, G.G., Siqueira, W., de Souza, A.A., Tsai, S.M., Zanca, A.S., Simpson, A.J., Brumbley, S.M., Setúbal, J.C., 2004. The genome sequence of the gram-positive sugarcane pathogen *Leifsonia xyli* subsp. *Xyli*. Mol Plant Microbe Interact. 17, 827-36.
- Nagendranatha Reddy, C., Naresh Kumar, A., Annie Modestra, J., Venkata Mohan, S., 2014. Induction of anoxic microenvironment in multi-phase metabolic shift strategy during periodic discontinuous batch mode operation enhances treatment of azo dye wastewater. Bioresour. Technol. 165, 241-249.
- Nguyen, C., Tan, W., Le, T.F., 1992. Genetic variability phosphate-solubilizing activity of the ectomycorrhizal fungus *Laccaria bicolor* (Maire) P.D. Orton. Plant Soil, 143 193-199
- Perez, E., M. Sulbarán, M. M. Ball and L. A. Yarzabal. 2007. Isolation and characterization of mineral phosphate-solubilizing bacteria naturally colonizing a limonitic crust in the southeastern Venezuelan region. Soil Biol. Biochem. 39:2905-2914
- Pikovskaya, R.I., 1948. Mobilization of phosphorus in soil in connection with the vital activity of some microbial species. Mikrobiologiya 17.
- Puente, M.E., Bashan, Y., Li, C. Y., Lebsky, V.K., 2004. Microbial populations and activities in the rhizoplane of rock weathering desert plants root colonization and weathering of igneous rocks. Plant Biol. 6,629-642.
- Rajasulochana, P., Krishnamoorthy, P., 2014. Marine algae for agricultural sector for high yield. Journal of Chemical and Pharmaceutical Sciences. 7, 369-372.
- Shahab, S., Ahmed, N., Khan, N.S., 2009. Indole acetic acid production and enhanced plant growth promotion by indigenous PSBs. African Journal of Agricultural Research. 4,1312-1316
- Sharma, M., 2014. Actinomycetes: Source, Identification, and Their Application. Int.J.Curr.Microbiol.App.Sci. 3, 801-832
- Spaepen, S., Vanderleyden, J., Remans, R., 2007. Indole-3-acetic acid in microbial and microorganism-plant signalling. FEMS Microbiol Rev. 31, 425-48
- Tamura, K., Dudley, J., Nei, M., Kumar, S., 2007. MEGA4: Molecular Evolutionary Genetics Analysis (MEGA) software version 4.0. *Mol Biol Evol* . 24, 1596-1599.
- Velineni, S., Brahmaprakash, G.P., 2011. Survival and Phosphate Solubilizing Ability of *Bacillus megaterium* in Liquid Inoculants under High Temperature and Desiccation Stress. J. Agr. Sci. Tech. 13, 795-802
- Venkata Mohan, S., Babu, V.L., Sarma, P.N., 2007. Anaerobic biohydrogen production from dairy wastewater treatment in sequencing batch reactor (AnSBR): Effect of organic loading rate. Enzyme Microb. Technol., 41, 506-515
- Venkata Mohan, S., Lenin babu, M., 2011. Dehydrogenase activity in association with poised potential during biohydrogen production in single chamber microbial electrolysis cell. Bioresour technol. 102,8457-8465
- Vessey, J.K., 2003. Plant growth promoting rhizobacteria as biofertilizers. Plant and Soil. 255, 571-586



Catalytic Hydrolysis of Cotton Stalk Biomass Using a Reusable Solid Carbon Acid Catalyst

Mandavi Goswami^a, S. Meena^a, S. Navatha^b, R.B.N. Prasad^b, B.L.A. Prabhavathi Devi^b, Rajeev Kumar Sukumaran^a, Ashok Pandey^{a*}

^aCentre for Biofuels, Biotechnology Division, CSIR-National Institute for Interdisciplinary Science and Technology, Trivandrum-695 019, India

^bCentre for Lipid Research, CSIR-Indian Institute of Chemical Technology, Hyderabad 500 007, India

ARTICLE INFO

Received : 31 August 2015
Revised : 30 September 2015
Accepted : 10 October 2015

Keywords:

cotton stalk, solid acid catalyst, carbonaceous acid catalyst, biomass hydrolysis, sulfonation, bioethanol

ABSTRACT

The aim of this work was to evaluate a glycerol-based carbon acid catalyst for the hydrolysis of acid and alkali pre-treated and cotton stalk when it released 23 and 67mg/g of total reducing sugars respectively on reaction at 160 °C for 6h with a biomass to catalyst ratio of 1:0.5. Increase in biomass to catalyst ratio resulted in a doubling of sugar yield. Optimization of the conditions for hydrolysis using a response surface method resulted in further increase of sugar yield from the alkali treated cotton stalk to 179mg/g, which corresponded to 21.01% conversion of sugar polymers. The catalyst could be reused albeit with some loss of efficiency. Catalytic hydrolysate of cotton stalk was fermented to alcohol with 41 % efficiency. Results demonstrated the potential use of the catalyst in biomass hydrolysis to generate fermentable sugars for bioethanol production.

© 2016 ISEES, All rights reserved

1. Introduction

Solid acid catalysts show unique advantages in the hydrolysis of lignocellulosic biomass. Various solid acid catalysts such as carbon acid catalysts, resins, metal oxides, zeolites, and others have been explored as potential heterogeneous catalysts for this purpose (Guo et al., 2012; Huang and Fu, 2013). The use of solid acid catalysts may address some of the challenges in biomass conversion to fermentable sugars due to their reusability and easy separation of sugars from reaction mixtures (Goswami et al., 2015).

The hydrolysis of lignocellulosic biomass is usually carried out using either acid or enzymes (Gustsch et al., 2012; Lee and Jeffries, 2011). The use of concentrated mineral acids is efficient at high temperature (170–240°C), but controlling the further degradation of monomers, corrosion and generation of large amounts of acid wastewater are the major drawbacks of acid hydrolysis (Taherzadeh and Karimi, 2007). In the enzymatic hydrolysis, the notable disadvantages include low activity, high cost of enzymes and separation issues restricting reusability.

The development of new, green and economical process (es) for the conversion of lignocellulosic biomass into glucose and xylose under mild conditions with high selectivity is therefore highly desired. Solid acid catalysts, which have favorable characteristics such as efficient activity, high selectivity, longer life and easiness in recovery and reuse, have great potential for efficiently transforming lignocellulosic biomass into biofuels

and could replace many conventional liquid acids for hydrolysis and pre-treatment. Recently, solid acid-catalyzed hydrolysis has attracted increasing attention with several types of solid acid catalysts being reported (Huang and Fu, 2013).

Carbonaceous solid acid catalysts (CSAC) are by far, considered as the most promising catalysts for cellulose hydrolysis, since they provide good access of reactants to the acidic sites of SO₃H groups and offers different reactive moieties on the graphene like structure which can participate in reaction or form bonds with the carbohydrate polymers aiding in the hydrolysis (Pang et al., 2010; Guo et al, 2012; Hara, 2015). While upto 75 % glucose yield has been obtained with sulfonated carbon catalyst (Pang et al., 2010), majority of the studies have used pure cellulose as the model substrate for hydrolysis and not lignocellulosic biomass. The behavior of catalyst with a lignocellulosic substrate can be entirely different from when cellulose is used. The major challenges for a catalytic process include low cellulose/liquid ratios (as low as 1:100) and the inability to convert the lignin.

Use of a glycerol-based solid carbon acid catalyst was previously demonstrated for acid catalyzed biodiesel production (Prabhavathi Devi et al., 2009), and later in the hydrolysis of rice straw (Goswami et al, 2015). In the current study the catalyst was evaluated for hydrolysis of Cotton stalk (CS), which is a post harvest residue generated in significant quantities in several countries and which is particularly resistant to enzymatic hydrolysis.

* Corresponding Author: pandey@niist.res.in; ashokpandey56@yahoo.co.in

2. Materials and methods

2.1. Carbon acid catalyst, biomass and pretreatment

The glycerol based solid carbon acid catalyst was synthesized at CSIR-IICT as previously described (Prabhavathi Devi et al., 2009). Cotton stalk (CS) was a kind gift from Reliance Industries, Mumbai, India. Cotton stalk was knife milled and sieved to a maximum particle size of 2 mm. The milled biomass was pretreated using dilute alkali (4% w/v NaOH at 120 °C for 60 min), or dilute acid (2.5 % w/v H₂SO₄ at 120°C for 60 min). The biomass loading was 15% (w/w). After autoclaving, the biomass slurry was neutralized by either 10 N H₂SO₄ or 10N NaOH followed by water wash. Pretreated materials were sun dried and stored in air tight containers until used. The compositional analysis of native and pretreated rice straw (RS) was carried out by the two stage acid hydrolysis protocol which was developed by National Renewable Energy Laboratory (Ruiz and Ehrman, 1996).

2.2. Hydrolysis of cotton stalk using the carbon acid catalyst

Catalytic hydrolysis was carried out as described by Goswami et al (2015). Hydrolysis was performed in acid digestion bombs having Teflon inserts. Specified quantity of feed stock and catalyst were mixed together and were placed inside the Teflon container inside the bomb and the lids were screwed in to seal the container. The bombs were heated to required temperature in a hot air oven and were held at that temperature for the specified duration. After completion of the reaction, the bombs were allowed to cool and then the hydrolysate was recovered after addition of enough water to make up the volume to 25ml. The contents were then centrifuged at 6000 x g for 10 min to separate the debris. The supernatant was recovered and analyzed for the presence of total reducing sugars by DNS method (Miller 1959) and individual sugars by HPLC (Sluiter et al, 2008) method and used for fermentation for ethanol production.

2.3. Optimization of the catalytic hydrolysis of cotton stalk

A response surface Box-Behnken design (Box and Behnken, 1960) was used for optimizing the hydrolysis of alkali pretreated cotton stalk. Biomass to catalytic ratio was kept constant at 1:1 and 0.2% Tween 80 was added into the reaction mixture for all experimental runs. The parameters studied were biomass loading (2, 4 and 6 % w/v), Temperature (160, 180 and 200 °C) and reaction time (4, 5 and 6h) and combinations of these parameters as per the experimental design matrix generated using Design Expert v 8.05 (Statease Inc, USA) were evaluated experimentally. The design matrix which included a total of 17 runs with four replicates of the midpoint is given in Table 2. The model constructed as a response function of the variables on sugar yield was a second order polynomial as follows:

$$Y = \beta_0 + \sum_{i=1}^n \beta_i X_i + \sum_{i=1}^n \beta_{ii} X_i^2 + \sum_{i=1}^n \sum_{j=1}^n \beta_{ij} X_i X_j + \epsilon$$

Where, Y is the predicted response; \hat{a}_0 is the offset term; \hat{a}_i is the linear effect; \hat{a}_{ii} is the squared effect, \hat{a}_{ij} is the interaction effect, X_i and X_j are coded terms for independent variables under study and ϵ is the error factor. Regression analysis and estimation of the coefficients were performed using Design Expert software. Three dimensional response surfaces were generated using the software. The ideal levels and combinations of parameters were identified by numerical optimization functions in the Design Expert software and were experimentally validated.

2.4. Catalyst Reusability

The reusability study was studied with 6% (w/w) of biomass loading and 100% (w/w) of catalyst loading at a temperature of 160 °C for 4 h. The supernatant containing sugars were separated by centrifugation after the first cycle. The slurry containing undigested biomass and catalyst was suspended in excess volume of water and was mixed in a vortex mixer. The suspension was allowed to stand for few minutes when the catalyst settled down. It was collected by decanting the top layer and the process was repeated to remove all the undigested material. The catalyst was then given a water wash followed by methanol wash and was used for the next cycle as above. Amount of sugar released was monitored for each cycle and the efficiency was expressed as percentage of sugar yield in the first cycle which was taken as 100%.

2.5. Fermentation

A preliminary evaluation of the fermentation of catalytic hydrolysate of cotton stalk was performed with hydrolysate concentrated to a glucose concentration of 22.8 g/L by vacuum centrifugation. Enzymatic hydrolysate of CS with a glucose concentration of 120g/L was generated using commercial cellulase and its fermentation was performed parallel to that of the catalytic hydrolysate under similar conditions for comparison. The hydrolysates were supplemented with yeast extract (0.25%), (NH₄)₂SO₄ (0.5%), MgSO₄·7H₂O (0.1%), KH₂PO₄ (0.2%) and pH was adjusted to 5.0. The hydrolysates were inoculated with *Saccharomyces cerevisiae* NCIM 3059 at a concentration of 5.0mg dry cells/ml and were incubated at 30 °C for 36h. Alcohol estimation was performed by NREL method (Templeton, 1994).

3. Results and Discussion

3.1. Hydrolysis of pretreated cotton stalk

The hydrolysis acid or alkali pretreated cotton stalk (CS) was performed using a biomass to catalyst ratio of 1:0.5 at 140 °C for 4h. Control experiments were performed with just biomass and no catalyst under the same conditions. The results presented in Table 1 indicated that alkali pretreated CS was hydrolyzed more efficiently by the solid acid catalyst compared to the acid pretreated CS. The sugar yields were 67.78 mg/g and 23 mg/g respectively for alkali and acid pretreated CS. These represented 4.1 and 7.9 % of the theoretical maximum conversion of available polysaccharides since the cellulose and hemicellulose content of native, acid pretreated and alkali pretreated CS were 33.88 and 23.93 %, 46.23 and 4.21 % and 59.4 and 17.3 % respectively. Carbonaceous solid acid catalysts (CSACs) are considered as highly efficient among heterogeneous catalysts for biomass hydrolysis and efficiencies as high as 65% has been reported for lignocellulose (milled bagasse) hydrolysis (Namchot et al, 2014). Previously we had reported 31% conversion

Table 1: Catalytic hydrolysis of native, acid and alkali pretreated cotton stalk

Biomass Type	Biomass Loading (% w/v)	Catalyst (% of Biomass)	Temp (°C)	Time (h)	Sugar Yield (mg/g)
Acid	5	*	140	4	6.88
Alkali	5	*	140	4	3.94
Acid	5	50	140	4	23.00
Alkali	5	50	140	4	67.78

* Without catalyst

Table 2: Box Behnken design matrix for optimization of catalytic hydrolysis of cotton stalk with responses for experimental runs

Run	(A)Biomass Loading (% w/w)	(B)Temp (°C)	(C) Time (h)	Sugar Yield (mg/g)
1	4	200	4	13.06
2	4	200	6	23.67
3	6	180	6	53.44
4	4	180	5	73.15
5	6	180	4	179.46
6	4	180	5	99.87
7	6	160	5	144.10
8	4	180	5	55.12
9	4	160	4	155.83
10	4	180	5	67.13
11	4	180	5	28.86
12	2	180	4	87.58
13	2	200	5	21.39
14	4	160	6	137.67
15	2	180	6	47.58
16	2	160	5	71.70
17	6	200	5	20.48

Table 3: Analysis of variance (ANOVA) for the response surface quadratic model

Source	Sum of Squares	DF	Mean Square	F Value	p-value
Model	36284	9	4032	4.2	0.037
A-Biomass Loading	3580	1	3580	3.7	0.096
B-Temperature	23188	1	23188	24.0	0.002
C-Time	3766	1	3766	3.9	0.089
AB	1344	1	1344	1.4	0.277
AC	1850	1	1850	1.9	0.209
BC	207	1	207	0.2	0.658
A ²	86	1	86	0.1	0.774
B ²	102	1	102	0.1	0.754
C ²	2163	1	2163	2.2	0.179
Residual	6773	7	968		
Lack of Fit	4083	3	1361	2.0	0.253
Pure Error	2690	4	673		
Cor Total	43058	16			

Table 4: Validation of conditions

Biomass (%)	Temp (°C)	Time (h)	Predicted (mg/g)	Experimental (mg/g)
6	160	5.0	150.29	144.0
6	140	4.0	225.82	155.0
6	160	4.9	151.80	139.0

Correlation coefficient: 0.9467

efficiency for alkali pretreated rice straw with the same catalyst (Goswami et al, 2015) but in that study the biomass to catalyst ratio used was 1:1. So an increased catalyst ration of 1:1 was evaluated for cotton stalk hydrolysis which improved the sugar yield to 14.46% (123.32 mg/g). It was therefore decided to optimize the hydrolysis conditions for the alkali pretreated CS so as to further improve the sugar yields.

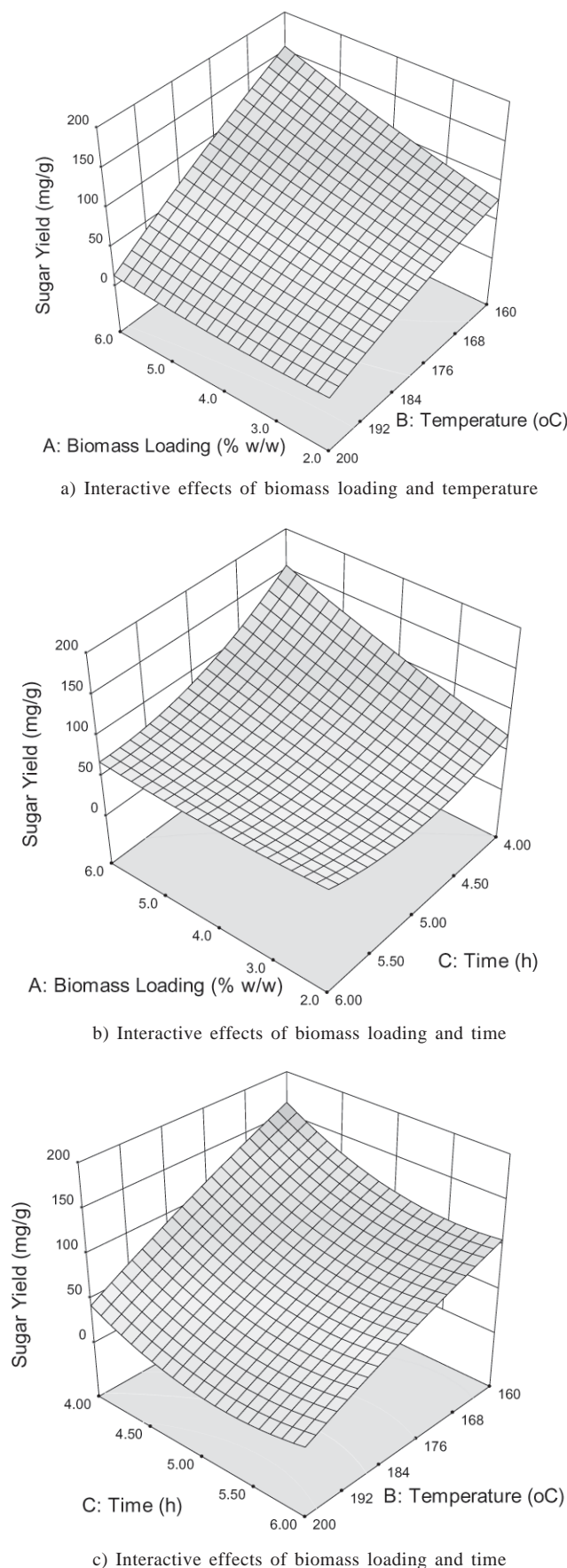
3.2. Optimization of the hydrolysis of alkali prtreated CS

Optimization of the parameters affecting total reducing sugar yield in the catalytic hydrolysis of cotton stalk (CS) was studied by following a response surface Box-Behnken design (Box and Behnken, 1960). The parameters studied were biomass loading, temperature of treatment and retention/holding time. Biomass to catalyst ratio was kept constant at 1:1 and 0. 2% w/v Tween 80 was also used in the hydrolysis experiments. Table 2 shows the experimental design matrix and the sugar yields obtained.

$$Y = 64.83 + 21.15A - 53.84B - 21.7C - 18.33AB - 21.51AC + 7.19BC + 4.52A^2 - 4.93B^2 + 22.66C^2$$

The maximum sugar yield obtained (179.46 mg/g, 21.01% conversion efficiency) was for run number 5 which used 6 % biomass loading and a time and temperature of 4h and 180 °C respectively. The data was analyzed by multiple regression analysis and the regression coefficients were determined. A second order polynomial equation (equation 1) was derived to represent the sugar yield as a function of the independent variables tested.

Where Y is the predicted sugar yield, and A, B and C are coded values of biomass loading, temperature and time respectively. The adequacy of the model was tested by Fischer's statistical test for the analysis of variance (ANOVA) using design expert software and the results are shown in Table 3. ANOVA suggested that the model was significant with a p value of 0.04 and an F value of 4.17. The only parameter with statistically significant effect was temperature with a p value of 0.0018 and none of the interactions had significant effects on sugar yield. Nevertheless all interactions had p values less than 1.0 indicating that these were not insignificant and hence their analyses were performed by plotting response surface curves. Figure 1a-c represent the response surfaces obtained for interaction effects of parameters tested. Increase in temperature had a negative impact on sugar yield at all the biomass loadings evaluated. However, the effect was more pronounced at higher biomass loadings (Fig 1a). Similarly, regardless of the temperature of hydrolysis higher sugar yields were obtained at higher biomass loadings. Increase in sugar yields with increase of biomass loadings can be attributed to the higher content of sugar polymer per unit reaction volume. Rapid decrease in

Figure 1: Response Surface Plots showing interactive effect of parameters on sugar yields for catalytic hydrolysis of cotton stalk

sugar yields with increase in temperature from 160 -200°C could be due to the increase degradation of the sugars released at high temperature.

Longer holding times at elevated temperatures can result in sugar degradation and this was evident at higher and lower biomass loadings. The decrease in sugar yield with increase in reaction time was more pronounced at higher biomass loadings (Fig 1b). This was also evident in the response surface of reaction time vs temperature, where again the highest sugar yields were obtained at lower temperature and lower reaction time (Fig 1c). The results indicated that the best conditions for maximal sugar yield were a biomass loading closer to 6.0 %, temperature near 160 °C and a reaction time of approximately 4h. Repetition of the experiment for run number 5 could result in a sugar yield of 219mg/g (25.67 %).

The numerical optimization function in Design Expert was used to predict the optimal conditions for maximal sugar production. Three randomly selected solutions and their predicted and experimental responses (sugar yields) are given in Table 4. A correlation analysis of the experimental and predicted response gave a value of 0.9467 for correlation coefficient validating the model. Nevertheless, the maximum yield was only 155mg/g (18.17%) against the predicted yield of 225.82mg/g (26.87%).

3.3. Catalyst hydrolyzes hemicellulose more efficiently

HPLC analysis of the hydrolysate indicated that the catalyst liberated more of hemicellulose derived sugars than glucose. The glucose and xylose concentrations in the hydrolysates of alkali pretreated cotton stalk were 4.07mg/ml (101.75mg/g) and 4.63 mg/ml (115.75 mg/g) respectively, which corresponded to conversion efficiencies of 15 % and 60 % respectively of cellulose and hemicellulose. Better efficiency in hydrolysis of hemicellulose by the catalyst was confirmed by hydrolysis of pure cellulose and hemicellulose using the catalyst. Experiments performed with microcrystalline cellulose and xylan independently under same conditions, resulted in sugar yields of 17.5mg/g (1.75%) and 850.1% (85 %) demonstrating the highly efficient hydrolysis of hemicellulose by the catalyst. Hydrolysis of native cotton stalk however resulted only in 17% and 21 % conversion of cellulose and hemicellulose respectively which indicated the possible inhibition of reaction by presence of lignin. Alkali pretreatment which removes lignin therefore was a better pretreatment option for catalytic hydrolysis as was evident from the hydrolysis results in Table 1.

3.4. Reusability of catalyst

Studies were made on the catalyst separation and its reusability. After first cycle of hydrolysis, the catalyst was recovered by filtration and washed with distilled water, followed by methanol washing. This was used for the second and subsequently after similar treatment for the third batch of the hydrolysis. The results showed good stability of the catalyst after second cycle with ~ 85% of the original hydrolysis ability retained while in the third cycles it was reduced to ~60%. Previously we had reported the repeated reusability of the same catalyst for hydrolysis of rice straw (Goswami et al., 2015). The loss in efficiency on reuse in this case might be due to the use of a higher temperature at which leaching of the sulfonyl groups might have occurred. Increase in the water to solids ratio could also negatively affect the acidity and catalytic activity. Reusability is the major advantage of solid acid catalysts since it reduces pollution and lower the operation costs (Guo et al., 2012). It is speculated that the optimization of these parameters might address the reduced yield and loss of efficiency in repeated re-use.

3.5. Fermentability of catalytic hydrolysate

A preliminary evaluation of the fermentation of catalytic hydrolysate of cotton stalk was performed with hydrolysate concentrated to a glucose concentration of 22.8 g/L by vacuum centrifugation. Enzymatic hydrolysate of CS with a glucose concentration of 120g/L was generated using commercial cellulase and its fermentation was performed parallel to that of the catalytic hydrolysate under similar conditions for comparison. Maximum ethanol yield obtained for catalytic hydrolysate of cotton stalk was 0.6% v/v which was 41 % of the theoretical maximum based on initial glucose concentration. In comparison, the maximum ethanol yield from enzymatic hydrolysates was 59.2 % indicating that the catalytic hydrolysate could have had some inhibitors which also were concentrated

along with the sugars. Cotton stalk contains relatively higher amounts of lignin (~35%) compared to other feedstock and also it contains other resins and tannins etc (~5.4 % extractives) which makes it a difficult substrate to hydrolyze. Apparently, better methods of pretreatment which can remove these components efficiently may improve both the hydrolysis and fermentation of this feedstock.

4. Conclusions

Glycerol based carbon acid catalyst hydrolyzed alkali treated cotton stalk with an efficiency of 7.9% at a biomass to catalyst ratio of 1:0.5. Increase in the biomass to catalyst ratio to 1:1 doubled the sugar yield and efficiency (14.46%). Optimization of hydrolysis conditions using response surface method resulted in the improvement of sugar yield to 179.46 mg/g (21.04). Results validated by random experiments at predicted conditions gave a correlation coefficient of 0.94 indicating the validity of the model used. The catalyst could be reused without much loss of activity for second cycle, but there was significant activity loss after the second cycle and the efficiency was only 60% during third cycle. Catalytic hydrolysate of the cotton stalk was fermented with 41 % efficiency, which although was less compared to enzymatic hydrolysate (59.2% efficiency). It could be concluded that the catalyst held promise in the hydrolysis of lignocellulosic biomass.

Acknowledgements

Authors would like to acknowledge financial support from Department of Science and Technology, Government of India to ICT and NIIST in the form of Project Grant-DST/TSG/AF/2011/90-G. We thank Dr Swaroop Sarangan, VP, R&D, Reliance Industries Ltd, Mumbai for the kind supply of cotton stalk used in this work.

References

1. Box, G. E. P., Behnken, D. W. 1960. Some new three level designs for the study of quantitative variables. *Technometrics*, 2: 455–475.
2. Goswami, M., Meena, S., Navatha, S., Prasanna Rani, K.N., Pandey, A., Sukumaran, R.K., Prasad, R.B.N., Prabhavathi Devi, B.L.A., 2015. Hydrolysis of biomass using a reusable solid carbon acid catalyst and fermentation of the catalytic hydrolysate to ethanol. *Bioresour. Technol.* 188: 99–102.
3. Guo, F., Fang, Z., Xu, C. C., Smith, R. L. 2012. Solid acid mediated hydrolysis of biomass for producing biofuels. *Prog. Energy Combust. Sci.* 38(5): 672-690.
4. Gütsch, J.S., Nousiainen, T., Sixta, H., 2012. Comparative evaluation of autohydrolysis and acid-catalyzed hydrolysis of *Eucalyptus globulus* wood. *Bioresour. Technol.* 2012. 109:77-85.
5. Hara, M., Nakajima, K., Kamata, K. 2015. Recent progress in the development of solid catalysts for biomass conversion into high value-added chemicals. *Sci. Technol. Adv. Mater.* 16(3): 034903-034924.
6. Huang, Y. B., Fu, Y. 2013. Hydrolysis of cellulose to glucose by solid acid catalysts. *Green Chem.* 15(5): 1095-1111.
7. Lee, J.W., Jeffries, T.W., 2011. Efficiencies of acid catalysts in the hydrolysis of lignocellulosic biomass over a range of combined severity factors. *Bioresour. Technol.* 102(10): 5884-90.
8. Miller, G. L., 1959. Use of dinitrosalicylic acid reagent for determination of reducing sugar. *Anal. Chem.* 31(3):426-8.
9. Namchot, W., Panyacharay, N., Jonglertjunya, W., Sakdaronnarong, C. 2014. Hydrolysis of delignified sugarcane bagasse using hydrothermal technique catalyzed by carbonaceous acid catalysts. *Fuel* 116: 608–616.
10. Pang, J.F., Wang, A.Q., Zheng, M.Y., Zhang, T., 2010. Catalytic Hydrogenation of Corn Stalk to Ethylene Glycol and 1,2-Propylene Glycol. *Chem. Commun.* 46, 6935–6937.
11. Prabhavathi Devi, B.L.A., Gangadhar, K.N., Sai Prasad, P.S., Jagannadh, B., Prasad, R.B.N., 2009. Glycerol-based carbon catalyst for the Preparation of Biodiesel. *Chem. Sus. Chem.*, 2(7): 617-620.
12. Ruiz, R., Ehrman, T. 1996. Determination of Carbohydrates in Biomass by High Performance Liquid Chromatography. National Renewable Energy Laboratory, Laboratory Analytical Procedure #002, Revision 12/08/1996.
13. Sluiter, A., Hames, B., Ruiz, R., Scarlata, C., Sluiter, J., Templeton, D. 2008. Determination of Sugars, Byproducts, and Degradation Products in Liquid Fraction Process Samples, NREL Technical Report-NREL/TO-510-42623, January 2008.
14. Taberzadeh, M.J., Karimi, K. 2007. Enzyme based hydrolysis process for ethanol from lignocellulosic materials: A review. *Bioresour. Com.* 2 (4): 707-738.
15. Templeton, D.W. 1994. Determination of ethanol concentration in biomass to ethanol fermentation supernatants by gas chromatography. National Renewable Energy Laboratory. Laboratory Analytical Procedure #011, Revision 05/05/1994.



Evolution, Trends and Applications of Endoscopy in Internal Combustion Engines

Avinash Kumar Agarwal*, Akhilendra Pratap Singh, Anuj Agarwal

Engine Research Laboratory, Department of Mechanical Engineering, Indian Institute of Technology Kanpur, Kanpur-208016, India

ARTICLE INFO

Received : 17 July 2015
Revised : 13 September 2015
Accepted : 22 September 2015

Keywords:

Endoscopy;
Combustion visualization;
Fuel spray;
Temperature distribution;
Soot distribution.

ABSTRACT

Due to increasing number of alternative fuels and strict emission norms globally, extensive experimental investigations are being conducted for understanding and improving fuel sprays and combustion of internal combustion (IC) engines. Main objective of this study is to assess the effect of advanced fuel injection equipment (FIE) and in-cylinder processes to improve efficiency and reduce pollutant emissions, in addition to improved understanding of combustion and pollutant formation mechanisms. In order to gain understanding of actual combustion processes and spray characteristics in production grade engines, researchers have developed various optical diagnostic techniques. Endoscopic optical visualization technique is a very effective and relatively cheaper but very challenging technique with great potential amongst them. This paper presents a summary of evolution of endoscopic optical visualization technique for analyzing spray and combustion characteristics in IC engines, current trends in engine endoscopy and some application case studies. This endoscopic technique has great scope in research and development activities for automotive industry.

© 2016 ISEES, All rights reserved

1. Introduction

Internal combustion (IC) engines are the most common power plants used in automotive systems such as cars, trucks, boats, ships, trains, as well as stationary power generating machines, earth moving equipment, construction machines and agricultural equipment. It is impossible to imagine modern transportation system without IC engines, as on today. Fuel economy and stringent emission norms are the major challenges being faced by automotive sector worldwide. In recent years, the urge for developing high engine power output with superior fuel economy and lower emissions from IC engines has increased tremendously. To satisfy these requirements and complying with contemporary stringent emission legislations, more effective and environmentally-friendly combustion systems have to be designed and manufactured. Therefore automotive industry is making research and development efforts to meet these challenges. Diesel engines are becoming increasingly popular because they offer greater thermal efficiency and are rugged in nature compared to their gasoline counterparts however a major concern with diesel-powered vehicles is relatively higher level of pollution, that they emit. Diesel engines are a source of two major pollutants; oxides of nitrogen (NOx) and particulate matter (PM) [Pierpont et al., 1995]. NOx contribute towards acid rain and ground-level ozone formation, whereas PM leads to major health hazards by penetrating deep into human lungs. To reduce such harmful emissions, some engine designer favor exhaust gas after-treatment, while others prefer more sophisticated fuel-injection system modifications and control of pollutants in the formation stage itself.

Improvements using these techniques were adequate to meet emission legislations upto Euro-IV however they are grossly inadequate to meet prevailing global emission legislations of Euro-V and above. Emission norms upto Euro-IV could be complied by combustion optimization and/ or by employing less expensive exhaust gas after-treatment methods. For achieving emission norms beyond Euro-IV, automotive industry has to consider expensive and more complex after-treatment technologies such as diesel oxidation catalysts (DOC), diesel particulate filters (DPF), selective catalytic reduction (SCR), lean NOx traps (LNT), etc. along with very efficient in-cylinder combustion control. However, the most effective way still remains is reducing the bulk emissions at source, and for this, they need to develop fuel-injection systems capable of meeting these requirements over entire range of engine operating conditions.

Combustion in diesel engines is strongly dependent on fuel-air mixing process and optimized in-cylinder flows [Bevan and Ghandi, 2005]. Bevan and Ghandi, 2005 suggested that improved fuel-air mixing rate is a significant factor resulting in shorter combustion duration and higher combustion efficiency, which improves overall engine efficiency. To examine this, researchers focused on homogenous fuel-air mixing in CI engines, which reduced NOx to negligible levels [Maurya and Agarwal, 2011; Singh et al., 2014] in HCCI combustion mode, however this concept has its own merits and demerits. Fuel-air mixing can be optimized by an engine control unit (ECU) controlled fuel injection system, which can control start of injection (SoI) timings, fuel injection pressure, injection duration, and number of injections. Fuel-air mixing also depends on fuel spray structure and atomization levels [Park et al., 2009], and is affected

* Corresponding Author: E-mail: akag@iik.ac.in; Phone: +91-512 2597982

by the fuel injection strategy. Fuel-air mixing strategies also affect the degree of completion of combustion, which is quite important for diesel engines because it controls PM formation inside the engine combustion chamber. Generally, turbulence adds value to in-cylinder flow structures however heat transfer is also influenced by the in-cylinder flows [Heywood, 1988]. Certain level of turbulence is required inside the engine combustion chamber for mixing the atomized fuel with compressed air to obtain efficient combustion. Therefore it is essential to understand the flow structures inside the cylinder in order to improve combustion and enhance IC engine performance. Engine design and combustion chamber geometry also affects the combustion. Different designs of combustion chambers for direct and in-direct injection of fuel are proposed by manufactures, which reduce emissions and improve engine performance.

For optimizing these characteristics, it is very important to closely observe the parameters, which directly affect the in-cylinder flow characteristics. In-cylinder visualization of fuel-air mixing and combustion becomes very important scientific study. In-cylinder combustion images can be captured by using a high-speed camera and associated visualization equipment in a customized engine. From these images, various combustion parameters and spray characteristics can be analyzed with the help of image processing software. However, optical access to the engine combustion chamber is the biggest challenge for applying optical diagnostic techniques to the IC engines. Optical access to the traditionally opaque cylinder is essential in order to enable researchers to apply optical diagnostic techniques to the IC engines. There are different ways for gaining optical access through the engine cylinder and it differs according to the requirements of measurement and available financial resources. Two main types of optical access arrangements can be done, namely; full optical access in an Optical research engine; and limited optical access using engine endoscopy in a production grade engine.

1.1 Optical research engine

An optical research engine allows full optical access to the combustion chamber. This special engine is used for studying the fuel-air mixing, in-cylinder flows, combustion, and flame propagation through the optical liner, which is made of high quality quartz and a transparent piston. Early efforts on gaining optical access were by using a transparent acrylic resin, which was assembled on the extended part of the cylinder. A quartz window was installed at the top of the extended piston, which enclosed a mirror inclined at 45° to observe the in-cylinder flows. Bowditch [1961]

modified a production grade engine for optical access through the piston crown and developed it as a new tool for combustion research in 1961. After that, several researchers and automotive companies improved this type of engine and implemented this technique with transparent window in strategic locations such as cylinder, cylinder head and piston for investigations in the firing conditions. Fully transparent cylinder was also implemented in some engines for non-firing studies. Normally, transparent windows are made by fused silica or high temperature quartz, which is able to withstand high temperature and high pressure prevailing during engine combustion. This type of engine can be fired for very short periods only because visibility of the optical window decreases due to soot deposition. Therefore, regular cleaning is required after each firing experiment. Optical engines can't be tested at higher loads and speeds [Pundir, 2010]. Allen et al. [2000] used new design of optical research engine, developed by Lotus Engineering for fuel spray and combustion investigations were done employing laser diagnostics. They tested the engine upto 5000 rpm and 60 bar peak in-cylinder pressure. Han et al. [2008] used optically accessible direct injection diesel engine for soot and temperature analysis using laser diagnostics. The main advantage of this engine was that entire combustion event could be captured for one full combustion cycle using suitable high-speed charge coupled device (CCD) camera. Hence this type of engine was very helpful in analyzing various combustion characteristics, which were not understood well using conventional techniques. Huang et al. [2004] used a transparent cylinder, which was made of Plexiglas and a section of aluminum cylinder. A chrome metal liner was inserted between the Plexiglas cylinder and the crankcase. An elongated hollow cylindrical aluminum frame was used instead of the original piston. The top end of the cylindrical frame was screwed to the piston head. Richter et al. [1999] used standard Bowditch layout, in which a quartz cylinder of 80 mm height was mounted to access the combustion chamber (Fig. 1 (a)).

Singh et al. [2015] used an optical research engine (AVL 5402) for PIV experiments in motored conditions. The engine had full optical access through the quartz optical liner and a transparent piston (Fig. 1 (b)), installed at Engine Research Laboratory, IIT Kanpur, India. Lotus single cylinder optical research engine (SCORE) was designed for optical diagnostics. The cylinder liner was made from fused silica and a sapphire window was inserted in the piston crown in order to provide full optical access to the combustion chamber (Fig. 1(c)). Optical diagnostics using full optical access is very useful for real time data analysis however optical engines have following limitations [Allen et al., 2000]:

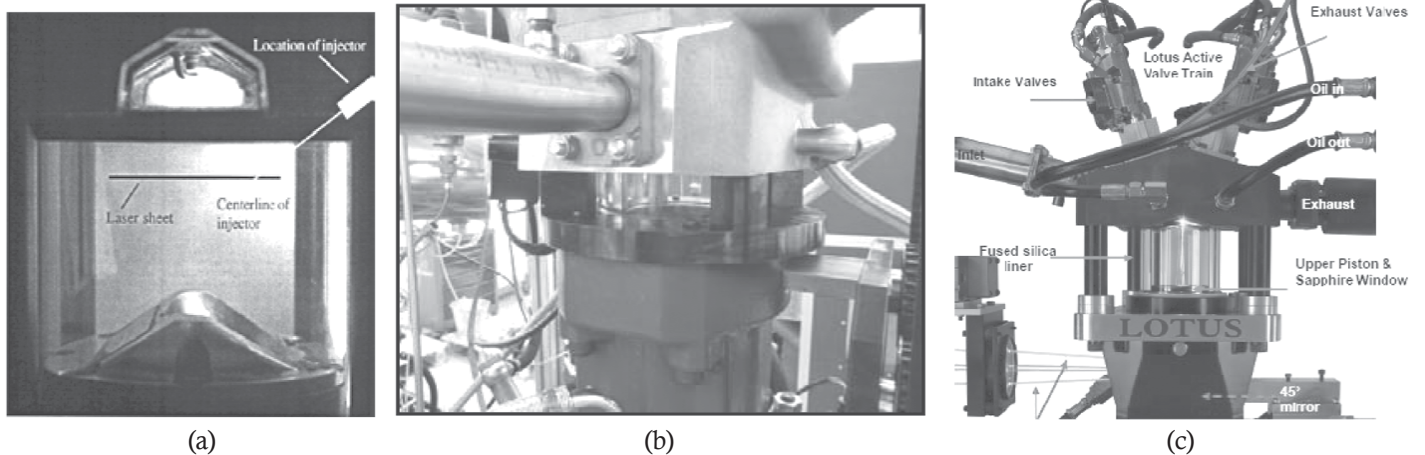


Fig. 1 (a): Optical access with 80 mm quartz liner [Richter et al., 1999]; (b): Single cylinder optical research engine; (c): Single cylinder optical research engine (SCORE) [Binjuwar, 2013]

- Optical research engines suffer from several restrictions such as balancing difficulty of a single cylinder, which is due to the added mass of the elongated piston. Therefore it limits engine's maximum speed.
- This type of engine can only be operated from low-to-medium loads and speeds because structural strength of the optical window is a limiting factor due to its large size.
- Quartz window is very expensive and a specific window is required for a particular engine according to its geometrical configuration. Hence, this technique can't be used in a production grade engine.

- It can only be used for research in a highly customized research engine test cell environment, which is prohibitively expensive.
- The optical engine can be operated for short durations only due to low heat transfer rates through the optical components and lack of cooling of the optical liner.
- The optical walls must be cleaned and combustion products must be removed very frequently. This is quite tedious task generally.

As a result of these limitations, several optical diagnostics techniques use optical access using an endoscope, which is relatively easier and

endoscopic technique can be applied to any production grade engine with some modifications to the engine hardware.

1.2 Engine endoscopy

Endoscopy is an important and useful optical diagnostics technique for spray and combustion diagnostics in an engine environment. It has the additional benefit that it can be implemented in any production grade engine and can be used in high loads and speeds. It needs a very small area for optical access into the engine cylinder and can be implemented with minor modifications/ structural changes in the cylinder head compared to the previous technique involving full optical access through the quartz liner and transparent piston top. The main advantage of this technique is that it can be implemented in a wide range of applications in both, SI and CI engines. Combustion in SI and CI engines can be visualized by modifying the cylinder head and piston appropriately, while mixture formation in the port fuel injected SI engine can be visualized by appropriate modifications in the intake manifold. This technique is used as a tool to diagnose engine combustion therefore it does not require special design of any engine component. This technique can be employed in any type of engine, ranging from conventional DI single cylinder generator engines to highly optimized variable speed automotive engines. It is useful in diagnosing the problems in the interior parts of the engine in a vehicle, where other visualization techniques can't be implemented.

Engine endoscopy always provides faster diagnostics and reduces material consumption and time required in disassembling the engine. Hardware required for this technique consists of a high-speed CCD/ IR camera, a high temperature industrial endoscope, an optical window and an optics protection arrangement. Most components such as optics protection sleeves and hole in the cylinder head can be easily custom-designed according to the application requirements. Therefore, it is not as expensive a technique for optical diagnostics as an optical engine.

In this study, important application areas of engine endoscopy have been discussed. Engine endoscopy is an economical technique for IC engine application and provides valuable information related to engine combustion and emissions. These aspects have been discussed in following sub-sections.

2. Evolution of endoscopes

Endoscopy is a very popular and effective optical visualization technique for several medical as well as industrial applications. This technique is normally used by doctors during complex medical surgeries, for capturing view of interior organs in a human body, while making very small incisions. It was used for the first time by Philippbonzzini (1806) in Mainz using light conductor for examining the cavity in a human body. After many improvements in this technique, Georg wolf (1873–1938) introduced rigid endoscopes in 1906. Flexible endoscopes were introduced in 1911. During the World War-II, several modern technologies emerged in medical science landscape. In 1945, Karl-Storz, who is famously known as “father of endoscopy” introduced a new endoscope, which was used with an external light source for investigations interiors of a human body. Afterwards, this concept was widely used in the industrial applications also for investigating various problems of the interior parts/ components of different machines, which had limited space for optical access.

Of late, this technique is being considered for myriad of applications in SI and CI engines e.g. combustion diagnostics, spray evolution diagnostics and fuel-air mixture formation studies etc. with minor modifications in existing production grade engines. Special endoscopes are designed for optical investigations in automotive applications; such as to capture the images of in-cylinder combustion, fuel sprays and fuel-air mixing along with assessing the effects of modifications in cylinder head, intake manifold etc.

3. Principle of endoscope

Endoscope is a large, thin tube, consisting of achromatic lens or rod lens combination, which is used for transferring images from the viewing end to the ocular (eye piece). Image is transferred through the image lenses and field lenses, which are set in the guide tube alternatively. These pairs of lenses form an image reversal system, which repeats the reversal of image and finally transfers the image straight through the endoscope (Fig. 2 (a)) [Dierksheide et al., 2001].

In Fig. 2 (a), object image is firstly projected at plane B1 and then it is transferred through the image reversal lenses (L1/L2) from there and projected on to the plane B2. Image on the plane B2 is a mirror image of plane B1. In the same way, image is again transferred on to plane B3, where the image is similar to the image at plane B1. C-mount adapter is attached to the ocular, which consists of a focusing arrangement.

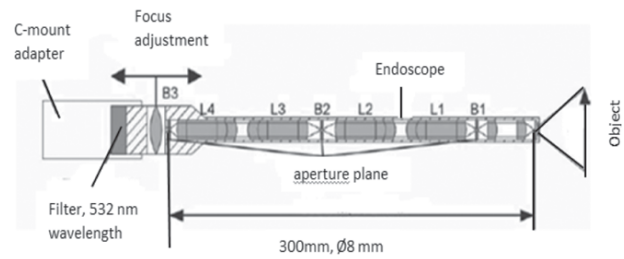


Fig. 2 (a): Image transformations through an endoscope [Dierksheide et al., 2001]

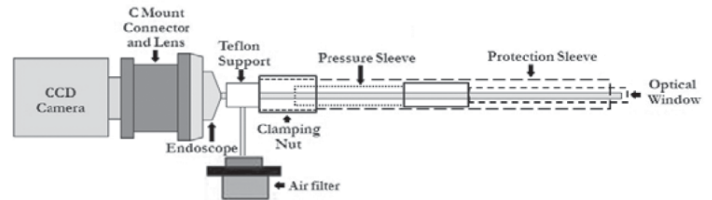


Fig. 2 (b): Schematic of the endoscopic access system [Agarwal et al., 2015]



Fig. 2 (c): Typical engine endoscope

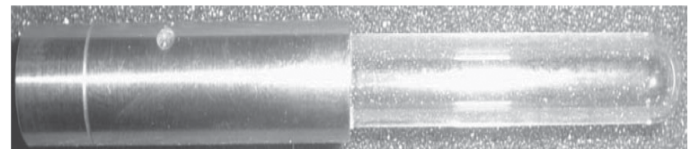


Fig. 2 (d): Optical window for 70° engine endoscope

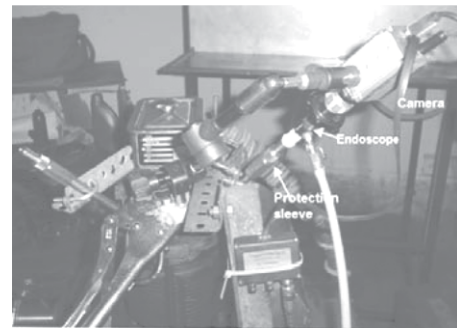


Fig. 2 (e): Common arrangement of engine endoscope with camera

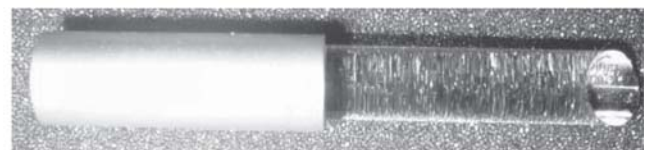


Fig. 2 (f): 70° degree Illumination Tip

Fig. 2: Principle and Components of the Engine Endoscopy

4. Engine endoscopy

Engine endoscopes gain access in to the engine combustion chamber through the cylinder head and modifications are required to be done in the cylinder head and the intake manifold for this, according to the specific application. For combustion and spray diagnostics in an IC engine, a hole is made in the cylinder head such that its endoscopic view can capture the illuminated area of interest and it covers maximum possible view of the combustion and fuel spray. Schematic of the engine combustion chamber endoscopic access is shown in Fig. 2 (b) and its components are described briefly in following subsections.

4.1 Engine endoscopes

Normally, two types of endoscopes are used for engine applications according to the cooling requirements, based on temperature and pressure conditions, namely combustion chamber endoscopes and general cavity endoscopes. Each engine endoscope is designed for different viewing angles (0° , 30° and 70°) of the front lens in order to capture the view of the combustion chamber because an endoscope has limited field of view.

4.1.1 Combustion chamber endoscope

Combustion chamber endoscopes are used for high temperature, high pressure applications such as visualization of in-cylinder combustion processes and fuel sprays. It provides direct access to the engine combustion chamber with the help of a quartz optical window, used for its thermal protection from hot, high pressure combustion chamber environment. This type of endoscope is coupled with an integral cooling arrangement to protect its optics from the high temperature and high pressure gases in the engine cylinder during combustion. Combustion images are captured in the absence of light because sufficient light is emitted by incandescence of soot formed in the combustion chamber. However for fuel spray visualization, illumination from an external light source is essential. Dry, pressurized, dust-free air is circulated through the endoscope assembly at ~ 5 -6 bar pressure to remove the heat convected to it from the high temperature combustion chamber environment, in order to avoid damage to the optics.

4.1.2 General cavity endoscope

General cavity endoscopes are used in low temperature, low pressure conditions, where external cooling is not required e.g. visualization of mixture formation in the intake manifold of a SI engine. An optical fiber is coupled with the lens system of the endoscope for transmission of light, which is used for illuminating the target area for capturing the images in the region of interest.

4.2 Protection sleeve and pressure sleeve

Protection sleeve is used for protecting the endoscope from engine vibrations. Protection sleeve is inserted into the cylinder head through a hole and held in place using external fine threads. The stainless steel sleeve with external threads is inserted into the hole having internal matching threads. The sleeve thus fits well in the cylinder head. Inside the protection sleeve, a pressure sleeve is inserted for protecting the endoscope from the high cylinder pressure environment. In cooled endoscopes, compressed air is circulated through the pressure sleeve in order to remove the heat from the endoscope. The hot air comes out from the holes, drilled in the upper part of the pressure sleeve and vented to the surroundings through the holes made in the clamping nut.

4.3 Optical window

Optical windows are very important and expensive component in the endoscopic system. They are cylindrical quartz tubes, fitted inside the steel tubes (Fig. 2 (d)).

An optical window is inserted into the protection sleeve. Quartz section of optical window directly faces the engine combustion chamber heat and pressure. Optical window provides optical access to the endoscope and protects it from exposure to high pressure and temperature (~ 60 bar, 2500 K) gas in the combustion chamber, which is undergoing combustion. The length and shape of quartz window may be different for every endoscope, depending on its viewing angle and the type of endoscope.

4.4 Camera

Normally CCD/ IR camera is used for engine endoscopy, depending on the objective of research. The camera is connected to the endoscope ocular with an optical connector. For real time in-cylinder combustion and spray imaging, it is synchronized with the crankshaft encoder and cam phase sensor signals, with the help of a micro-controller based circuit. A common arrangement of the engine endoscope with the camera is shown in Fig. 2 (e). For high speed optical investigations such as particle imaging velocimetry (PIV), images are captured using a high-resolution double-frame CCD camera with 1024×1280 pixels for each frame, and 12-bit dynamics [Dierksheide et al., 2001].

4.5 Lighting unit and illumination tip

This unit is used during low intensity engine applications such as spray imaging, mixture formation investigations etc. It includes an illumination tip and a light guide. Illumination tip (Fig. 2 (f)) is inserted into the protection sleeve, which is fitted into another hole in the cylinder head. Illumination tips are designed according to the endoscopy angle.

5. Research trends and applications of endoscopy in IC engines

Endoscopy has been used to investigate different combustion and spray parameters in IC engines since long time. It has been combined with laser diagnostic techniques to understand complex engine geometries and used for combustion characterization and mixture formation in DI and IDI engines. Endoscopy was successfully used for optimizing fuel utilization and reducing soot emissions from modified combustion chambers. Off-late, endoscopy has been used in several other advanced applications in automotive industry, which were otherwise difficult for conventional techniques, such as determining piston temperature, study of pilot diesel spray combustion, understanding the effect of intake change condition on the combustion chamber temperature distribution and in-situ soot formation etc. Diverse applications of this technique are briefly discussed in the following sub-sections.

5.1 Combustion analysis in CI and SI engines

Combustion analysis is very important for optimizing the performance of Internal Combustion engines. Many researchers used endoscopic technique for diagnosing the effect of different spray parameters such as fuel injection angle, injection timing etc. on the engine combustion. Hampson and Reitz [1998] investigated the effect of double injections over single injection on in-cylinder combustion temperatures and in-cylinder soot distribution using endoscopic visualization. They captured combustion images in a modern, heavy-duty diesel engine equipped with common rail electronically-controlled fuel injection system, which injected fuel at very high pressure compared to normal injection systems. Combustion temperature distribution and soot distribution were analyzed using two-colour pyrometry technique on the endoscopic combustion images. They also developed multi-dimensional simulation model for verifying the data and there was good agreement between experimental and simulation results. They explained the reasons for lower soot with split injection and advanced injection using endoscopic images in conjunction with modeling results. Main aim of their research was to understand the benefits of split injection. The combustion images and contours of temperature, and soot KL factor are shown in Fig. 3 (a)-(c).

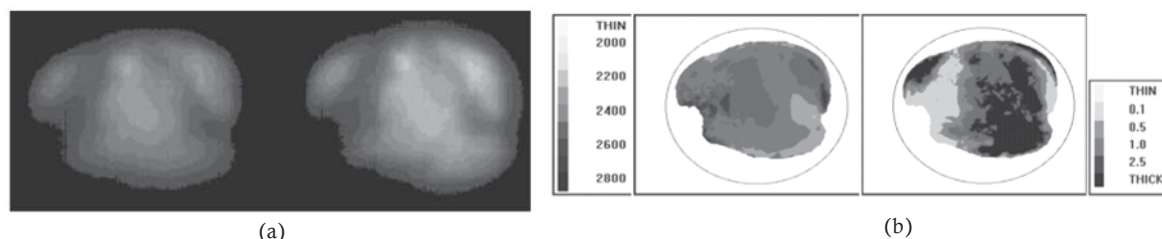


Fig. 3 (a): Combustion image captured by an endoscope; [Hampson and Reitz, 1998]

Fig. 3 (b): Temperature distribution and soot distribution obtained by an engine endoscope [Hampson and Reitz, 1998]

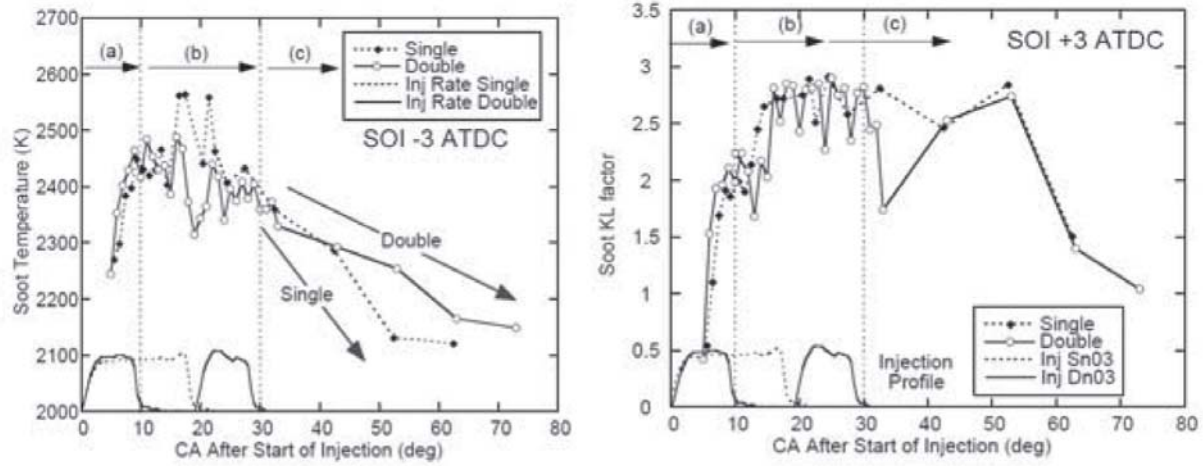
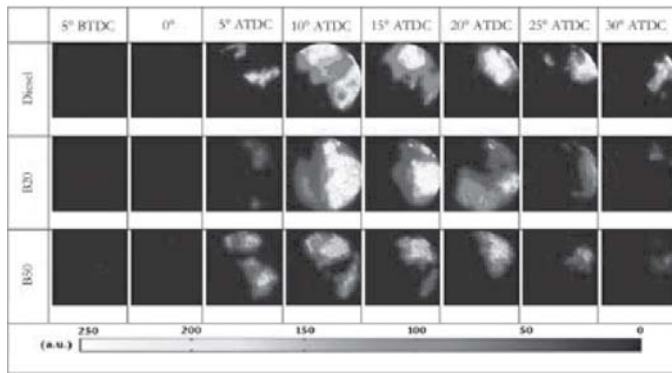
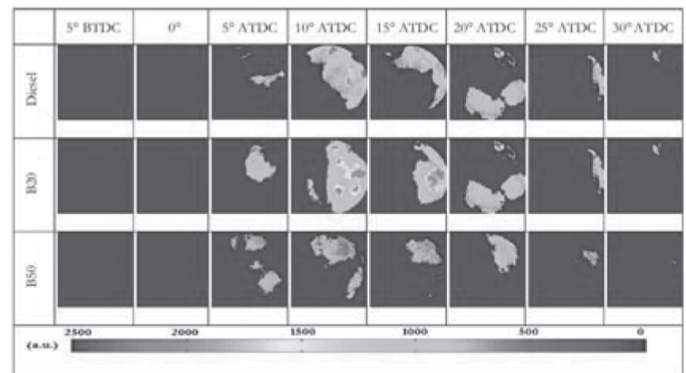


Fig. 3 (c): Soot temperature vs. crank angle after SOI [Hampson and Reitz, 1998]



(d)



(e)

Fig. 3 (d): Contours of R intensity for different test fuels using engine endoscopy [Agarwal et al., 2015]

Fig. 3 (e): Spatial and time resolved in-cylinder flame temperature distribution for different fuels using engine endoscopy [Agarwal et al., 2015]

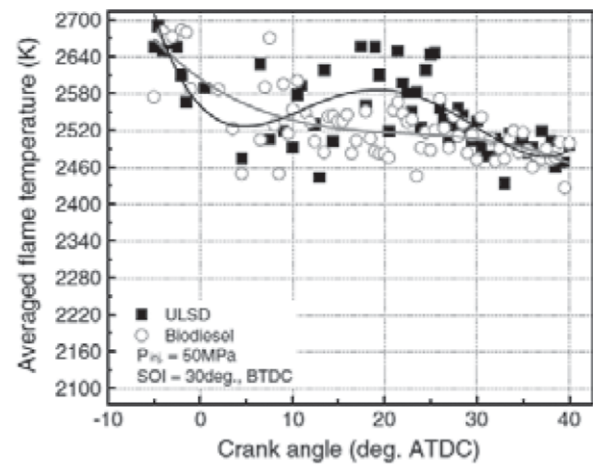
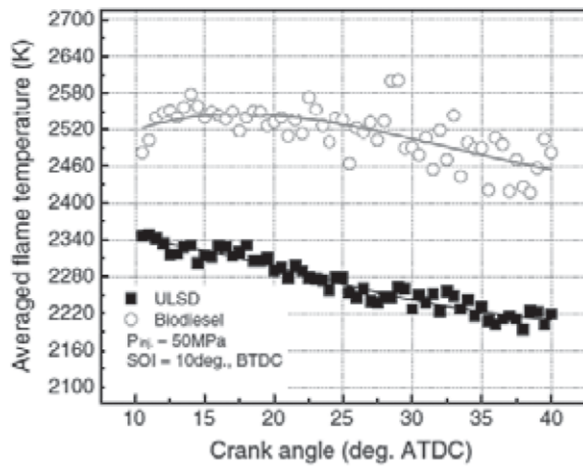


Fig. 3 (f): Average flame temperature of biodiesel and ULSD at two injection timings [Jeon et al., 2013]

Behavior of maximum temperature and KL factor are plotted w.r.t. crank angle for both single and multiple injections (Fig. 3 (c)). The temperature and soot distribution plots (Fig. 3 (b)), which were determined from the endoscopic images clearly showed that soot temperatures reduced with increasing crank angle and were followed by increased in-cylinder temperature during phase (b) due to combustion of fuel injected during second injection pulse. While in case of single injection; rise in temperature was due to termination of injection. It can also be observed that soot factor was higher in single injection due to continuous injection of fuel, while during double injection, it dropped due to end of first injection. It substantially dropped at 30° after SoI due to end of second injection. Hence, reduction in soot concentration was clearly observed in double injection case. Eismark et al. [2009] performed the experiments on a heavy-duty diesel engine to investigate soot oxidation by statistical analysis of the engine data. They also used in-cylinder high speed photography using endoscope along with CFD simulations to examine large scale in-cylinder fluid motion.

Agarwal et al. [2015] investigated soot distribution in a diesel, and biodiesel (B20 and B50) fuelled diesel engine. They investigated the behavior of soot distribution during combustion at different engine loads. They reported that spatial distribution of soot in the combustion chamber increased after the start of combustion (SoC). However after attaining maxima, it started to decrease, which represented oxidation of soot particles in late combustion phase. Fig. 3 (d) shows the variation in R intensity for different test fuels at different crank angle positions. R intensity is defined as the intensity of red color in the diffusion flame, which denotes the soot induced digital coloration of the flames. They also discussed a very important finding that endoscopic combustion visualization of highly oxygenated fuels is not as effective as mineral diesel because intensity and color of the combustion images are slightly inferior due to lower emission of radiations from the unburned soot particles. In the same study, Agarwal et al. [2015] also investigated variations in flame temperature distribution. Fig. 3 (e) shows the variation of flame temperature distribution for different test fuels during combustion. Results showed that higher biodiesel blends showed relatively lower flame radiation temperature however it was primarily due to lower soot radiations. However higher oxygen content of biodiesel led to higher NO_x formation during combustion.

Jeon et al. [2013] also carried out engine endoscopy with ultra-low sulfur diesel (ULSD) and biodiesel and measured flame temperature distribution. Fig. 3 (f) shows that during ULSD combustion, the flame develops rapidly and the flame temperature is distributed uniformly. However, biodiesel flame distribution develops both slowly and locally. Due to slow evaporation rate and the lower atomization of biodiesel, the fuel-air mixture is not as homogeneous as that of ULSD, even though the ignition delay of biodiesel is longer. They also examined the effect of SoI on flame temperature distribution. Fig. 3 (f) shows the difference between the average flame temperatures. It is evident that biodiesel flame temperature is distributed around 2500 K, while ULSD flame temperature is scattered between 2220 K and 2340 K. However this is true, when the SoI was at 10° BTDC. If the SoI was advanced to 30° BTDC, the difference between the flame temperature of biodiesel and ULSD vanishes (Fig. 3 (f)).

In-cylinder combustion phenomenon was also investigated by Spicher et al. [2000] in a direct injection spark ignition (DISI) engine using endoscopy. They analyzed combustion characteristics such as flame propagation speed [Koch et al., 2002], flame radiations and compared them for homogeneous and stratified modes of combustion. Optical spark plug and endoscope were inserted in place of an exhaust valve in a 4-valve engine cylinder head. Combustion flame fronts were captured at every 0.20° CA and plotted contours. These contours show the increasing flame-front till the maximum propagation and decreasing flame-front upto the end of combustion (EoC). It was found that maximum flame propagation for stratified charge was lower than homogenous charge due to unburnt mixtures. It was also found that flame-front propagation was uniform from maximum flame-front to the observation center in the homogenous charge mode due to homogenous fuel-air mixing, while behavior of flame-front was rather irregular in case of stratified charge mode. Sauter et al. [2006] modified the DISI engine and observed the flame area using endoscopic access system. Effect of ignition angle on the flame area was analyzed using image analysis and the flame area was found to be lesser for later ignition angle due to lower cylinder pressure and temperature.

5.2 Determining ignition sites in diesel engines

Ryan et al. [1994] used endoscopy in a 4-valve diesel engine to analyze the effect of fuel injection pressure and intake air density on ignition and combustion location at different engine speeds, loads, injection

pressures and intake air pressures. They captured the movie of combustion using high speed camera and found that increased fuel injection pressure or intake air density reduced the ignition delay, leading to start of ignition near the nozzle. Locations of ignition and combustion are independently affected by fuel injection pressure and intake air pressure. They also found that spray tip velocity and wall impingement increased if fuel injection pressure was higher than 150 MPa. These observations were helpful in improving fuel-air mixing in order to optimize emissions.

Ignition sites for pilot injection were investigated by Ricart and Reitz [1996] and Ricart et al. [1997] using engine endoscopy in a heavy-duty single cylinder engine. They conducted experiments for different fuel quantities (during pilot injection), which were 10, 15 and 20% of the total fuel injected at 75% engine load, and 1600 RPM at different SoI timings. They captured combustion images for pilot injection and characterized the combustion by ignition sites, which were located below the point, where spray hits the piston bowl surface. They observed that majority of combustion started at multiple ignition sites, at the bottom of the piston bowl and spread along the bowl edges. SoI mainly retarded due to ignition sites existing above the spray impingement point.

5.3 Combustion characteristics of alternative fuels

Several studies were conducted for comparing combustion characteristics of different alternative fuels vis-à-vis mineral diesel using engine endoscopy. The main aim of these studies was to develop efficient substitute of mineral diesel by improving combustion characteristics of these alternative fuels. Endoscopes proved to be very helpful in such studies because different real-time characteristics could be analyzed by changing different engine variables and the fuel injection system. Miersat et al. [2004] conducted similar studies on Sun-diesel, which is an alternative biodiesel derived from wood chips. Endoscope was installed in a Mercedes A-class turbocharged DI engine equipped with common rail direct injection (CRDI) system. They analyzed soot concentration factor from the combustion images for both test fuels at different SoI timings. They found that peak of soot concentration factor becomes higher for advanced SoI timings. However, for late combustion cycles, soot concentration factor was higher for retarded SoI. This was due to reduction in turbulence and in-cylinder pressure, which reduced the soot oxidation rate in late combustion cycle. For Sun-diesel, rate of soot production was higher compared to diesel, primarily due to shorter ignition delay and relatively higher viscosity. Agarwal et al. [2015] compared the combustion characteristics of mineral diesel and biodiesel blends (B20 and B50) using endoscopic imaging. They reported that area of luminous flame zone was higher in B20 compared to mineral diesel. On the other hand, the area of luminous flame zone decreased on further increasing biodiesel content in the test fuel upto B50 at the same engine load. Dominating nature of two different properties of biodiesel, lower calorific value and higher oxygen content were responsible for such a trend.

5.4 Fuel-air mixing optimization

Endoscopy was used for investigating the mixture formation process in SI engines. Air-fuel mixing is a very critical process for SI engines, which strongly affects engine performance and emission characteristics. Mixture formation images were captured by Schänzlin et al. [2001] in a DISI engine using fiber endoscope, which was coupled with a 300 W xenon light source (Fig. 4 (a)).

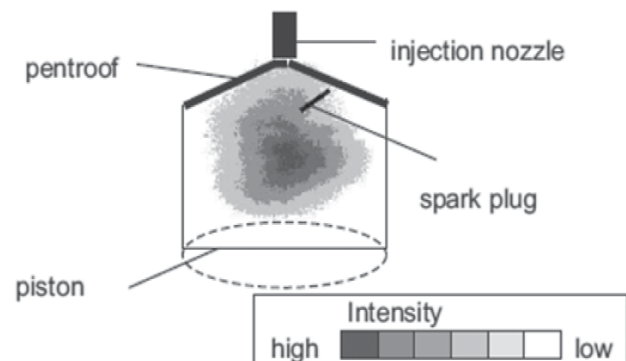


Fig. 4 (a): Endoscopic view of the observed mixture formation region [Schänzlin et al., 2001]

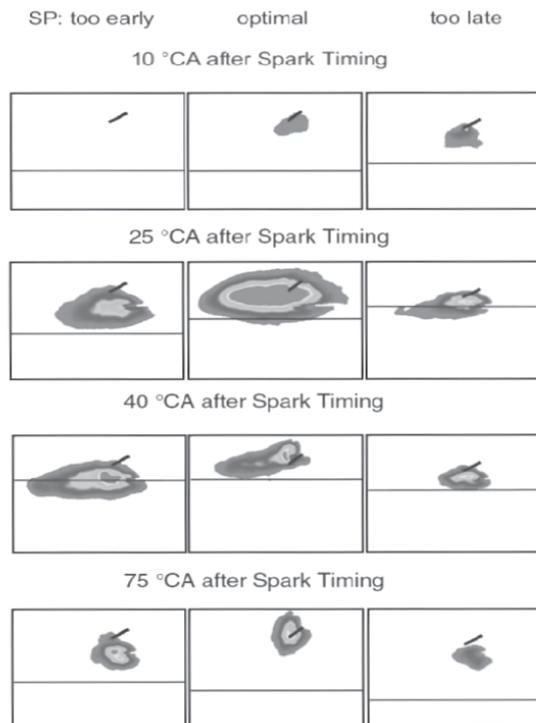


Fig. 4 (b): Endoscopic combustion images with different spark timings in stratified charge mode [Schänzlin et al., 2002]

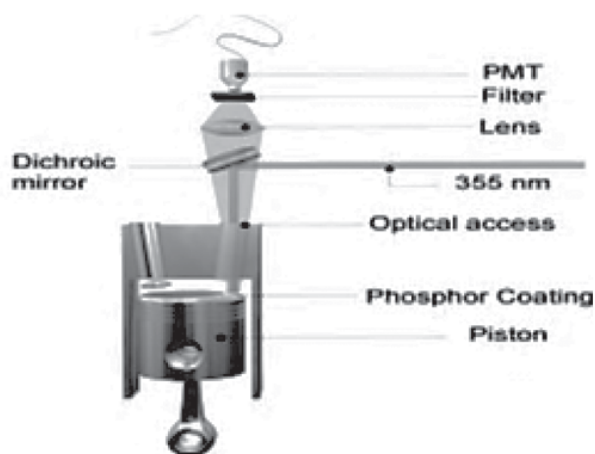


Fig. 4 (c): Experimental setup for piston temperature measurement [Husberg et al., 2005]

They visualized three different phases of mixture formation process in three different modes: homogenous mode; stratified mode; and stratified low temperature mode. They compared the effect of fuel injection pressure, swirl level and engine load for all test modes. They reported that swirl level has highest effect and injection parameters have lowest effect on combustion. They also reported that stratification is very important for initiating optimum combustion reactions. Schänzlin et al. [2001] discovered compact burning zone in high-swirl case and widespread combustion in low-swirl case. They further investigated the effect of spark timings on combustion. If spark timing was too advanced, flame surface was very small and the fuel spread was due to improper mixing with air. In case of too retarded spark timing, fuel and air mixed homogeneously and produced lowest soot, which is shown by lowest soot intensity in Fig. 4 (b).

During optimum spark timing, when the fuel consumption was lowest, advanced SoC was observed. It was also observed that fuel spreads in wider area, burning fuel-air mixture became leaner and the flames propagated very slowly. In Toyota Motor Company, Sakata et al. [1990] developed a Toyota Reflex Burn (TRB) system to optimize the fuel-air

mixture formation in a DI diesel engine. At that time, gaseous and particulate emissions were a huge environmental concern for small DI diesel engines. They modified the combustion chamber shape, which generated complex air motion with high turbulence. Endoscope with a high-speed camera was used to visualize the mixture formation, and spray and flame behavior to achieve optimum impingement intensity. TRB system generated complex air motion from the impingement with a reflex edge in the combustion chamber cavity, which generated highly turbulent air motion. They found that deflection of fuel spray away from the reflex edge reduced wall-wetting, which reduced the particulate emissions. Werlberger and Cartellieri [1987] also used endoscopic high-speed combustion imaging in a high speed direct injection (HSDI) diesel engine to investigate the effect of pilot injection on fuel-air mixing and combustion. They also observed the effect of wall temperature on the combustion development.

5.5 Optimizing combustion chamber geometry

Endoscopy has proved to be a very successful technique for investigating the effect of combustion chamber geometry on combustion parameters. Flame propagation during combustion was observed by Zhang et al. [1995] for three different combustion chamber geometries. Average flame velocity vector and flame distribution was calculated using statistical cross-correlation method for different combustion chamber geometries (Dish type, Re-entrant type, Production type). They analyzed combustion images by endoscopy and reported that ignition delay was almost similar for all combustion chamber geometries however average flame velocity was highest for production type combustion chamber geometry due to highly swirling air motion. Smoke emission was also lowest for production type combustion chamber geometry due to better utilization of inducted air.

5.6 Determination of ignition delay and combustion timings

Ignition delay and combustion duration are very important factors for combustion in diesel engines because they influence soot and NO_x formation. Endoscopic technique is very helpful in analyzing SoC because combustion can be easily seen in the combustion images. Several studies were carried out to determine the ignition delay and combustion duration for different fuels [Bittle et al., 2010; Hotti and Hebbal, 2011; Huang et al., 2004]. Researchers calculated ignition delay and combustion duration from the heat release curves and mass burn fraction curves as well. Mtui et al. [1996] used engine endoscopy for investigating ignition delay and combustion duration in case of pilot injected liquid diesel with high pressure direct injection of natural gas and compared it with 100% diesel fuelling at the same speed and load conditions. They also investigated the effect of gas injection on pilot liquid flames. For calculating the ignition delay and combustion duration, they used endoscopic combustion imaging and mass burn fraction (MBF) calculations and got almost similar results by both methods. They captured the endoscopic images using CCD camera for (i) 100% diesel, (ii) 30% pilot diesel and 70% natural gas injection and (iii) only pilot diesel injection. From the combustion images, combustion duration and ignition delay were calculated and it was found that there was no effect on combustion duration and ignition delay on natural gas injection with diesel compared to 100% diesel.

For validating the endoscopic results, Sauter et al. [2006] analyzed the start of flame detection, maximum flame detection and end of flame detection from endoscopic images and correlated them with 5%, 50% and 95% mass burn fraction (MBF) timings respectively for different engine operating conditions. They found linear results with high regression coefficient (~ 1) for 5% and 50% MBF but there were huge fluctuations in correlating the end of combustion flame with 95% MBF, because a small irregularity in beginning could have a significant impact on the end of combustion process [Reckers et al., 2002]. Jeon et al. [2013] performed endoscopic experiments to compare the combustion characteristics of ULSD and biodiesel. They concluded that ULSD had a similar ignition delay as biodiesel, higher peak combustion pressure and higher BMEP compared to biodiesel due to its similar cetane number and relatively higher heating value for the same fuel quantity injected. In another study, Jeon et al. [2014] used endoscopes for visualization of combustion in a DME fuelled diesel engine. The experiments were performed at different conditions and results showed similar ignition delay at different engine speeds. DME combustion was relatively faster and resulted in higher peak combustion pressure than ULSD.

Agarwal et al. [2015] also performed engine endoscopy in a production grade engine and validated the results obtained from engine endoscopy with combustion results from the thermodynamic analysis. In their experiments, they investigated the combustion of diesel, and biodiesel blends (B20 and B50) and found significantly different combustion pattern for each test fuel. They also compared the results obtained by

thermodynamic combustion analysis and endoscopic images for SoC and combustion duration for each of these test fuels.

5.7 Spray analysis

Endoscopy is very useful in spray characterization inside an engine because this technique provides direct optical access to the combustion chamber and can focus on the nozzle tip. Several studies [Dent, 1971; Lefebvre, 1989; Park et al., 2009; Agarwal and Chaudhury, 2010; Lee et al., 2005] were carried out for spray investigations using other visualization techniques however they were limited to constant volume spray chambers

and not in real firing engines. Using endoscopes along with lighting arrangement has proved to be a very successful tool for capturing the spray images during combustion events [Poster et al., 2000]. General cavity endoscopes are used for such low light applications. Light is passed through an optical fiber, which is coupled to the endoscope. Alam et al. [2005] captured the spray images in a diesel engine for different blends of dyglyme with diesel (20% w/w dyglyme blended with BP15 (“O-20”), 40% w/w dyglyme blended with BP15 (“O-40”) and 95% w/w dyglyme blended with BP15 (“O-95”). They compared the Sol timings and spray penetration length for these fuels and reported that O-20 had earliest Sol and O-95 had shortest spray penetration length.

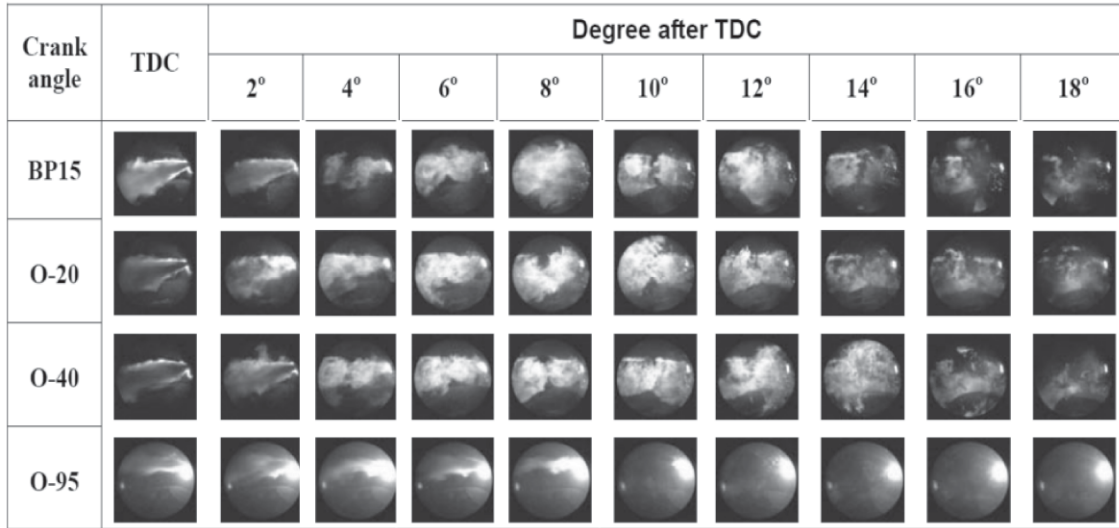


Fig. 5 (a): Spray and combustion visualization of a direct injection diesel engine operated with diglyme-diesel blends [Alam et al., 2005]

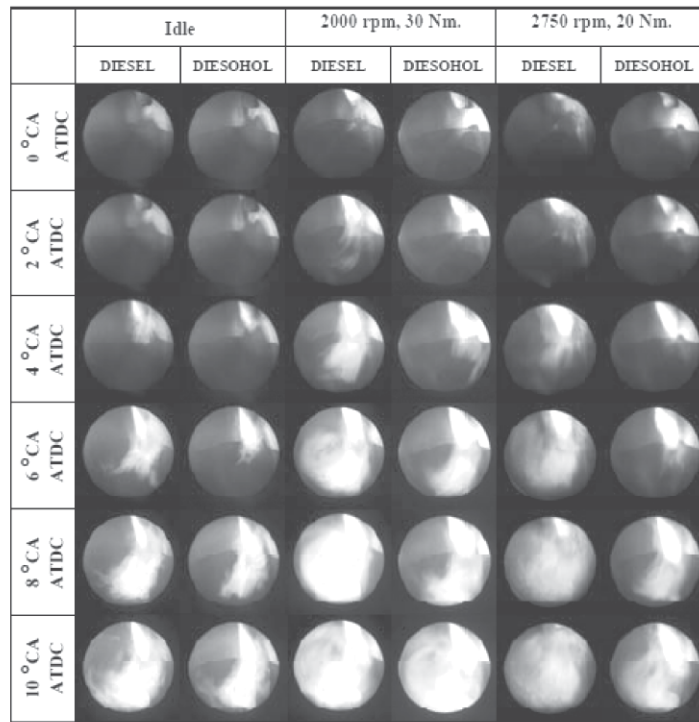


Fig. 5 (b): Images of spray formation in pre-chamber for reference diesel and diesohol at selected operating points [Wattanavichien and Azetsu, 2004]

Jeon et al. [2014] also investigated the spray and combustion behavior of DME fueled single cylinder engine. They investigated effect of various engine operating conditions such as different injection timings; engine speeds and engine loads on DME fuel spray atomization, combustion and emission characteristics. They used endoscopic visualization system consisting of a CCD camera, an endoscope, an illumination device, and AVL ThermoVision software. The endoscope equipped with CCD camera was installed on the cylinder head, to visualize the upper combustion chamber.

Wattanavichien and Azetsu [2004] also used an endoscopic visualization system with lighting arrangement to compare the fuel sprays of diesohol and mineral diesel in an IDI engine. They captured the spray images from low to medium loads with all other injection parameters fixed. They observed relatively superior atomization, longer spray penetration length and wider spray angle for diesohol due to its lower viscosity compared to mineral diesel. Schänzlin et al. [2001] implemented endoscopic technique in a spray-guided DISI gasoline engine. They performed in-cylinder optical investigations to provide information on the liquid phase distribution of fuel in the combustion chamber at different times after the start of fuel injection. They also performed numerical analysis for liquid phase fuel distribution and found a good qualitative agreement between the simulation results and endoscopic results. This technique was also extended to multi-cylinder engines fuelled with alternative fuels such as alcohols, and biofuels to investigate fuel-air mixing, flow pattern inside the combustion chamber and complex combustion characteristics [Disch et al., 2013; Allocca et al., 2013].

5.8 Piston temperature distribution and other in-cylinder applications

Apart from investigations of combustion and fuel-air mixture formation in IC engines, endoscopy is also widely used for various other challenging applications. Husberg et al. [2005] measured piston temperature in a single cylinder engine using endoscopy. They used a thin coating of thermographic phosphor on the surface of the piston and installed an optical window for endoscopy by removing one of the exhaust valves (Fig. 4 (c)).

As seen in Fig. 4 (c), Nd-YAG laser was directed into the combustion chamber with the help of an optical prism and a dichroic mirror for exciting the thermographic phosphor. Excited photonic emissions with

wavelength in visible light range were transmitted through the same mirror and then detected by a photomultiplier tube, which was mounted along with the endoscope. Photomultiplier tube sensed the exponential decay of excited phosphor emissions through the endoscope and produced a voltage signal corresponding to the lifetime of the phosphor emissions. Piston temperature was previously calibrated with the lifetime of the phosphor material, which was chosen according to the range of temperatures expected on the piston surface.

Nikolic and Iida [2007] used endoscopic imaging in a single cylinder rapid compression machine (RCM), which was used for simulating diesel combustion. They investigated the effect of CO₂ concentration, used for diluting intake air in the EGR to control NO_x formation. Soot distribution and ignition properties were analyzed with the help of endoscopic combustion images. They captured and compared the combustion images at 0, 4.3, 9.5, 14.3 % CO₂ concentrations in the intake air. The flame temperature and maximum soot concentration decreased upon increasing CO₂ concentration in the intake air, which in-turn also prolonged the ignition delay.

Korczewski [2011] investigated the component failure mechanism in a marine engine using endoscopy. They concluded that endoscopic imaging helps in evaluating technical state of directly accessible construction elements of an engine. Many material defects on the surface of components such as piston, liner and bearing, which limit working of an IC engine, can be detected by endoscopy. On the basis of the character and dimensions of the identified damages, it is possible to evaluate and make technical corrections of such faulty components. Therefore endoscopy has emerged as one of the newest methods in technical diagnostics.

5.9 Engine flow analysis: Endoscopic PIV

Nishiyama et al. [2012] used an air-cooled endoscope in a PIV experiments to investigate exhaust gas flow in a SI engine. They performed experiments in a 2.5 l, four-cylinder spark-ignited engine with a four valve per cylinder, pent-roof combustion chamber. Endoscopic setup comprised of a quartz lens and a stainless steel cage for adequate heat resistance. For direct observation of the interiors of the exhaust manifold, the endoscope chosen had outer diameter 15 mm and length 175 mm. A sapphire window with cooling-air passage was used for observation (Fig. 6 (a)).

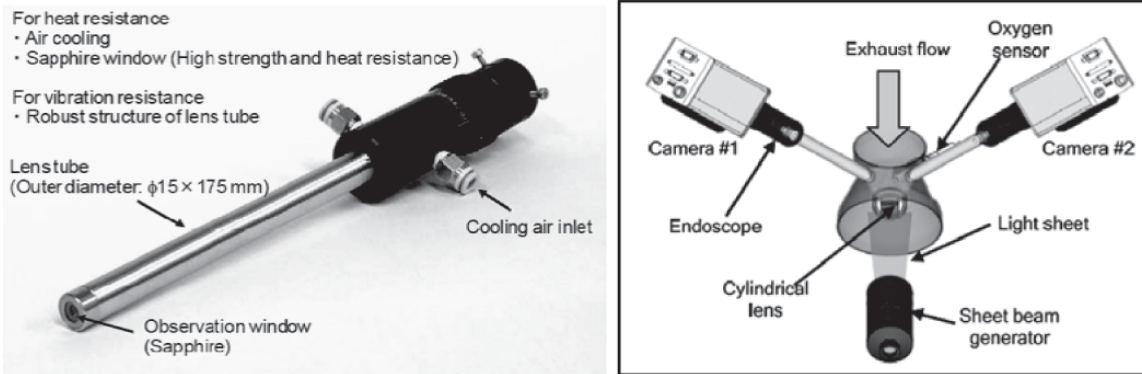


Fig. 6 (a): Schematic view of endoscopic PIV [Nishiyama et al., 2012]

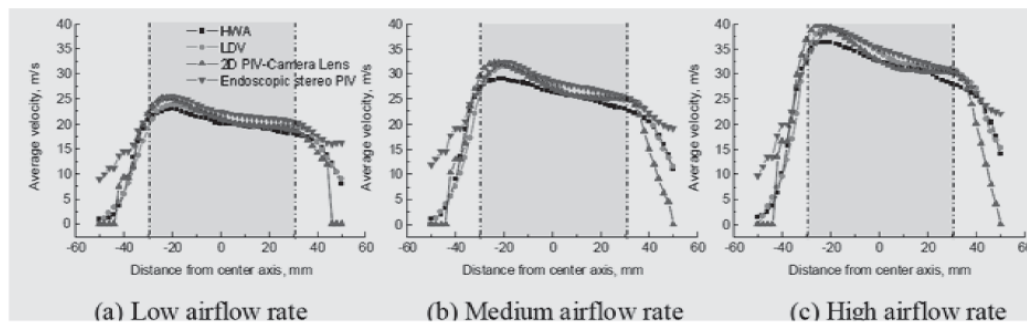


Fig. 6 (b): Comparison of HWA, LDV and stereo PIV results in the steady-flow test rig [Nishiyama et al., 2012]

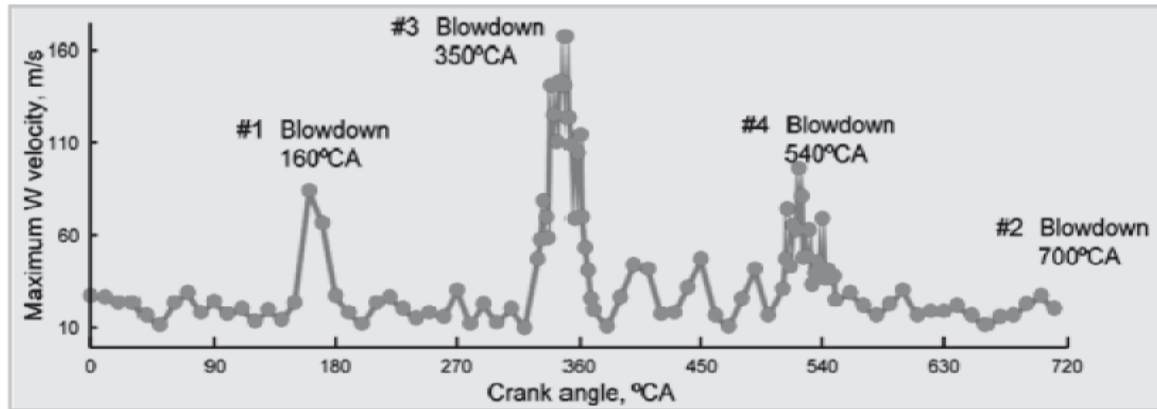
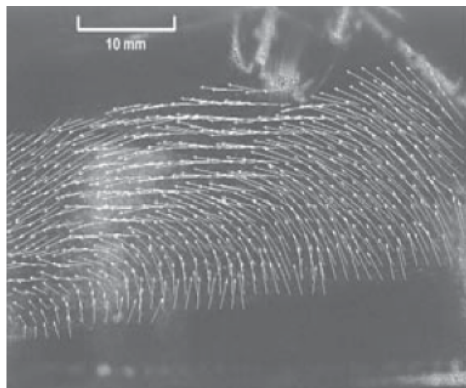
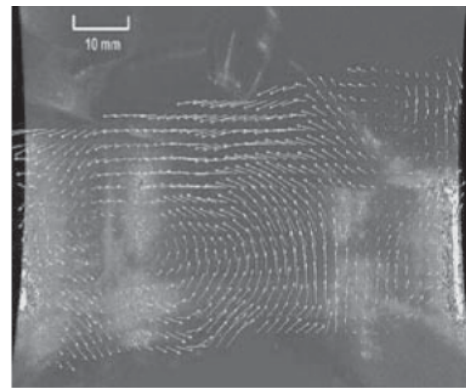


Fig. 6 (c): Maximum downstream velocity with crank angle [Nishiyama et al., 2012]



Tumble flow via large window;



Tumble flow via endoscopic

Fig 6 (d): Comparison of flow-field through full optical access and endoscopic access [Dierksheide et al., 2001]

They performed an experimental evaluation of the endoscope's performance and compared the results with established flow measurement techniques such as hot wire anemometry (HWA), laser Doppler velocimetry (LDV), and 2D-PIV. A comparison of results (Fig. 6 (b)) showed that various measurements were in good agreement with each other for all mean velocities.

Main objective of the study was to measure 3D velocity field in the exhaust of an engine using endoscopic PIV. The blow-down behavior of each cylinder was identified under firing condition (Fig. 6 (c)). The results showed that a strong downstream flow greater than 60 m/s was produced after the exhaust valve opening of each cylinder. However, the velocity distribution pattern and maximum velocities were different, depending on the cylinder.

PIV is a technique, which is non-intrusive in nature and has been in practice for many years now and is being widely used for flow visualization of fluids. PIV can be either macroscopic or microscopic. Macroscopic PIV is generally used with full optical access however microscopic PIV is applied with endoscopic access. Singh et al. [2015] used full optical access in an optical research engine using tomographic PIV and investigated the effect of engine speed on air-flow pattern in the engine cylinder under motored conditions. However this is quite expensive and challenging technique. Therefore several research groups have performed endoscopic optical diagnostics in IC engines however they were unable to determine air-flow characteristics in the engine cylinder due to limited access. Dierksheide et al. [2001] presented and compared endoscopic PIV measurements through an 8 mm optical access in an IC engine using endoscopy and compared the results with the measurements using standard optical access using a large window in the same area of interest. They demonstrated that the use of endoscopic devices, both for illumination of

the light-sheet plane and for the recording of the PIV images, has proved to be successful for the investigation of in-cylinder flow structures developed in IC engine. It was also noticeable that the amount of information about the in-cylinder flow structures increased, when endoscopic device was used (Fig. 6 (e)). Nauwerck et al. [2000] used endoscopy to investigate the in-cylinder flow structures during the gas exchange process inside a small two-stroke engine. They successfully implemented this system for PIV under a variety of engine operating conditions and speeds upto 6000 rpm, which is certainly not possible in an optical engine.

6. Conclusions

Engine endoscopy is an important optical technique for analysis of engine combustion and spray formation process. It can be used in wide variety of engine investigations ranging from fuel-air mixing in SI engines to combustion visualization in CI engines. Endoscopy can be also used to optimize the engine design parameters e.g. shape of combustion chamber, piston bowl etc. in addition to analyzing the effect of designs of different component on engine performance, combustion and emissions. Engine endoscopy is widely used for determining spatial flame temperature distribution and spatial soot distribution. Spray visualization in the engine combustion chamber is another important application of endoscopy. Several researchers also employed endoscopy to the exhaust manifold in order to investigate the exhaust flow behavior. Endoscopy offers enormous advantages in engine experiments due to limited space for optical access. Another major advantage offered by this technique is that the measurements can be done in production grade engine at high speeds and loads, rather than special configuration complex optical engines with limited operating range, which are extremely complex and expensive.

References

- Agarwal AK, Agarwal A, Singh AP, 2015, Time resolved in-situ biodiesel combustion visualization using engine endoscopy, *Measurement*, 69, 236–249.
- Agarwal AK, Chaudhary VH, 2010, Spray characteristics of biodiesel/ blends in a high pressure constant volume spray chamber, *Exp. Therm. Fluid Sci.*, 42, 212–218.
- Alam M, Song KH, Boehman A, 2005, Spray and combustion visualization of a direct injection diesel engine operated with diglyme fuel blends, *Int. J. Engine Res.*, 7, 503–521.
- Allen J, Law D, Pitcher G, Williams P, 2000, A New optical access research engine for advanced fuel spray and combustion analysis using laser based diagnostics, Monograph of 33rd International Symposium on Automotive Technology and Automation (ISATA), Dublin, Ireland.
- Allocca L, Catapano F, Montanaro A, Sementa P, 2013, Study of E10 and E85 effect on air fuel mixing and combustion process in optical multi-cylinder GDI engine and in a spray imaging chamber, SAE Technical Paper 2013-01-0249.
- Bevan KE, and Ghandhi JB, 2005, PIV measurements of in-cylinder flow in a four-stroke utility engine and correlation with steady flow results, SAE Small Engine Technology Conference & Exposition, 2004-32-0005.
- Binjuwair SA, 2013, Characterization of flow structures inside an engine cylinder under steady state condition, Doctoral Thesis, Department of Aeronautical and Automotive Engineering, Loughborough University.
- Bittle JA, Knight BM, Jacobs TJ, 2010, Interesting behavior of biodiesel ignition delay and combustion duration, *Eng. Fuel.*, 24, 4166–4177.
- Bowditch FW, 1961, A new tool for combustion research: A quartz piston engine, SAE Technical Paper 610002.
- Dent JC, 1971, Basis for the comparison of various experimental methods for studying spray penetration, SAE Technical Paper 710571.
- Dierksheide U, Meyer P, Hovestadt T, Hentschel W, 2001, Endoscopic 2D-PIV flow field measurements in IC, 4th International Symposium on Particle Image Velocimetry Göttingen, Germany.
- Disch C, Kubach H, Spicher U, Pfeil J, 2013, Investigations of spray induced vortex structures during multiple injections of a DISI engine in stratified operation using high-speed-PIV, SAE Technical Paper 2013-01-0563.
- Dowell LJ, Gillies GT, 1991, Errors caused by baseline offset and noise in the estimation of exponential lifetimes, *Rev. Sci. Instrum.*, 62(1), 242–243.
- Eismark J, Balthasar M, Karlsson A, Benham T, 2009, Role of late soot oxidation for low emission combustion in a diffusion-controlled, high-EGR, heavy duty diesel engine, SAE Technical Paper 2009-01-2813.
- Hampson GJ., Reitz RD, 1998, Two-colour imaging of in-cylinder soot concentration and temperature in a heavy-duty DI diesel engine with comparison to multidimensional modelling for single and split injections, SAE Technical Paper 980524.
- Han YT, Ki-bum K, Lee G, 2008, The investigation of soot and temperature distributions in a visualized direct injection diesel engine using laser diagnostics, *Meas. Sci. Technol.* 19, 115402–115412.
- Heywood JB, 1988, *Internal Combustion Engine Fundamentals*, McGraw-Hill.
- Hotti SR, Hebbal O, 2011, Performance and combustion characteristics of single cylinder diesel engine running on karanja oil/diesel fuel blends, *Engineering*, 3(4), 371–375.
- Huang Z, Lu H, Jiang D, Zeng K, Liu B, Zhang J, Wang X, 2004, Combustion behaviors of a compression-ignition engine fuelled with diesel/methanol blends under various fuel delivery advance angles, *Bioresour. Technol.*, 95(3), 331–341.
- Husberg T, Gjørja S, Denbratt I, 2005, Piston temperature measurement by use of thermo-graphic phosphors and thermocouples in a heavy-duty diesel engine run under partly premixed conditions, SAE Technical Paper 2005-01-1646.
- Jeon J, Jong Lee T, Lim YS, Kwon SI, Park YH, Cha J, Lee K, Park S, 2013, Flame temperature distributions of biodiesel fuel in a single-cylinder diesel engine, *Fuel Process. Technol.*, 110, 227–234.
- Jeon J, Kwon SI, Park YH, Oh Y, Park S, 2014, Visualizations of combustion and fuel/air mixture formation processes in a single cylinder engine fueled with DME, *Appl. Energy*, 113, 294–301.
- Koch T, Schänzlin K, Boulouchos K, 2002, Characterization and phenomenological modeling of mixture formation and combustion in a direct injection spark ignition engine, SAE Technical Paper 2002-01-1138.
- Korczewski Z, 2011, Endoscopic image processing and analysis of pistons service failures of marine diesel engines, *Journal of Polish CIMAC*, 6(2), 127–136.
- Lee CS, Park SW, Kwon SI, 2005, An experimental study on the atomization and combustion characteristics of biodiesel-blended fuels, *Eng. Fuel.*, 19, 2201–2208.
- Lefebvre AH, 1991, Measurement and modeling of diesel sprays, *Atomization Spray*, 1(4), 467–478.
- Maurya RK, Agarwal AK, 2011, Experimental study of combustion and emission characteristics of ethanol fuelled port injected homogeneous charge compression ignition (HCCI) combustion engine, *Appl. Energy*, 88, 1169–1180.
- Miers SA, Ng H, Ciatti SA, 2005, Emissions, performance, and in-cylinder combustion analysis in a light-duty diesel engine operating on a fischer-tropsch, biomass-to-liquid fuel, SAE Powertrain & Fluid Systems Conference & Exhibition 2005-01-3670.
- Mtuli PL, Hill PG, 1996, Ignition delay and combustion duration with natural gas fueling of diesel engines, SAE Technical Paper 961933.
- Nauwerck A, Gindele J, Spicher U, Roskamp H, 2000, Investigation of the transient in-cylinder flow inside a two stroke engine with particle image- velocimetry, SAE Technical Paper 2000-01-0902.
- Nikolic D, Iida N, 2007, Effects of intake CO₂ concentrations on fuel spray flame Temperatures and soot formations, *P. I. Mech. Eng. D-J Aut.*, 221(12), 1567–1573.
- Nishiyama A, Jeong H, Ikeda Y, Sawada R, 2012, Application of endoscopic stereo PIV to 3D exhaust gas flow measurements in a practical SI engine, 16th Int. Symp on Applications of Laser Techniques to Fluid Mechanics, Lisbon, Portugal.
- Omrane A, Ossler F, Alden M, 2002, Two dimensional surface temperature measurements of burning materials, *P. Combust. Inst.*, 29(2), 2653–2659.
- Park SH, Hyung JK, Suh HK, Lee CS, 2009, Experimental and numerical analysis of spray-atomization characteristics of biodiesel fuel in various fuel and ambient temperatures conditions, *Int. J. Heat. Fluid. Fl.*, 30 (5), 960–970.
- Park SH, Hyung JK, Suh HK., Lee CS, 2009, A study on the fuel injection and atomization characteristics of soybean oil methyl ester (SME), *Int. J. Heat. Fluid. Fl.*, 30(1), 108–116.
- Pastor JV, Garcia JM, Molin S, 2000, Analysis methodology of diesel spray and flame by means of in-cylinder endoscopic imaging, *Advanced Sensors and Instrumentation Systems for Combustion Processes IEEE Seminar*, Birmingham, 13, 1-4.
- Pierpont DA, Montgomery DT, Reitz RD, 1995, Reducing particle and NO_x using multiple injection and EGR in a D.I. diesel, SAE Technical Paper 950217.
- Pundir BP, 2010, I. C. Engines: Combustion and Emissions, Narosa Publishing House, New Delhi, India.
- Reckers W, Schwab H, Weiten C, Befrui B, Kneer R, 2002, Investigation of flame propagation and cyclic combustion variations in a DISI engine using synchronous high-speed visualization and cylinder pressure analysis, 5th International Symposium on Internal Combustion Diagnostics, AVL Deutscwand, 27-32.
- Ricart LM, Reitz RD, 1996, Visualization and modelling of pilot injection and combustion in diesel engines, SAE Technical Paper 960833.
- Ricart LM, Xin J, Bower GR, Reitz RD, 1997, In-cylinder measurement and modelling of liquid fuel spray penetration in a heavy-duty diesel engine, SAE Technical Paper 971591.
- Richter M, Axelsson B, Aldén M, Josefsson G, Carlsson L-O, Dahlberg M, Nisbet J, Simonsen H, 1999, Investigation of the fuel distribution and the in-cylinder flow field in a stratified charge engine using laser techniques and comparison with CFD modeling, SAE International Fuels & Lubricants Meeting & Exposition, 1999-01-3540.
- Ryan TW, Shahed SM, 1994, Injection pressure and intake air density effects on ignition and combustion in a 4-valve diesel engine, SAE Technical Paper 941919.
- Sakata I, Ishisaka K, Yanagihara H, Sami H, 1990, Development of TOYOTA reflex burn (TRB) system in DI diesel, SAE Technical Paper 900658.
- Sauter W, Nauwerck A, Han K-M, Pfeil J, Velji A, Spicher U, 2006, High-speed visualization of combustion in modern gasoline engines, Second International Conference on Optical and Laser Diagnostics (ICOLAD 2005), *J. Phys.: Conf. Ser.*, 45, 120-132.
- Schänzlin K, Koch T, Boulouchos K, 2002, Characterization of the Combustion in a Direct Injection Spark Ignition Engine, SAE Technical Paper 2002-01-0834.
- Schänzlin K, Koch T, Tzannis A, Boulouchos K, 2001, Characterization of mixture formation in a direct injected spark ignition engine, SAE Technical Paper 2001-01-1909.
- Singh AP, Gupta A, Agarwal AK, 2015, Tomographic particle image velocimetry for flow analysis in a single cylinder optical engine, *SAE Int. J. Mater. Manf.* 8(2):472-481.
- Singh G, Singh AP, Agarwal AK, 2014, Experimental investigations of combustion, performance and emission characterization of biodiesel fuelled HCCI engine using external mixture formation technique, *Sust. Energy. Technol. and Asses.*, 6, 116-128.
- Spicher U, Kölmel A, Kubach H, Töpfer G, 2000, Combustion in spark ignition engines with direct injection, SAE Technical Paper 2000-01-0649.
- Wattanavichien K, Azetsu A, 2004, Studies of visualized diesohol combustion phenomena in IDI engine, C-2, CNG and Alternative Fuels, Oxygenated Fuels, 423-430, 6th International Symposium on Diagnostics and Modeling of Combustion in Internal Combustion Engines (COMODIA), Thailand.
- Werlberger P, Cartellieri W, 1987, Fuel injection and combustion phenomena in a high speed di diesel engine observed by means of endoscopic high speed photography, SAE Technical Paper 870097.
- Zhang L, Ueda T, Takatsuki T, Yokota K, 1995, A study of the effects of chamber geometries on flame behavior in a di diesel engine, SAE Technical Paper 952515.



A Review on the Effects of Biodiesel Blends on Compression Ignition Engine NO_x Emissions

Arun Balakrishnan*, Ramkumar N. Parthasarathy, Subramanyam R. Gollahalli

Combustion and Flame Dynamics Laboratory, School of Aerospace and Mechanical Engineering, University of Oklahoma, Norman, OK 73019, USA

ARTICLE INFO

Received : 26 August 2015
 Revised : 30 October 2015
 Accepted : 31 October 2015

Keywords:

biodiesel
 blends
 compression ignition engine
 NO_x emission
 fuel composition
 iodine number
 cetane number
 injection parameters
 fluid dynamics
 non-monotonicity.

ABSTRACT

Biodiesels are produced by the transesterification of corresponding triglyceride feedstocks of vegetable (example: soybean, canola, palm, karanja) or animal fat sources. Currently, the leading feedstocks are soybean oil in the U.S., canola oil and rapeseed oil in Canada and Europe, and palm, karanja, jatropha and other oils in Asia. Due to the cost and production considerations of these biodiesels, blending biodiesels with the petroleum fuels appears to be a prudent option in the near-term. The use of biodiesels in compression ignition engines results generally in a reduction in the emissions of carbon monoxide (CO), hydrocarbons (HC), and particulate matter (PM), but a slight increase in the oxides of nitrogen (NO_x) emission. The reported NO_x emissions do not exhibit definitive trends and the results are significantly influenced by many factors, including engine type and design, test cycle, start of injection, ignition delay, fuel composition, adiabatic flame temperature, radiative heat transfer, fluid dynamics and combustion phasing. Due to appreciable variations in the physical properties and the highly nonlinear nature of the combustion process, the NO_x emission with biodiesel blends *does not vary monotonically with the percentage of biodiesel* in the blend. Hence, the intricate dependence of NO_x on biodiesel and its blending effect cannot be completely explained under all engine type and operating conditions. Although the literature contains several studies on the performance and emissions of compression ignition engines fueled with neat biodiesels, the information on the effects of blends is scattered and has not yet achieved a definitive status to explain the blending effect on NO_x. Hence, this work was motivated to review the available data with respect to the NO_x emission from engines fueled with the petroleum diesel/biodiesel blends.

© 2016 ISEES, All rights reserved

1. Introduction

Biodiesels, considered as alternative fuels to petroleum diesel, are defined as fatty acid methyl or ethyl esters derived from triglycerides of vegetable oils or animal fats. The utilization of biodiesels reduces greenhouse gas emissions, assists in sustainable energy development, and enhances energy independence due to the renewable and biodegradable nature of these fuels. Besides being close to environmentally carbon-neutral, biodiesels have properties similar to those of petroleum fuels and can be blended with petroleum fuels and used in existing engines without major modifications. Furthermore, they contain fuel-bound oxygen while being free of aromatic content; therefore, blends of biodiesels and petroleum fuels present the capability of reducing soot emissions from engines. Extensive studies have been conducted on the potential of biodiesels and the feasibility of commercializing them in the long run, as presented in comprehensive reviews [Van Gerpen, 2005; Meher et al., 2006; Agarwal, 2007]. With the current understanding of combustion characteristics of biodiesels, only blending of biodiesel (usually in volumetric percentage) with petroleum fuels is considered feasible in the near-term due to limited current availability of the commercial biodiesels and the lack of experience on the long-term effects of handling,

transportation, storage, and combustion of these biodiesels and blends on the engines and the environment. Currently, there are about 250 biodiesel fueling stations in the United States providing a range of biodiesel blends ranging from B20 to B100 (number indicating the volumetric percent of biodiesel) with B20 being the widely available blend [Alternative Fuels Data Center, 2015]. However, the commercial use of biodiesel has not been widely popular. One reason is a dearth of definitive understanding about the long-term impact of biodiesel and their blends with petroleum fuels on engines, especially on the engine power performance and regulated gaseous emissions. Previous studies have revealed that the use of biodiesels and their blends in a compression-ignition engine resulted in an appreciable reduction in the emissions of particulate matter, HC and CO, but an increase in NO_x emissions, compared to the use of diesel fuel. This increase in NO_x emission is termed the biodiesel NO_x effect, which has remained a prolonged issue over this decade. The US Environmental Protection Agency [2002] has categorized NO_x as one of the key pollutants in engine emissions that can affect the human respiratory system.

The biodiesel usage in the U.S alone is expected to reach 4000 million gallons (15000 million liters) in 2030. Hence, a comprehensive knowledge of the effects of biodiesels and their blends on NO_x is required for the use

* Corresponding Author: E-mail: arun.bala@ou.edu

of biodiesels to become prevalent. Therefore, it is crucial to understand the effects of fuel properties and operating characteristics of the engines on biodiesel NO_x emission to develop enhanced mitigation and abatement techniques. The objective of this review article is to provide a comprehensive picture of the influence of fuel composition, engine calibration settings, fuel fluid dynamic parameters, and interactions of thermo-fluid-chemical parameters on the compression-ignition engine NO_x emission when fueled with biodiesel and their blends with petroleum fuels. Throughout this article, biodiesel blends are referred to as Bxx, where B stands for biodiesel irrespective of the feedstock and xx stands for the volumetric percent of biodiesel in the blend. For example, a B20 blend consists of 20% biodiesel and 80% petroleum diesel (by volume).

1.1. Statistics and significance of literature review

The United States Environmental Protection Agency, EPA [2002] has published a technical evaluation of the impact of biodiesel on exhaust emissions from compression ignition engines. EPA [2002] reported the averaged results of all these studies in which the use of biodiesel and its blends has a conspicuous and persistent favorable impact on the emissions of carbon monoxide (CO), hydrocarbons (HC), particulate matter (PM) and a relatively small negative influence on NO_x emission. The averaged results show a monotonic increase of up to 10% NO_x with neat biodiesel and a reduction of up to 50% and 68% of CO and HC respectively. Although the report provided an approximate trend of biodiesel effect on emissions of regulated pollutants, it does not contain sufficient experimental results for the blends having greater than 20% of biodiesel. The statistical

data employed for this study predominantly constitute emission results from B20 and B100. Moreover, these correlations have been developed based on a maximum likelihood curve-fitting approach instead of least-square regression. Hence, to provide a visual assessment of the goodness of fit, the report also compared the actual percent change in NO_x emissions of biodiesel and its blends from the corresponding emissions of the base fuel, which typically is the No. 2 diesel in most of the studies. The average effect of biodiesel on NO_x emission was seen to be small, but with a high variance, which resulted in difficulty in discerning a clear pattern. In the current review article, the engine NO_x literature has been updated with more recent works and findings along with the assessment compiled by Hoekman et al. [2011]; the total number of studies considered for this review with a breakdown of different volumetric proportion of blends and resultant change in NO_x emissions are presented in Table 1. This table contains the emission data from the engine tests reported and is grouped together as biodiesel (irrespective of the fuel feed stock), yet most of these studies employed biodiesel from soybean oil. Similar to the study by EPA, B20 constitutes the major data points with a scarce representation of higher biodiesel blend levels. We have plotted Figure 1 based on the data from Table 1 and Figure 2, an average value of the percentage variation of NO_x emission index (g/kW-hr) with biodiesel content in the blends. The wide scatter in the results from these studies reveals the indefinite trend of NO_x emission with the biodiesel content. This assessment again shows that the NO_x emission and its dependence on the fuel chemistry and content of biodiesel are difficult to ascertain since the effects are highly variable.

Table 1: Statistics of the effect of biodiesel content in the blend on NO_x emission from studies considered in this review

Biodiesel blend level (vol. %)	^a Average reduction of thermal input (MJ/kg) from base (diesel) fuel with biodiesel blending (%)	^b Variation of NO_x with biodiesel content					
		No of studies that show an increase	No of studies that show decrease	No of studies that show no change	Total number of studies considered	Average percentage variation of NO_x from base (diesel) fuel	Standard deviation of percentage variation of NO_x from base (diesel) fuel
1	0.05	1	3	6	10	-1	2
2	0.10	0	2	0	2	-3	1
3	0.14	8	0	2	10	5	4
5	0.24	17	6	1	24	4	5
6	0.29	2	1	0	3	4	7
7	0.34	2	1	0	3	1	3
10	0.48	19	17	2	38	1	8
20	0.96	163	67	5	235	2	9
30	1.44	18	5	1	24	5	9
35	1.68	7	2	1	10	3	9
40	1.92	16	3	0	19	7	9
50	2.41	21	13	6	40	3	8
65	3.13	2	0	0	2	5	0
100	4.81	92	27	3	122	7	14
Total		368	147	27	542		

^a Considering heating value of diesel as 44MJ/kg and average value of biodiesel as 39.6 MJ/kg (from Table.3); ^b Includes data collected from [Hoekman et al., 2011]

In summary, a potential drawback in compiling these results from a wide range of experimental studies would be an inconsistent comparison of emission data in terms of engine type, load settings, engine speed settings, and fuel-air ratio during combustion which are not the characteristics of fuels alone. These presentations pose a risk of observing trends that may not correspond only to the parameters under study. Based on these developed correlations, it is difficult to confidently predict the amount of NO_x emitted from any biodiesel-fueled engine and to conclude the biodiesel blending effect on NO_x emissions.

2. NO_x formation mechanisms with biodiesels

Nitrogen oxides present in atmosphere induce photochemical smog formation. The nitrogen oxides of environmental interest are NO, N_2O and NO_2 , among which the NO and NO_2 are collectively referred to as NO_x [Lissianski et al., 2000; Fattah et al., 2013]. The more stable NO always predominates over the other oxides of nitrogen in the combustion flue gas. The coupled concentrations of NO and NO_2 are decided by the fast radical reactions: NO_2 reacts with O, H and OH to form NO and NO

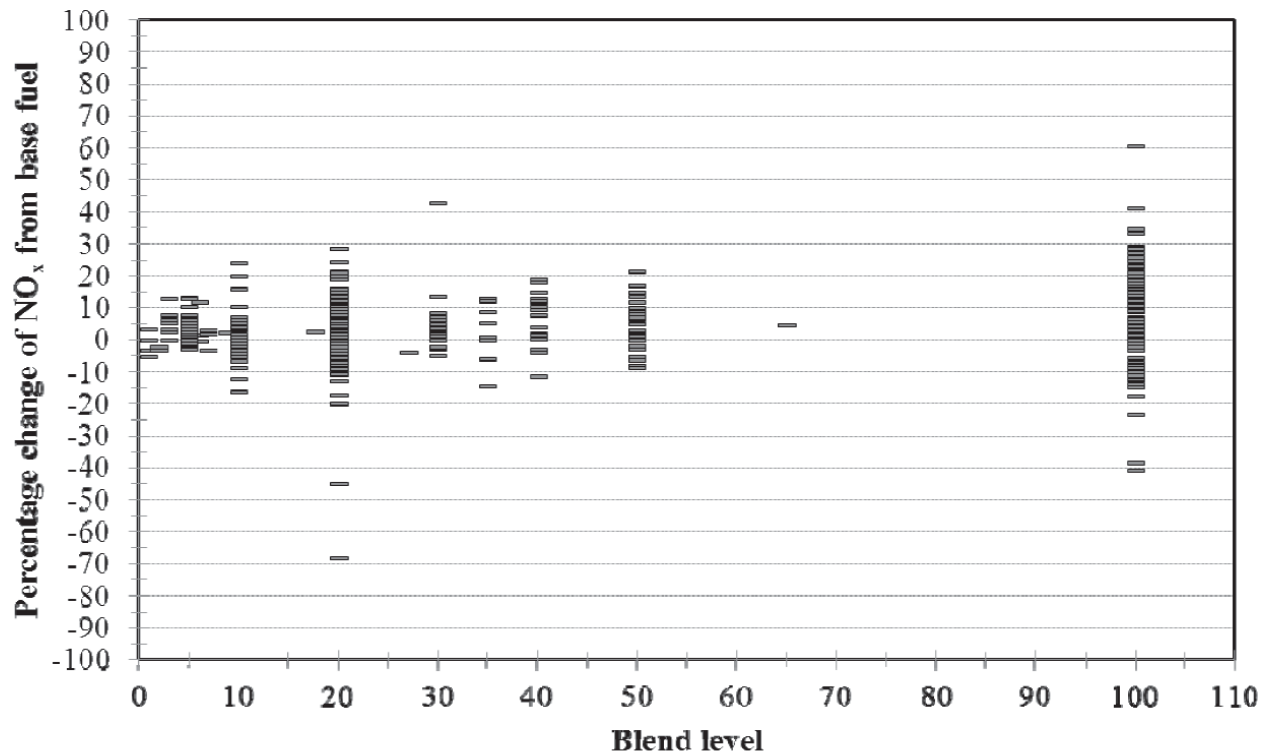


Figure 1 Percentage variations of NO_x emission from studies considered in this review

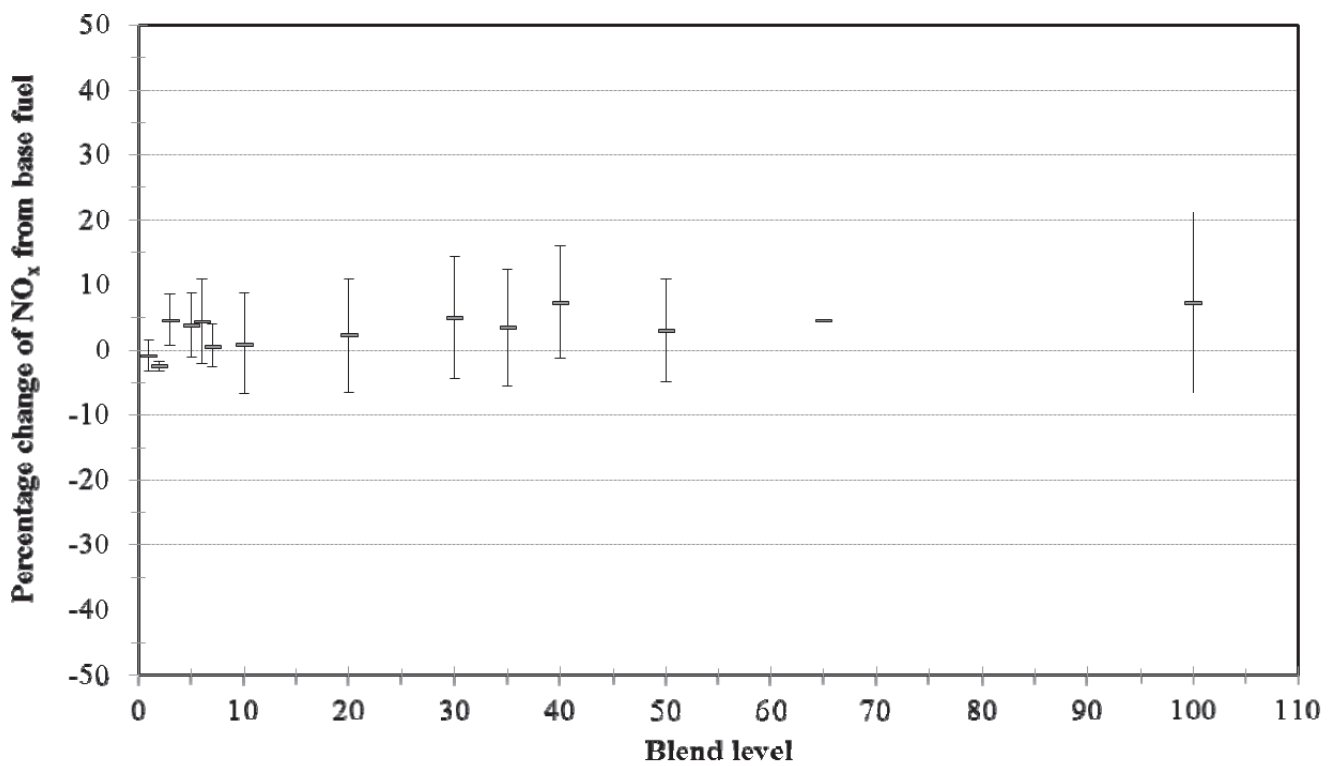


Figure 2 Average values of percentage variations of NO_x emission with standard deviation from tests considered in this review

reacts with HO₂ to form NO₂ [Lissianski et al., 2000]. In several high-temperature combustion processes, the predominant form of NO_x is produced as nitric oxide (NO), while the concentrations of NO₂ are typically less than 5% of total NO_x levels. NO_x abatement techniques require a basic understanding of the kinetics behind the NO_x-forming reactions. Although the NO_x reaction mechanisms have been detailed in the literature, the following section outlines some recent literature pertaining to the various mechanisms contributing to the formation of NO, and the general reactions involved in the formation of NO₂ and N₂O.

2.1 Nitric oxide (NO) emission

The atmospheric nitrogen is the prevalent source of nitrogen for NO production during the combustion of petroleum and FAME (Fatty Acid Methyl Ester)-derived fuels with air as the oxidizer. The thermal (Zeldovich), prompt (Fenimore), N₂O pathway, fuel-bound nitrogen and the NNH mechanism are the identified mechanisms for NO formation in diesel combustion which are summarized below.

2.1.1. Thermal mechanism

Thermal mechanism is the primary route by which NO formation occurs at temperatures typically above 1800K [Hoekman and Robbins,

2012]. At this high temperature, nitrogen (N₂) and oxygen (O₂) react through a set of chemical reactions in which the NO formation rate increases exponentially with temperature. The fundamental kinetic equations for thermal NO formation (R1-R3) along with their reaction kinetic parameters are presented in Table 2. The NO reaction rate is influenced by temperature, residence time and concentrations of nitrogen and oxygen in the combustion environment [Varatharajan and Cheralathan, 2012]. A correlation for the thermal NO emission index in automobile engines was developed by Saravanan et al. [2012]:

where NEI is the NO_x emission index (ppm), D is the density of fuel (kg/m³), C = 1 for loaded condition and C = 0 for unloaded condition, L is the load percentage (%), ID is the ignition delay (ms) and T_f is the flame temperature (K). It was observed that the NO_x emission index

$$NEI = 20956.69 * D * [1 + C[-9.91 * 10^{-3}L^2 + 1.608L - 18.431]] * \exp(2.9 * ID - 19.627) * \exp(4626.44/T_f) \quad (E.1)$$

predicted using this correlation agreed with experimental measurements within 20%.

Table 2 List of reactions with kinetic parameters*

	Reactions	A cm ³ /(gmol-s)	n	E _a / R _u K	Reference
R1	O + N ₂ ↔ NO + N	1.95E+14	0	38367	Loffler et al. [2006]
R2	N + O ₂ ↔ NO + O	6.40E+09	1	3160	Loffler et al. [2006]
R3	N + OH ↔ NO + H	3.80E+13	0	0	Loffler et al. [2006]
R4	CH + N ₂ ↔ HCN + N	4.40E+12	0	11060	Dean and Bozzelli [2000]
R5	CH ₂ + N ₂ ↔ HCN + NH	1.00E+13	0	37240	Dean and Bozzelli [2000]
R6	HCN + OH ↔ CN + H ₂ O	3.90E+06	1.83	5180	Dean and Bozzelli [2000]
R7	CN + O ₂ ↔ NCO + O	1.00E+13	0	0	Dean and Bozzelli [2000]
R8	O + N ₂ + M ↔ N ₂ O + M	4.13E+10	0	7890	Loffler et al. [2006]
R9	N ₂ O + O ↔ NO + NO	6.60E+13	0	13390	Loffler et al. [2006]
R10	O + NNH ↔ NO + NH	5.00E+13	0	0	Loffler et al. [2006]
R11	HO ₂ + NO ↔ NO ₂ + OH	2.20E+12	0	240	Dean and Bozzelli [2000]
R12	O + NO ₂ ↔ NO + O ₂	3.90E+12	0	120	Dean and Bozzelli [2000]
R13	H + NO ₂ ↔ NO + OH	1.30E+14	0	180	Dean and Bozzelli [2000]
R14	NH + NO ↔ N ₂ O + H	3.00E+18	-1.65	720	Dean and Bozzelli [2000]
R15	NCO + NO ↔ N ₂ O + CO	1.40E+18	-1.73	384	Dean and Bozzelli [2000]

*Rate constants are given by, $k = AT^n \exp(-E_a/R_u T)$

2.1.2. Prompt mechanism

Fenimore identified another important pathway resulting in NO formation which is termed as prompt NO mechanism. It is significant in some combustion environments where low-temperature fuel-rich conditions prevail, while the residence time is short [Fenimore, 1971]. Prompt NO is produced when hydrocarbon radicals react with nitrogen to form highly reactive cyano radicals such as HCN in the combustion chamber [Fernando et al., 2006]. Prompt NO is also more sensitive to the fuel chemistry than thermal NO because of the dependence on hydrocarbon radicals. Miller and Bowman [1989] studied the mechanism and modeling of nitrogen chemistry in combustion and concluded that the prompt NO mechanism was important in the NO formation and could not be neglected while estimating the total NO_x production, particularly in a fuel-rich combustion environment. The prompt NO mechanism involves a set of chemical reactions as shown by reactions R4 to R7 in Table 2. Prompt NO formation increases with equivalence ratio due to the availability of CH, CH₂ and HCN radicals that are prevalent in fuel-rich hydrocarbon flames, reach a peak, and decreases because of lack of oxygen. These hydrocarbon and cyano radicals are considered to be the significant contributors of prompt NO.

2.1.3. Fuel NO mechanism

Fuel NO is formed when the fuel-bound nitrogen reacts with excess oxygen during combustion and is negligible for both diesel and biodiesel combustion because of low nitrogen levels in the fuel; biodiesel has a

mean nitrogen concentration of only 0.02%. The presence of nitrogen-containing compounds such as pyridine, pyrrole etc. may also tend to form more fuel NO. This is due to the weaker C-N bond present in these chemical compounds compared to the N-N bond in molecular nitrogen. The fuel NO pathway involves the formation of nitro-radicals such as HCN, NH₂, NH, or CN, which then be oxidized to form NO [Fernando et al., 2006].

2.1.4. N₂O Intermediate mechanism

The intermediate mechanism (N₂O pathway) is another essential mechanism that becomes significant in high-pressure combustion processes [Dean and Bozzelli, 2000]. In this mechanism, the reaction occurs between N₂ and atomic oxygen to form intermediate N₂O by a three-body recombination reaction (R8) where the collision partner M collectively represents all the molecules present in the combustion medium and plays a key role in the execution of this reaction. The N₂O formed in reaction (R9) can then react to form NO.

2.1.5. The NNH mechanism

Under certain combustion regions like flame fronts where atomic concentrations are high, (R10) contributes to NO production. This mechanism requires interaction between hydrogen atoms and molecular nitrogen to form highly reactive NNH radicals which further react with atomic oxygen to form nitric oxide [Dean and Bozzelli, 2000].

2.2 Nitrogen dioxide (NO_2) emission

In the previous section, several reactions that lead to the formation of NO were discussed. Under certain conditions, a significant amount of NO can be converted to NO_2 . The fastest flame reaction forming NO_2 is R11 (Table.2), which is important whenever the concentration of HO_2 is significant, typically in the temperature range of 600 to 1000 K under fuel-lean conditions. However, at higher temperatures HO_2 dissociates quickly into H atoms and O_2 , and the higher prevailing concentrations of H, O and OH lead to more rapid NO_2 loss through the reactions (R12 and R13). This rapid loss of NO_2 is significant and is reflected as a lower NO_2 concentration in the combustion flue gas.

2.3 Nitrous oxide (N_2O) emission

At low combustion temperatures and high pressures, nitrous oxide formation by the ter-molecular reaction (R8) is significant. The N_2O formed in this reaction reacts with oxygen atoms exothermally to form NO (as discussed in section 2.1.4). Various nitrogen-containing radicals contribute to the formation of N_2O as in R14 and R15. However, the N_2O formed in these reactions undergoes further reactions forming NO which is more stable than N_2O .

In a compression ignition engine, the combustion reactions are characterized by high temperature, varying residence time depending on the injection timing, localized fuel rich conditions (though overall fuel lean) and high pressure. These reactions favor NO formation predominantly, in different pathways described above, out of which the thermal and prompt mechanisms are considered to be significant in the biodiesel engine combustion.

3. Experimental evidences of biodiesel impact on NO_x emission from compression-ignition engine exhaust

This section reviews the experimental studies on various aspects of engine operation, fuel properties and combustion processes and their influence on the emission of NO_x measured in the engine exhaust.

3.1. Effects of fuel composition

The fuel composition is a broad factor which comprises of influential parameters such as fuel feedstock, level of unsaturation, biodiesel blend level, oxygen content and cetane number. The following section discusses the effect of these parameters on the NO_x emission from the compression ignition engines.

3.1.1 Biodiesel feedstock / Level of unsaturation

Several studies reported differences in NO_x emission of biodiesels from different feedstocks [Graboski et al., 2003; Saravanan et al., 2009; Saravanan et al., 2010; Hoekman and Robbins, 2012; Varatharajan and Cheralathan, 2012]. Graboski et al. [2003] conducted experiments with neat methyl esters and ethyl esters in a 6- cylinder, 4- stroke, direct injection diesel engine to understand the effect of hydrocarbon chain length on the NO_x formation with saturated methyl esters based on their composition - lauric (C12), palmitic (C16) and stearic (C18) acids and found that esters with shorter carbon chain produced higher NO_x emissions. For example, the specific NO_x emission index of methyl stearate (C18) was about 8% lower than that of methyl laurate (C12). The authors also found a strong linear relationship between increasing NO_x with level of saturation (number of double bonds) in the fuel. For example, the specific NO_x emission index of C18 ester with three double bonds was 16% higher than that of C18 ester with one double bond. Possibly, the double bonds resulted in some pre-combustion chemistry that increased NO_x formation. Finally, the authors concluded that the NO_x emissions increased due to the decrease in average carbon chain length and increase in level of unsaturation; therefore, the most intrinsic way to revamp the emission performance was to alter the fuel chemistry, since molecular structure was the basis of fuel properties such as cetane number, density, boiling point and ignition delay. It is now widely acknowledged that increasing unsaturation and decreasing carbon chain length both lead to an increase in NO_x emission. This information has been developed from the experimental and numerical demonstration in several works [Graboski et al., 2003; Sun et al., 2010; Xue et al., 2011; Hoekman and Robbins, 2012; Varatharajan and Cheralathan, 2012; Palash et al., 2013] involving pure FAME components as well as practical biodiesel fuels employing a wide variety of engines and test cycles. Lin et al. [2009] found that palm oil methyl ester (POME) and palm kernel oil methyl ester (PKOME) resulted in a lower increase (15% and 5% respectively) in NO_x concentration (ppm) and a significant reduction (59% and 73% respectively) in smoke emissions than petroleum diesel and vegetable oil

methyl ester (VOME) fuels (soy methyl ester, peanut oil methyl ester, corn oil methyl ester, sunflower oil methyl ester, rapeseed methyl ester and waste fried oil methyl ester). The authors attributed this behavior to the more saturated carbon bonds of POME (about 50%) and PKOME (about 80%), when compared to other VOME fuels, and suggested that a fuel with more saturated carbon bonds would result in reduced NO_x emissions. The exact pathways by which the fuel composition effects influence NO_x are still ambiguous, but these parameters are recognized to critically influence the observed NO_x emissions.

3.1.2 Biodiesel content

Many publications in the literature suggest that NO_x emission increased with the biodiesel content in the blend. Lertsathapornasuk et al. [2008] noted that the NO_x emission index (g/kW-h) increased about 12% and 3% for neat palm biodiesel (B100) and B50 than diesel at 25% load condition; and an increase of about 26% and 9% in NO_x emission index for B100 and B50 while maintained the engine speed at 1500 rpm. A study by Luján et al. [2009] on high speed direct injection, 4-cylinder, diesel engine with high pressure common-rail fuel injection system during the standardized MVEG-A cycle (European Motor Vehicle Emission Group A) simulated the road load conditions. It was fueled by biodiesel (from vegetable oil) and its blends B30, B50 and B100. The authors observed that the increase in NO_x concentration (ppm) for B30, B50 and B100, compared to the base diesel fuel, was 21%, 26% and 45%, respectively. Similar trend was observed by Buyukkaya [2010] with rapeseed methyl ester/ diesel blends. Gumus and Kasifoglu [2010] tested three blends of apricot seed kernel oil methyl ester (B5, B20 and B50) with diesel fuel in a compression ignition engine and found a monotonic increase in NO_x concentration with the biodiesel content. They attributed this behavior to the fuel-bound oxygen of the biodiesel.

On the other hand, Kalligeros et al. [2003] found a monotonic decreasing trend of NO_x concentration in the biodiesel blends containing 10%, 20%, and 50% of two types of methyl esters from sunflower oil and olive oil, in a single-cylinder diesel engine. At 3.80 kW load, B10, B20 and B50 of sunflower oil methyl ester with marine diesel produced about 3%, 5% and 6% lower NO_x concentration, while B10, B20 and B50 of olive oil methyl ester produced about 8%, 14% and 14.5% lower NO_x concentration than marine diesel. The variation in the NO_x reduction potential between the different biodiesel feedstock was attributed to the difference in cetane number of biodiesels; it was hypothesized that the higher cetane number of olive oil methyl ester (CN: 61) than that of sunflower oil methyl ester (CN: 58) resulted in increased reduction of NO_x concentration; the cetane index of marine diesel was reported as 46.

Interestingly, some other publications in the literature showed that the NO_x emissions varied non-monotonically with the biodiesel content in the blend [Labeckas and Slavinskas, 2006; Lin et al., 2007; Pereira et al., 2007; Fontaras et al., 2009; Aydin and Bayindir, 2010]. The authors attributed these variations to the differences in the degree of evaporation and the combustion processes in the engine, since the calibration settings of the conventional diesel engine could have been not ideal for all proportion of biodiesel blends at all operating regimes. A non-monotonic NO_x variation was observed in a water-cooled direct injection diesel engine fueled with polanga methyl ester and its blends (20, 40, 60, and 80%) with diesel [Sahoo et al., 2007]. The NO_x concentration from B20 was found to be 2% higher than diesel while neat biodiesel produced 4% lower NO_x . The authors attributed the variations to the differences in compression ratio, residence time and temperature distribution among the tested fuels. Biodiesels derived from jatropha, karanja and polanga oil and their blends (B20, B50 and B100) were tested in a 3 cylinder compression ignition engine [Sahoo et al., 2009]. It was observed that the karanja and polanga biodiesels and their blends had a monotonically increasing NO_x with the biodiesel content (with peak NO_x occurred with neat biodiesels; KB100 and PB100 produced about 15% and 21% higher NO_x (g/kW-h) than that of diesel), while a non-monotonicity was observed in NO_x with jatropha oil biodiesel. JB20 showed a 20% increase in brake specific NO_x emission index (g/kW-h) compared to baseline diesel, whereas JB50 and JB100 showed an increase of 15% and 17% respectively when compared to diesel. Several of these studies suggested that it was not appropriate to linearize the biodiesel blending effect on NO_x emissions due to the varied operating conditions, engine calibration and combustion phases.

3.1.3 Oxygen content

The fuel-bound oxygen content of the blend is proportional to the volumetric concentration of biodiesel in the blend. Generally, the increased NO_x emissions in biodiesel and their blends are attributed to the higher

oxygen content in the biodiesel [Godiganur et al., 2010; Gumus and Kasifoglu, 2010] due to a linear increasing trend of NO_x with the increase in mass percentage of fuel oxygen. However, there are studies that do not agree with this linear increase; a linear decrease [Kalligeros et al., 2003] in NO_x emission or a non-monotonic increase or decrease with the oxygen content in the fuel [Sahoo et al., 2007; Fontaras et al., 2009; Aydin and Bayindir, 2010] have been documented.

Canakci [2005] studied No. 2 diesel fuel (no fuel bound oxygen), No. 1 diesel fuel (no fuel-bound oxygen), SME (11% oxygen by mass / 3.6% oxygen by volume) and B20 (20% SME and 80% No.2 diesel) (2.2 % oxygen by mass / 0.7 % by volume) in a turbocharged diesel engine and observed the brake specific NO_x index (g/kWh) of the SME and B20 blend were increased by 11% and 1%, respectively compared to the No. 2 diesel. Surprisingly, the NO_x emission index of No. 1 diesel fuel was 6% lower than that of No. 2 diesel fuel, while there was no appreciable difference of oxygen concentration in the exhaust between the fuels tested. Therefore, in addition to the fuel-bound oxygen effect of biodiesel, more research is required to identify the properties that impact the combustion reactions favoring NO_x emission. Puhan et al. [2005] questioned the availability of fuel-bound oxygen for NO_x formation and argued that the esters might decarboxylate and form CO_2 early during the combustion. It is evident that additional studies are essential to understand the significance of fuel-bound oxygen effect, especially their impact in the formation of NO_x during combustion in engines.

3.1.4 Effects of cetane and iodine numbers

Auto-ignition of the injected fuel is a critical factor in the performance and operation of compression ignition engines. Cetane number is a property of the fuel that quantifies the self-ignition characteristics and ignition delay time of a fuel in an engine cycle; the higher the cetane number, the shorter the ignition delay [Pulkrabek, 2004]. Cetane numbers for various esters of the saturated fatty acids ranging from C8 to C18 have been determined according to ASTM D-613. For methyl esters, the cetane numbers were found to increase nonlinearly with the fatty acid chain length [Klopfenstein, 1985]. The higher cetane number of biodiesel reduces the ignition delay and also leads to the advancement in combustion. Consequently, with the availability of oxygen, higher temperature together with longer residence time, may lead to the increase of NO_x emissions. Several researchers, e.g., Lim et al. [2014] used this reasoning to describe the increased NO_x emissions with biodiesel content. However, this reasoning is debatable. Higher cetane number results in not only an early onset of combustion, but also leads to lower amount of fuel burning in the premixed-combustion mode, which result in lower temperature and residence time in the combustion chamber, causing a lower NO_x formation. Wu et al. [2009] observed that the brake specific NO_x emission index (g/kWh) of palm methyl ester (PME) was 7% lower than that of waste oil methyl ester (WME), even though both had almost the same oxygen content of about 11.2% by mass. This was credited to the higher cetane number of PME (64 for PME compared to 56 for WME) which could reduce ignition delay and the amount of fuel consumed in the premixed phase, resulting in a reduction of in-cylinder temperature and subsequently reduced NO_x emission. Many authors [Graboski et al., 2003; Kalligeros et al., 2003; Puhan et al., 2005; Knothe et al., 2006; Karavalakis et al., 2009] concluded that NO_x emissions decreased with an increase in cetane number.

3.2. Influence of type of engine and test cycle

Engine type and its test cycles could strongly influence the NO_x emission of biodiesel. Tat [2003] demonstrated that the NO_x emission from compression ignition engines was significantly influenced by the variation in injection timing and advance due to the impact of fluid properties such as density, isentropic bulk modulus (compressibility) and viscosity. Karavalakis et al. [2009] studied the exhaust emission characteristics of ultra-low sulphur diesel and soy biodiesel blends at proportions of 10% and 30% by volume in a Euro 4 common rail injection diesel engine over various engine test cycles namely New European Driving Cycle (NEDC) and non-legislated Artemis driving cycles which simulate urban, rural and highway driving conditions in Europe. It is interesting to note that driving test cycles significantly influence the amount of NO_x emitted during the operation. Among the three Artemis driving cycle conditions, B10 and B30 produced higher NO_x (g/km) than the base line diesel. During rural driving condition, B10 and B30 produced the highest increase in NO_x as 14% and 18% respectively. However, in NEDC test cycle, NO_x emissions were slightly reduced for both B10 and B30 by 3% and 4% respectively. The authors attributed this observed reduction in NO_x to the smooth acceleration profile of NEDC, which dominated the NO_x emission

mechanism than the physicochemical characteristics of biodiesel. Moreover, the Artemis driving cycles were more aggressive and transient, which would inherently favor the increase of NO_x emissions. Hence, although the physicochemical properties and fuel chemistry properties such as saturation level and cetane number play certain roles in the NO_x emissions, their relative importance when compared to the engine parameters and the nature of test cycle in certain conditions are inconclusive. As a part of the program to quantify the effect of biodiesel fuels on engine NO_x emissions, EPA [2010] examined chassis dynamometer tests on heavy duty diesel engines to study the NO_x effects of soy-based biodiesel over light, medium and heavy duty cycles. The results indicated that brake specific NO_x index increased as a function of average cycle load, by about 5% for high loaded cycles; 2.5% increase in medium loaded cycles. However, in lightly loaded cycle, results showed inconclusive trends in NO_x emissions (where a decrease and increase in NO_x emissions was observed by 1% and 2% respectively in two different trials), and hence the load-dependent nature of test cycles and their influence on NO_x emissions could not be neglected. Osborne et al. [2011] tested soy biodiesel, diesel and their blends (B2, B10, B20) in a locomotive operated in two different cycles namely line haul and switch cycle. The changes in cycle weighted average of NO_x (g/kWh) for B2, B10 and B20 were comparable between two cycles, while B100 in switch cycle increased NO_x by about 15% over the line haul cycle. Fontaras et al. [2014] studied rapeseed methyl ester and its blends B10, B20 and B50 with diesel in three different vehicles (equipped with different exhaust after treatment technologies) over test cycles namely NEDC, which is a standard test cycle in Europe and real world testing cycles such as Artemis Urban and Artemis Road. In general, among all the tested conditions, NO_x (g/km) increased up to 20% with B50 in some cases while most showed an increase in the range of 1 to 10% depending on the blend and the vehicle. Serrano et al. [2015] tested diesel and 20% biodiesel blend (from soy and palm feedstock) in three different test cycles, namely NEDC, URBAN and EXTRA URBAN test cycle. In all three cycles, B20 had lower NO_x emission index (g/km) than diesel, but the reduction percentage varied with cycles as 10%, 20% and 5% respectively. In summary, all these studies reported different trends with different combination of engine test cycles, biodiesel feedstock and content. Hence the biodiesel and its blending effect on NO_x are inconclusive in terms of engine test cycle since several engine and combustion parameters influence the emission characteristics of a particular test cycle which can overshadow the actual emission potential of a particular fuel or fuel blend.

3.3. Effect of injection timing

The fuel injection is an important process in the engine operation and the timing of fuel injection into the combustion chamber is critical and affects performance and emissions to a large extent. The injection process is greatly influenced by the fluid dynamic properties of the fuel and NO_x formation appeared to be dependent on the start of injection timing in compression ignition engines. [Tat et al., 2000; Tat and Van Gerpen, 2003; Boehman et al., 2004; Agarwal et al., 2013]. Carraretto et al. [2004] studied the effect of advance in injection timing (at three crank angles namely, 21°, 24° and 27°) with neat biodiesel produced from vegetable oil in a 4-stroke diesel engine. They observed that NO_x concentration (ppm) increased with the injection advance by about 41% between 21° and 24° and by about 67% between 24° and 27° at both maximum torque and power speeds. Tsolakis et al. [2007] observed that the retarded injection timing by 3° reduced NO_x concentration (ppm) while testing with rapeseed methyl ester (by about 17%) and its 50% blend (by about 23%) with diesel in a diesel engine. Szybist et al. [2007] studied the influence of methyl oleate (mono-unsaturated fatty compound) present in soy biodiesel. The experiments were conducted at three different injection timings - early, mid and late. In early injection mode, where more premixed burn fractions occur, neat soy biodiesel and B20 produced about 11% and 3% more brake-specific NO_x (g/kWh) than ULSD. As the fuel injection timing was retarded, in mid and late injection modes, the differences in NO_x emissions between the fuels were reduced. In late injection mode, where more diffusion burn fractions occur, the NO_x emitted from all tested fuels were comparable. Hence, the authors suggested that retarding the injection timing was a potential way of reducing NO_x emissions. In agreement with this claim, a reduction in brake-specific NO_x emission index was observed with the retarded start of combustion (SOC) timing for SME/diesel blends [Moscherosch et al., 2010] and CME/diesel blends [Sequera et al., 2011].

3.4. Effect of engine speed

Engine speed also plays a critical role in the formation of NO_x in

compression ignition engines. Several studies proposed that NO_x emissions decreased with engine speed [Lin and Li, 2009; Imtenan et al., 2014]. The NO_x concentration (ppm) decreased by about 23% between engine speeds of 800 rpm and 2000 rpm for petroleum diesel and biodiesels from cooking oil and marine fish oil in a 4-stroke direct injection, naturally aspirated diesel engine [Lin and Li, 2009]. The authors concluded that, although the increased engine speed caused an increase in the temperature and pressure of burning gas, the reduction of ignition delay resulted in the reduction of residence time available for NO_x formation. Interestingly, different trends of NO_x emission was reported at two different engine speeds (2000 and 4000 rpm) at the full load condition when diesel, biodiesel from waste cooking oil and their blends of 10%, 20%, 40% and 60% (by volume) were studied in a common rail Euro 3 diesel engine [Zhang et al., 2008]. At 2000 rpm, a monotonic increase of NO_x concentration (ppm) was observed with the biodiesel content in the blend, especially with blends higher than 40% of biodiesel content. B100 had about 13% higher NO_x concentration than the diesel. However, at 4000 rpm, the NO_x concentration did not show any variation with biodiesel content. The authors attributed the observed trends to the common rail injection system where the impact of advanced injection of biodiesel due to higher bulk modulus, density and mechanical pump is no longer a significant factor.

Moreover, a non-monotonic variation of NO_x was observed with engine speeds in some studies. Usta [2005] observed different effects of engine speed on NO_x concentration (ppm) at different conditions, that is, as engine speed was increased (between 1500 rpm and 3000 rpm), the NO_x concentration increased by about 74% at full load, and increased by about 33% at three fourth of rated load, but gradually decreased by 28% at half load for both diesel and its blend (D82.5/TSOME17.5, by volume) with tobacco seed oil methyl ester. Non-monotonic variation of NO_x was also reported in several other studies which employed biodiesels different feedstocks ranging from waste frying oil [Utlu and Kocak, 2008], tall oil [Keskin et al., 2008], vegetable oil [Chokri et al., 2012], cooking oil [Arslan, 2011], calophyllum inophyllum linn oil which consists of mostly unsaturated fatty acids [Fattah et al., 2014]. A limited source of explanation has been reported in the literature on the engine speed effect on NO_x formation. Several studies attributed various parameters such as availability of oxygen, in-cylinder combustion temperature and residence time to the variation of NO_x between fuels; but no explanation was given to the non-monotonic effect of engine speed on NO_x emissions.

3.5. Effect of engine load

The biodiesel NO_x effect was significantly influenced by engine load when tested with biodiesel and its blends with diesel in diesel engines. Several studies reported a monotonic increase in NO_x with engine load due to higher temperature generated at higher engine load [Zhang and Boehman, 2007], while employing biodiesel blends from different feedstock as Neem oil [Sharma et al., 2009], Mahua and Fish oil [Godiganur et al., 2010], Jatropha oil [Tan et al., 2012; Padhee and Raheman, 2015] and Croton oil [Osawa et al., 2015]. The authors attributed this monotonic increase of NO_x emissions to the increased engine temperature and pressure, availability of oxygen and increased flow rate of the biodiesel blends.

However, Murillo et al. [2007] found a surprising decrease in NO_x emissions with load in a single-cylinder, naturally aspirated direct injection diesel engine. A substantial reduction of about 60% in the specific NO_x emission (g/kWh) between 25% load and full load when tested with B100 was observed. The authors attributed this trend to the increase in turbulence inside the cylinder, which contributed to a quicker combustion and resulted in lower residence time of the species in the high temperature zones. Agarwal and Rajamanoharan [2009] tested karanja biodiesel and blends (B10, B20, B50 and B75) with diesel in a single cylinder agricultural engine. The authors observed that the neat biodiesel and all the tested blends had comparable NO emission index (g/kWh), while they were about 45% lower than that of diesel at 20% load.

On the other hand, a non-monotonic response of NO_x for the use of biodiesels and their blends with diesel has been widely reported in the literature [Raheman and Phadatar, 2004; Sureshkumar et al., 2008; Dhar et al., 2012; Agarwal and Dhar, 2013; Chavan et al 2015]. A non-monotonic variation of NO_x with the biodiesel content over a wide range of loads was observed by Raheman and Phadatar [2004] while testing karanja methyl ester and its blends (B20, B40, B60, B80, by volume) with diesel in a single cylinder, 4-stroke, water-cooled direct injection diesel engine. At full load condition, B20 and B80 produced about 23% lower NO_x concentration (ppm) than diesel; while B60 and B100 produced about 38% lower NO_x than diesel and B40 recorded about 15

% lower NO_x than diesel. Hence, it is clear that NO_x is sensitive to load where changes in the loading conditions could possibly reverse the NO_x formation trends. Sureshkumar et al. [2008] also observed a non-monotonic variation in NO_x concentration with biodiesel content for a wide range of loading conditions while testing pongamia pinnata methyl ester and its blends (B20, B40, B60, B80, by volume) in a similar engine. At 75% load condition, B20 and B100 produced 8% and 25% lower NO_x concentration (ppm) than diesel; while B40, B60 and B80 produced about 38% lower NO_x than diesel. Though the NO_x concentration was decreased with the biodiesel content in the blend, the extent of reduction in NO_x was not proportional with the biodiesel content. Agarwal and Dhar [2013] tested karanja biodiesel and blends (B10, B50) with mineral diesel in a direct injection diesel engine. It was observed that B50 and B20 consistently produced higher NO (g/kWh) on an average of about three times than diesel, while B10 and B100 produced comparable or slightly higher NO_x than diesel. Chavan et al. [2015] studied the emission characteristics of jatropha biodiesel and its blends B10, B20 and B30 with petroleum diesel in a 4-stroke variable compression ratio engine at five different compression ratios (CRs) namely 14, 15, 16, 17 and 18 over a range of loads. It was observed that NO_x concentration (ppm) increased with increasing load and compression ratio. It may be due to the increase in temperature at high loads and lower ignition delay due to higher compression ratio that would result in increased pressure and temperature inside the cylinder. However the NO_x emission due to biodiesel and blending effect had neither a monotonic increase nor a monotonic decrease with load and CRs. For example at full load, diesel had lowest NO_x concentration (ppm) at CR 14 and CR 16; B100 had lowest NO_x concentration at CR 15; B30 had lowest NO_x concentration at CR 18 while diesel and B30 had lowest NO_x concentration at CR 17. Similarly, a non-monotonic trend was observed with different loads at a given compression ratio. Hence, the engine parameters and the associated phasing of combustion complicate the understanding of already entangled biodiesel and its blending effect on NO_x formation in compression ignition engines.

3.6. Fluid dynamics effects

Fluid dynamics of the fuel spray is an important and highly complex phenomenon that significantly influences the phasing of combustion [Sirignano, 1993]. The fuel spray characteristics such as injector penetration length, atomization and mean droplet size along with flow field and heat transfer interactions between droplets are critically influenced by various physical properties of the fuel. Especially, the differences in properties such as density, viscosity, surface tension, etc., between biodiesel and petroleum fuels influence the combustion process and can affect NO_x emission [Allen and Watts, 2000; Lee et al., 2005; Ejim et al., 2007; Suñ et al., 2007; Yuan et al., 2007]. The fuel viscosity and surface tension of fifteen neat biodiesels were reported in [Allen and Watts, 2000] using a regression model developed based on experimental results from five different biodiesels. The authors claimed that viscosity and surface tension, in turn the Sauter mean diameter (SMD) of the spray, could be predicted from the fatty acid composition of biodiesels. A maximum reduction of 50% in viscosity and 8% in surface tension between rapeseed methyl ester and coconut oil methyl ester was predicted and was attributed to the differences in carbon chain lengths; major fatty acid constituents in coconut oil methyl ester have shorter carbon chain length while rapeseed methyl ester has constituents with longer carbon chain length. The SMD of coconut oil methyl ester spray was comparable to that of petroleum diesel spray, also confirmed by Ejim et al. [2007], while rapeseed methyl ester spray had 40% higher SMD than that of diesel spray; other biodiesel sprays have about 25% - 29% higher SMDs than diesel fuel spray. It is also indicated that the discrepancies in the reported data among literature sources could not be verified since most of the studies did not report the extent of the reaction and the presence of triglycerides in the fuel after the transesterification process. The authors concluded that even a 6% by mass of triglyceride (canola oil) in the canola methyl ester could result in a 12% increase in viscosity of the biodiesel. The biodiesel blending effects on the viscosity and surface tension of the final blended fuel was studied by Lee et al. [2005] in a common-rail diesel engine with soy biodiesel and its 10%, 20% and 40% volumetric blends with petroleum diesel. It was observed that the kinematic viscosity and surface tension of the fuel linearly increased with the biodiesel content; however, the blending ratio had a minimal effect on the spray development. Lower injection velocity of biodiesel due to higher viscosity, and the associated increase in friction between biodiesel spray and nozzle surface causes shorter spray tip penetration; while higher SMD of the biodiesel spray causes a longer tip penetration. These two compensating effects resulted in a similar spray tip

penetration between diesel, biodiesel and their blends. Ejim et al. [2007] reassessed the findings by Allen and Watts [2000] and reported comparable SMDs among neat palm, soybean, cotton seed, peanut and canola biodiesel and their corresponding B5 and B20 blends with No.2 diesel. In a computational study by Yuan and group [2007], for a given engine speed and load, the maximum spray cone angle of diesel and soy biodiesel was found to be 47.5° and 30° and soy biodiesel produced about 8% higher brake-specific NO_x than diesel. When the spray cone angle of soy biodiesel was matched with diesel (47.5°), the brake-specific NO_x was reduced by 15% between cone angles of 30° and 47.5° of soy biodiesel spray. The authors concluded that a narrow spray angle could significantly emit higher NO_x since the narrow sprays induce strong stratification of fuel vapor which brings about local rich or stoichiometric regions that contribute to higher NO_x. Yuan and Hansen [2009] predicted that NO_x (g/kWh) decreased up to 3.5% when the viscosity of SME was decreased to match with petroleum diesel fuel. They also suggested that smaller spray cone angles and advanced start of injection were the main reasons for increased NO_x emission of biodiesel. They concluded that the decreased spray cone angle and increased spray penetration might increase NO_x emission. Agarwal and Chaudhury [2012] investigated the spray characteristics in a constant volume spray chamber with diesel, karanja biodiesel and their blends, B5 and B20, and concluded that B100 had highest spray tip penetration, cone angle and spray area followed by B20, B5 and diesel.

In addition to density, surface tension and viscosity, the boiling point of biodiesel could also significantly alter the spray characteristics; higher boiling point of biodiesel increases the combustion duration and cylinder gas temperature both of which could favor NO formation [Oszezen et al., 2008]. In a recent study, the spray, combustion and exhaust emission characteristics of soy biodiesel in a direct injection common-rail diesel engine were investigated by Yoon et al. [2009] who observed that biodiesel produced larger droplet size (about 12%), similar spray structure, and longer spray tip penetration (about 8% higher) into the cylinder than conventional diesel, which resulted in an increased indicated specific NO_x emissions of soy biodiesel by about 19% higher than that of diesel. Ye and Boehman [2010] studied the effect of engine injection strategies on the biodiesel NO_x effect with a direct injection diesel engine fueled with ultra-low sulphur diesel and its blend with soy biodiesel (B40). For a given speed and load, a higher volume of biodiesel has to be supplied because of its lower heating value compared to petroleum diesel. The increase of fuel consumption could be accomplished by either higher injection pressure or injection duration, which would result in increased NO_x emission. Injection characteristics such as mean injection rate, mean injection pressure, injection delay and injection duration increase with the biodiesel content, which could favor NO_x formation at certain conditions. Hence, the above discussed physical properties and their effects on the fluid dynamics of the fuel spray and atomization have critical impact on the combustion and emission characteristics of a fuel at any particular operating condition.

4. Conclusions

In this article, the key parameters that influence NO_x emissions in diesel engines fuelled with biodiesel blends were identified and broadly classified as fuel chemistry effects, engine control effects and fluid dynamics effects. In most engine studies, with a few exceptions, biodiesel or biodiesel blends resulted in increased NO_x emission compared to baseline diesel; however, *the change in NO_x emission for blends varied non-monotonically* with the biodiesel content due to a complex dependence of NO_x formation on various factors at various conditions. The relative significance and extent of influence of various physico-chemical factors reviewed in this article differ with engine type, cycle and operating conditions. Hence, a holistic approach is needed to investigate the biodiesel blending effect on NO_x emission by discerning the influential factors and then integrating the appropriate individual findings along with the corresponding coupled effects of thermo-fluid-chemical interactions for the particular combustion environment.

Acknowledgment

The authors acknowledge the financial support received from National Science Foundation, U.S. Department of Energy and John Zink LLC.

References

- Agarwal AK, 2007, Biofuels (alcohols and biodiesel) applications as fuels for internal combustion engines, Progress in energy and combustion science, 33, 233-271. doi:10.1016/j.pecs.2006.08.003.
- Agarwal AK, Rajamanoharan K, 2009, Experimental investigations of performance and emissions of Karanja oil and its blends in a single cylinder agricultural diesel engine, Appl Energy, 86, 106-112. doi:10.1016/j.apenergy.2008.04.008.

Table 3 Physical and Chemical properties of various methyl esters of fatty acids*

Biodiesel Type	Density kg/m ³	Kine-matic Viscosity at 40°C mm ² /s	Surface Tension mN/m	Iodine value	Cetane number	Boiling point K	Flash point K	Pour point K	Heating value MJ/kg	Saturated fatty acids %w	C %m	H %m	O %m	S %m
Canola	912	4.02	27.21	110-120	52	607-623	519		39.7	7.0	77.00	12.2	10.8	
Coconut	918	2.73	24.01	8-10	68		410	269	36.9	81.5				
Corn	910	4.36	28.86	103-128	55	620-649	550		39.5	12.7	76.31	11.14	10.9	0.0003
Cottonseed	915	4.00	26.81	90-119	51	617-652	483	258-279	39.4	23.8			10.6	0.000005
Fish oil	860	7.20			51				41.4	37.3	80.01	12.75	7.2	
Jatropha	940	4.80	30.10	95-105	52	> 633	421	277	38.7	26.2	76.22	12.49	11.29	0.000011
Linseed	924	3.75		168-204	55		514	275	39.3	7.9				
Mahua	882	3.98		88	51	563-583	471		39.4	46.2				
Neem	919	5.21		65-80	51				32.8	39.6				0.001
Olive	880	4.50	28.55	75-94	57		383	270	39.9	20.2				0.0005
Palm	879	4.95	26.16	44-58	56	575-622	408	287-289	39.7	45.6	75.66	12.17	11.3	0.0011
Peanut	903	5.25	26.93	84-100	54		466		39.7	20.8	75.39	11.98	11.0	
Polanga	869	3.99			54		413	277	41.4					
Karanja	936	4.37		117	51		436	278	42.1	29.2	76.83	11.83	11.34	0.000009
Rapeseed	885	4.59	27.82	94-120	54	638-647	420-443	261	39.9	4.34	76.05	12.14	10.8	0.000006
Rice-bran	919	4.96		99-108	51					14.2-21.1				
Soybean	885	4.08	27.15	117-143	46	616-625	414-440	266-272	39.7	15.22	77.00	12.18	10.8	<0.005
Sunflower	885	4.22	28.96	110-143	47	673-657	383	270	39.9	9.34	76.38	11.3	10.9	0.0004
Tallow		4.82	28.39	54	59	610-613			40.1	47-63				
Yellow grease	872	5.92		80-100	63					36.51	76.66	12.33	11.0	<0.005

*Kalligeros et al., 2003; Yuan et al., 2005; Ejim et al., 2007; Sahoo et al., 2007; Benjumea et al., 2008; Sureshkumar et al., 2008; Lin and Li, 2009; Lin et al., 2009; Oszezen et al., 2009; Sahoo et al., 2009; Sanin et al., 2009; Wu et al., 2009; Yuan and Hansen, 2009; Karmakar et al., 2010; Pugazhavadu and Sankarnarayanan, 2010; Varatharajan and Cheralathan, 2012; Chhetri and Watts, 2013; Fattah et al., 2013; Palash et al., 2013; Sonar et al., 2015; Arbab Iqbal et al., 2015; Mistri et al., 2016.

- [3] Agarwal AK, Chaudhury VH, 2012, Spray characteristics of biodiesel/blends in a high pressure constant volume spray chamber, *Exp Therm Fluid Sci*, 42,212-218. doi:10.1016/j.expthermflusc.2012.05.006.
- [4] Agarwal AK, Dhar A, 2013, Experimental investigations of performance, emission and combustion characteristics of Karanja oil blends fuelled DICl engine, *Renew Energy*, 52, 283-291. doi:10.1016/j.renene.2012.10.015.
- [5] Agarwal AK, Srivastava DK, Dhar A, Maurya RK, Shukla PC, Singh AP, 2013, Effect of fuel injection timing and pressure on combustion, emissions and performance characteristics of a single cylinder diesel engine, *Fuel*, 111, 374-383. doi:10.1016/j.fuel.2013.03.016.
- [6] Allen CAW, Watts KC, Ackman RG, 1999, Predicting the surface tension of biodiesel fuels from their fatty acid composition, *J Am Oil Chem Soc*, 76, 317-323. doi:10.1007/s11746-999-0238-5.
- [7] Allen CAW, Watts KC, 2000, Comparative analysis of the atomization characteristics of fifteen biodiesel fuel types, *Trans ASAE-American Soc Agric Eng*, 43, 207-212.
- [8] Alptekin E, Canakci M, 2009, Characterization of the key fuel properties of methyl ester-diesel fuel blends, *Fuel*, 88, 75-80. doi:10.1016/j.fuel.2008.05.023.
- [9] Alternative Fuels Data Center: Biodiesel Fueling Station Locations. http://www.afdc.energy.gov/fuels/biodiesel_locations.html (accessed June 27, 2015).
- [10] Arslan R, 2013, Emission characteristics of a diesel engine using waste cooking oil as biodiesel fuel, *African J Biotechnol*, 10, 3790-3794. doi:10.5897/AJB10.2202.
- [11] Aydin H, Bayindir H, 2010, Performance and emission analysis of cottonseed oil methyl ester in a diesel engine, *Renew Energy*, 35, 588-592. doi:10.1016/j.renene.2009.08.009.
- [12] Benjumea P, Agudelo J, Agudelo A, 2008, Basic properties of palm oil biodiesel-diesel blends, *Fuel*, 87, 2069-2075. doi:10.1016/j.fuel.2007.11.004.
- [13] Boehman AL, Morris D, Szybist J, Esen E, 2004, The impact of the bulk modulus of diesel fuels on fuel injection timing, *Energy & Fuels*, 18, 1877-1882. doi:10.1021/ef049880j.
- [14] Buyukkaya E, 2010, Effects of biodiesel on a DI diesel engine performance, emission and combustion characteristics, *Fuel*, 2010, 89, 3099-3105. doi:10.1016/j.fuel.2010.05.034.
- [15] Canakci M, 2005, Performance and emissions characteristics of biodiesel from soybean oil, *Proc Inst Mech Eng Part D J Automob Eng*, 219, 915-922. doi:10.1243/095440705X28736.
- [16] Carraretto C, Macor A, Mirandola A, Stoppato A, Tonon S, 2004, Biodiesel as alternative fuel: experimental analysis and energetic evaluations, *Energy*, 29, 2195-2211. doi:10.1016/j.energy.2004.03.042.
- [17] Chavan SB, Kumbhar RR, Kumar A, Sharma YC, 2015, Study of biodiesel blends on emission and performance characterization of VCR engine, *Energy & Fuels*, 29, 4393-4398. doi:10.1021/acs.energyfuels.5b00742.
- [18] Chhetri AB, Watts KC, 2013, Surface tensions of petro-diesel, canola, jatropha and soap nut biodiesel fuels at elevated temperatures and pressures, *Fuel*, 104, 704-710. doi:10.1016/j.fuel.2012.05.006.
- [19] Chokri B, Ridha E, Rachid S, Jamel B, 2012, Experimental Study of a Diesel Engine Performance Running on Waste Vegetable Oil Biodiesel Blend, *J Energy Resour Technol*, 134, 32202. doi:10.1115/1.4006655.
- [20] De Soete GG, 1975, Overall reaction rates of NO and N₂ formation from fuel nitrogen, *Symp. Combust*, 15, Elsevier; 1975, p. 1093-102.
- [21] Dean AM, Bozzelli JW, 2000, Combustion chemistry of nitrogen. In: *Gas-phase Combustion Chemistry*, Springer New York, pp. 125-341. doi:10.1007/978-1-4612-1310-9_2.
- [22] Dhar A, Kevin R, Agarwal AK, 2012, Production of biodiesel from high-FFA neem oil and its performance, emission and combustion characterization in a single cylinder DICl engine, *Fuel Process Technol*, 97, 118-129. doi:10.1016/j.fuproc.2012.01.012.
- [23] Ejim CE, Fleck BA, Amirfazli A, 2007, Analytical study for atomization of biodiesels and their blends in a typical injector: surface tension and viscosity effects, *Fuel*, 86, 1534-1544. doi:10.1016/j.fuel.2006.11.006.
- [24] Environmental Protection Agency US, 2002, Comprehensive analysis of biodiesel impacts on exhaust emissions - Draft Technical Report, EPA420-02-001. Assessment and Standards Division, Office of Transportation and Air Quality.
- [25] Environmental Protection Agency US, 2010, Renewable Fuel Standard Program (RFS2) Regulatory Impact Analysis - EPA-420-R-10-006, Assessment and Standards Division, Office of Transportation and Air Quality.
- [26] Fattah IMR, Masjuki HH, Liaquat AM, Ramli R, Kalam MA, Riazuddin VN, 2013, Impact of various biodiesel fuels obtained from edible and non-edible oils on engine exhaust gas and noise emissions, *Renew Sustain Energy Rev*, 18,552-567. doi:10.1016/j.rser.2012.10.036.
- [27] Fattah IMR, Masjuki HH, Kalam MA, Wakil MA, Ashrafal AM, Shahir SA, 2014, Experimental investigation of performance and regulated emissions of a diesel engine with Calophyllum inophyllum biodiesel blends accompanied by oxidation inhibitors, *Energy Convers Manag*, 83, 232-240. doi:10.1016/j.enconman.2014.03.069.
- [28] Fenimore CP, 1971, Formation of nitric oxide in premixed hydrocarbon flames, *Symp. Combust*, 13, 373-380. doi:10.1016/S0082-0784(71)80040-1.
- [29] Fernando S, Hall C, Jha S, 2006, NOx reduction from biodiesel fuels, *Energy & Fuels*, 20, 376-382. doi:10.1021/ef050202m.
- [30] Fontaras G, Karavalakis G, Kousoulidou M, Tzamkiozis T, Ntziachristos L, Bakeas E, Stournas S, Samaras Z, 2009, Effects of biodiesel on passenger car fuel consumption, regulated and non-regulated pollutant emissions over legislated and real-world driving cycles, *Fuel*, 88, 1608-1617. doi:10.1016/j.fuel.2009.02.011.
- [31] Fontaras G, Kalogiros M, Grigoratos T, Pistikopoulos P, Samaras Z, Rose K, 2014, Effect of rapeseed methyl ester blending on diesel passenger car emissions-Part 1: Regulated pollutants, NO/NOx ratio and particulate emissions, *Fuel*, 121, 260-270. doi:10.1016/j.fuel.2013.12.025.
- [32] Godiganur S, Murthy CS, Reddy RP, 2010, Performance and emission characteristics of a Kirloskar HA394 diesel engine operated on fish oil methyl esters, *Renew Energy*, 35, 355-359. doi:10.1016/j.renene.2009.07.007.
- [33] Gumus M, Kasifoglu S, 2010, Performance and emission evaluation of a compression ignition engine using a biodiesel (apricot seed kernel oil methyl ester) and its blends with diesel fuel, *Biomass and Bioenergy*, 34, 134-139. doi:10.1016/j.biombioe.2009.10.010.
- [34] Graboski MS, McCormick RL, Alleman TL, Herring AM, 2003, The effect of biodiesel composition on engine emissions from a DDC series 60 diesel engine, National Renewable Energy Laboratory (Report No: NREL/SR-510-31461).
- [35] Hoekman SK, Broch A, Robbins C, Ceniceros E, 2011, Investigation of biodiesel chemistry, carbon footprint and regional fuel quality. CRC Proj AVFL-17a 2011.
- [36] Hoekman SK, Robbins C, 2012, Review of the effects of biodiesel on NOx emissions, *Fuel Process Technol*, 96, 237-49. doi:10.1016/j.fuproc.2011.12.036.
- [37] Imtenan S, Masjuki HH, Varman M, Kalam MA, Arbab MI, Sajjad H, Ashrafur Rahman SM, 2014, Impact of oxygenated additives to palm and jatropha biodiesel blends in the context of performance and emissions characteristics of a light-duty diesel engine, *Energy Convers Manag*, 83, 149-158. doi:10.1016/j.enconman.2014.03.052.
- [38] Iqbal MA, Varman M, Hassan MH, Kalam MA, Hossain S, Sayeed I, 2015, Tailoring fuel properties using jatropha, palm and coconut biodiesel to improve CI engine performance and emission characteristics, *J Clean Prod*, 101, 262-270. doi:10.1016/j.jclepro.2015.04.011.
- [39] Kalligeros S, Zannikos F, Stournas S, Lois E, Anastopoulos G, Teas C, Sakellaropoulos F, 2003, An investigation of using biodiesel/marine diesel blends on the performance of a stationary diesel engine, *Biomass and Bioenergy*, 24, 141-149. doi:10.1016/S0961-9534(02)00092-2.
- [40] Karavalakis G, Stournas S, Bakeas E, 2009, Light vehicle regulated and unregulated emissions from different biodiesels, *Sci Total Environ*, 407, 3338-3346. doi:10.1016/j.scitotenv.2008.12.063.
- [41] Karmakar A, Karmakar S, Mukherjee S, 2010., Properties of various plants and animals feedstocks for biodiesel production, *Bioresour Technol*, 101, 7201-7210. doi:10.1016/j.biortech.2010.04.079.
- [42] Keskin A, Güri M, Altıparmak D, 2008, Influence of tall oil biodiesel with Mg and Mo based fuel additives on diesel engine performance and emission, *Bioresour Technol*, 99, 6434-6438. doi:10.1016/j.biortech.2007.11.051.
- [43] Klopfenstein WE, 1985, Effect of molecular weights of fatty acid esters on cetane numbers as diesel fuels. *J Am Oil Chem Soc*, 62, 1029-1031. doi:10.1007/BF02935708.
- [44] Knothe G, Sharp CA, Ryan TW, 2006, Exhaust emissions of biodiesel, petrodiesel, neat methyl esters, and alkanes in a new technology engine, *Energy & Fuels*, 20, 403-408. doi:10.1021/ef0502711.
- [45] Labeckas G, Slavinskas S, 2005, The effect of rapeseed oil methyl ester on direct injection diesel engine performance and exhaust emissions, *Energy Convers Manag*, 47, 1954-1967. doi:10.1016/j.enconman.2005.09.003.
- [46] Lee CS, Park SW, Kwon S II, 2005, An experimental study on the atomization and combustion characteristics of biodiesel-blended fuels, *Energy & Fuels*, 19, 2201-2208. doi:10.1021/ef050026h.
- [47] Lertsathapornuk V, Pairintra R, Aryusuk K, Krisnangkura K, 2008, Microwave assisted in continuous biodiesel production from waste frying palm oil and its performance in a 100 kW diesel generator, *Fuel Process Technol*, 89, 1330-1336. doi:10.1016/j.fuproc.2008.05.024.
- [48] Lim C, Lee J, Hong J, Song C, Han J, Cha J-S, 2014, Evaluation of regulated and unregulated emissions from a diesel powered vehicle fueled with diesel/biodiesel blends in Korea, *Energy*, 77, 533-541. doi:10.1016/j.energy.2014.09.040.
- [49] Lin Y, Wu YG, Chang C-T, 2007, Combustion characteristics of waste-oil produced biodiesel/diesel fuel blends, *Fuel*, 86, 1772-1780. doi:10.1016/j.fuel.2007.01.012.
- [50] Lin BF, Huang JH, Huang DY, 2009, Experimental study of the effects of vegetable oil methyl ester on DI diesel engine performance characteristics and pollutant emissions, *Fuel*, 88, 1779-1785. doi:10.1016/j.fuel.2009.04.006.
- [51] Lin CY, Li RJ, 2009, Engine performance and emission characteristics of marine fish-oil biodiesel produced from the discarded parts of marine fish, *Fuel Process Technol*, 90, 883-888. doi:10.1016/j.fuproc.2009.04.009.
- [52] Lissianski V, Zamansky V, Gardiner W, 2000, Combustion Chemistry Modeling. In: Gardiner Jr. WC, editor. *Gas-Phase Combustion Chemistry*, Springer New York pp. 1-123. doi:10.1007/978-1-4612-1310-9_1.
- [53] Löffler G, Sieber R, Harasek M, Hofbauer H, Hauss R, Landauf J, 2006, NO x formation in natural gas combustion—a new simplified reaction scheme for CFD calculations, *Fuel*, 85, 513-23.
- [54] Luján JM, Bermúdez V, Tormos B, Pla B, 2009, Comparative analysis of a DI diesel engine fuelled with biodiesel blends during the European MVEG-A cycle: Performance and emissions (II), *Biomass and Bioenergy*, 33, 948-956. doi:10.1016/j.biombioe.2009.02.003.
- [55] Meher LC, Sagar DV, Naik SN, 2006, Technical aspects of biodiesel production by transesterification - a review, *Renewable and sustainable energy reviews*, 10, 248-268. doi:10.1016/j.rser.2004.09.002.

- [56] Miller JA, Bowman CT, 1989, Mechanism and modeling of nitrogen chemistry in combustion, *Prog Energy Combust Sci*, 15, 287-338. doi: 10.1016/0360-1285(89)90017-8.
- [57] Mistri GK, Aggarwal SK, Longman D, Agarwal AK, 2016, Performance and Emission Investigations of Jatropa and Karanja Biodiesels in a Single-Cylinder Compression-Ignition Engine Using Endoscopic Imaging, *J Energy Resour Technol*, 138, 11202. doi:10.1115/1.4031317.
- [58] Moscherosch BW, Polonowski CJ, Miers SA, Naber JD, 2010, Combustion and emissions characterization of soy methyl ester biodiesel blends in an automotive turbocharged diesel engine, *J Eng Gas Turbines Power*, 132, 92806. doi:10.1115/1.4000607.
- [59] Murillo S, Miguez JL, Porteiro J, Granada E, Moran JC, 2007, Performance and exhaust emissions in the use of biodiesel in outboard diesel engines, *Fuel*, 86, 1765-1771. doi:10.1016/j.fuel.2006.11.031.
- [60] Osawa WO, Sahoo PK, Onyari JM, Mulaa FJ, 2015, Experimental investigation on performance, emission and combustion characteristics of croton megalocarpus biodiesel blends in a direct injection diesel engine, *Int J Sci Technol*, 4, 26-33.
- [61] Osborne D, Fritz S, Glenn D, 2011, The effects of biodiesel fuel blends on exhaust emissions from a general electric tier 2 line-haul locomotive, *J Eng Gas Turbines Power*, 133, 102803. doi:10.1115/1.4002916.
- [62] Ozsezen AN, Canakci M, Sayin C, 2008, Effects of biodiesel from used frying palm oil on the exhaust emissions of an indirect injection (IDI) diesel engine, *Energy & Fuels*, 22, 2796-2804. doi:10.1021/ef800174p.
- [63] Padhee D, Raheman H, 2015, Performance, Emissions and Combustion Characteristics of a Single Cylinder Diesel Engine Fuelled with Blends of Jatropa Methyl Ester and Diesel, *Int J Renew Energy Dev*, 3, 125-131. doi:10.14710/ijred.3.2.125-131.
- [64] Palash SM, Kalam MA, Masjuki HH, Masum BM, Fattah IMR, Mofijur M, 2013, Impacts of biodiesel combustion on NO_x emissions and their reduction approaches, *Renew Sustain Energy Rev*, 23, 473-490. doi:10.1016/j.rser.2013.03.003.
- [65] Pereira RG, Oliveira CD, Oliveira JL, Oliveira PCP, Fellows CE, Piamba OE, 2007, Exhaust emissions and electric energy generation in a stationary engine using blends of diesel and soybean biodiesel, *Renew Energy*, 32, 2453-2460. doi:10.1016/j.renene.2006.05.007.
- [66] Pugazhvidivu M, Sankaranarayanan G, 2010, Experimental studies on a diesel engine using mahua oil as fuel, *Indian J Sci Technol*, 3, 788-92.
- [67] Puhana S, Vedaraman N, Ram BV, Sankaranarayanan G, Jeychandran K, 2005, Mahua oil (Madhuca Indica seed oil) methyl ester as biodiesel-preparation and emission characteristics, *Biomass and Bioenergy*, 28, 87-93. doi:10.1016/j.biombioe.2004.06.002.
- [68] Pulkrabek WW, 2004, *Engineering fundamentals of the internal combustion engine*, Pearson Prentice Hall, 2004.
- [69] Raheman H, Phadatar AG, 2004, Diesel engine emissions and performance from blends of karanja methyl ester and diesel, *Biomass and Bioenergy*, 27, 393-397. doi:10.1016/j.biombioe.2004.03.002.
- [70] Sahoo PK, Das LM, Babu MKG, Naik SN, 2007, Biodiesel development from high acid value polanga seed oil and performance evaluation in a CI engine, *Fuel*, 86, 448-454. doi:10.1016/j.fuel.2006.07.025.
- [71] Sahoo PK, Das LM, Babu MKG, Arora P, Singh VP, Kumar NR, Varyani TS, 2009, Comparative evaluation of performance and emission characteristics of jatropa, karanja and polanga based biodiesel as fuel in a tractor engine, *Fuel*, 88, 1698-1707. doi:10.1016/j.fuel.2009.02.015.
- [72] Sarin A, Arora R, Singh NP, Sharma M, Malhotra RK, 2009, Influence of metal contaminants on oxidation stability of Jatropa biodiesel, *Energy*, 34, 1271-1275. doi:10.1016/j.energy.2009.05.018.
- [73] Sequera AJ, Parthasarathy RN, Gollahalli SR, 2011, Effects of fuel injection timing in the combustion of biofuels in a diesel engine at partial loads, *J Energy Resour Technol*, 133, 22203. doi:10.1115/1.4003808.
- [74] Serrano L, Lopes M, Pires N, Ribeiro I, Cascão P, Tarelho L, Monteiro A, Nielsen O, Gameiro da Silva M, Borrego C, 2015, Evaluation on effects of using low biodiesel blends in a EURO 5 passenger vehicle equipped with a common-rail diesel engine, *Appl Energy*, 146, 230-238. doi:10.1016/j.apenergy.2015.01.063.
- [75] Sharma D, Soni SL, Mathur J, 2009, Emission reduction in a direct injection diesel engine fueled by neem-diesel blend, *Energy Sources, Part A*, 31, 500-508. doi:10.1080/15567030701715542.
- [76] Sirignano WA, 1993, Fluid dynamics of sprays - 1992 Freeman scholar lecture, *J Fluids Eng*, 115, 345-378. doi:10.1115/1.2910148.
- [77] Sonar D, Soni SL, Sharma D, Srivastava A, Goyal R, 2014, Performance and emission characteristics of a diesel engine with varying injection pressure and fuelled with raw mahua oil (preheated and blends) and mahua oil methyl ester, *Clean Technol Environ Policy*, 1-13. doi:10.1007/s10098-014-0874-9.
- [78] Song H, Tompkins BT, Bittle JA, Jacobs TJ, 2012, Comparisons of NO emissions and soot concentrations from biodiesel-fuelled diesel engine, *Fuel*, 96, 446-453. doi:10.1016/j.fuel.2012.01.004.
- [79] Suh HK, Rho HG, Lee CS, 2007, Spray and combustion characteristics of biodiesel fuel in a direct injection common-rail diesel engine, *ASME/IEEE 2007 Jt. Rail Conf. Intern. Combust. Engine Div. Spring Tech. Conf.*, American Society of Mechanical Engineers, 487-496. doi:10.1115/JRC/ICE2007-40082.
- [80] Sun J, Caton JA, Jacobs TJ, 2010, Oxides of nitrogen emissions from biodiesel-fueled diesel engines, *Prog Energy Combust Sci*, 36, 677-695. doi:10.1016/j.pecc.2010.02.004.
- [81] Sureshkumar K, Velraj R, Ganesan R, 2008, Performance and exhaust emission characteristics of a CI engine fueled with Pongamia pinnata methyl ester (PPME) and its blends with diesel, *Renew Energy*, 33, 2294-2302. doi:10.1016/j.renene.2008.01.011.
- [82] Szybist JP, Song J, Alam M, Boehman AL, 2007, Biodiesel combustion, emissions and emission control, *Fuel Process Technol*, 88, 679-691. doi:10.1016/j.fuproc.2006.12.008.
- [83] Tan P, Hu Z, Lou D, Li Z, 2012, Exhaust emissions from a light-duty diesel engine with Jatropa biodiesel fuel, *Energy*, 39, 356-362. doi:10.1016/j.energy.2012.01.002.
- [84] Tat ME, Van Gerpen JH, Soyulu S, Canakci M, Monyem A, Wormley S, 2000, The speed of sound and isentropic bulk modulus of biodiesel at 21 C from atmospheric pressure to 35 MPa, *J Am Oil Chem Soc*, 77, 285-289. doi:10.1007/s11746-000-0047-z.
- [85] Tat ME, 2003, Investigation of oxides of nitrogen emissions from biodiesel-fueled engines, Ph.D. Dissertation, Digital Repository at Iowa State University. <http://lib.dr.iastate.edu>, 2003.
- [86] Tat ME, Van Gerpen JH, 2003, Measurement of biodiesel speed of sound and its impact on injection timing, *National Renewable Energy Laboratory, NREL/SR-510-31462*. 2003.
- [87] Tsolakis A, Megaritis A, Wyszynski ML, Theinnoi K, 2007, Engine performance and emissions of a diesel engine operating on diesel-RME (rapeseed methyl ester) blends with EGR (exhaust gas recirculation), *Energy*, 32, 2072-2080. doi:10.1016/j.energy.2007.05.016.
- [88] Usta N, 2005, An experimental study on performance and exhaust emissions of a diesel engine fuelled with tobacco seed oil methyl ester, *Energy Convers Manag*, 46, 2373-2386. doi:10.1016/j.enconman.2004.12.002.
- [89] Utlu Z, Koçak MS, 2008, The effect of biodiesel fuel obtained from waste frying oil on direct injection diesel engine performance and exhaust emissions, *Renew Energy*, 33, 1936-1941. doi:10.1016/j.renene.2007.10.006.
- [90] Van Gerpen J, 2005, Biodiesel processing and production, *Fuel processing technology*, 86, 1097-1107. doi:10.1016/j.fuproc.2004.11.005.
- [91] Varatharajan K, Cheralathan M, 2012, Influence of fuel properties and composition on NO_x emissions from biodiesel powered diesel engines: a review, *Renew Sustain Energy Rev*, 16, 3702-3710. doi:10.1016/j.rser.2012.03.056.
- [92] Wu F, Wang J, Chen W, Shuai S, 2009, A study on emission performance of a diesel engine fuelled with five typical methyl ester biodiesels, *Atmos Environ*, 43, 1481-1485. doi:10.1016/j.atmosenv.2008.12.007.
- [93] Xue J, Grift TE, Hansen AC, 2011, Effect of biodiesel on engine performances and emissions, *Renew Sustain Energy Rev*, 15, 1098-1116. doi:10.1016/j.rser.2010.11.016.
- [94] Ye P, Boehman AL, 2010, Investigation of the impact of engine injection strategy on the biodiesel NO_x effect with a common-rail turbocharged direct injection diesel engine, *Energy & Fuels*, 24, 4215-4225. doi:10.1021/ef1005176.
- [95] Yoon SH, Suh HK, Lee CS, 2009, Effect of spray and EGR rate on the combustion and emission characteristics of biodiesel fuel in a compression ignition engine, *Energy & Fuels*, 23, 1486-1493. doi:10.1021/ef800949a.
- [96] Yuan W, Hansen AC, Zhang Q, 2005, Vapor pressure and normal boiling point predictions for pure methyl esters and biodiesel fuels, *Fuel*, 84, 943-50. doi:10.1016/j.fuel.2005.01.007.
- [97] Yuan W, Hansen AC, Zhang Q, 2007, Computational modelling of NO_x emissions from biodiesel combustion, *Int J Veh Des*, 45, 12-32. doi:10.1504/IJVD.2007.013668.
- [98] Yuan W, Hansen AC, 2009, Computational investigation of the effect of biodiesel fuel properties on diesel engine NO_x emissions, *Int J Agric Biol Eng*, 2, 41-48. doi:10.3965/j.
- [99] Zhang Y, Boehman AL, 2007, Impact of biodiesel on NO_x emissions in a common rail direct injection diesel engine, *Energy & Fuels*, 21, 2003-2012. doi:10.1021/ef0700073.
- [100] Zhang X, Wang H, Li L, Wu Z, Hu Z, Zhao H, 2008, Characteristics of Output Performances and Emissions of Diesel Engine Employed Common Rail Fueled with Biodiesel Blends from Wasted Cooking Oil, *SAE Tech Pap*, 10. doi:10.4271/2008-01-1833.



Advances in Granular Growth Anaerobic Membrane Bioreactor (G-AnMBR) for Low Strength Wastewater Treatment

Cheng Chen, Wenshan Guo, Huu Hao Ngo*

Centre for Technology in Water and Wastewater, School of Civil and Environmental Engineering, University of Technology Sydney, Sydney, NWS 2007, Australia

ARTICLE INFO

Received : 22 August 2015
Revised : 05 October 2015
Accepted : 10 October 2015

Keywords:

granular growth anaerobic membrane bioreactor, low strength wastewater treatment, granular technology, membrane based separation

ABSTRACT

The concept of sustainability has been evolved in the recent years and widely used in reassessing the feasibility of various wastewater treatment technologies. Nowadays, anaerobic bioprocesses are considered as a sustainable technology which has no requirement of oxygen (low cost) while producing bioenergy with low sludge yield. Currently, granular growth anaerobic membrane bioreactor (G-AnMBR), a newly discovered hybrid anaerobic biotechnology, which integrates the granular technology and membrane based separation, has attracted increasing number of studies due to its competitive advantages of less fouling and high energy efficiency. In face of the significance of this hybrid technology, this paper presents an up-to-date review on the performance enhancements of G-AnMBR in low strength wastewater treatment over the last decade while highlighting future research direction in the conclusion.

© 2016 ISEES, All rights reserved

1. Introduction

Anaerobic biotechnology has long been considered as a sustainable approach, which incorporates waste management with the recovery of useful byproducts and renewable bioenergy. The worldwide application of anaerobic processes would not only alleviate environmental pollution but also ease the stress on energy insecurity, global demand on fossil fuels, continuous exploitation of limited natural resources and the emission of toxic air pollutants, particularly greenhouse gases to the atmosphere [Khanal, 2008]. Moreover, compared to the aerobic counterparts, the operational costs of aeration and sludge dewatering/disposal in anaerobic bioprocesses are distinctly reduced as no oxygen is required and sludge yield is much lower. Additionally, anaerobic treatment has the storage capability unfed for several months without serious deterioration and still generates biogas [Lim and Kim, 2014].

Anaerobic granulation is an autoimmobilization in which fluffy biosolids assemble and agglomerate as dense and compact granules under controlled operational conditions. Compared to the conventional bioflocs, anaerobic granules have a regular and well-defined shape, strong structure, and good settling velocities. They enable high biomass retention and withstand high strength wastewater and shock loadings. This means that the formation of anaerobic granular sludge allows the decoupling of hydraulic retention time (HRT) and solid retention time (SRT), and therefore the efficient treatment of wastewater can be carried out at much

higher organic loading rates (OLRs) with a significantly reduced reactor footprint. Anaerobic granular sludge bioreactor (AnGSB) technology has been extensively employed in industrial and municipal wastewater treatment practices since 1980 [Lettinga et al., 1984]. However, AnGSB technology has to overcome some drawbacks which includes: (i) the requirement of extremely long start-up period, (ii) a relatively high operation temperature, (iii) unsuitability for low strength organic wastewater such as municipal wastewater, (iv) poor capability of removing nutrients, and (v) post treatment required to meet discharge standards [Liu and Tay, 2004; Liu et al., 2004; Lim and Kim, 2014]. Recent research efforts have been mainly directed to the discovery of specific high rate AnGSB technology that could resolve the above-mentioned disadvantages. Theoretically, the sufficient inoculation of seed granular sludge in operating AnGSB has the advantage of achieving high organics removal within an accelerated startup period. Some researchers also added additives such as natural polymers, cationic polymers and hybrid polymers to promote particle agglomeration, in order to realize shortening of startup time and enhancement of granulation [Show et al., 2004; Wang et al., 2004; Jeong et al., 2005; Tiwari et al., 2005; Cao et al., 2010]. Zhang et al. [2009] showed that rapid startup could be successfully accomplished by using a hybrid upflow anaerobic blanket (UASB) – anaerobic fixing filter (AFF) reactor with internal hydraulic circulation and external sludge circulation. Jung et al. [2013] also adopted high rate circulation to

* Corresponding Author: Email address: h.ngo@uts.edu.au, ngohuuhaol21@gmail.com; Tel: +61 2 9514 2745;

accelerate the formation of hydrogen-producing granules in a UASB. Many investigators have also devoted themselves into modifying the reactor design and developing hybrid anaerobic systems for treating various types of wastewaters. Ikuo et al. [2010] reported that an expand granular sludge bed (EGSB) bioreactor, a modified UASB configuration, has the capability of treating low strength wastewaters at low temperature. Li et al. (2007) studied the performance of an integrated EGSB-Zeolite bed filtration (EGSB-ZBF) hybrid system for the removal of carbon and nutrients from low strength wastewater at 35°C for 7 month and the combined system could effectively reduce the COD concentration by 71.58%, and completely remove Ammonia and phosphate. Anaerobic Ammonium Oxidation (ANAMMOX) - EGSB combined system is a novel nitrogen removal process that achieved the nitrogen remove efficiency up to 94.68% [Chen et al., 2011]. As advanced membrane-based separations are well suited to water recycling and reuse, membrane coupled AnGSB technology (so called granular growth anaerobic membrane bioreactor G-AnMBR) is now experiencing a rapid growth as a tertiary treatment process for treating municipal wastewater as compared to suspended growth anaerobic membrane bioreactors (S-AnMBRs) [Salazar-Pelaez et al., 2011a; Salazar-Pelaez et al., 2011b; Herrera Robledo et al., 2010; Herrera-Robledo et al., 2011; Liu et al., 2013].

There are several reviews papers which focused on the specific factors affecting granulation in UASB [Abbasi and Abbasi, 2012], the applicability of UASB, EGSB and static granular bed reactor (SGBR) [Lim and Kim, 2014], the application of anaerobic hydrogen-producing granules [Li and Yu, 2013], the feasibility of granule-based anaerobic baffled bioreactor (GAnBR) [Hassan and Dahlan, 2013], and performance enhancement of upflow anaerobic sludge blanket (UASB) reactors [Chong et al. 2012], theories on anaerobic sludge granulation [Hulshoff Pol et al., 2004]. However, there is still a lack of reviews and documentation on the enhancements of G-AnMBR with collective information. With the rapid development of G-AnMBR technology, a comprehensive analysis of recent research progress would be useful.

Thus, the main objective of this review is to provide an in-depth literature review to the recent advances made in developing sustainable G-AnMBR, with emphasis on G-AnMBR performance for municipal wastewater treatment, to serve as a guideline for rapid granulation process, as well as to provide a solid platform for the development of novel G-AnMBR.

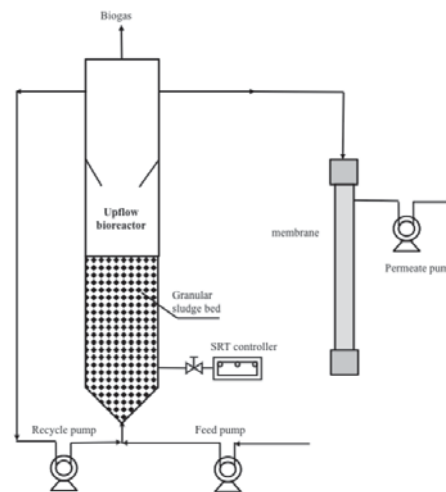
2. Granular growth anaerobic membrane bioreactor (G-AnMBR)

2.1. G-AnMBR reactors

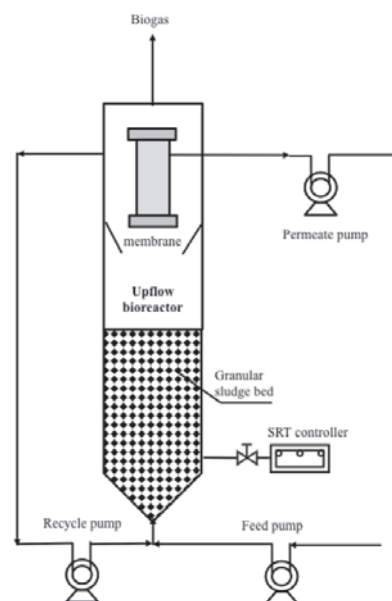
In the recent years, G-AnMBR has experienced increasing applications due to its superior performance such as high effluent quality, complete biomass retention, high biomass content, less sludge bulking problem, relatively low-rate sludge production, higher loading capacity, compact design and rapid start-up period. The G-AnMBR consists of an anaerobic granular growth bed reactor such as upflow anaerobic sludge blanket (UASB) and a membrane module. Membrane unit could be externally connected to the granule bed system as the side-stream mode (Fig. 1a), submerged in the granular sludge bed reactor (Fig. 1b) or immersed in a separated bioreactor (Fig. 1c). Polymeric membranes such as polyvinylidene fluoride (PVDF) and polyethersulfone (PES) were predominantly used in G-AnMBR mainly due to economic concerns. In regards to filtration, both microfiltration (MF) and ultrafiltration (UF) membranes are the most common ones, with membrane pores ranging from 0.4 μm [Diez et al. 2012], 0.2 μm [Lew et al., 2009] or 0.1 μm [Liu et al., 2013] in the MF region to values as low as 30kDa [Gao et al., 2010] in the UF region. Hollow fiber membrane configuration gained the most popularity as compared to flat sheet (plate or frame) and tubular modes in G-AnMBR studies.

2.2. Granular growth AnMBR versus Suspended growth AnMBR

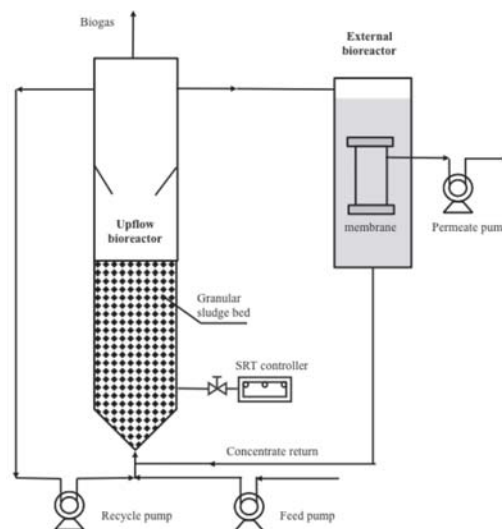
G-AnMBR offers a promising alternative approach to the traditional suspended growth AnMBR (S-AnMBR). These conventional AnMBRs generally consist of completely stirred tank reactors (CSTRs) with either internal or external membrane separation devices, and they are operated based on suspended growth pattern. AnMBRs studies by far were predominantly S-AnMBRs [Huang et al., 2011; Martinez-Sosa et al., 2011; Martinez-Sosa et al., 2012], because of the ease of use and construction. However, critical obstacles including membrane fouling, low flux and high operational costs still exist and limit the wider application of S-AnMBR. Traditional AnMBR was usually operated at a lower biomass concentration compared to high rate anaerobic reactors (HRARs)



(a) External crossflow G-AnMBR (membrane as solo polishing step)



(b) G-AnMBR with membrane place directly in the reactor (Membrane as part of G-AnMBR)



(c) SAnMBR with the membrane immersed in a separated bioreactor (Membrane as part of G-AnMBR)

Figure 1. Schematic of G-AnMBR configurations

mainly due to fouling issues, corresponding to a lower OLR (<10 kg COD/m³/d) [Lin et al., 2013]. To maintain a well mixed flow regime and sufficient mass transfer, rigorous mechanic mixing is required, which is energy intensive. In addition, the membrane unit is directly exposed to the bulk sludge, and the high suspended solid concentration subjected to MF/UF membrane filtration worsen cake deposition and compaction in all CSTR configurations [Liao et al., 2006, Ozgun et al., 2013]. More rapid and dense cake layer build-up results in heavy membrane fouling and low flux, as under sufficient mixing, effluent solids concentration of CSTRs remains the same as the bulk solids concentration. To resolve this

issue, frequent physical and chemical cleaning, interval operation, and likely sub-critical flux operation to sustain the flux should be in place. Moreover, a dramatic decrease in the sludge floc size owing to sludge recirculation through the membrane feed pump can result in severe membrane fouling [Ozgun et al., 2013], particularly in the side-stream membrane configurations. The high shear stress may also impact the biological activities of anaerobic microbes due to negatively impacted juxtapositioning of acetogens and methanogens, restricting the essential hydrogen transport for acquiring a superior specific methanogenic activity (SMA).

Table 1 Comparison of conventional aerobic treatment, anaerobic treatment, S-AnMBR and G-AnMBR

Feature aerobic treatment	Conventional anaerobic treatment	Conventional	S-AnMBR	G-AnMBR
Organic removal efficiency	High	High	High	High
Effluent quality	High	Moderate to poor	High	High
Organic loading rate	Moderate	Moderate	High	High
Sludge production	High	Low	Low	Low
Footprint	High	High	Low	Low
Biomass Retention	Low to moderate	Low	High	Excellent
Nutrient requirement	High	Low	Low	Low
Alkalinity requirement	Low	High	High to moderate	High to moderate
Energy requirement	High	Moderate to low	Moderate to low	Low
Bioenergy recovery	No	Yes	Yes	Yes
Mode of treatment	Total	Essentially pretreatment	Total or pretreatment	Total or pretreatment
Mode of Operation	Continuous	Batch/continuous	Continous	Continuous
Start-up time	2-4 weeks	2-4 months	< 2 weeks	<1 weeks or 2-4 month
Types of Wastewaters	Low to moderate	High to moderate	High to low	High to low
Membrane fouling	-	-	High to moderate	Moderate to low
Mode of Operation	Continuous	Batch/continuous	Continuous	Continuous

Table 1 represents a comparison of conventional aerobic treatment, anaerobic treatment, S-AnMBR and G-AnMBR. It is apparent that as a hybrid system, G-AnMBR combines the advantages of granular technology and MBR technology, yielding maximum joint benefits. Firstly, biomass retention is achieved by the spontaneous formation of granular sludge, and the granule bed systems are characterized by total suspended solids (TSS) concentrations ranging between 20 and 40 g/L reactor volume; whereas significantly lower effluent total solids (TS) concentration at 50 mg/L was possible [An et al., 2009] and this makes them feasible for high organic and hydraulic loadings. Since biomass is not directly exposed to a membrane module in this reactor design, less apparent dense cake layer formation and consolidation will occur in comparison with conventional S-AnMBR when coupling these reactors with a membrane module. Secondly, the natural occurring turbulence caused by the rising biogas bubbles and liquid upflow force, which buoy the granular sludge, provides sufficient substrate and microorganism contact so as mechanical mixing is no longer required and relevant operational cost would be greatly decreased [Chong et al., 2012]. In addition, less severe fouling is found in G-AnMBR configuration, thus allowing enhanced operation with reduced gas sparging demand and increased fluxes [Martin-Garcia, 2010]. Mathioudakis et al. [2012] reported that the net specific operational energy demand of a G-AnMBR based flowsheet treating 10,000 m³d⁻¹ domestic sewage was around 0.14kWhm⁻³ whereas the values for immerse AnMBR configurations could be as high as 3.57 kWhm⁻³. The potential of the proposed GAnMBR offers high treatment efficiency with significantly reduced energy demand as compared to traditional sewage treatment. For example, for the typical specific net energy demand of a typical activated sludge plant utilizing anaerobic sludge digestion can be more than 0.6kWhm⁻³ [Martin et al., 2011]. Most importantly, the granule structure offers ideal conditions for syntrophic associations such as those between H₂-accumulating acetogenic bacteria and H₂-consuming methanogens, allowing high chemical oxygen demand (COD) removal efficiencies even under presence of toxicity or hydraulic loading events [Ozgun et al., 2013]. The compactness of the granules also renders a more compact reactor design, resulting in a much smaller footprint to apply this technology. Apart from the above-mentioned benefits, the capital cost of UASB reactors can also be reduced when coupling a membrane unit and it is by eliminating the necessity for a gas-liquid-solids (GLS) separator in a UASB [Liao et al., 2006]. However, the high sludge carry over to the effluent can occur with increased biogas production when operating in the absence of GLS. Last but not least, the granulation process and start-up period can be greatly reduced due to the membrane absolute barrier to provide the complete retention of methanogens.

2.3. G-AnMBR development

Recent studies on G-AnMBRs were predominantly applied to low strength municipal wastewater treatment rather than high strength organic industrial wastewaters such as brewery and alcohol-distillery wastewater. Municipal wastewater has long been categorized into complex wastewater due to its high fraction of particulate organic material, moderate biodegradability and its low strength. For this reason, domestic sewage treatment by anaerobic means is still challenging due to the kinetic limitations of anaerobic metabolism. Low substrate affinity of anaerobic biomass compared to aerobic bacteria and the rate-limiting step of hydrolysis of particulate matter into dissolved molecules particularly under low temperature (<20 °C) conditions have made it hardly practical to achieve low effluent chemical oxygen demand (COD) concentrations and to fulfill more stringent legislation for wastewater reclamation and reuse [Ozgun et al., 2013; Lin et al., 2013]. G-AnMBRs have offered the most sustainable options of municipal wastewater treatment and reuse essential in all the land-scarce, water-short and energy-poor countries. **Table 2** presents a number of studies that have used G-AnMBRs for treating domestic wastewater under various operating conditions. G-AnMBRs have typically shown high COD/TOC removal efficiencies with 77%-97% and this high efficiency could be sustained even at psychrophilic temperature and high hydraulic loading rate.

2.3.1. Membrane as solo polishing step

A pilot scale UASB reactor followed by a post-treatment external UF membrane operating at different HRTs (12-4 h) was able to achieve permeate free of total suspended solids (TSS), and with COD concentration less than 120 mg/L for the treatment of real domestic wastewater with a high variability in its characteristics [Salazar-Pelaez et al., 2011a]. In spite of high variations in COD, total solids (TS), volatile total solids (VTS) and total suspended solids (TSS) concentrations by sediments washout from pipelines in the rainy seasons, the combined system consistently produced permeate fulfilling the Mexican standards established for wastewater reclamation in public services at all times. Similarly, such a system of lab scale yielded a slightly better total COD removal (89 and 82% respectively at HRT of 8 and 12h) than that of a UASB reactor alone at the steady state in treating synthetic wastewater with average COD concentration at 350 mg/L at ambient temperature [Salazar-Pelaez et al., 2011b]. However, as suggested by the authors, the transition to lower HRT (12 to 4 h) deteriorated the AnMBR performance by inducing a higher production of soluble microbial products (SMP) and extracellular polymeric substances (EPS) and particle release in UASB

Table 2 Summary of G-AnMBR performance for municipal wastewater treatment

Type of wastewater	Innoculum	Scale	Volume (L)	Reactor configuration	Characteristics of membrane	Operating condition	Removal efficiency (%)	Reference
Domestic wastewater (COD=100-2600 mg/L)	Digested sludge	L	17.7	Hybrid upflow anaerobic bioreactor + submerged membrane	PE Hollow fibre UF pore size: 0.03µm Surface area: 0.3 m ²	OLR= 0.5 - 12.5 kg COD/m ³ /d HRT=6 and 4 h Ambient temperature SRT=150 d Flux= 5 LMH MLSS=16-22.5 g/L	COD= 97%	Wen et al. (1999)
Synthetic wastewater (COD=383-849 mg/L)	Granular sludge	L	4.7	EGSB with submerged membrane	PE Hollow fibre MF pore size: 0.1µm Surface area: 0.1 m ²	UV ^b = 2-8 m/h OLR= 1.6- 4.5 kg COD/m ³ /d HRT=3.5, 4.6 and 5.7 h Temp= 25, 20 and 15°C	COD= 85-96%	Chu et al. (2005)
Raw municipal wastewater (COD=58-348 mg/L)	Digested sludge	P	34	UASB+ external membrane	Polyacrylonitrile Module 1: ID/OD of 1.2/2.1 mm, 0.2m ² Module 2: ID/OD of 1.9/2.9 mm, 0.2 m ² Module 3: ID/OD of 3.0/3.9 mm, 0.2 m ²	OLR= 0.3-0.9 kg OD/m ³ /d Temp= 27-30 ° CCHRT= 5.5-10 h MLSS=12-32 g/L SRT=α	COD= 77-81%	An et al. (2009)
Pre-settled domestic wastewater (COD=540 mg/L)	Granular sludge	L	180	Upflow anaerobic bioreactor + External membrane	PVDF Hollow fibre MF Pore size: 0.20µm Surface area: 4 m ²	OLR= 1.08, 2.16, 4.32 kg COD/m ³ /d Temp= 25 °C SRT=α HRT= 12, 6 and 4.5 h Flux=3.75, 7.5, 11.25 LMHMLSS=14-80 g/L	COD> 88%	Lew et al. (2009)
Synthetic wastewater (COD=500 mg/L)	Granular sludge	L	10	UASB + External membrane	PVDF and PEI Flat sheetUF, 100 kDa MWCO and 30 kDa MWCO Surface area: 0.052 m ²	OLR= 5 kg COD/m ³ /d Temp= 30 °C HRT= 24 h MLSS=12-32 g/L SRT= 50 d	COD= 96%	Gao et al. (2010)
Real municipal wastewater (COD=646 mg/L)	-	L	3.5	UASB+ external membrane	TubularUF, 40 kDa MWCO Surface area: 81 cm ²	Temp= 20-25 °C HRT= 3 hSRT= 60, 100 d	COD= 86-87%	Herrera-Robledo et al. (2010)
Raw sewage (COD=445 ± 138mg/L)	-	L	849	UASB+ external membrane	PVDF Tubular UF, 100 kDa MWCO Surface area: 5.10 m ²	Uv=0.64 m/h Temp=22±3°C Flux=6LMHHRT=6 h SRT=180 d	COD= 93%	Herrera-Robledo et al. (2011)
Synthetic wastewater (COD=350±10 mg/L)	Granular sludge	L	12.5	UASB+ external membrane	PVDF Tubular UF, 100 kDa MWCO	UV ^b = 0.122, 0.061 and 0.041 m/h Temp= 27-30 ° C HRT= 4, 8 and 12 hpH= 7, Flux=5 LMH	COD= 81-89%	Salazar-Pelaez et al. (2011b)
Real domestic wastewater (COD=285-2,088 mg/L)	Granular sludge	P	700	UASB + External membrane	PVDF TubularUF, 100 kDa MWCO Surface area: 0.84 m ²	SRT=150 dAmbient temperature HRT= 4, 8, 12 h	COD= 86-96%	Salazar-Pelaez et al. (2011a)
Settled primary wastewater (COD=338±74 mg/L)	Granular sludge	P	125	Upflow anaerobic tank+ external membrane	PVDF Hollow fibre UF pore size: 0.08µm Surface area: 0.93 m ²	Uv=0.7-1 m/hTemp=8-22°C Flux=6LMHHRT=16h	COD= 84-86%	Garcia et al. (2013)
Synthetic wastewater (COD=500±10 mg/L)	Granular sludge	L	10	UASB with submerged membrane	PVDF Hollow fibre MF pore size: 0.1µm Surface area: 1 m ²	UV ^b = 2.5m/hOLR= 1 and 6 kg COD/m ³ /dTemp= 27-30 ° CHRT= 2 and 12 hFlux=5 LM HMLSS= 1.6 and 10.1 g/L	COD= 97%	Liu et al.(2012) Liu et al.(2013)
Synthetic wastewater (530±40mg/L)	Flocculent anaerobic sludge	L	7	UASB+ external MBR	PES TubularUF pore size: 30nm Surface area: 0.0038 m ²	UV ^b = 0.6 m/hOLR= 2 kg COD/m ³ /dTemp= 25 °C HRT= 6 h Flux= 12.3LMH	COD= 92%	Ozgun et al. (2015)

effluent, thus eventually increased COD and solids concentrations in both, UASB effluent and permeate (total COD removal 81% vs 89% in the case of Salazar-Pelaez et al., 2011b). The authors attributed declined removal efficiency to the following reasons. Firstly, the operation of UASB reactor at a low HRT consequently resulted in higher upflow velocity and OLR, therefore increasing shear forces inside the reactor and biogas production. Both facts caused solids washout as well as particle disaggregation and stress in microorganisms and promote biopolymer release in its effluent [Wang et al., 2009]. Secondly, the lower removal efficiency was mainly due to the limited contact time between microorganisms and substrate for the physical and biological processes at low HRTs. The last but not least, the system was incapable of retaining UASB sludge, and therefore had the decreased filtration capacity of the sludge bed at higher upflow velocities [Leitão et al., 2005]. The enhanced release of biopolymeric substances in the effluent at lowest HRT also worsened the fouling propensity in the UASB effluent by increasing the fouling rate and the specific cake resistance and decreasing particle sizes. Therefore, both studies recommended to avoid operating AnMBR (UASB + external UF arrangement) at HRTs lower than 4 hours in order to control SMP and EPS fouling potential, and maintain better COD removal performance.

On the other hand, An et al. [2009] showed that with gradually decreasing HRT from 10 to 5.5 h, the application of membrane filtration as a polishing unit of UASB effluent could achieve better TOC removal efficiency from 80% to 85%, and much higher biogas yield from 61.8 to 120.7 mL/g COD_{removed} in treating raw municipal wastewater at ambient temperature in Singapore. Such a behavior at lower HRT was attributed to the increased upflow velocity which improved water distribution and provided more even contact between substrate and microorganism, and higher sludge loading rate in a low-strength wastewater treatment system, which favored the anaerobic microorganisms activity. Their investigation also indicated that periodic 20 seconds backwash every 10 min suction presented the best result to reduce fouling and membrane cleaning frequency and prolonged membrane longevity.

Herrera-Robledo et al. [2010] showed that with HRTs (3h) more than three times lower than those in full-scale UASB applications for municipal wastewater treatment, the operation of UASB+MBR process at ambient temperature in southern Mexico City was still feasible. They compared the performance of this combined system operated at two different SRTs (100 and 60 d) at local temperatures of 20-25°C, and found there was no difference on COD removal efficiency (COD_i and COD_s removal efficiencies of over 85% and 73% were achieved in the parallel systems, compared to 50% in the UASB reactors alone, suggesting that such a hybrid system operated at relatively low HRT and SRT is viable at the Mexican climate conditions. Their investigation also indicated that longer SRTs operation during long-term operation of 500 h resulted in more repetitive sudden TMP and flux changes which might be explained by a fouling lay collapse and compression hypothesis for cross-flow membrane ultrafiltration, suggesting a stronger fouling layer structure. Furthermore, Herrera-Robledo et al. [2011] demonstrated the efficacy of a high rate UASB-MBR for raw sewage treatment at HRT and SRT of 6 h and 180 d in producing an effluent free of suspended solids, pathogens (fecal coliforms) and parasite ova, with 93% COD removal and 73% phosphorous reduction (sorption by the biofouling or even chemical precipitation through biomineralization), that met official Mexican regulation for direct urban water reclamation. Based on fouling analysis, SMP with size lower than membrane pores (89 mg/L) tended to absorb on membrane surface or inside the pores, and were considered significant for fouling development. It was also suggested that a mild cleaning procedure using chlorine (NaClO at 300 mg/L, for 30 min) accomplished a limited removal of fouling mass per unit area (13%), and the biofouling remnants was partly resulted from biologically-induced mineralization materials that were synthesized (massive EPS secretion from colonizing cells) in response to cleaning procedure, and may be the basis of irreversible membrane fouling.

The studies mentioned above have used the membrane unit as a solo polishing step after the UASB reactor. In such a configuration, the concentrate streams were not recycled back to the bioreactors, and therefore the hydraulics and biogranulation in the UASB reactors remained undisturbed from the membrane incorporation, resulting in continuous selection of stable granules with good settling properties for efficient anaerobic digestion. Nevertheless, Ozgun et al. [2015] elucidated that the addition of membrane as an absolute barrier could cause a detrimental effect on the suspended solids (SS) accumulation in the membrane tank situated after UASB reactors, contributing to an intensifying increase in the SS loading on the membrane unit and subsequent high tendency to foul.

2.3.2. Membrane as part of G-AnMBR

A great number of studies have suggested employing membranes as an element of a G-AnMBR system to provide nearly absolute biomass retention and allow for operation at high SRTs via concentrate flow recycle to the granular reactor, thus leading to the enhanced reactor performance subject to psychrophilic methanogenesis, high loading events, loading shocks and climate temperature fluctuations [Chu et al., 2005; Liu et al., 2012; Liu et al., 2013]. Membranes in these systems are either located as an external side-stream [Lew et al., 2009; Garcia et al., 2013; Ozgun et al., 2015] in which the concentrate is recycled back to the granular bioreactor or submerged at the top of the reactor [Chu et al., 2005; Liu et al., 2013; Wen et al., 1999]. In such a setup, the membrane is not simply regarded as a physical barrier, but also facilitates a general cultural adaptation to the prevailing loading conditions of the reactor environment.

Liu et al. [2012] utilized a granule based AnMBR system in which a MF hollow fiber membrane was immersed in the expanded section to evaluate the impact of food-to-microorganisms (F/M) ratio on the system performance and fouling treating low strength wastewater at 27-30°C. They reported impressive reclamation with the TOC removal efficiency of more than 96% in the high load AnMBR. However, they observed more severe fouling in the high load G-AnMBR as compared to the low load system, with cake resistance responsible for over 98% of the total fouling in both systems. This higher cake resistance was attributed to higher amounts of SMP and higher tightly-bound to loosely-bound EPS ratio in the cake layer whereas the greater amount of fine particles in the high loading system was also responsible for more serious fouling. The authors pointed out that membrane filtration deteriorate sludge biofloculation, which in turn exacerbated membrane fouling, and a lower F/M ratio and strategies for cake layer elimination were preferred for the long term sustainable operation of AnMBRs. Thereafter, Liu et al. [2013] used the same system to evaluate specific enhancement of the UASB performance by incorporating submerged membrane to the overloaded reactor at mesophilic temperatures, and obtained similar TOC removal of 97% at HRT of 2 h and specific organic loading rate (SOLR) of 3.8 kg COD/kg MLSS/d. Linear increased TOC removal from 55% to 91% by bulk sludge mainly accounted for the enhanced performance, implying that submerged membrane addition overcame the upper SOLR limit in the UASB reactor treating low strength wastewater and significantly enhanced biological activity of the suspended sludge when encountering the high loading events. One of the major advantages of this system was the membrane retention of biomass with sufficiently high SMA and an especially beneficial and diverse microbial community structure predominated by Methanotrix-like bamboo shaped rods when the loading rate is too high for sufficient sludge retention and when the high quality effluent is required for reclamation. The author also suggested that the enhancement by the membrane incorporation to the UASB was featured by two phenomenal behaviors: (1) the comparatively higher removal by the membrane at the early transition stage when the process was adapting to the introduced membrane, and (2) dramatic increase in the bulk removal during the adaption stage as well as gradual decrease in the membrane removal to the steady state.

On the other hand, Ozgun et al. [2015] reported that the introduction of membrane to a UASB reactor significantly affects the system in both biological and physical perspectives. Membrane incorporation induced the deterioration of sludge settleability and more frequent sludge washout, due to the decreasing of particle size distribution (PSD) caused by an accumulation of fine particles and decreasing EPS, thus causing a resultant increase in COD and total suspended solids (TSS) and SMP concentrations in the UASB effluent. The authors justified that, despite the SMA and stability of the UASB sludge deteriorated after membrane incorporation, the increase in microbial community index in both richness and evenness was found, and hence the enhancement in overall system performance was observed in terms of higher COD removal efficiency of 92% (72% COD reduction before membrane addition) and more methane production at HRT of 6 h, due to the complete retention of all particulate and colloidal matter and biomass inside the reactor by the membrane. In addition, the stable transmembrane pressure (TMP) was observed at 85 mbar in average during AnMBR operation, indicating no severe membrane fouling propensity was encountered.

Lew et al. [2009] on the other hand, suggested that at temperature of 25°C, using an HRT and OLR ranging from 4.5 to 12 h, and 1.08 to 4.32 kg COD/m³/d, an innovative external G-AnMBR, in which the traditional cross-flow external membrane unit was replaced by a microfiltration, hollow fiber, dead end external unit placed below the bioreactor effluent exit, would provide the most energy efficient measure of municipal wastewater treatment than other AnMBR configurations, due to the enough

transmembrane pressure provided by the height difference between the bioreactor and the membrane which allowed no pump used for recirculation or transmembrane pressure enhancement, promoting energy savings. Furthermore, as suggested by the authors, intermittent backwash was adopted for fouling amelioration instead of gas bubbling scouring most often found in other studies [Garcia et al., 2013; Huang et al., 2011; Lin et al., 2009], and the best backwash frequency for energy savings and fouling mitigation of 30-60 min. EPS was found as the fouling agent during slow linear increase of fouling rate, according to the observation of the sulfate and aliphatic accumulation on the membrane.

In order to widely apply G-AnMBR technology, anaerobic reclamation of low strength municipal sewage should be maintained under ambient temperature (7-20°C) due to the excessive energy cost for heating [Martin et al., 2011]. However, problems still remain in terms of psychophilic methane fermentation. For instance, the anaerobic process requires a long start-up period, its performance may be unstable, and the kind of wastewater that can be treated is limited due to the activity of methanogen [Ikko et al., 2010]. Lettinga et al. [2001] suggested that AnMBR operation at psychophilic temperature is technically feasible, although sludge retention time (SRT) must be maintained twice those commonly applied in mesophilic operation, causing SRTs of 120-160 d. Nevertheless, in light of the limitation of anaerobic metabolism below 20°C, only partial solid hydrolysis and incomplete digestion of volatile fatty acids into methane are achieved, resulting in the increase in colloidal and soluble solids content in anaerobic effluents and on membrane fouling propensity [Kashyap et al. 2003]. Garcia et al. (2013) compared the treatment efficiency and membrane performance of a granular and suspended growth anaerobic membrane bioreactor (G-AnMBR and S-AnMBR respectively) for 250 days treating settled sewage under UK weather conditions, and concluded the impact of configuration was negligible with COD and BOD removal of 80-95% and >90%. As temperature dropped from 20°C to 10°C, COD removal efficiency experienced noticeable reduction from 97% to 78%, due to the production of non-biodegradable organics rather than the accumulation of VFAs at lower temperatures. This study also confirmed the lower fouling potential in the G-AnMBR as compared to the S-AnMBR, due to the reduced solid and colloidal load (by a factor of 10 and 3) to the membrane which was allowed by the enhanced interception of solids in the granule bed of the G-AnMBR as a result of mixed liquid recycle from the membrane tank to the bioreactor at a low upflow velocity. Similarly, van Voorthuizen et al. [2008] reported the much severer fouling in an anaerobic MBR as compared to an UASB coupled to membrane unit due to the accumulation of higher amount of colloidal matter. They suggested the reduced colloidal matter was mainly due to G-AnMBR biodegradation of dissolved organics taken place predominately within the granules, and colloidal particles arising from the influent solids [Lant and Hartley, 2007] physically adsorbed and retained in the granule bed protecting the membrane from their influence on fouling. Therefore, the granular system would require lower gas sparging intensity and lower energy requirements for fouling control [van Voorthuizen et al., 2008]. Moreover, energy efficiency could be further enhanced especially when backwashing was implemented within the granular AnMBR [Garcia et al. 2013].

Singh et al. [2006] reported that the dead space of the UASB reactor was 10%-11% and it is dependent upon the operating temperature, which meant the smaller volume of mixing zone the more by-pass flow can occur in the reactor when low temperature is applied. Therefore, UASB reactors treating municipal wastewater at low and moderate temperatures are sometimes characterized by a poor mixing regime, which causes a decrease in soluble COD treatment efficiency. To resolve this issue, tall reactors with a higher ratio of height to width and external or internal effluent recirculation, so-called EGSB reactors, are increasingly applied to provide a very high mixing intensity and efficient wastewater-biomass contact induced by the high upflow velocity. In the study of Chu et al., [2005], a U shape hollow fiber membrane submerged in the upper part of EGSB, was utilized for treating domestic wastewater during 7-month period in the range 11–25°C, and at HRT of 3.5 to 5.7 h. At temperatures above 15°C, the combined system had the capability of removing 85–96% of total COD and 83–94% of TOC despite HRT variations. However, at 11°C, increasing HRT from 3.5 to 5.7 h contributed to the enhanced COD removal from 76 to 81%, which indicated the significance of HRT for low strength wastewater treatment at lower temperature. Upflow velocity, as the other important parameter governing hydraulic mixing, was found significant in achieving better effluent removal efficiency, and a higher membrane permeability due to a rinsing effect on the membrane at the low temperature. Nevertheless, the granule segregation was also induced by the high upward velocity, which was found from granule size

distribution and SMA test along the sludge bed. This study showed that psychophilic sewage treatment using EGSB reactor coupled with membrane technology is feasible, due to the intensified mass transfer between substrate and microbes and viable retention of granule sludge comprised predominantly of filamentous Methanothrix-like species.

Although many studies have proved the competitive advantages of such G-AnMBRs configurations in municipal wastewater treatment, hydraulic selection pressure required for granulation is minimized by the membrane barrier in these cases, through the avoidance of the washout of flocculent sludge with poor immobilization characteristics [Ozgun et al., 2013], thus resulting in a sludge bed with poor settling properties in granule reactors in the long term. Furthermore, the high fraction of partly degradable particulate matter in domestic wastewater, which can be entrapped and gradually accumulated in the granular sludge bed, may further impede the applicability of granular reactors in an G-AnMBR system configuration in the long-term operation.

3. Conclusion

G-AnMBR can be seen as a promising technology for low strength wastewater treatment (e.g. municipal wastewater) compared to traditional S-AnMBR due to its better treatment efficiency with significantly low energy consumption. G-AnMBR has superior quality of granular sludge, which leads to less fouling propensity, enhanced operation with no mechanical mixing, reduced gas sparging demand, and increased membrane flux. G-AnMBR has strong potential to cope with high hydraulic loading events and high organic loading events despite the need of further investigation on granular deterioration. In light of the inherent eco-friendly nature of psychophilic G-AnMBR without heating, and so as to overcome the temperature constraints on anaerobic bioprocesses, further studies are necessary to investigate microbial community structure of granules at lower temperature and their influence on process stability towards accomplish kinetic perspective-based improvement of biogas production.

Acknowledgements

This work was supported by Centre for Technology in Water and Wastewater (CTWW), School of Civil and Environmental Engineering (CEE), University of Technology Sydney (UTS) and Australian Postgraduate Award.

References

- [1] Abbasi T, Abbasi SA, 2012, Formation and impact of granules in fostering clean energy production and wastewater treatment in upflow anaerobic sludge blanket (UASB) reactors, *Renewable and Sustainable Energy Review*, 16, 1696-1708.
- [2] An YY, Yang FL, Buccioli B, Wong FS, 2009, Municipal wastewater treatment using a UASB coupled with cross-flow membrane filtration, *Journal of Environmental Engineering*, 135, 86–91.
- [3] Cao Y, Zhang M, Shan S, 2010, Effect of two-added powdered bamboo-charcoal on sludge granulation of UASB reactor, *Chinese Society of Agricultural Engineering*, 26(5), 246-50.
- [4] Chen TT, Zheng P, Tang CJ, Wang S, Ding S, 2011, Performance of ANAMMOX-EGSB reactor, *Desalination*, 278, 281-287.
- [5] Chong S, Sen TK, Kayaalp A, Ang HM, 2012, The performance enhancements of upflow anaerobic sludge blanket (UASB) reactors for domestic sludge treatment- A State-of-the-art review, *Water Research*, 46, 3434-3470.
- [6] Chu LB, Yang FL, Zhang XW, 2005, Anaerobic treatment of domestic wastewater in a membrane-coupled expanded granular sludge bed (EGSB) reactor under moderate to low temperature, *Process Biochemistry*, 40(3-4), 1063-70.
- [7] Diez V, Ramos C, Cabezas JL, 2012, Treating wastewater with high oil and grease content using an Anaerobic Membrane Bioreactor (AnMBR), *Filtration and cleaning assays*, *Water Science Technology*, 65 (10), 1847–1853.
- [8] Gao DW, Zhang TC, Tang YY, Wu WM, Wong CY, Lee YH, Yeh DH, Criddle CS, 2010, Membrane fouling in an anaerobic membrane bioreactor: differences in relative abundance of bacterial species in the membrane foulant layer and in suspension, *Journal of Membrane Science*, 364, 331–338. (
- [9] Garcia IM, Moksosch M, Soares A, Pidou M, Jefferson B, 2013, Impact of reactor configuration on the performance of anaerobic MBRs: Treatment of settled sewage in temperature climates, *Water Research*, 47, 4853-4860.
- [10] Hassan SR, Dahlan I, 2013, Anaerobic wastewater treatment using anaerobic baffled bioreactor: a review, *Central European Journal of Engineering*, 3(3), 389-399.
- [11] Herrera-Robledo M, Morgan-Sagastume JM, Noyola A, 2010, Biofouling and pollutant removal during long-term operation of an anaerobic membrane bioreactor treating municipal wastewater, *Biofouling*, 26 (1), 23–30.
- [12] Herrera-Robledo M, Cid-Leon DM, Morgan-Sagastume JM, Noyola A, 2011, Biofouling in an anaerobic membrane bioreactor treating municipal sewage, *Separation and Purification Technology*, 81, 49–55.
- [13] Hulshoff Pol LW, de Castro Lopes SI, Lettinga G, Lens PNL, 2004, Anaerobic sludge granulation, *Water Research*, 38, 1376-1389.

- [14] Huang Z, Ong SL, and Ng HY, 2011, Submerged anaerobic membrane bioreactor for low-strength wastewater treatment: effect of HRT and SRT on treatment performance and membrane fouling, *Water Research*, 45, 705–713.
- [15] Ikuo T, Wilasinee Y, Hiroki Y, Nobuo A, Kazuaki S, 2010, Microbial community structure and population dynamics of granules developed in expanded granular sludge bed (EGSB) reactors for the anaerobic treatment of low-strength wastewater at low temperature. *Journal of Environmental Science and Health, Part A: Toxic/Hazardous Substances and Environmental Engineering*, 45:6, 754-766.
- [16] Jeong HS, Kim YH, Yeom SH, Song BK, Lee SI, 2005, Facilitated UASB granule formation using organic-inorganic hybrid polymers, *Process Biochemistry*, 40(1), 89-94.
- [17] Jung KW, Cho SK, Yun YM, Shin HS, Kim DH, 2013, *International Journal of Hydrogen Energy*, 38, 9097-9103.
- [18] Kashyap DR, Dadhich KS, Sharma SK, 2003, Biomethanation under psychrophilic conditions: a review, *Bioresource Technology*, 87(2), 147–153.
- [19] Khanal SK, 2008. Overview of Anaerobic Biotechnology, in *Anaerobic Biotechnology for Bioenergy Production: Principles and Applications*, Khanal SK (Eds.), *Anaerobic Biotechnology for Bioenergy Production: Principles and Applications*, Wiley-Blackwell, Oxford, UK
- [20] Lant P, Hartley K, 2007, Solids characterisation in an anaerobic migrating bed reactor (AMBR) sewage treatment system, *Water Research* 41(11), 2437-2448.
- [21] Leitão, RC, Silva-Filho JA, Sanders W, Van Haandel AC, Zeeman G, Lettinga G, 2005, The effect of operational conditions on the performance of UASB reactors for domestic wastewater treatment, *Water Science and Technology*, 52 (1–2), 299–305.
- [22] Lettinga G, Hulshoff Pol LW, Koster IW, Wiegant WM, de Zeeuw WJ, Rinzema A, 1984, High-rate anaerobic wastewater treatment using the UASB reactor under a wide range of temperature conditions, *Biotechnology & Genetic Engineering Reviews*, 2, 253–84.
- [23] Lettinga G, Rebac S, Zeeman G, 2001, Challenge of psychrophilic anaerobic wastewater treatment, *Trends in Biotechnology*, 19 (9), 363-370.
- [24] Lew B, Tarre S, Beliaevski M, Dosoretz C, Green M, 2009, Anaerobic membrane bioreactor (AnMBR) for domestic wastewater treatment, *Desalination*, 243, 251–257.
- [25] Li X, Guo L, Yang Q, Zeng G, Liao D, 2007, Removal of carbon and nutrients from low strength domestic wastewater by expanded granular sludge bed-zeolite bed filtration (EGSB-ZBF) integrated treatment concept, *Process Biochemistry*, 42(8), 1173-9.
- [26] Li WW, Yu HQ, 2013, Anaerobic Granule Technologies for Hydrogen Recovery from Wastes: The Way Forward, *Critical Reviews in Environmental Science and Technology*, 43(12), 1246-1280.
- [27] Liao BQ, Kraemer JT, Bagley DM, 2006, Anaerobic membrane bioreactors: Applications and research directions, *Critical Reviews of Environmental Science and Technology*, 36, 489–530.
- [28] Lim SJ, Kim TH, 2014, Applicability and trends of anaerobic granular sludge treatment processes, *Biomass and Bioenergy*, 60, 189-202.
- [29] Lin HJ, Xie K, Mahendran B, Bagley DM, Leung KT, Liss SN, Liao BQ, 2009, Sludge properties and their effects on membrane fouling in submerged anaerobic membrane bioreactors (SAnMBRs), *Water Research*, 43, 3827–3837.
- [30] Lin H, Peng W, Zhang M, Chen J, Hong H, Zhang Y, 2013, A review on anaerobic membrane bioreactors: Applications, membrane fouling and future perspectives, *Desalination*, 314, 169–188.
- [31] Liu Y, Tay JH, 2004, State of the art of biogranulation technology for wastewater treatment, *Biotechnology Advances*, 22, 533-563.
- [32] Liu Y, Yang SF, Tay JH, Liu QS, Qin L, Li Y, 2004, Cell hydrophobicity is a triggering force of biogranulation, *Enzyme and Microbial Technology*, 34, 371-379.
- [33] Liu Y, Liu HN, Cui L, Zhang KS, 2012, The ratio of food-to-microorganism (F/M) on membrane fouling of anaerobic membrane bioreactors treating low-strength wastewater, *Desalination*, 297, 97-103.
- [34] Liu Y, Zhang KS, Bakke R, Li CM, Liu HN, 2013, Membrane installation for enhanced upflow anaerobic sludge blanket (UASB) performance, *Journal of Bioscience and Bioengineering*, 116(3), 357-361.
- [35] Martin I, Pidou M, Soares A, Judd S, Jefferson B, 2011, Modeling the energy demands of aerobic and anaerobic membrane bioreactors for wastewater treatment, *Environmental Technology* 32, 921-932.
- [36] Martin-Garcia I, 2010, Sludge free and energy neutral treatment of sewage, Ph.D. thesis, Cranfield University, UK.
- [37] Martinez-Sosa D, Helmreich B, Netter T, Paris S, Bischof F, 2011, Anaerobic submerged membrane bioreactor (AnMBR) for municipal wastewater treatment under mesophilic and psychrophilic temperature conditions, *Bioresource Technology*, 102, 10377–10385.
- [38] Martinez-Sosa D, Helmreich B, Horn H, 2012, Anaerobic submerged membrane bioreactor (AnMBR) treating low-strength wastewater under psychrophilic temperature conditions, *Process Biochemistry*, 47, 792–798.
- [39] Mathioudakis VL, Soares A, Briens H, Martin-Garcia I, Pidou M, Jefferson B, 2012, Treatment and energy efficiency of a granular sludge anaerobic membrane bioreactor handling domestic sewage, *Procedia Engineering*, 44, 1977-1979.
- [40] Ozgun H, Dereci RK, Ersahin ME, Kinaci C, Spanjers H, van Lier JB, 2013, A review of anaerobic membrane bioreactors for municipal wastewater treatment: Integration options, limitations and expectations, *Separation and Purification Technology*, 118, 89-104.
- [41] Ozgun H, Gimenez JB, Ersahin ME, Tao Y, Spanjers H, van Lier JB, 2015, Impact of membrane addition for effluent extraction on the performance and sludge characteristics of upflow anaerobic sludge blanket reactors treating municipal wastewater, *Journal of Membrane Science*, 479, 95-104.
- [42] Salazar-Pelaez ML, Morgan-Sagastume JM, Noyola A, 2011a, Influence of hydraulic retention time on UASB post-treatment with UF membranes, *Water Science Technology*, 64, 2299–2305.
- [43] Salazar-Pelaez ML, Morgan-Sagastume JM, Noyola A, 2011b, Influence of hydraulic retention time on fouling in a UASB coupled with an external ultrafiltration membrane treating synthetic municipal wastewater, *Desalination*, 277 (1–3), 164–170.
- [44] Show KY, Wang Y, Foong SF, Tay JH, 2004, Accelerated start-up and enhanced granulation in upflow anaerobic sludge blanket reactors, *Water Research*, 38, 2293-2304.
- [45] Singh KS, Viraraghavan T, Bhattacharyya D, 2006, Sludge blanket height and flow pattern in UASB reactors: temperature effects, *Journal of Environ Engineering*, 132(8), 895-900.
- [46] Tiwari MK, Guha S, Harendranath CS, Tripathi S, 2005, Enhanced granulation by natural ionic polymer additives in UASB reactor treating low-strength wastewater, *Water Research*, 39(16), 3801-10.
- [47] van Voorhuizen E, Zwijnenburg A, van der Meer W, Temmink H, 2008, Biological black water treatment combined with membrane separation, *Water Research*, 42 (16), 4334-4340.
- [48] Wang Y, Show KY, Tay JH, Sim, KH, 2004, Effects of cationic polymer on start-up and granulation in upflow anaerobic sludge blanket reactors, *Journal of Chemical Technology and Biotechnology*, 79(3), 219-28.
- [49] Wang Z, Wu Z, Tang S, 2009, Extracellular polymeric substances (EPS) properties and their effects on membrane fouling in a submerged membrane bioreactor, *Water Research* 43 (9), 2504–2512.
- [50] Wen C, Huang X, Qian Y, 1999, Domestic wastewater treatment using an anaerobic bioreactor coupled with membrane filtration, *Process Biochemistry*, 35, 335–340.
- [51] Zhang YB, Ma YG, Quan X, Jing YW, Dai SC, 2009, Rapid startup of a hybrid UASB-AFF reactor using bi-circulation, *Chemical Engineering Journal*, 155, 266-271.

a footnote to that author's name. The address at which the author actually did the work must be retained as the main, affiliation address. Superscript Arabic numerals are used for such footnotes.

Abstract

A concise and factual abstract is required. Each paper should be provided with an abstract of about 150-200 words. The abstract should state firstly the aim of the study and then give main results. Do not give any introductory remarks here and it should not contain any reference.

Keywords

Immediately after the abstract, provide a maximum of five keywords.

Abbreviations

Define abbreviations in the text itself on first appearance. Avoid any non-standard abbreviation, or give them as a separate section.

Units

Follow internationally accepted rules and conventions: use the international system of units (SI). If other units are mentioned, please give their equivalent in SI.

Math formulae

Present simple formulae in the line of normal text where possible and use the solidus (/) instead of a horizontal line for small fractional terms, e.g., X/Y . In principle, variables are to be presented in italics. Powers of e are often more conveniently denoted by exp. Number consecutively any equations that have to be displayed separately from the text (if referred to explicitly in the text).

Footnotes

As far as possible, footnotes should be avoided. In the tables, indicate each footnote with a superscript lowercase letter

Figures and captions

There can be a maximum of SIX figures in the article, which must be numbered. All photographs, schemas, graphs and diagrams to be referred to as figures. Ensure that each figure has a caption. Captions should be supplied separately on a page. Multiple figures can be expressed as one figure (for e.g. 1a, 1b, 1c, etc). The Journal discourages publication of simple one line graphs/figures, pattern figures, conventional spectra (X-ray, FTIR, UV, NMR, etc) and SEM photographs of a routine nature.

Tables

There can be a maximum of SIX tables in the article, which must be numbered. Heading should be placed above the table. Do not put vertical rules in the table. The Journal discourages publication of simple one parameter tables; such information should be preferably described in the text itself.

References

- In the text, reference should be given by the names of authors and years in square brackets. Only essential references (from SCI journals only), which are directly referred to in the text, should be included in the reference list.
- There can be maximum 40 and 100 references for the original and review articles, respectively.
- No non-English reference should be included.

Citation in text

Ensure that every reference cited in the text is present in the reference list (and *vice-versa*). Unpublished results and personal communications are not recommended in the reference list, but may be mentioned in the text.

Web references

As a minimum, the full URL should be given and the date when the reference was last accessed. Any further information, if known (DOI, author names, dates, reference to a source publication, etc.), should also be given.

Reference style

Text: All citations in the text should refer to:

1. *Single author:* the author's name (without initials) and the year of publication;

2. *Two authors:* both authors' names (without initials) and the year of publication;
3. *Three or more authors:* first author's name (without initials), followed by 'et al.' and the year of publication.

Citations: Citations may be made directly or parenthetically. Examples: 'as demonstrated [Allan, 2000a, 2000b, 1999; Allan and Jones, 1999]. Kramer et al. [2010] have recently shown'

List: References should be arranged first alphabetically and numbered then numerically to show the total number of references in the article. More than one reference from the same author(s) in the same year must be identified by the letters 'a', 'b', 'c', etc., placed after the year of publication.

Examples:

- Reference to a journal publication: Van der Geer J, Hanraads JAJ, Lupton RA, 2010, The art of writing a scientific article, *Journal of Scientific Communications*, 163, 51–59
- Reference to a book: Strunk Jr W, White EB, 2000. *The Elements of Style*, 4th Edn, Longman, New York, USA
- Reference to a chapter in an edited book: Mettam GR, Adams LB, 2009. How to prepare an electronic version of your article, In: Jones BS, Smith RZ (Eds.), *Introduction to the Electronic Age*, E-Publishing Inc, New York, USA pp. 281–304
- References in the list should be placed in alpha-bet order and then numbered numerically as shown below.
 - [1]. Mettam GR, Adams LB, 2009, How to prepare an electronic version of your article, In: Jones BS, Smith RZ (Eds), *Introduction to the Electronic Age*, E-Publishing Inc., New York, USA, pp. 281-304
 - [2] Strunk Jr, W, White EB, 2000, *The Elements of Style*, 4th Edn, Longman, New York, USA
 - [3] Van der Geer J, Hanraads JAJ, Lupton RA, 2010, The art of writing a scientific article. *Journal of Scientific Communications*, 163, 51-59

Journal abbreviations source:

Journal names should be abbreviated according to the List of title word abbreviations: <http://www.issn.org/2-22661-LTWA-online.php>.

Publication of the Articles

After the acceptance of the article, the journal will publish the articles as soon as possible, both online and in print.

Proofs

One set of page proofs (as PDF files) will be sent to the corresponding author by email. PDF proofs can be annotated for corrections, or you may list the corrections (including replies to the Query Form) and return them to Elsevier by email e-mail. Please list your corrections quoting line number. If, for any reason, this is not possible, then mark the corrections and any other comments (including replies to the Query Form) on a printout of your proof and return by fax, or scan the pages and send by e-mail. Please use the proof only for checking the typesetting, editing, completeness and correctness of the text, tables and figures. Significant changes to the article as accepted for publication will only be considered at this stage with permission from the Editor. Corrections must be returned within 48 hours.

Offprints

The corresponding author, at no cost, will be provided with a PDF file of the article via e-mail. Paper reprint can be obtained on charge basis, which must be ordered at the time of proofs correction.

Copyright

Upon acceptance of an article, authors will be asked to complete a 'Journal Publishing Agreement', which will be sent to the corresponding author for transferring the copyright to the International Society for Energy, Environmental and Sustainability. Authors will have rights to reuse the work for themselves or their institution with due citation for internal purposes. Permission must be sought to re-use it for external purposes.

Journal of Energy and Environmental Sustainability (JEES)

[An official publication of the International Society for Energy, Environment and Sustainability]

Guide for authors

Submission of papers: Manuscripts should be submitted to the editor-in-chief, Prof Avinash Agarwal by email at editor@jees.in as single PDF file containing text, tables and figures. A separate file containing the covering letter should also be submitted.

Covering letter to the editor: When submitting the manuscript, it is mandatory to include a covering letter to the editor. The covering letter must state/provide the followings:

- that it is the original work of the authors,
- that all the authors mutually agree that it should be submitted to the JEES,
- state the novelty of the work,
- names and addresses (including email) of 3-4 experts as possible reviewers,
- select the sub-topic of the work from the subject classification list (select ONE only from the list given below).

Scope and subject classification

10.000 ENERGY SUSTAINABILITY

- 10.010 Energy saving and education
- 10.020 Energy storage
- 10.030 Modeling
- 10.040 Social/economic studies
- 10.050 Sustainable fuels and energy sources

20.000 ENVIRONMENTAL SUSTAINABILITY

- 20.010 Climate change
- 20.020 Emission control
- 20.030 Energy and green-house gases balances
- 20.040 Environment impact assessment
- 20.050 Legislations and regulations
- 20.060 Life cycle assessment

30.000 FOSSIL AND NON-FOSSIL SOURCES OF ENERGY

- 30.010 Coal and lignite
- 30.020 Emission and emission control
- 30.030 Energy materials
- 30.040 Natural gas and oil
- 30.050 Non-hydrocarbon energy

40.000 NEW AND RENEWABLE SOURCES AND PROCESSES OF ENERGY

- 40.010 Algae
- 40.020 Biomass
- 40.030 Catalysis
- 40.040 Combustion
- 40.060 Pyrolysis

50.000 SOLID WASTE MANAGEMENT

- 50.010 Incineration
- 50.020 Recycling
- 50.030 Urban/landfill mining

60.000 THERMAL ENERGY DEVICES

- 60.010 Boilers & Combustors
- 60.020 Fuel Cells
- 60.030 Internal Combustion Engines
- 60.040 Gas Turbines
- 60.050 Steam Turbines
- 60.060 Hydraulic Turbines

70.000 WASTE TREATMENT

- 70.010 Industrial effluent treatment
- 70.020 Municipal waste treatment

Referees

Please submit, with the manuscript, the names, addresses and e-mail addresses of three-four potential experts as possible referees to the work. These persons should not have worked with you closely in recent past. Note that the editors retain the sole right to decide whether or not to use the suggested reviewers.

Preparation of the manuscript

Authors must follow the guide for authors strictly, failing which the manuscripts could be rejected without review. Editors reserve the right to adjust the style to certain standards of uniformity.

Structure

Follow this order when preparing the manuscripts: Title, Authors, Affiliations, Abstract, Keywords, Introduction, Materials and Methods, Results and Discussion, Conclusions, Acknowledgements, References, Figure Captions, Tables and Figures. The corresponding author (one only) should be identified with an asterisk and footnote. Email id of all the authors must be provided.

Text Layout

Use double spacing and wide (3 cm) margins on white paper. Avoid full justification, i.e., do not use a constant right-hand margin. Ensure that each new paragraph is clearly indicated. Each table and figure should be placed on separate pages at the end of the manuscript. Number all the pages consecutively, use 12-point Roman font throughout.

Page length

Maximum page length can be 35 and 45 pages (double space typed, Roman 12 font) for original article and review paper, respectively, including text, references, tables and figures. Each figure/table must be placed on separate page.

Article structure

Subdivision - numbered sections: Divide your article into clearly defined and numbered sections. Subsections should be numbered 1.1 (then 1.1.1, 1.1.2, ...), 1.2, etc. (the abstract is not included in section numbering).

Introduction: Provide an adequate background, avoiding a detailed literature survey or a summary of the results on the topic. Most recent and relevant developments on the topic must be brought out here. The last paragraph should state the objective of the study.

Material and Methods: This section should provide sufficient detail to allow the work to be reproduced. Methods already published should be indicated by a reference: only relevant modifications should be described.

Results and Discussion: Results should be clear and concise and be part of a single section, discussing the significance of the results of the work, not repeat them. Extensive citation and discussion of the published literature should be avoided.

Conclusions: The main conclusions drawn from results should be presented in a short Conclusions section (maximum 150 words).

Title page information

- Title should be concise and informative. It must not contain any abbreviation.
- Author names and affiliations. Where the family name may be ambiguous (e.g., a double name), please indicate this clearly. Present the authors' affiliation addresses (where the actual work was done) below the names. Indicate all affiliations with a lower-case superscript letter immediately after the author's name and in front of the appropriate address. Provide the full postal address of each affiliation, including the country name and, if available, the e-mail address of each author.
- Corresponding author: Indicate one author who will handle correspondence at all the stages of refereeing, publication and post-publication. Provide the phone and fax numbers (with country and area code), e-mail address and complete postal address.
- Present/permanent address. If an author has moved since the work described in the article was done, or was visiting at the time, a 'Present address' (or 'Permanent address') may be indicated as

(Continued on inside back cover)